DOE Award No.: DE-FE0031544

Final Report

Reporting Period End Date: March 31, 2023

Integration of seismic-pressure-petrophysics inversion of continuous active-seismic monitoring data for monitoring and quantifying CO_2 plume

Project Period: January 24, 2018- December 30, 2022

Report Submission Date: May 02, 2023

Submitted by
Tieyuan Zhu

Tieyuan Zhu

Signature

Project team: Tieyuan Zhu (Penn State), Eugene Morgan (Penn State), Sanjay Srinivasan (Penn State), Jonathan Ajo-Franklin (Rice University), Alexander Sun (UT-Austin)

The Pennsylvania State University
College of Earth and Mineral Sciences
Department of Geosciences
406 Deike Building, University Park, PA, 16802, USA.
Phone Number: 814-863-7112
E-mail: tyzhu@psu.edu
Duns Number: 003403953

Prepared for:
United States Department of Energy
National Energy Technology Laboratory

DISCLAIMER

EXECUTIVE SUMMARY

The overall objective of this project is to develop and validate an integrated package of joint seismic-pressure-petrophysics inversion (jSPPI) of continuous active-source seismic monitoring dataset capable of providing real-time monitoring of CO_2 plume during geologic carbon sequestration (GCS). **The three specific developments include:**

(a) the methodologies for fast seismic full waveform inversion of continuous active source seismic monitoring, (CASSM) datasets for simultaneously estimating velocity and attenuation, and with data assimilation;

(b) joint Bayesian petrophysical inversion of seismic models and pressure data for providing and updating CO_2 saturation models;

(c) the methods using multiple datasets including (Crainfield and Frio-II borehole) synthetic, laboratory, and field CASSM datasets.

The outcomes of jSPPI include (a) a workflow for processing CASSM data, (b) Bayesian inversion algorithms using CASSM data and pressure response data, and (c) integration with data assimilation algorithms for continuously updating site-specific models used for prediction and reservoir management. The validation of joint FWI will be conducted using synthetic models based on the Cranfield and Frio experiments as well as field CASSM datasets collected as part of the Frio-II pilot injection. To quantify and map the mass and distribution of CO_2 (saturation), we will jointly invert velocity and attenuation measurements from the FWI with a Bayesian approach using a rock physics model for attenuation (e.g., White's attenuation model with two selected patch sizes (White, 1976; Dutta and Seriff, 1979)). The Bayesian inversion will be applied to each time step in the CASSM survey in an updating scheme, which integrates with an ensemble of reservoir simulations at each step. A more complete experimental validation dataset will be collected as part of a mesoscale (2-3 m) gas-CO_2 injection experiment utilizing a higher frequency version of the CASSM system developed for laboratory studies; the integrated inversion will be demonstrated using this dataset which will provide both a dense geometry as well as more precise secondary confirmation measurements (e.g. saturation) typically not available in the field. The resulting real-time map of CO_2 saturation is able to provide a deeper scientific understanding of the complex, time-varying dynamics of subsurface fluid flow migration path as well as the rapid detection of CO_2 leakage hazards.

Our final technical report include six chapters. In 1st chapter, we describe the fast joint FWI framework for the CASSM system to obtain seismic velocity and attenuation models. In 2nd chapter, we validate the method on simulated and field CASSM datasets in the Frio and Cranfield sites followed by development of time-lapse FWI methodologies suitable for reliable real-time monitoring. In 3rd and 4th chapters, we present a reservoir modeling and Bayesian petrophysical inversion framework, and subsequently integrate this petrophysical inversion with fluid flow modeling. In 5th chapter, we describe the laboratory test of the proposed seismic-petrophysical inversion approach with the CASSM monitoring system in a controlled subsurface experiment. In 6th chapter, we describe the application of the integrated method to a field CASSM dataset. The primary novel scientific contribution of our proposal is the development of integrated full waveform seismic-petrophysical inversion with existing CASSM technologies to allow quantitative analysis of the CO2 saturation during long-term monitoring. In the final chapter, we introduce a future direction – combining our algorithm with machine learning.

Table of Contents

Introduction

A major challenge for geological storage of anthropogenic carbon dioxide (CO_2) as an effective and environmentally sound mitigation strategy is to demonstrate that the injected CO_2 will be safely contained within the intended formations. In this regard, the ability to accurately monitor and map the position of the CO_2 plume over time in subsurface environments, as well as detecting and quantifying any potential leakage, is crucial. Accurately and rapidly generated monitoring results provide engineers critical time to respond to possible hazards (CO_2 leakage). Achieving these goals is challenging for current seismic monitoring strategies, with sparse time-lapse surveys and based on single seismic velocity measurement. Sparse time-lapse surveys present only poor temporal resolution of the evolution of the CO_2 plume and easily introduce spatial artifacts of the CO_2 plume boundaries because of non-repeatability noise between surveys. Continuous active-source seismic monitoring (CASSM) provides the highest resolution in the time and remains a promising technology for improving the spatial resolution. Moreover, P-wave velocity has been theoretically and experimentally found to be relatively insensitive to CO_2 saturation at higher saturation levels while seismic attenuation is sensitive to large gas saturations up to 30–50% (Carcione et al., 2006; Lei and Xue, 2009; Azuma et al., 2014; Caspari et al., 2014). Monitoring and quantifying the CO_2 plume requires a systematic approach that integrates both seismic velocity and attenuation models at the seismic scale. In addition, pressure-based monitoring technology is a sensitive technique for early leakage detection and is broadly deployed in GCS (Sun et al. 2013). Integration of seismic- and pressure-based technologies could maximize the beneficial use of both techniques and further reduce uncertainty. Such integration is further strengthened with the advent of Bayesian inversion incorporating multi-physics reservoir simulation and rock physics models that will achieve the most accurate characterization of the CO_2 plume.

In this project, we develop and validate an integrated package of joint seismic-pressure-petrophysics inversion (jSPPI) of continuous active-source seismic monitoring dataset capable of providing real-time monitoring of CO2 plume during geologic carbon sequestration (GCS). The major research objectives are to

(a) develop methodologies for fast seismic full waveform inversion of CASSM datasets for simultaneously estimating velocity and attenuation, and with data assimilation;
(b) develop joint Bayesian and deep learning petrophysical inversion of seismic models and pressure data for providing and updating CO2 saturation models;
(c) demonstrate the methods using multiple datasets including (surface and borehole) synthetic, laboratory, and field CASSM datasets.

The outcomes of jSPPI will include (a) a workflow for processing CASSM data, (b) Bayesian inversion algorithms using CASSM data and pressure response data, and (c) integration with data assimilation algorithms for continuously updating site-specific models used for prediction and reservoir management. The results will be presented in below 6 chapters.

Joint full waveform inversion of seismic velocity and attenuation

The objectives of the task include:
(1) Derive a viscoacoustic wave equation to model the seismic wavefields in attenuating media;
(2) Develop a multiparameter full waveform inversion algorithm to recover both velocity and attenuation structures simultaneously;
(3) Study the Frio II CO2 injection model to understand the applicability of the seismic methods in the CASSM setting.

1 Viscoacoustic wave equation

1.1 Kjartansson model

The complex modulus representing the mathematical frequency-independent Q model is given by Kjartansson (1979):

$$M(\omega) = M_0 \left(\frac{i\omega}{\omega_0}\right)^{2\gamma}, \tag{1}$$

where ω_0 is the reference angular frequency, M_0 is a real parameter with the dimension of bulk modulus and $\gamma = \frac{1}{\pi}\arctan\left(\frac{1}{Q}\right)$ is a dimensionless parameter roughly proportional to Q^{-1}. Based on this mathematical model, we obtain the Kjartansson complex wavenumber:

$$k(\omega) = \frac{1}{c}\omega_0^{\gamma}\omega^{1-\gamma}e^{i\left(-\frac{\pi\gamma}{2}\right)}, \tag{2}$$

where $c = \sqrt{\frac{M_0}{\rho_0}} = c_0\cos\left(\frac{\pi\gamma}{2}\right)$, ρ_0 is the ambient density and c_0 is the reference phase velocity defined at reference frequency ω_0. The real and imaginary parts of the complex wavenumber govern the two attenuation associated effects, i.e., the velocity dispersion and amplitude decay, respectively. Quantitatively, the dispersion of the phase velocity c_p and the attenuation factor α are expressed as: $c_p(\omega) = c_0\left(\frac{\omega}{\omega_0}\right)^{\gamma}$ and $\alpha(\omega) = \frac{\omega}{c_0}\left(\frac{\omega}{\omega_0}\right)^{-\gamma}\tan\left(\frac{\pi\gamma}{2}\right)$.

1.2 Derivation of the fractional viscoacoustic wave equation

Our goal is to derive an approximate viscoacoustic wave equation that produces the Kjartansson complex wavenumber so that both attenuation-associated effects (dispersion and dissipation) are honored. In the meantime, we require that the spatial derivatives in the time-space domain equation only consists of fixed power (fractional) Laplacian operators so as to be effectively handled using the pseudospectral method. The Fourier transform of the fractional Laplacian is given by Chen & Holm (2004) as $(-\nabla^2)^{\frac{\epsilon}{2}} \overset{\mathcal{F}}{\rightarrow} k^{\epsilon}$ while for time derivative we have $i\omega \overset{\mathcal{F}}{\rightarrow} \frac{\partial}{\partial t}$. Hence, a tentative form of the frequency-wavenumber domain wave equation can meet the aforementioned requirements:

$$\omega^2 = \beta_1 k + \beta_2 k^2 + \beta_3 k^3 + \beta_4 (i\omega)k + \beta_5 (i\omega)k^2 + \beta_6 (i\omega)k^3, \tag{3}$$

where $\beta_1, \beta_2 \ldots \beta_6$ are real parameters related to media properties. The problem is converted to determining these parameters $\beta = (\beta_1, \beta_2 \ldots \beta_6)$ so that the solution of Equation (3) approximates the wavenumber given in Equation (2) for all the frequencies. Thus, we plug Equation (2) into Equation (3) and seek for appropriate parameters β to make the left- and right-hand sides equal. To do that, we apply a change of variable $\omega = (1 + x)\omega_0$ and conduct a Taylor analysis. By

selecting a proper reference frequency for the calculation, e.g., setting $\omega_0 = \frac{1}{2}(\omega_{min} + \omega_{max})$ to be the center for the frequency band of interest, we have $-1 \le x \le 1$.

The workflow of the derivation process is shown in Figure 1. To make both sides approximately equal for all the frequencies, we match the coefficients of the real and imaginary parts of the leading terms including x, x^2 and x^3 on both sides. This becomes a 6×6 linear system problem. We then normalize the dimension of the unknown β by solving for $\tilde{\beta} = \left(\frac{1}{c\omega_0}\beta_1, \frac{1}{c^2}\beta_2, \frac{\omega_0}{c^3}\beta_3, \frac{1}{c}\beta_4, \frac{\omega_0}{c^2}\beta_5, \frac{\omega^2}{c^3}\beta_6\right)$.

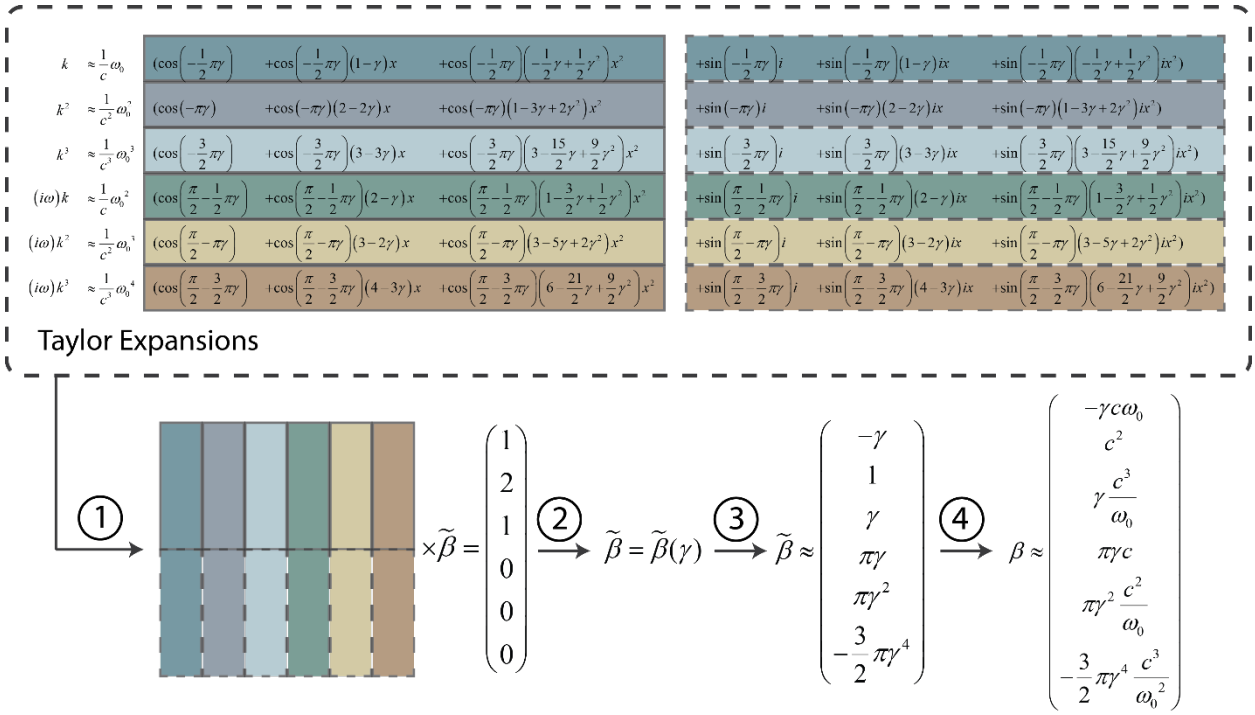

Figure 1. The workflow of the derivation process of the new viscoacoustic wave equation. We start from the Taylor expansions for each term of Equation (2). Different colors indicate the coefficients of different terms while the solid and dashed borders correspond to real and imaginary parts, respectively. The processes marked by numbers are: (1) plug the Taylor expansion expressions into Equation (3) and formulate the 6×6 linear system problem; (2) analytically solve the linear system and obtain a complicated closed form representation of $\tilde{\boldsymbol{\beta}}$, which is a function of $\boldsymbol{\gamma}$; (3) apply a second Taylor expansion with respect to $\boldsymbol{\gamma}$ and preserve the leading term; (4) convert the dimension-normalized parameters $\tilde{\boldsymbol{\beta}}$ back to $\boldsymbol{\beta}$.

The solution of this linear system is a complicated closed-form representation of $\tilde{\beta}$. To further reduce the complexity, we apply a second Taylor expansion for $\tilde{\beta}$ in terms of γ. Taking advantage of symbolic computing (Meurer et al., 2017), which automatically simplifies expressions that are too complicated for manual manipulation into succinct forms, we obtain the clean form of $\tilde{\beta}$ by preserving the leading term. So the resultant β is:

$$(\beta_1, \beta_2, \beta_3, \beta_4, \beta_5, \beta_6) \approx \left(-\gamma c\omega_0, c^2, \gamma\frac{c^3}{\omega_0}, \pi\gamma c, \pi\gamma^2\frac{c^2}{\omega_0}, -\frac{3}{2}\pi\gamma^4\frac{c^3}{\omega_0^2}\right), \quad (4)$$

where the last term β_6 can be safely omitted as it contains γ^4. Substituting Equation (4) into

Equation (3) followed by taking the inverse Fourier transform yields the time-space domain viscoacoustic wave equation:

$$\mathbf{L}u = (\mathbf{L_0} + \mathbf{L_1} + \mathbf{L_2})u = f, \tag{5}$$

where $\mathbf{L}$ is the viscoacoustic wave propagator, $\mathbf{L_0} = \frac{1}{c^2}\frac{\partial^2}{\partial t^2} - \nabla^2$ is the lossless acoustic wave propagator, $\mathbf{L_1} = -\gamma\frac{\omega_0}{c}(-\nabla^2)^{\frac{1}{2}} + \gamma\frac{c}{\omega_0}(-\nabla^2)^{\frac{3}{2}}$ is the phase dispersion corrector, $\mathbf{L_2} = (\pi\gamma\frac{1}{c}(-\nabla^2)^{\frac{1}{2}} - \pi\gamma^2\frac{1}{\omega_0}\nabla^2)\frac{\partial}{\partial t}$ is the amplitude loss (dissipation) corrector, u is the pressure wavefield, f is the source term.

Because of the setup of this wave equation, we can obtain the dispersion-dominated wave equation by dropping the dissipation term:

$$(\mathbf{L_0} + \mathbf{L_1})u = f. \tag{6}$$

Similarly, only preserving the latter dissipation correction term leads to the loss-dominated wave equation:

$$(\mathbf{L_0} + \mathbf{L_2})u = f. \tag{7}$$

This decoupling property has been showed to facilitate the implementation of the Q-compensated reverse time migration (e.g., Zhu, 2014; Zhu et al., 2014)

Figure 2 compares the theoretical and approximate dispersion relations with the Pierre Shale *in situ* data. The comparisons indicate that the approximate curves (solution of Equation 3) agree with the theoretical ones (Equation 2) as well as the measurements, except for the slight phase velocity discrepancy at low frequencies. Hence, our proposed fractional viscoacoustic wave equation can be accurately applied to model wavefields in frequency-independent Q media.

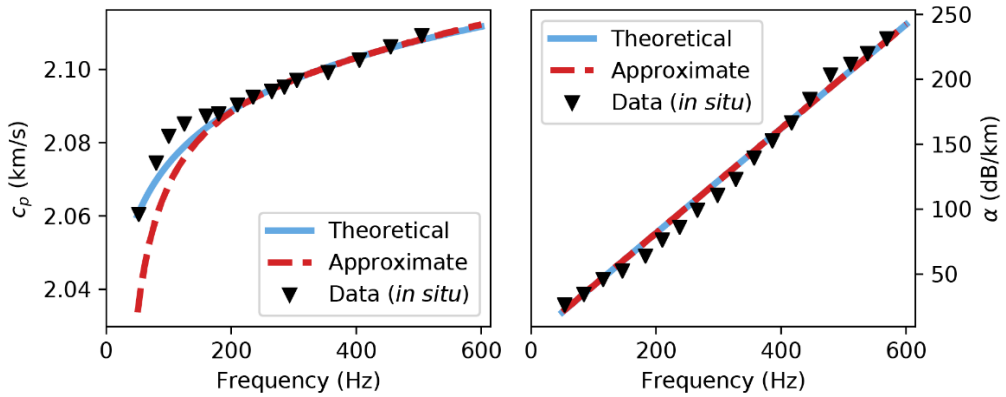

Figure 2. Comparisons between the theoretical (blue solid lines, Equations 2), approximate (red dashed lines, Equation 3) and in situ measured (black triangles) dispersion relations of the Pierre Shale for phase velocity and attenuation factor.

1.3 Numerical examples

The fractional wave equation (5) is implemented using the pseudospectral method to model the viscoacoustic wavefield accurately and efficiently. Following the Pierre Shale seismic parameters, we study the attenuation effects on waveforms in a homogeneous model by testing different quality factors, i.e., acoustic ($Q = \infty$), $Q = 100$, $Q = 32$ and $Q = 10$. The simulations are performed on a 2-D grid with a spacing of 2 m in both directions. A Ricker wavelet source with center frequency of 35 Hz is excited and the response is recorded by a receiver with 400 m offset. The time step is

0.25 ms. Figure 3 compares the numerical solutions with the analytical solutions obtained by convolving the source wavelet with the Green's functions. We observe that as Q decreases, the peak amplitude becomes smaller while the waveform distorts more severely with comparison to the acoustic case. The numerical and analytical solutions agree with each other almost perfectly well for all simulations except for the low Q case where the shapes of waveforms exhibit subtle differences, which might be caused by the inaccuracy in the phase velocity dispersion (Figure 2).

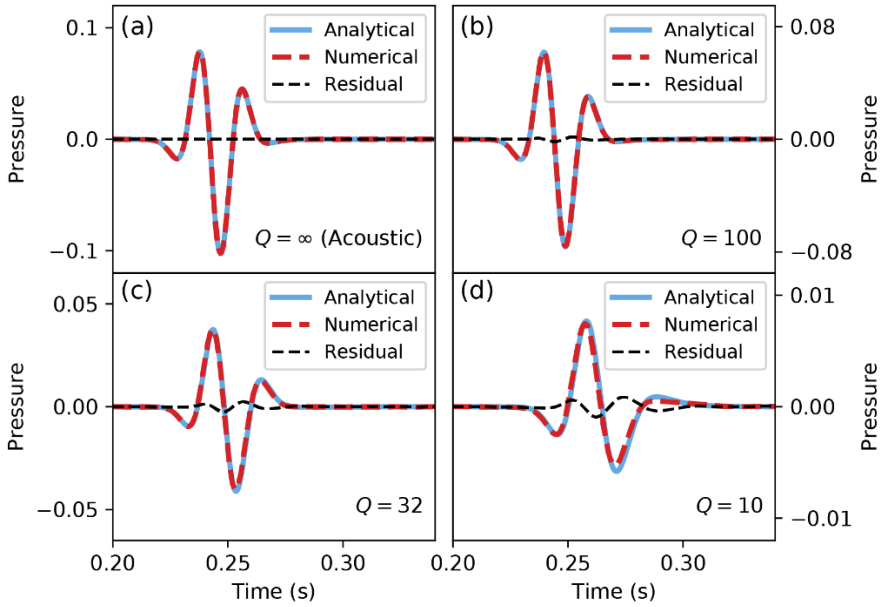

Figure 3. Comparison of the analytical (blue solid lines) and the numerical synthetic seismograms (red dashed lines) as well as their residuals (black dashed lines) in homogeneous media for (a) $Q = \infty$ (acoustic); (b) $Q = 100$; (c) $Q = 32$ and (d) $Q = 10$.

To demonstrate the property of attenuation effects decoupling, we recompute the high attenuation ($Q = 10$) case on a square 400×400 grid with the source located at the center of the model (400 m, 400 m). Four simulations are conducted using the acoustic, the loss-dominated (Equation 7), the dispersion-dominated (Equation 6) and the viscoacoustic wave equations (Equation 5), respectively. The wavefield snapshots at 210 ms for all the four simulations are shown in Figure 4. As shown, the dispersion-dominated case produces wavefront that exhibits the same amplitude as the acoustic case but has a phase delay; the loss-dominated wavefield has a reduced amplitude but shares the same phase as the acoustic wavefront. Not surprisingly, the viscoacoustic snapshot has the phase of the dispersion-dominated wavefield and the amplitude of the loss-dominated one.

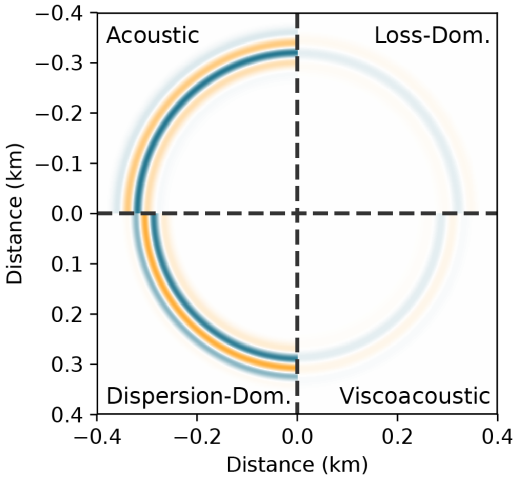

Figure 4. Wavefield snapshots at 210 ms for four simulations in homogeneous media. Each quadrant corresponds to a specific wave equation: acoustic, loss-dominated, dispersion-dominated and viscoacoustic.

Gas chimney model

In this section, we test our scheme on a highly heterogeneous realistic geological model (Zhu et al., 2014). Figure 6 shows its velocity model at 100 Hz and its Q model. It is a typical model of gas chimney characterized by the low velocity and low Q zone at the central top. The model is discretized on a 161×398 grid with 12.5 m spacing. The source is located in the water layer at (2500 m, 25 m) with a Ricker wavelet of 15 Hz. The receivers are deployed on all the grid points at the same depth (25 m) as the source and the time step is 1 ms.

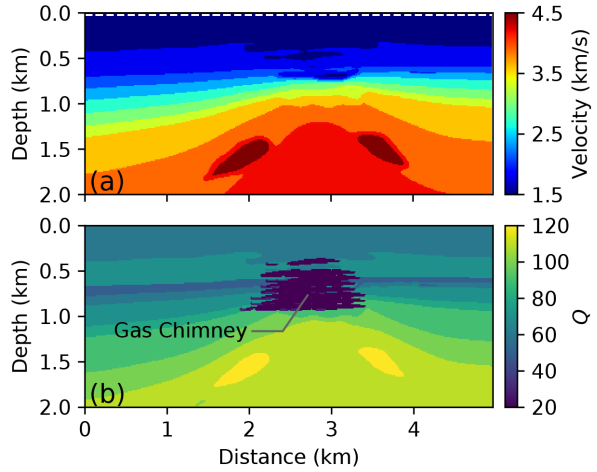

Figure 6. The gas chimney model: (a) velocity model at 100 Hz; (b) Q model. The white dashed line denotes the depth of the source and the receivers.

We conduct simulations including the acoustic modeling and two viscoacoustic modelings using both the new scheme and the Z-H scheme. Again, we conduct an accurate reference viscoacoustic simulation using the region-wise implementation of Z-H wave equation. In this case, the gas chimney Q model consists of 10 regions with unique Q values so the fractional Laplacians are computed separately for each region. The snapshots taken at 800 ms for all the simulations are

shown in Figure 7 along with the residuals of the two viscoacoustic schemes compared to the reference. The shot gathers are shown in Figure 8. The synthetics recorded by the receiver at x=3500 m are compared with each other as shown in Figure 9 (direct arrivals are muted).

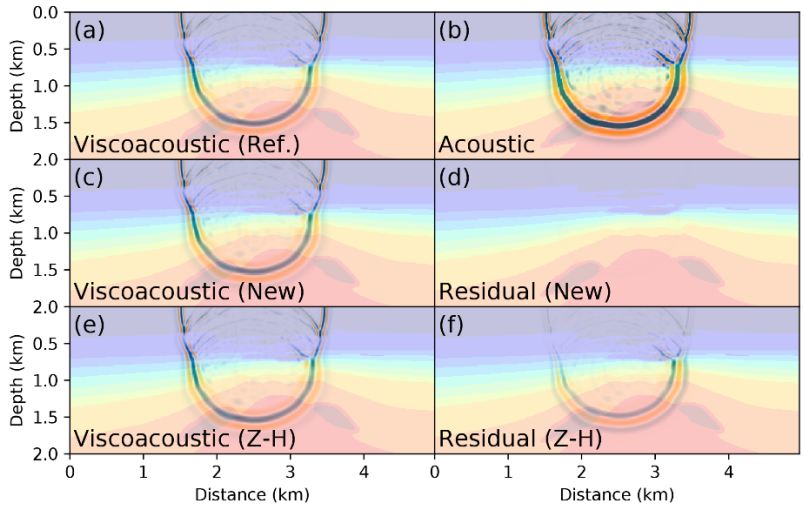

Figure 7. Wavefield snapshots taken at 800 ms overlaid on the velocity model background for (a) reference viscoacoustic modeling; (b) acoustic modeling; (c) viscoacoustic modeling with the new scheme; (d) residual between the new scheme and the reference; (e) viscoacoustic modeling with the Z-H scheme; (f) residual between the Z-H scheme and the reference. The color scales are the same for all the snapshots and the residual.

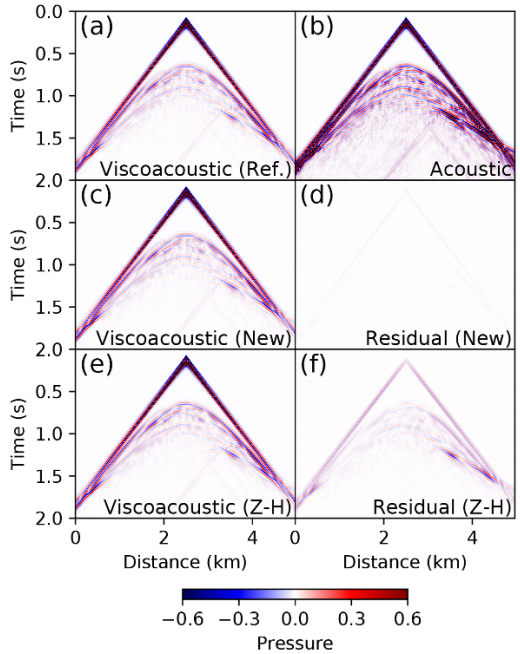

Figure 8. Synthetic shot gathers for (a) reference viscoacoustic modeling; (b) acoustic modeling; (c) viscoacoustic modeling with the new scheme; (d) residual between the new scheme and the reference; (e) viscoacoustic modeling with the Z-H scheme; (f) residual

between the Z-H scheme and the reference. The color scales are the same for all the shot gathers and the residual.

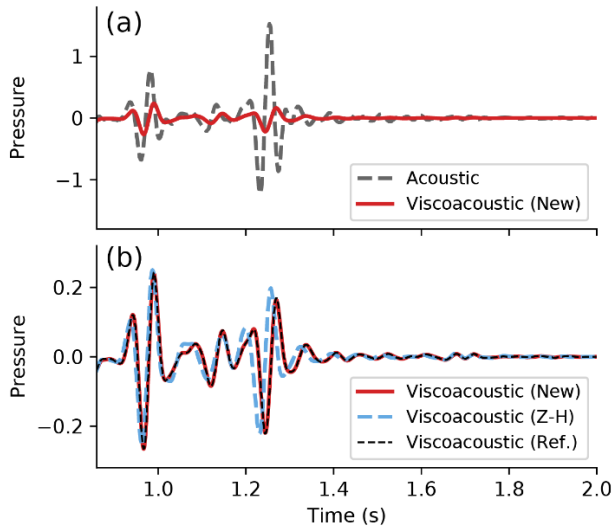

Figure 9. Synthetic seismograms (direct arrivals are muted) recorded by the receiver at x=3500 m. (a) Comparison between the acoustic modeling (gray dashed line) and the viscoacoustic modeling with the new scheme (red solid line); (b) comparison between viscoacoustic modelings using the new scheme (red solid line), the Z-H scheme (blue dashed line) and the reference (black dashed line).

By comparing the acoustic and viscoacoustic modeling, significant amplitude decay can be seen in Figures 7(b)–(c), Figures 8(b)–(c) and Figure 9(a) while the seismogram comparison in Figure 9(a) exhibits the phase shift. The residual for the new scheme is negligible while that for the Z-H scheme is significant (Figures 7c-f, 8c-f and 9b), which is attributed to their difference in dealing with attenuation heterogeneity. The Z-H scheme adopts average γ in the pseudospectral method to represent the heterogeneous Q distribution, which shows underestimated attenuation for the waves that sample anomalous Q areas, i.e., the gas cloud zone in this model. This inference is confirmed by our results (Figure 8f and Figure 9b) as the most significant waveform residuals occur at the reflection phases that sample the gas chimney after 1 s.

2 Fréchet kernels based on the viscoacoustic wave equation

Following the Lagrangian multiplier method (Plessix, 2006), we can formulate the computation of Fréchet kernel K with forward modeling wave equation as well as two extra equations for adjoint modeling and wavefield interaction, respectively:

$$\mathbf{L}^{*}\lambda = \frac{\partial J}{\partial u}, \tag{8}$$

$$K = \frac{dJ}{dm} = -\langle \lambda, \frac{\partial \mathbf{L}}{\partial m} u \rangle, \tag{9}$$

where $*$ denotes adjoint, λ is the adjoint wavefield, J is the objective function and m is the model parameter.

Objective functions

We consider three objective functions, i.e., the misfit of waveform, cross-correlation traveltime and amplitude. For different objective functions, the adjoint wavefields are excited by different adjoint sources $\frac{\partial J}{\partial u}$. The waveform objective function $J_W = \frac{1}{2}(u-d)^2$ (for simplicity, we omit the sampling operator at the receiver location hereinafter) is adopted in the full waveform inversion (FWI), where u and d are synthetic and observed seismograms, respectively. Its corresponding adjoint source is

$$\frac{\partial J_W}{\partial u} = u - d. \tag{10}$$

Besides, we introduce the traveltime and amplitude objective function (Tromp et al., 2005): $J_T = \frac{1}{2}\Delta T^2$ with $\Delta T = T_u - T_d$, where T_u and T_d are the traveltimes for synthetic and observed seismograms, respectively; $J_A = \frac{1}{2}\Delta A^2$ with $\Delta A = \frac{A_u - A_d}{A_d}$, where $A_u = \int_{t_1}^{t_2} u^2 dt$, $A_d = \int_{t_1}^{t_2} d^2 dt$ and (t_1, t_2) defines the time window to measure the misfit. Hence, their formulations of the adjoint sources can be derived using implicit differentiation technique (Luo and Schuster, 1991; Dahlen and Baig, 2002):

$$\frac{\partial J_T}{\partial u} = \Delta T \cdot \frac{\dot{u}}{\int_{t_1}^{t_2} u\ddot{u} dt}, \tag{11}$$

$$\frac{\partial J_A}{\partial u} = \Delta A \cdot \frac{u}{A_u A_d}. \tag{12}$$

Adjoint operator

In order to materialize Equation (8), we need to derive the explicit form of $\mathbf{L}^* = \mathbf{L_0^*} + \mathbf{L_1^*} + \mathbf{L_2^*}$. Recall $(\nabla^2)^* = \nabla^2$ and $\left(\frac{\partial}{\partial t}\right)^* = -\frac{\partial}{\partial t}$, we can infer that the acoustic propagator is self-adjoint: $\mathbf{L_0^*} = \mathbf{L_0}$. Hence, we have $\mathbf{L_1^*} = \mathbf{L_1}$ and $\mathbf{L_2^*} = -\mathbf{L_2}$ so that $\mathbf{L}^* = \mathbf{L_0} + \mathbf{L_1} - \mathbf{L_2}$. Physically, it means that the adjoint operator of the viscoacoustic propagator compensates (anti-attenuates) the amplitude of the waves while preserves the velocity dispersion character. However, since we simulate the adjoint wavefield in a time reversal mode, the reversed adjoint wavefield attenuates rather than compensates the amplitude as the forward wavefield:

$$\mathbf{L}q^{\ddagger} = \left(\frac{\partial J}{\partial u}\right)^{\ddagger}, \tag{13}$$

where ‡ indicates the time reversal.

2.1 Wavefield interaction

The last step to compute the Fréchet kernel is interacting the forward and adjoint wavefields. The Fréchet kernel K can be separated into three parts as $\mathbf{L}$ does: $K = K_1 + K_2 + K_3$, where $K_i = -\langle \lambda, \frac{\partial \mathbf{L_i}}{\partial m} u \rangle$ $(i = 1, 2, 3)$. In this study, we regard c and γ as the model parameters. Then the operators $\frac{\partial \mathbf{L_i}}{\partial m}$ can be derived directly from Equations (5).

2.2 Numerical examples

We implement the adjoint formulations derived in the previous section to compute the Fréchet kernels of a homogeneous model for the three different objective functions. To do that, we set up a 2-D target model on a 400×200 grid with spacing of 10 m in both directions. The target model

has a reference phase velocity 3.05 km/s at 20 Hz with the quality factor $Q = 80$. We put a receiver at (3.7, 1) km and the source at (0.3, 1) km with a 20 Hz Ricker wavelet. We simulate the synthetic seismogram with 1 ms time interval as the ground truth data. In the meantime, we set up an initial model on the same grid with 3 km/s reference phase velocity and $Q = 100$. According to the algorithm we have established, we show the resultant Fréchet kernels for this homogeneous model.

The first column of Figure 10 shows the velocity c kernel of different operator ($\mathbf{L_0}$, $\mathbf{L_1}$ and $\mathbf{L_2}$) contributions as well as their summation for the waveform objective function. The waveform kernels of attenuation γ are shown in the first column of Figure 11. Besides, the c and γ kernels for the traveltime and amplitude objective functions are shown in the rest of Figure 10 and 11, respectively. It appears that the c kernel is dominated by the contribution of acoustic propagator $\mathbf{L_0}$ compared to $\mathbf{L_1}$ and $\mathbf{L_2}$. On the contrary, γ has absolutely no sensitivity of $\mathbf{L_0}$ but is determined by the dispersion term $\mathbf{L_1}$ and the dissipation term $\mathbf{L_2}$. Moreover, the $\mathbf{L_2}$ contribution dominates the γ kernel for each of the objective functions, which is consistent with the fact that the amplitude loss is the first order viscoacoustic phenomenon compared to the velocity dispersion.

Furthermore, since the target model has higher c compared to the initial model, we would expect that the majority of the c kernel to be negative. In this sense, the traveltime kernel is more likely to benefit the convergence compared to the other two. On the other hand, the target model also has higher γ (lower Q) as both the waveform and the amplitude γ kernels capture this feature almost equally well. However, the traveltime γ kernel has a flipped polarity. Since the attenuation is barely sensitive to the traveltime phase shift, the traveltime γ kernel generally should not be used to update the model.

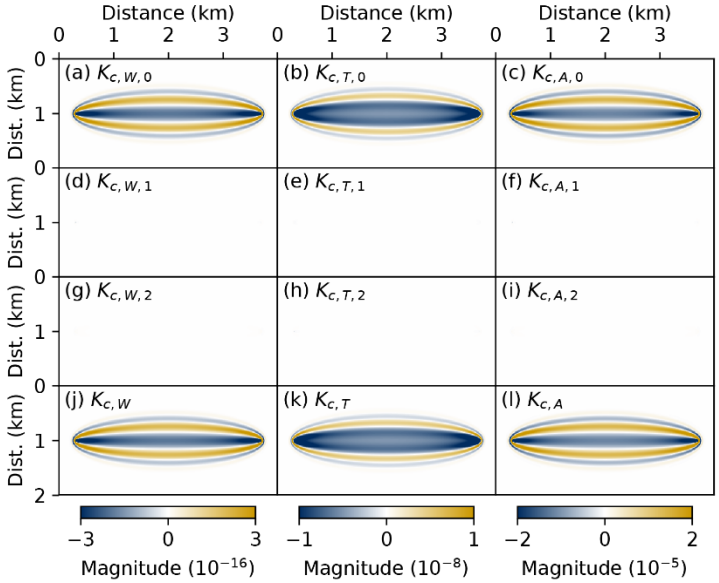

Figure 10. Velocity Fréchet kernels for waveform, traveltime and amplitude objective functions.

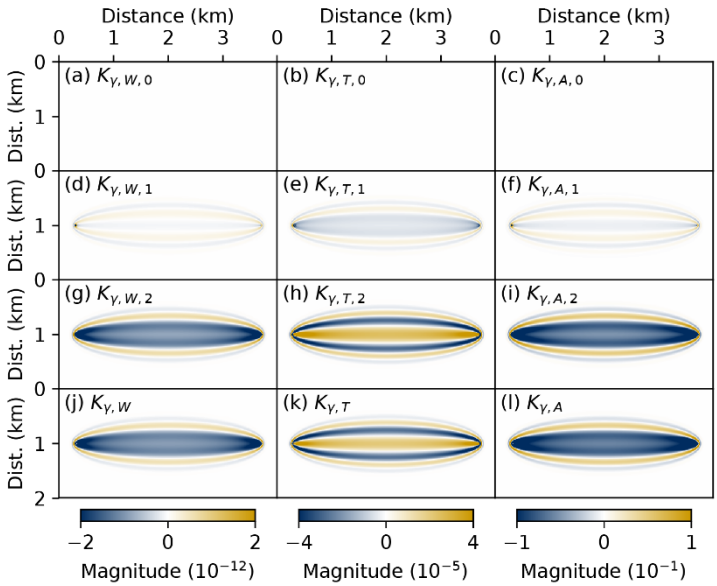

Figure 11. Attenuation Fréchet kernels for waveform, traveltime and amplitude objective functions.

3 Multiparameter viscoacoustic FWI

One major challenge faced by the multiparameter full waveform inversion (FWI) is the crosstalk (or trade-off) phenomenon, where the data-synthetic residual introduced by one model parameter is mistakenly assigned to another. In the viscoacoustic case, the phase information of the seismograms could be attributed to either velocity or the dispersion caused by Q. On the other hand, both Q and the impedance contrast, which can be derived from velocity heterogeneity, could explain the amplitude of the data. Thus, we would expect a serious crosstalk between velocity and Q in the multiparameter viscoacoustic FWI, particularly in the classic gradient-based FWI.

One approach to mitigate the crosstalk is to take into account the information of the 2nd-order Fréchet derivative, i.e., the Hessian. In particular, the off-diagonal blocks of the Hessian measure the coupling effect between different model parameters. Thus, applying the inverse Hessian operator on the gradient is expected to suppress the crosstalk issue. However, storing and inverting the Hessian matrix requires huge memory space and computational load beyond the current hardware capability.

In this study, we aim to incorporate the Hessian information using the Newton-CG (also known as truncated Newton) algorithm. This algorithm approximates the gradient preconditioned by the inverse Hessian at each iteration via an internal loop (Nocedal and Wright, 2006). This internal loop solves a linear system using the conjugate gradient (CG) method and only needs the computation of Hessian-vector product instead of the inverse Hessian. In particular, the second-order adjoint-state method (Fichtner and Trampert, 2011; Métivier et al., 2014; Yang et al., 2018) makes it computational feasible by conducting the Hessian-vector multiplication in a matrix-free fashion.

Our proposed multiparameter has a nested loop structure. The internal loop takes advantage of the CG method to approximately solve the linear system $H\Delta m = -g$, where H is the Hessian matrix,

Δm is the model update vector and g is the gradient, i.e., the first order Fréchet derivative. In the external loop, we update both velocity (c) and attenuation (γ) models according to the vector Δm. In this section, we present several crucial steps of this algorithm.

3.1 Hessian-vector product

The internal CG loop requires computing the Hessian-vector product in an efficient way. Instead of calculating the Hessian matrix explicitly, the 2nd-order adjoint-state method offers an option to conduct the multiplication in a matrix-free fashion. The 1st-order adjoint-state method is used to compute the gradient as described in section 3. In particular, using waveform residual as the objective function, the adjoint simulation (Equation 8) becomes

$$\mathbf{L}^*\lambda = R^*(Ru - d), \tag{14}$$

Where d is the data; R is the operator that samples the wavefield at the receivers, which makes R^* the operator that pads zeros at non-receiver locations. Moreover, according to the 2nd-order adjoint-state method, for an arbitrary model space vector v, the product Hv for each source can be computed at the cost of two more simulations (one forward and one adjoint) and three more interactions:

$$\mathbf{L}\mu_2 = -\langle v,\ \frac{\partial \mathbf{L}}{\partial m}u\rangle_M\,, \tag{15}$$

$$\mathbf{L}^*\mu_1 = R^*R\mu_2 - \langle v,\ \left(\frac{\partial \mathbf{L}}{\partial m}\right)^*\lambda\rangle_M\,, \tag{16}$$

$$Hv = -\langle \mu_1,\ \frac{\partial \mathbf{L}}{\partial m}u\rangle_U - \langle \mu_2,\ \frac{\partial \mathbf{L}^*}{\partial m}\lambda\rangle_U - \langle v,\ \langle \lambda,\ \frac{\partial^2 \mathbf{L}}{\partial m^2}u\rangle_U\rangle_M\,, \tag{17}$$

where $\langle\cdot\,,\ \cdot\rangle_M$ denotes the inner product in the model space M; μ_2 and μ_1 are the 2nd-order forward and adjoint wavefields, respectively.

To illustrate the physical meaning of the product Hv, we assume that the model space vector v represents a scatterer with velocity or attenuation perturbation. As a result, the source of the 2nd-order forward wavefield μ_2 has only non-zero values at the location of the scatterer v (Equation 15), which makes μ_2 propagates outward from the scatterer. The two terms on the right-hand side of the Equation (16) indicate that the 2nd-order adjoint wavefield μ_1 has two sources. The first source (Source a) is located at the receiver while the second source (Source b) is at the scatterer. Their corresponding wavefields are denoted by μ_{1a} and μ_{1b}, respectively.

The Hessian-vector product Hv constitutes of three interactions (Equation 17) denoted by $(Hv)_1$, $(Hv)_2$ and $(Hv)_3$. In particular, $(Hv)_1$ has two parts $(Hv)_{1a}$ and $(Hv)_{1b}$ corresponding to μ_{1A} and μ_{1B}, respectively. The interaction between μ_{1a} and the forward wavefield u gives rise to $(Hv)_{1a}$. Hence, it is influenced by the Fresnel zone between the source and the receiver. Similarly, $(Hv)_{1b}$ marks the area between the source and the scatterer while $(Hv)_2$ is sensitive to the area between the receiver and the scatterer. The last interaction $(Hv)_3$ only has non-zero values at the location of the scatterer and it accounts for the non-linearity introduced by the parameterization (Fichtner and Trampert, 2011).

3.2 Internal CG loop

Equipped with the efficient computation of Hessian-vector product, we can construct the internal CG loop following Nocedal and Wright (2006), as shown in Algorithm 1.

Algorithm 1 Conjugate gradient method to solve $H\Delta m = -g$

Input: Gradient g, maximum iteration k_{max}, residual tolerance J_{tol}
Require: Computation method of $H\nu$ for arbitrary ν
Output: Model parameter update Δm
Initialization: $\Delta m \leftarrow 0$, $r \leftarrow g$, $p \leftarrow -r$, $J_1 \leftarrow r^T r$, $k \leftarrow 0$
while $J_1 > J_{tol}$ & $k < k_{max}$ **do**
  $\xi \leftarrow Hp$
  $\alpha \leftarrow \frac{J}{p^T \xi}$
  $r \leftarrow r + \alpha \xi$s
  $\Delta m \leftarrow \Delta m + \alpha p$
  $J_2 \leftarrow r^T r$
  $\beta \leftarrow \frac{J_2}{J_1}$
  $p \leftarrow -r + \beta p$
  $J_1 \leftarrow J_2$
  $k \leftarrow k + 1$
end while

The early iterations of the CG algorithm account for the largest eigenvalues of the Hessian matrix. Hence, a truncation strategy for the internal loop has an intrinsic regularization effect, as confirmed by previous studies (Métivier et al., 2014). Therefore, we only run the CG internal loop for a few iterations ($k_{max} \sim 5$) in our viscoacoustic FWI problem. The resultant Δm is not reliable in terms of magnitude. So we apply a line search for different model parameters after the completion of the internal loop.

In addition, to guarantee a balanced update between model parameters, we normalize both velocity c and attenuation γ to the range of $[-1, 1]$. This is equivalent to applying a simple preconditioner to the Hessian matrix in the CG loop so as to improve the spectral property of the Hessian and accelerate the convergence.

3.3 Born-based multiparameter step length computation

The output of the internal CG loop Δm provides us the update direction, but we have to conduct a line search to determine the step length along the direction. In particular in the viscoacoustic FWI, the step lengths for both velocity (α_c) and attenuation (α_γ) are needed to optimize the reduction of the waveform residual. One of the most popular line search algorithms for FWI implementation is based on the Born modeling (e.g., Pica et al., 1990). In the multiparameter FWI, we need to take into account the interaction between different parameter classes in optimizing the step lengths. Hence, we generalize the Born-based method to the multiparameter case and propose a Born-based multiparameter step length computation (BMPSLC) algorithm.

In our viscoacoustic FWI problem, we separate the model update Δm into two vectors $\Delta m = \Delta m_c + \Delta m_\gamma$ so that Δm_c only has non-zero values in the first half (velocity part) while Δm_γ only has non-zero values in the second half (attenuation part). Thus, the objective function after the model update would be:

$$\begin{aligned} & J\left(m + \alpha_c \Delta m_c + \alpha_\gamma \Delta m_\gamma\right) \\ &= \frac{1}{2}\left\| d - f\left(m + \alpha_c \Delta m_c + \alpha_\gamma \Delta m_\gamma\right)\right\| \\ &= \frac{1}{2}\left\| d - f(m) - \frac{\delta f}{\delta m}\left(\alpha_c \Delta m_c + \alpha_\gamma \Delta m_\gamma\right)\right\|, \end{aligned}$$

where the Taylor expansion is conducted; and f denotes the forward modeling operator, which makes $\frac{\delta f}{\delta m}$ the linear Born modeling operator. Taking the partial derivative with respect to both α_c and α_γ and letting them to be zero yields:

$$\langle \frac{\delta f}{\delta m}\Delta m_c,\ \frac{\delta f}{\delta m}\Delta m_c\rangle_D\ \alpha_c + \langle \frac{\delta f}{\delta m}\Delta m_\gamma,\ \frac{\delta f}{\delta m}\Delta m_c\rangle_D\ \alpha_\gamma = \langle d - f(m),\ \frac{\delta f}{\delta m}\Delta m_c\rangle_D\,, \tag{18}$$

$$\langle \frac{\delta f}{\delta m}\Delta m_c,\ \frac{\delta f}{\delta m}\Delta m_\gamma\rangle_D\ \alpha_c + \langle \frac{\delta f}{\delta m}\Delta m_\gamma,\ \frac{\delta f}{\delta m}\Delta m_\gamma\rangle_D\ \alpha_\gamma = \langle d - f(m),\ \frac{\delta f}{\delta m}\Delta m_\gamma\rangle_D\,, \tag{19}$$

where $\langle \cdot\,,\ \cdot\rangle_D$ denotes the inner product in data space D. Two Born modelings are required to obtain the coefficients of Equations (18)-(19). In our study, we conduct the Born modelings in a finite-difference fashion:

$$\frac{\delta f}{\delta m}\Delta m_i \approx \frac{f(m + \epsilon\Delta m_i) - f(m)}{\epsilon},\quad (i = c, \gamma) \tag{20}$$

where ϵ is a small scalar to guarantee that the resultant maximum perturbation max ($|\epsilon\Delta m|$) is less than a few percent of the model parameters. Hence, the two step lengths α_c and $\alpha_\gamma$can be achieved by solving the linear system Equations (18)-(19) at the cost of two additional forward modeling per source.

3.4 FWI workflow

In summary, we put together all the aforementioned steps and construct the multiparameter viscoacoustic FWI algorithm, as shown in Algorithm 2.

Algorithm 2 Viscoacoustic FWI

Input: Data d, initial models c_{init} and γ_{init}
Output: Final models c_{final} and γ_{final}
Initialization: $m_c \leftarrow c_{init}$, $m_\gamma \leftarrow \gamma_{init}$
while (Not converge) **do**
  Compute gradient g (adjoint-state method)
  Approximately solve $H\Delta m = -g$ (Algorithm 1, internal CG loop)
  Calculate step lengths α_c and α_γ (BMPSLC)
  $m_c \leftarrow \alpha_c \Delta m_c$
  $m_\gamma \leftarrow \alpha_\gamma \Delta m_\gamma$
end while
$c_{final} \leftarrow m_c$, $\gamma_{final} \leftarrow m_\gamma$

3.5 Numerical examples

3.5.1 Hessian-vector product

In this section, we validate the computation of the Hessian-vector product based on the 2nd-order adjoint-state method. In particular, we set up a homogeneous 2-D target model on a 400 × 200 grid with spacing of 8 m in both x and z directions. The target model has a quality factor $Q = 80$ and a reference phase velocity $c_0 = 3.05$ km/s at 20 Hz. We put a source at (0.24, 0.8) km with a 20 Hz Ricker wavelet and one receiver is located at (2.96, 0.8) km. Using this target model, we simulate the synthetic seismogram, which is considered as the ground truth data. Meanwhile, we build a homogeneous initial model on the same grid with slightly different velocity and attenuation ($c_0 =$ 3.00 km/s, $Q = 100$). To demonstrate the physical meaning of the Hessian-vector product, we set up the model space vector v as a scatterer with 20 m/s velocity perturbation located at (1.36, 0.64) km. In another word, the vector v has only one non-zero entry, which is located in its first half (velocity part).

We conducted two forward simulations (Equations 5 and 15) and two adjoint simulations (Equations 14 and 16). Taking the interactions between the resultant wavefields (Equation 17) leads to the Hessian-vector product (Hv), which has the same dimension as the model space vector and includes both velocity (c) and attenuation (γ) parts. Four constituent parts ($(Hv)_{1a}$, $(Hv)_{1b}$, $(Hv)_2$ and $(Hv)_3$) are shown in Figure 12 along with their summation. As we can expect, each of the four constituent parts has the shape as described in section 4.2.1.

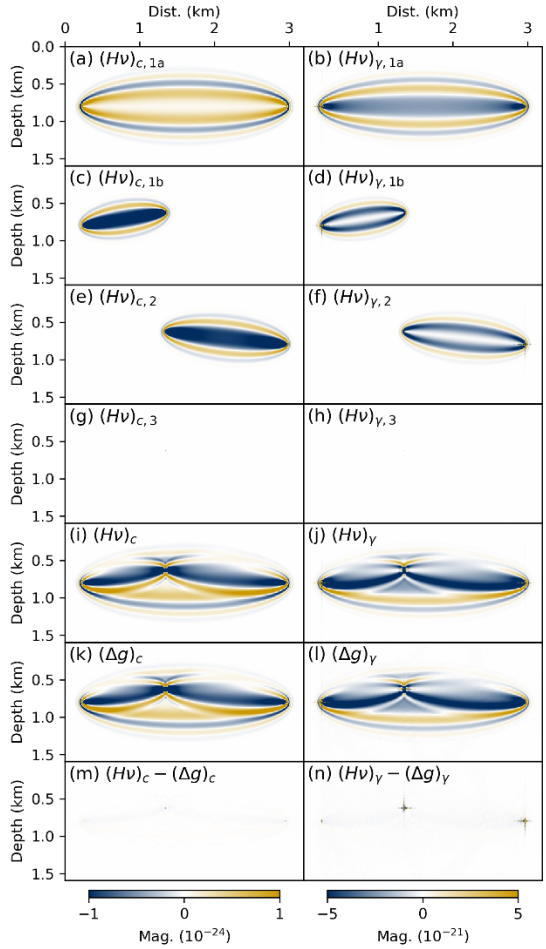

Figure 12. Hessian-vector product. Left column: velocity (c) part; right column: attenuation (γ) part. (a)-(h): Constituent parts of the product; (i)-(j) the product computed using the 2nd-order adjoint-state method; (k)-(l) the product computed using the finite-difference method; (m)-(n) the residual between the two methods.

To further validate the accuracy of the algorithm, we use the finite-difference method to compute the product with the same vector v. In particular, the definition of Hessian indicates

$$Hv \approx g(m+v) - g(m) \tag{21}$$

when v is sufficiently small, where $g(m)$ and $g(m+v)$ are the gradients evaluated at the initial model m and the perturbed model $m+v$, respectively. We conducted this finite-difference computation and the resultant Hessian-vector product is shown in Figures 12(k)-(l). It turns out that the product computed using both methods appear to be the same and their residuals (Figures 12m-n) are negligible except for some cross-shape artifacts in the attenuation part. These artifacts

are located at the locations of the source, the receiver and the scatterer (ν), all of which are actually source locations, either forward or adjoint, either first-order or second-order. These cross-shape artifacts are due to the singularity of the point source, which is processed by fractional Laplacian operators when taking the interactions (Equation 17). In practice, we use a Gaussian function to taper the source/receiver region wavefields to remove these artifacts. This solution will not affect the model updates because the source/receiver regions are not updated in the FWI workflow anyway. In addition, the ν vector is generally not singular, so the artifact will not show up at the scatterer.

3.5.2 Cross-well FWI example

In this section, we use a toy model to examine the performance of our proposed multiparameter viscoacoustic FWI algorithm, especially its capability to mitigate the crosstalk problem. To mimic the CASSM geometry in the CO_2 injection setting, we set up a 2-D model on a 101 × 151 grid (0.8 m interval) with a cross-well acquisition system: 15 sources on the left edge and 36 receivers on the right edge. The target model (Figure 13) has a homogeneous background ($c_0 = 3.00$ km/s at 150 Hz, $Q = 100$) with a velocity anomaly ($c_0 = 3.05$ km/s at 150 Hz) on the top left and an attenuation anomaly ($Q = 50$) on the bottom right. We start from homogeneous initial models without the anomalies for both velocity and attenuation.

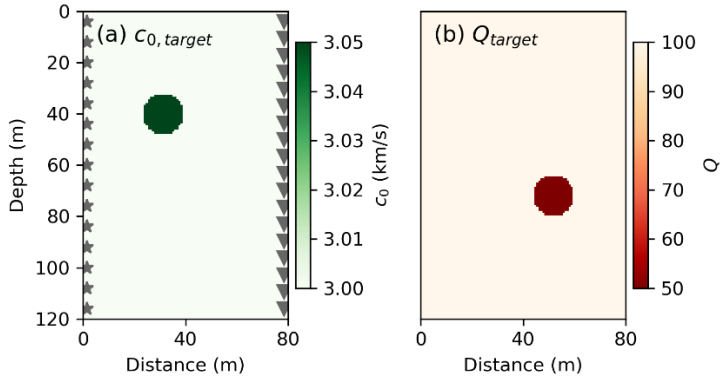

Figure 13. Target models: (a) phase velocity; (b) quality factor. Gray stars and triangles denote the sources the receivers, respectively.

For the gradient-based classic FWI, the update direction is the negative gradient ($-g$); while for our proposed Hessian-based method (Algorithm 2), the direction is the (approximate) preconditioned negative gradient (Δm) produced by the internal CG loop (Algorithm 1). At the very first iteration of our example, we show the directions computed using both methods in Figure 17. In the gradient-based FWI, both velocity and attenuation direction can capture the anomalies but the velocity anomaly is mistakenly mapped to the attenuation direction. In particular, the maximum value of the attenuation direction is located at the velocity anomaly (Figure 17b), leading to a significant crosstalk. The Hessian-based direction, on the other hand, is generally sharper than the gradient-based ones. More importantly, the crosstalk artifact in the attenuation direction is substantially reduced (Figure 17d). This comparison demonstrates the capability of the internal CG loop to mitigate the crosstalk.

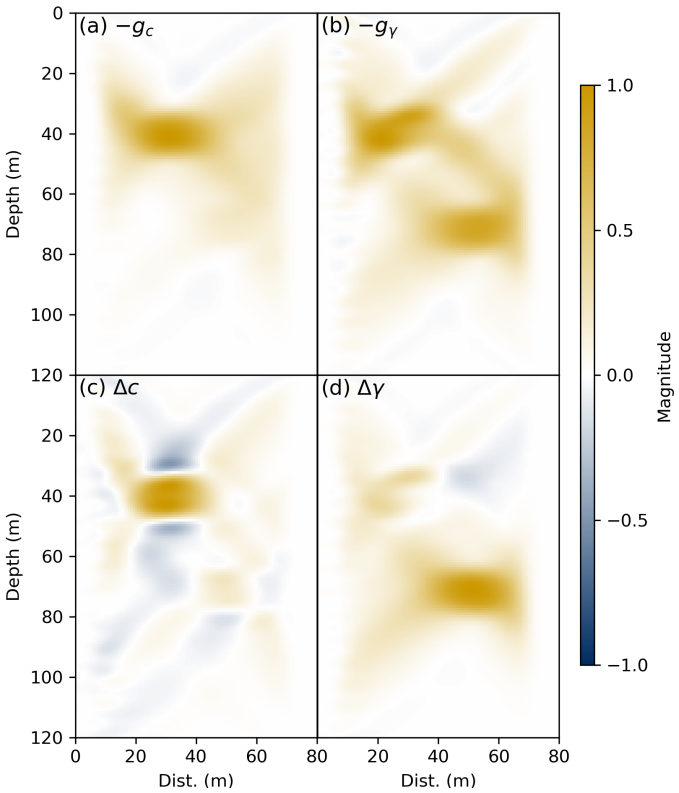

Figure 14. Normalized model update direction: (a)-(b) gradient-based method; (c)-(d) proposed Hessian-based method. Left column: velocity (c); right column: attenuation (γ). Note that each direction is normalized by their maximum absolute value.

In Figure 15, we show the final velocity and attenuation models after 20 iterations of the external loop. Both anomalies are recovered with little crosstalk artifacts. The magnitudes of the anomalies, however, are slightly less than the target model, while the shapes of both anomalies are wider than they are supposed to be. Both imperfections are due to the limitation of the cross-well acquisition system, where the horizontal resolution is better than the vertical one, leading to less constraints on the width of the anomalies and the reduction in the magnitude. This argument can be confirmed by comparison of the seismograms. An observed shot gather is shown in Figure 16(a) and its corresponding data residuals for the initial and final models are shown in Figures 16(b) and (c), respectively. The negligible residual of the final model suggests that the final models (Figure 15) can produce the same seismograms as the target model (Figure 12) under the current cross-well geometry. Furthermore, if we add 9 sources on the top margin and 23 receivers on the bottom, the resultant final models (after 20 iterations) are shown in Figure 17. With better ray coverage, the resolutions of both anomalies are improved and the magnitudes are extremely close to the target.

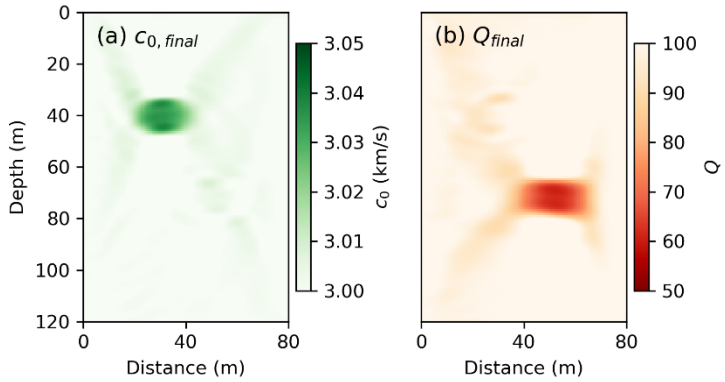

Figure 15. Final models: (a) phase velocity; (b) quality factor.

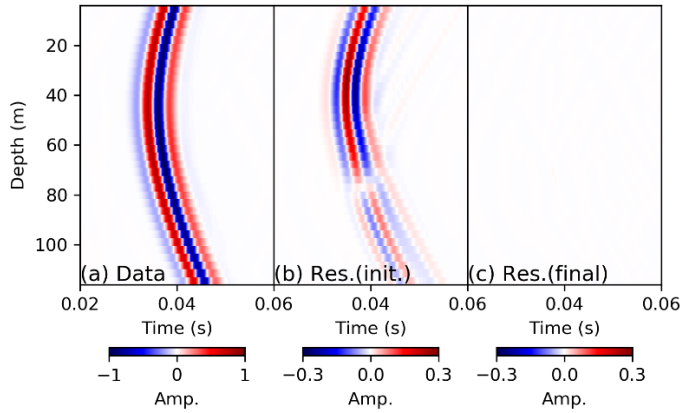

Figure 16. (a) Observed seismogram (data generated by the target model); (b) seismogram residual of the initial model; (c) seismogram residual of the final model. Note that the color scale is different between (b), (c) and (a).

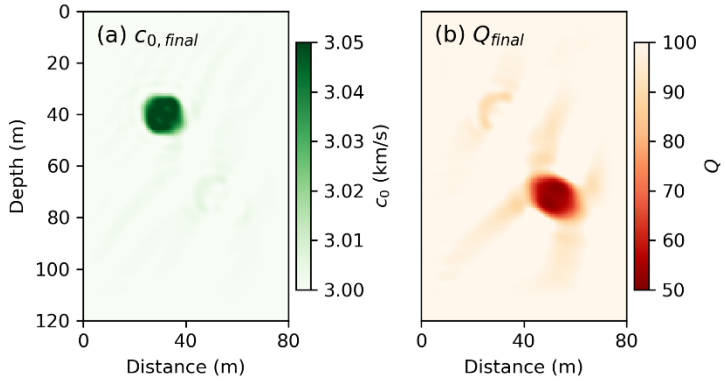

Figure 17. Final models for the FWI with more sources and receivers: (a) phase velocity; (b) quality factor.

4 Conclusions

In this task (task 2), we derive a new fractional viscoacoustic wave equation to model the seismic wavefield in attenuating media. This equation is featured by the fractional Laplacian operators, which guarantee its accuracy and computational efficiency. Based on it, we formulate the Fréchet

kernels for both velocity and attenuation. We found that the acoustic propagator dominates the velocity kernel while the dissipation corrector dominates the attenuation kernel. The Fréchet kernels play a fundamental role in the full waveform inversion while they produce significant crosstalk artifacts. To deal with that, we develop a multiparameter viscoacoustic FWI algorithm. In particular, we take advantage of the Newton-CG framework to incorporate the Hessian so that the crosstalk is significantly mitigated. This algorithm sheds light upon recovering both velocity and attenuation structures simultaneously. In addition, we conducted a synthetic study on the Frio II CO_2 injection model. The attenuation signature can be captured in the forward modeling, which shows a promise to monitor and quantify the CO_2 plume using the multiparameter viscoacoustic FWI.

5 References

Chen, W., & Holm, S. (2004). Fractional Laplacian time-space models for linear and nonlinear lossy media exhibiting arbitrary frequency power-law dependency. The Journal of the Acoustical Society of America, 115(4), 1424-1430.

Dahlen, F. A., & Baig, A. M. (2002). Fréchet kernels for body-wave amplitudes. Geophysical Journal International, 150(2), 440-466.

Daley, T. M., Solbau, R. D., Ajo-Franklin, J. B., & Benson, S. M. (2007). Continuous active-source seismic monitoring of CO 2 injection in a brine aquifer. Geophysics, 72(5), A57-A61.

Fichtner, A., & Trampert, J. (2011). Hessian kernels of seismic data functionals based upon adjoint techniques. Geophysical Journal International, 185(2), 775-798.

Kjartansson, E. (1979). Constant Q-wave propagation and attenuation. Journal of Geophysical Research: Solid Earth, 84(B9), 4737-4748.

Luo, Y., & Schuster, G. T. (1991). Wave-equation traveltime inversion. Geophysics, 56(5), 645-653.

Métivier, L., Bretaudeau, F., Brossier, R., Operto, S., & Virieux, J. (2014). Full waveform inversion and the truncated Newton method: quantitative imaging of complex subsurface structures. Geophysical Prospecting, 62(6), 1353-1375.

Meurer, A., Smith, C. P., Paprocki, M., Čertík, O., Kirpichev, S. B., Rocklin, M., ... & Rathnayake, T. (2017). SymPy: symbolic computing in Python. PeerJ Computer Science, 3, e103.

Nocedal, J., & Wright, S. (2006). Numerical optimization. Springer Science & Business Media.

Pica, A., Diet, J. P., & Tarantola, A. (1990). Nonlinear inversion of seismic reflection data in a laterally invariant medium. Geophysics, 55(3), 284-292.

Plessix, R. E. (2006). A review of the adjoint-state method for computing the gradient of a functional with geophysical applications. Geophysical Journal International, 167(2), 495-503.

Quan, Y., & Harris, J. M. (1997). Seismic attenuation tomography using the frequency shift method. Geophysics, 62(3), 895-905.

Xing G. and Zhu T., (2019) Modeling frequency-independent Q viscoacoustic wave propagation in heterogeneous media, *Journal of Geophysical Research: Solid Earth*, 124(11), 11568-11584 https://doi.org/10.1029/2019JB017985

Yang, P., Brossier, R., Métivier, L., Virieux, J., & Zhou, W. (2018). A time-domain preconditioned truncated Newton approach to visco-acoustic multiparameter full waveform inversion. SIAM Journal on Scientific Computing, 40(4), B1101-B1130.

Zhu, T. (2014). Time-reverse modelling of acoustic wave propagation in attenuating media. Geophysical Journal International, 197(1), 483-494.

Zhu, T., Ajo-Franklin, J. B., & Daley, T. M. (2017). Spatiotemporal changes of seismic attenuation caused by injected CO2 at the Frio-II pilot site, Dayton, TX, USA. Journal of Geophysical Research: Solid Earth, 122(9), 7156-7171.

Zhu, T., Harris, J. M., & Biondi, B. (2014). Q-compensated reverse-time migration. Geophysics, 79(3), S77-S87.

Time-lapse full waveform inversion with data assimilation

The objectives of this study include:
(1) Derive a new data assimilation TLFWI method based on task 2's developed viscoacoustic wave equation to model the seismic wavefields in attenuating media;
(2) Develop a data assimilation multiparameter TLFWI algorithm to recover both time-lapse velocity and attenuation models simultaneously;
(3) Develop the software of data assimilation TLFWI with examples of the Frio II and Cranfield CO2 injection models to understand the applicability of the seismic methods in the CASSM setting.

1 Time-lapse viscoacoustic full waveform inversion (TLQFWI)

Viscoacoustic full waveform inversion (**Q**FWI) of seismic data can be expressed as the minimization of a cost function of the difference between the modeled data u and the observed data d as

$$E = \frac{1}{2}|d - u(\boldsymbol{m})|^2, \quad (1)$$

where $\boldsymbol{m}$ is the model parameter (e.g., P-wave velocity, quality factor and density) to be recovered. In this paper, we focus on P-wave velocity and quality factor, hence we replace $\boldsymbol{m}$ with $\begin{bmatrix}\boldsymbol{v}\\ \boldsymbol{Q}\end{bmatrix}$, hereafter. $u(\boldsymbol{v}, \boldsymbol{Q})$ is the synthetic data generated by numerically solving the viscoacoustic wave equation with an initial velocity model $\boldsymbol{v}$ and quality factor model $\boldsymbol{Q}$. It can be expressed in the frequency domain:

$$u(\boldsymbol{v}, \boldsymbol{Q}) = G(\boldsymbol{v}, \boldsymbol{Q})S(\omega)\delta(\boldsymbol{x} - \boldsymbol{x}_r)\,, \quad (2)$$

where G is the Green's function, S is the source function, ω is the angular frequency, and $\boldsymbol{x}_r$ is the position of receivers. To solve this optimization problem, iterative gradient-based searching methods can be used, mathematically written as

$$\begin{bmatrix}\boldsymbol{v}\\ \boldsymbol{Q}\end{bmatrix}_{i+1} = \begin{bmatrix}\boldsymbol{v}\\ \boldsymbol{Q}\end{bmatrix}_i + \begin{bmatrix}\boldsymbol{\alpha^v g^v}\\ \boldsymbol{\alpha^Q g^Q}\end{bmatrix}_i, \quad (3)$$

where $\boldsymbol{\alpha^v}$ and $\boldsymbol{\alpha^Q}$ are the step length for the parameters of velocity and quality factor. $\boldsymbol{g^v}$ and $\boldsymbol{g^Q}$ are the gradient of the cost function E with respect to $\boldsymbol{v}$ and $\mathbf{Q}$ at the ith iteration and can be derived using the adjoint-state method or scattering-integral approach. We then iteratively update the velocity model $\boldsymbol{v}$ and quality factor $\mathbf{Q}$ simultaneously using equation 3 until the cost function reaches its minimum. The final velocity model $\boldsymbol{v}$ and quality factor $\mathbf{Q}$ are the output of QFWI.

The purpose of TLQFWI is to reveal changes of $\boldsymbol{v}$ and $\mathbf{Q}$ over time. TLQFWI involves two or more QFWIs on baseline and monitoring data. The time-lapse images of changes are obtained by subtracting the background parameter models from the inverted parameter models obtained from QFWIs of monitoring data.

To simulate the seismic data in attenuation media, we adopt the wave equation proposed by Xing and Zhu (2018) which can be expressed as follows:

$$\left(\frac{1}{v^2}\frac{\partial^2}{\partial t^2} - \nabla^2\right)u - \left(\gamma\frac{\omega_0}{v}(-\nabla^2)^{\frac{1}{2}} - \gamma\frac{v}{\omega_0}(-\nabla^2)^{\frac{3}{2}}\right)u + \left(\pi\gamma\frac{1}{v}(-\nabla^2)^{\frac{1}{2}} - \pi\gamma^2\frac{1}{\omega_0}\nabla^2\right)\frac{\partial u}{\partial t} = f$$

where u is the pressure wavefield, f is the source term and v is a reference velocity. The Q-related parameter $\gamma = \frac{1}{\pi}\arctan\left(\frac{1}{Q}\right)$ and ω_0 is the reference angular frequency. The purpose of TLQFWI is to reveal changes of $\boldsymbol{v}$ and $\mathbf{Q}$ over time. TLQFWI involves two or more QFWIs on baseline and monitoring data. The time-lapse images of changes are obtained by subtracting the background parameter models from the inverted parameter models obtained from QFWIs of monitoring data.

2 Extended Kalman Filter (EKF) for time-lapse seismics with attenuation

In data assimilation, extended Kalman filter (EKF) uses the state $\boldsymbol{x}$ and measurements $\boldsymbol{z}$ to describe the dynamic evolution of a system according to

$$\boldsymbol{x}_{k+1} = F\boldsymbol{x}_k + \boldsymbol{w}_{k+1} \tag{4}$$

$$\boldsymbol{z}_{k+1} = h(\boldsymbol{x}_{k+1}) + \boldsymbol{e}_{k+1}, \tag{5}$$

where F is the state transition matrix and h is a measurement function which related measurements $\boldsymbol{z}$ to the state $\boldsymbol{x}$. $\boldsymbol{w}_{k+1} \sim N(0, W_{k+1})$ and $\boldsymbol{e}_{k+1} \sim N(0, R_{k+1})$ are the state error and measurement noise at time lapse $k+1$ with zero mean and known covariances, respectively. In the context of seismic forward modeling, equation 5 can be replaced by equation 2, and the commonly used random walk model (Vauhkonen et al. 1998) in equation 6 is applied to describe the velocity model evolution. Then the time-lapse seismics can be expressed as a dynamic evolution problem using the following equations

$$\boldsymbol{m}_{k+1} = \boldsymbol{m}_k + \boldsymbol{w}_{k+1} \tag{6}$$

$$\boldsymbol{d}_{k+1} = G(\boldsymbol{m}_{k+1})S(\omega)\delta(\boldsymbol{x} - \boldsymbol{x}_r) + \boldsymbol{e}_{k+1}, \tag{7}$$

where the model parameter $\boldsymbol{m}$ is a vector and $\boldsymbol{m} = \begin{bmatrix}\boldsymbol{v}\\ \boldsymbol{Q}\end{bmatrix}$, $\boldsymbol{v}$ is the subsurface velocity model, $\boldsymbol{Q}$ is the quality factor and $\boldsymbol{d}$ is the observed seismic data in the frequency domain, where $\boldsymbol{w}_{k+1} \sim N(0, W_{k+1})$ and $\boldsymbol{e}_{k+1} \sim N(0, R_{k+1})$ are the model error and observed data noise at time lapse $k+1$, respectively.

To solve equations 6 and 7, the EKF schemes are classically formalized in two steps: predict and update. In the prediction step, EKF predicts a velocity model in the current time lapse using information from the last time lapse. Therefore, the estimation from the prediction step is an *a priori* estimation. Then in the update step, EKF combines the prior velocity model and the observed data obtained in the current time lapse together to update the velocity model. This update can be treated as a weighted average between the prior model and the measured model. Hence the estimation from the update step is an *a posteriori* estimation. The formulation of the two steps are described as follow:

predict

$$\widehat{\boldsymbol{m}}_{k+1}^{-} = \widehat{\boldsymbol{m}}_k \tag{8}$$

$$\boldsymbol{P}_{k+1}^{-} = \boldsymbol{P}_k + \boldsymbol{W}_k \tag{9}$$

update

$$\boldsymbol{K}_{k+1} = \boldsymbol{P}_{k+1}^{-}\boldsymbol{H}_{k+1}^{T}(\boldsymbol{H}_{k+1}\boldsymbol{P}_{k+1}^{-}\boldsymbol{H}_{k+1}^{T} + \boldsymbol{R}_{k+1})^{-} \tag{10}$$

$$\widehat{\boldsymbol{m}}_{k+1} = \widehat{\boldsymbol{m}}_{k+1}^{-} + \boldsymbol{K}_{k+1}(\boldsymbol{d}_{k+1} - G(\widehat{\boldsymbol{v}}_{k+1}^{-})S(\omega)\delta(\boldsymbol{x} - \boldsymbol{x}_r)) \tag{11}$$

$$\boldsymbol{P}_{k+1} = (I - \boldsymbol{K}_{k+1}\boldsymbol{H}_{k+1})\boldsymbol{P}_{k+1}^{-} \tag{12}$$

where $\widehat{\boldsymbol{m}}_{k+1}^{-} = \begin{bmatrix}\widehat{\boldsymbol{v}}_{k+1}^{-}\\ \widehat{\boldsymbol{Q}}_{k+1}^{-}\end{bmatrix}$ and $\widehat{\boldsymbol{m}}_{k+1} = \begin{bmatrix}\widehat{\boldsymbol{v}}_{k+1}\\ \widehat{Q}_{k+1}\end{bmatrix}$ are the prior and posterior estimation of velocity and quality factor models. $\boldsymbol{P}_{k+1}^{-}$ and $\boldsymbol{P}_{k+1}$ are the prior and posterior covariance matrices at time lapse $k+1$ with the dimension of $m \times m$, where m is the total number of discretized subsurface model

parameters. $\boldsymbol{K}_{k+1}$ is the Kalman gain which acts as the weights between the a priori and measured model, and $\boldsymbol{H}_{k+1}$ is the derivative of wavefield with respect to velocity $\boldsymbol{v}$ and quality factor $\boldsymbol{Q}$, respectively. $\boldsymbol{W}_k$ is the model error covariance with the dimension of $m \times m$, and $\boldsymbol{R}_{k+1}$ is the observation error covariance with the dimension of $n \times n$, where n is the number of receivers.

From equations 8-12, it is clear that the covariance matrices $\boldsymbol{P}$ and $\boldsymbol{W}$ need be stored and calculated in each step. The amount of storage for the covariance matrices $\boldsymbol{P}$ and $\boldsymbol{W}$ is proportional to the squared number (m^2) of discretized model parameters. Taking a 3D velocity model with discretized grid size of $100 \times 100 \times 100$ for example, the number of model parameters m equals to 10^6. Hence the size of matrices $\boldsymbol{P}$ or $\boldsymbol{W}$ is $10^6 \times 10^6$ and to store $\boldsymbol{P}$ or $\boldsymbol{W}$ in memory takes up to about 4 TB. Such a high memory cost is still unaffordable for most of current computer clusters. Therefore, EKF algorithm is only suitable to small-scale 2D problems.

3 $\mathcal{H}^2$-matrices powered extended Kalman filter (HiEKF)

To avoid explicitly storing and calculating the covariance matrices $\boldsymbol{P}$ and $\boldsymbol{W}$, following the $\mathcal{H}^2$-matrices approach proposed by Li et al. (2014), we define the priori and posteriori cross-covariance matrices $\boldsymbol{C}^-$ and $\boldsymbol{C}$ as

$$\boldsymbol{C}_{\boldsymbol{k+1}}^- = \boldsymbol{P}_{k+1}^- \boldsymbol{H}_{k+1}^{\boldsymbol{T}} \text{ and } \boldsymbol{C}_{\boldsymbol{k+1}} = \boldsymbol{P}_{\boldsymbol{k+1}} \boldsymbol{H}_{k+1}^{\boldsymbol{T}}, \tag{13}$$

and the model error cross-covariance matrix $\boldsymbol{A}$

$$\boldsymbol{A}_{\boldsymbol{k+1}} = \boldsymbol{W}_{\boldsymbol{k+1}} \boldsymbol{H}_{k+1}^{\boldsymbol{T}} \quad . \tag{14}$$

Substituting equations 13 and 14 into equations 8-12 and approximating $\boldsymbol{P}_{\boldsymbol{k}} \boldsymbol{H}_{k+1}^{\boldsymbol{T}} \cong \boldsymbol{P}_{\boldsymbol{k}} \boldsymbol{H}_{\boldsymbol{k}}^{\boldsymbol{T}} = \boldsymbol{C}_{\boldsymbol{k}}$ as velocity and quality factor model form one time lapse to the next time lapse wouldn't change rapidly yields the $\mathcal{H}^2$-matrices powered extended Kalman filter (we call it HiEKF hereafter) formulation as below:

predict

$$\widehat{\boldsymbol{v}}_{k+1}^- = \widehat{\boldsymbol{v}}_k \tag{15}$$

$$\boldsymbol{C}_{\boldsymbol{k+1}}^- = \boldsymbol{C}_{\boldsymbol{k}} + \boldsymbol{A}_k \tag{16}$$

update

$$\boldsymbol{K}_{k+1} = \boldsymbol{C}_{\boldsymbol{k+1}}^- \left(\boldsymbol{H}_{k+1} {\boldsymbol{C}_{k+1}^-}^{\boldsymbol{T}} + \boldsymbol{R}_{k+1} \right)^- \tag{17}$$

$$\widehat{\boldsymbol{v}}_{k+1} = \widehat{\boldsymbol{v}}_{k+1}^- + \boldsymbol{K}_{k+1} (\boldsymbol{d}_{k+1} - G(\widehat{\boldsymbol{m}}_{k+1}^-) S(\omega) \delta(\boldsymbol{x} - \boldsymbol{x}_r)) \tag{18}$$

$$\boldsymbol{C}_{k+1} = (I - \boldsymbol{K}_{k+1} \boldsymbol{H}_{k+1}) \boldsymbol{C}_{\boldsymbol{k+1}}^- \quad . \tag{19}$$

And the posterior variance δ^2 that is the diagonal of covariance matrix $\boldsymbol{P}$ in equation 12 can be calculated using the following equation:

$$\delta_{k+1}^2 = \delta_k^2 - \sum_{j=1}^n (K_{k+1})_{ij} \, (C_{k+1}^-)_{ij} \, . \tag{20}$$

In the new formulation, rather than storing and updating the covariance matrices $\boldsymbol{P}$ and $\boldsymbol{W}$ with the size of $m \times m$ in original EKF (equations 8-12), we store and update the cross-covariance $\boldsymbol{C}$ and $\boldsymbol{A}$ with the size of $m \times n$ instead ($m \gg n$). To calculate the cross-covariance $\boldsymbol{A}$ in equation 14, we adopt a $\mathcal{H}^2$-matrices approach to avoid an explicit expression of the model error covariance $\boldsymbol{W}$. The $\mathcal{H}^2$-matrices approach is a data-sparse representation method which relies on the $\mathcal{H}^2$-matrices structure. This structure allows these matrices to be recursively subdivided into subblocks based on a tree structure, and most subblocks at different levels in the tree can be well approximated using a low-rank block. After representing the dense matrix $\boldsymbol{W}$ using low-rank blocks, we can calculate the matrix product $\boldsymbol{A}$ using the fast multipole method at a reduced storage and computational cost. Therefore, explicitly usage of covariance matrices $\boldsymbol{P}$ and $\boldsymbol{W}$ can be avoided in the HiEKF. By replacing covariance matrices $\boldsymbol{P}$ and $\boldsymbol{W}$ with cross-covariance $\boldsymbol{C}$ and $\boldsymbol{A}$

in HiEKF, the maximum matrices storage size reduces from $m \times m$ to $m \times n$ and the total computational cost decreases from $\mathcal{O}(nm^2)$ to $\mathcal{O}(mn^2)$. Since $m \gg n$ is always true in large-scale geophysical inverse problems, the storage and computational cost of HiEKF are dramatically reduced compared to original EKF.

4 TLQFWI plus $\mathcal{H}^2$-matrices powered extended Kalman filter (TLQFWI-HiEKF)

Due to the first-order Taylor expansion approach in EKF, HiEKF is only suitable to weak nonlinearity problems. To extend the applicability of HiEKF to nonlinear problems, following our previous study (Huang & Zhu 2019), we modify equation 6 by adding a velocity perturbation term as follows:

$$\boldsymbol{m}_{k+1} = \boldsymbol{m}_k + \delta\boldsymbol{m}_{k+1} + \boldsymbol{w}_{k+1}, \tag{21}$$

where $\delta\boldsymbol{m}_{k+1} = \begin{bmatrix} \delta v_{k+1} \\ \delta Q_{k+1} \end{bmatrix}$ is the velocity and quality factor changes produced from TLQFWI at time lapse $k+1$. By this modification, rather than the random walk model in equation 6, the high spatial resolution velocity and quality changes $\begin{bmatrix} \delta v_{k+1} \\ \delta Q_{k+1} \end{bmatrix}$ generated from TLQFWI can help HiEKF to predict a good *a priori* velocity and quality factor models, which reduces the nonlinearity of the targeted problems and is likely to grantees the weak nonlinearity requirement of the HiEKF. To solve the new dynamic evolution problem defined by equations 21 and 7, we only need to revise the equation 15 in the HiEKF formulation (equations 13-20) as

$$\begin{bmatrix} \widehat{\boldsymbol{v}}_{k+1}^{-} \\ \widehat{\boldsymbol{Q}}_{k+1}^{-} \end{bmatrix} = \begin{bmatrix} \widehat{\boldsymbol{v}}_k \\ \hat{Q}_k \end{bmatrix} + \begin{bmatrix} \delta v_{k+1} \\ \delta Q_{k+1} \end{bmatrix}. \tag{22}$$

Together with equations 13, 14, 16- 20, we name them as the TLQFWI-HiEKF algorithm.

5 Synthetic examples

This section will present synthetic tests of the scheme of TLFWI-HiEKF in two different time-lapse seismic monitoring datasets collected in two CO_2 sequestration sites: Frio-II and Cranfield. In Frio-II, dense 2D crosswell time-lapse seismic surveys were carried out while relatively sparse 3D surface time-lapse seismic surveys were conducted in Cranfield.

Frio-II model

The Frio-II CO_2 pilot was a small-scale injection of supercritical CO_2 into a high permeable reservoir at the depth of 1650 m to test geologic storage in saline aquifers (Daley et al. 2007). The baseline P-wave velocity model (i.e., a velocity map before CO_2 injection) of the Frio-II site is derived from 2D extrapolation of logs acquired in the Frio injection well with a local dip determined from gamma ties (Figure 2a). The velocity values range from 2650 through 2765 m/s with a background velocity of 2700 m/s outside the Blue Sand. Figure 2b shows the simulated CO_2-induced velocity reduction after five-days of injection in Frio-II site. The seismic velocity changes due to CO_2 plumes are predicted by rock physics modeling of velocity and saturation from a 3D multiphase flow model (Daley et al. 2011). We have totally 41 time-lapse seismic models with 3-hour intervals. Figure 3a shows three time-lapse P-wave velocity (v_p) models at 3 hour, 48 hour, and 93 hour.

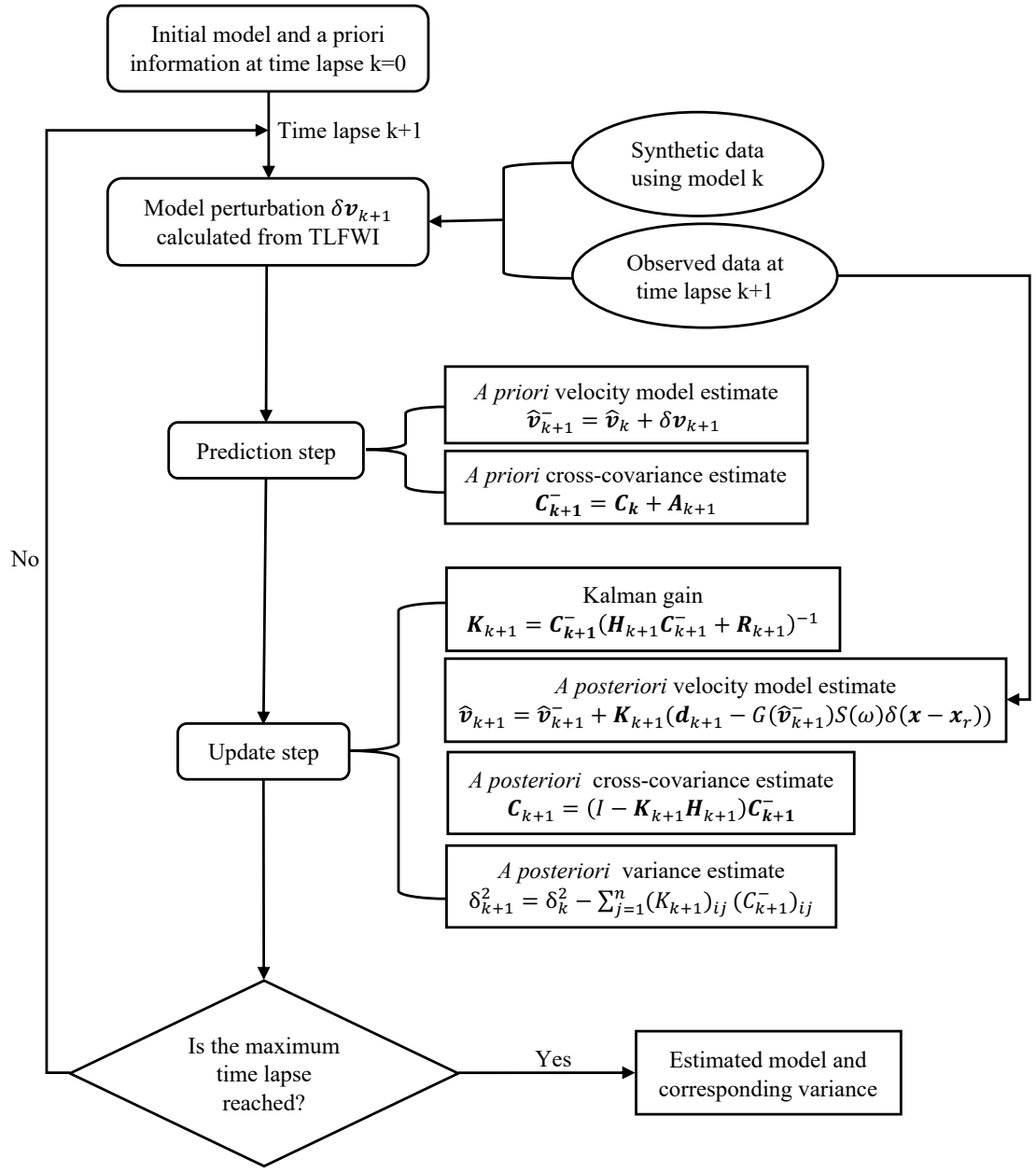

Figure 1. Workflow for the TLFWI-HiEKF method.

To mimic the field survey in our test, we simulate synthetic time-lapse seismic crosswell data every 3 hours. We use 32 time-lapse models for forward simulations. In each time-lapse experiment, 32 active sources are deployed at the injection well and 140 receivers are deployed in the observation well (Figure 2b). The observed seismic data is simulated by a finite-difference scheme with 8th-order accuracy in space and second-order in time. Gaussian white noise is added in the observed seismic data, and the signal-to-noise ratio is defined as

$$SNR = 10log_{10}\frac{\|d\|_2^2}{\|\sigma\|_2^2}, \tag{27}$$

where d is the observed data, and σ^2 is the noise variance. The signal to noise ratio of observed data is 25 after adding noise. The source function is a Ricker wavelet with the dominant frequency of 250 Hz. The grid size is $0.45\ m \times 0.45\ m$ and the model size is about $69.3\ m \times 64.35\ m$.

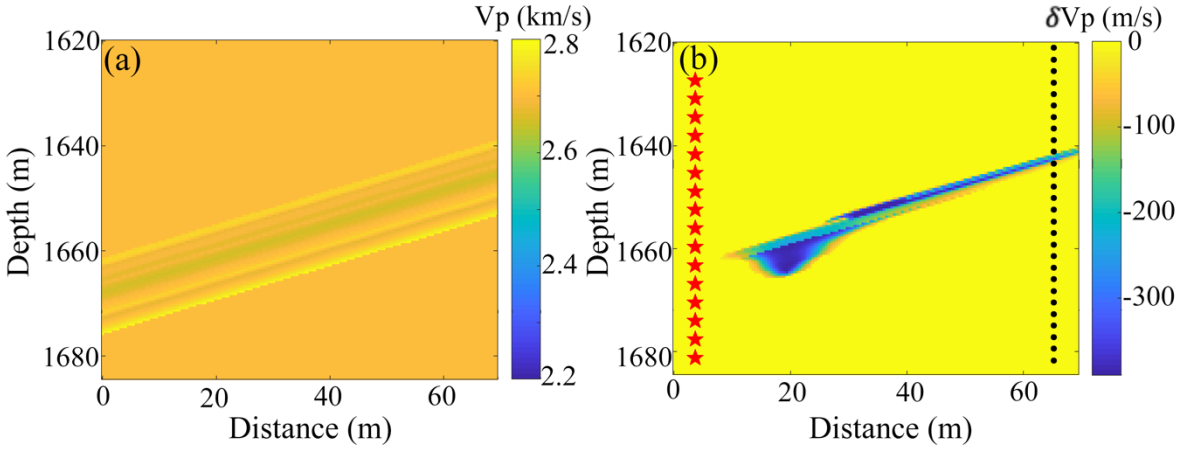

Figure 2. (a) Baseline velocity model for Frio-II tests; (b) time-lapse velocity changes after 120 hours CO_2 injection (red stars indicate sources and black dots stand for receivers).

During the test, we use the baseline velocity model as the initial model for the proposed TLFWI-HiEKF method at the first time-lapse. The frequency selection for TLFWI is from 13.5 Hz to 313.5 Hz with an interval of 12.5 Hz. These frequencies are divided into three groups: the first group is ranging from 13.5 Hz to 151 Hz, the second is [151 Hz, 238.5 Hz], and the third is [238.5 Hz, 313.5 Hz]. The initial value of δ^2 is set as 90000 $(m \cdot s^{-1})^2$ assuming we have no prior information about the model. The noise matrix $\boldsymbol{R}$ in the seismic data is set diagonal with a constant value equal to the noise variance. The model error covariance matrix of $\boldsymbol{Q}$ is constructed from an exponential function (Li et al. 2014)

$$\boldsymbol{Q}(r) = \exp\left(-\sqrt{\frac{r}{L}}\right), \tag{28}$$

where r is the distance between two points, and L is the correlation length.

TLFWI-HiEKF inversion results

After processing simulated time-lapse seismic data in 32 timeframes using TLFWI-HiEKF, we reconstruct the corresponding maps of velocity changes induced by CO_2 injection. Figure 3b shows the inverted results at three time lapses (3 hours, 48 hours and 93 hours). Comparing the inverted results to true velocity models, the primary velocity changes (blue zones in Figures 3a and 3b) induced by CO_2 injection are captured with a comparable resolution. The perturbation results indicate the spatiotemporal changes of the injected CO_2 gas. We notice some oscillations (pointed by arrow in Figure 3b) in the inverted results. The oscillations are likely caused by the limited frequency band we used for inversion. It is possible that we can broaden the inversion frequency band to improve the quality of inverted results, but large number of frequencies would cause extra computational cost.

Figure 3c shows the estimated standard deviation (SD) δ (the square root of diagonal of the posterior covariance matrix) distributions in which the standard deviation value represents the

degree of uncertainty, i.e., small standard deviation indicates low uncertainty, vice versa. We found that the uncertainty distribution is somehow consistent to the illumination distribution of the crosswell geometry of seismic surveys. Overall, the estimated velocity between the two wells have less uncertainty compared to the remainder of the model. We also observed that the standard deviation is decreasing over lapsed time. It indicates that with more time-lapse seismic data, the accuracy of the recovered model is increasing, which proves that our method can impose temporal constraints on velocity changes and update the model well over time. For comparison, the model error distributions are also plotted in Figure 4. The error maps show the absolute value differences between true and inverted models while the uncertainty (standard deviation) maps show how much we can trust on our inverted results. We can see that the values of model error and the standard deviation are at the same level.

To measure the accuracy of the inverted result, we calculate relative model error e_t by

$$e_t = \frac{\|\boldsymbol{v}_{est} - \boldsymbol{v}_{true}\|_2}{\|\boldsymbol{v}_{true}\|_2}. \tag{29}$$

The $\boldsymbol{v}_{est}$ and $\boldsymbol{v}_{true}$ are the inverted and true velocity models at time lapse t. Figure 5 plots the relative estimation error as a function of time. As shown, the predictions become increasingly accurate over time as more data have been assimilated, which is consistent with the decreasing trend of the standard deviation values in Figure 3c.

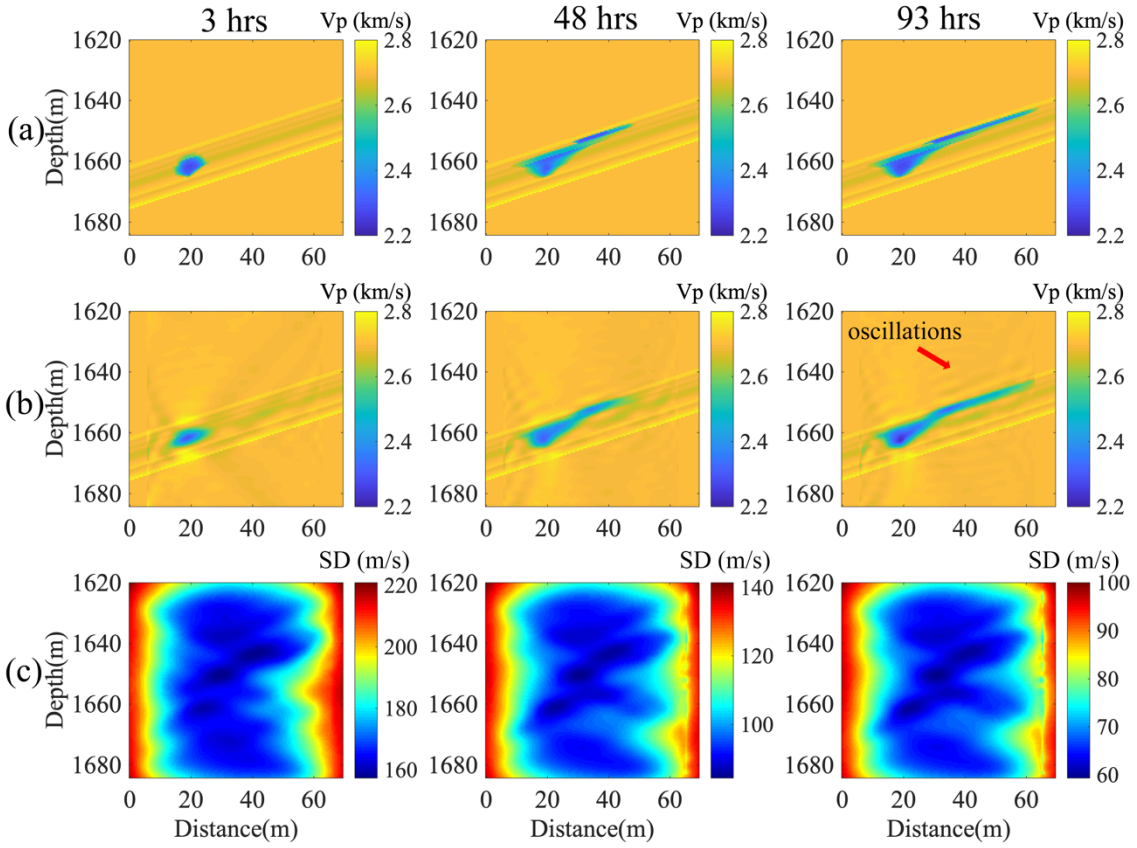

Figure 3. (a) True time lapse velocity models, (b) inverted results, and (c) the corresponding standard deviation (in m/s) distribution at the injection time of 3 hours, 48 hours and 93 hours, respectively.

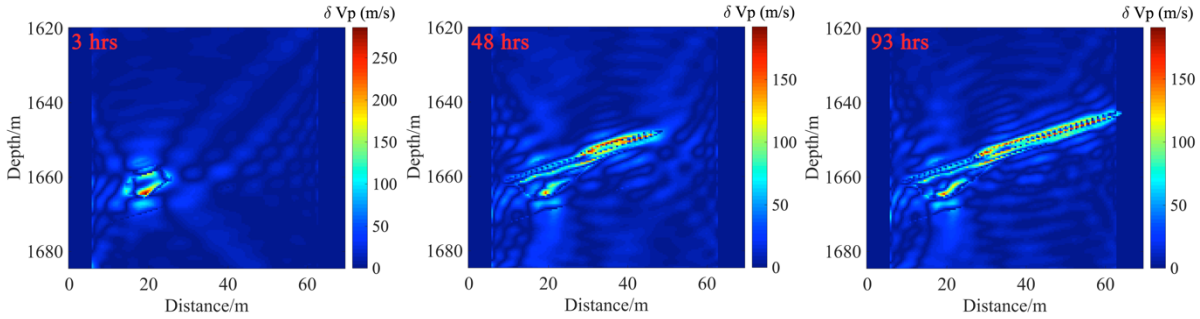

Figure 4. The velocity model error distribution at the injection time of 3 hours, 48 hours and 93 hours, respectively.

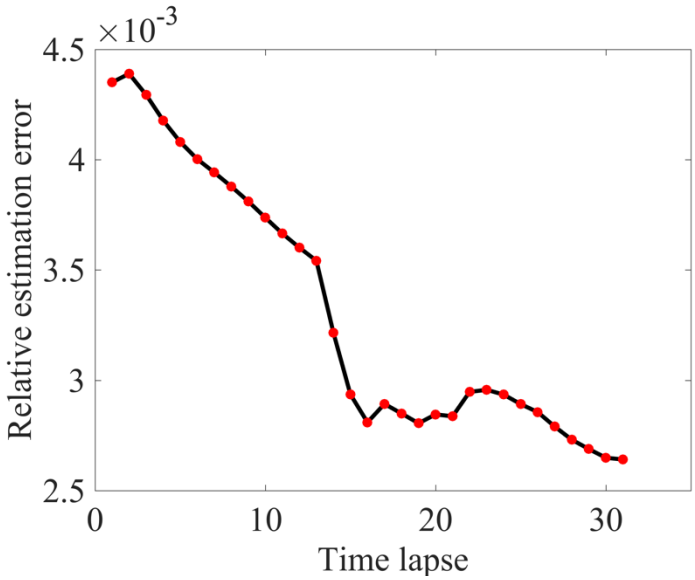

Figure 5. Estimated model error relative to the true solution verse time lapses.

To measure the accuracy of the results in terms of data matching, we compare seismic shot gather using inverted and true velocity models in Figure 6. We first generate two synthetic seismograms using the final velocity model (blue wiggles in Figure 6b) and its corresponding initial model (black wiggles in Figure 6a) at the time lapse of 3 hour, then compare two synthetic seismograms with observed seismic waveforms (red wiggles in Figure 6), respectively. We can see that the synthetic data with the final velocity model matches the observed data much better than when using the initial model. We repeat comparisons at other two other time lapses (48 hours and 93 hours) in Figures 6c-6f. By comparing the data matching over time (from left to right in Figure 6), it seems that the residual between the synthetic and observed data is decreasing over time lapses, which confirms that the TLFWI-HiEKF method is able to increase the accuracy of results over time by assimilating more observed time-lapse data with effective temporal constraints.

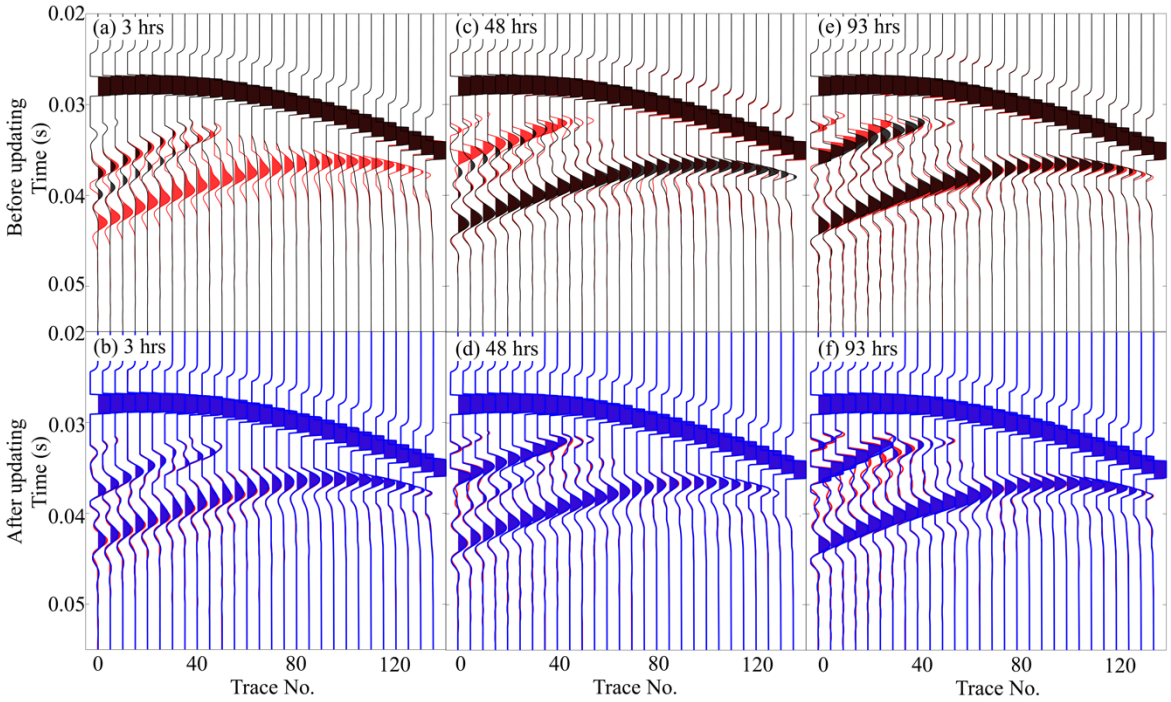

Figure 6. Waveform comparisons before inversion (a), (c) and (e) at the injection time of 3 hours, 48 hours, and 93 hours. Waveform comparisons after inversion (b), (d) and (f) at the injection time of 3hours, 48 hours and 93 hours (Red stands for the observed data, black stands for the predicted data before inversion and blue stands for the predicted data after inversion at different time lapses).

TLQFWI-HiEKF inversion results

This subsection will present a synthetic test of the scheme of TLQFWI-HiEKF in time-lapse seismic monitoring datasets collected in Frio-II CO2 sequestration site. In Frio-II, dense 2D cross-well time-lapse seismic survey was carried out.

The base line Q model is assumed to be homogenous (Figure 7). The time-lapse models of both velocity and Q are retrieved from the Frio-II CO2 flow simulations using the rocks physics White's model (Daley et al., 2011). Figure 8 shows the simulated CO2-induced velocity and attenuation changes after five-days of injection in Frio-II site. The seismic velocity and Q changes due to CO2 plumes are predicted by rock physics modeling of velocity and saturation from a 3D multiphase flow model (Daley et al. 2011). We have totally 41 time-lapse seismic models with 3-hour intervals. Figure 9 shows three time-lapse P-wave velocity (vp) and attenuation (γ) models at 3 hour, 48 hour, and 93 hour.

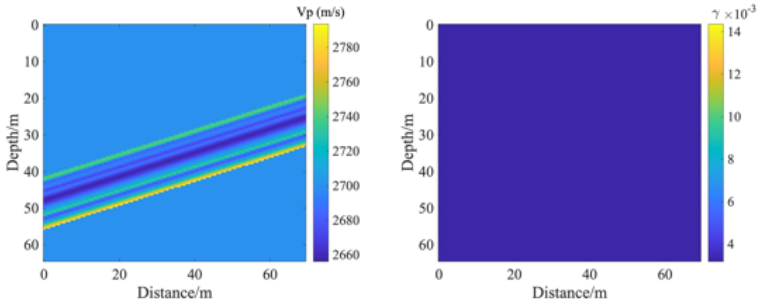

Figure 7: The base line velocity and attenuation models.

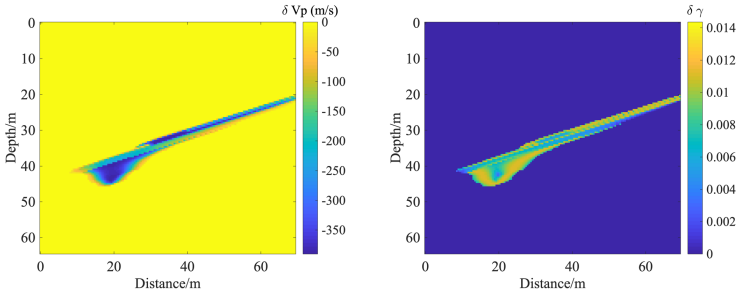

Figure 8: The induced velocity and attenuation changes after five days injection of CO2 gas.

We simulate synthetic time-lapse seismic crosswell data every 3 hours. We use 32 time-lapse models for forward simulations. In each time-lapse experiment, 32 active sources are deployed at the injection well at $x = 4.5\ m$ and 128 receivers are deployed in the observation well at $x = 65.25\ m$. The observed seismic data is simulated by a finite-difference scheme. We add zero mean Gaussian noise to the synthetic observed seismic data. The signal to noise ratio of observed data is 25 after adding noise. The source function is a Ricker wavelet with the dominant frequency of 250 Hz. The grid size is 0.45 m×0.45 m and the model size is about 69.3 m×64.35 m. During the test, we use the baseline velocity and attenuation models as the initial models for the proposed TLQFWI-HiEKF method at the first time-lapse. The frequency selection for TLQFWI is from 13.5 Hz to 313.5 Hz with an interval of 12.5 Hz. The initial value of σ_v^2 and σ_γ^2 are set as 300 $(m \cdot s^{-1})^2$ and 0.009 respectively assuming we have no prior information about the model.

After processing simulated time-lapse seismic data in 32 timeframes using TLQFWI-HiEKF, we reconstruct the corresponding maps of velocity and attenuation changes induced by CO2 injection. Figure 10 shows the inverted results at three time lapses (3 hours, 48 hours and 93 hours). Comparing the inverted results to true velocity and attenuation models, the primary velocity and attenuation changes induced by CO2 injection are captured with a comparable resolution. The perturbation results indicate the spatiotemporal changes of the injected CO2 gas. Figure 11 shows the estimated variance (diagonal of the posterior covariance matrix) distributions in which the variance value represents the degree of uncertainty, i.e., small variance indicates low uncertainty, vice versa. We found that the uncertainty distributions of velocity and attenuation are somehow consistent to the illumination distribution of the crosswell geometry of seismic surveys. Overall, the estimated velocity and attenuation between the two wells have less uncertainty compared to

the remainder of the model. We also observed that the variance is decreasing over lapsed time. It indicates that with more time-lapse seismic data, the accuracy of the recovered model is increasing, which proves that our method can impose temporal constraints on velocity and attenuation changes and update the model well over time.

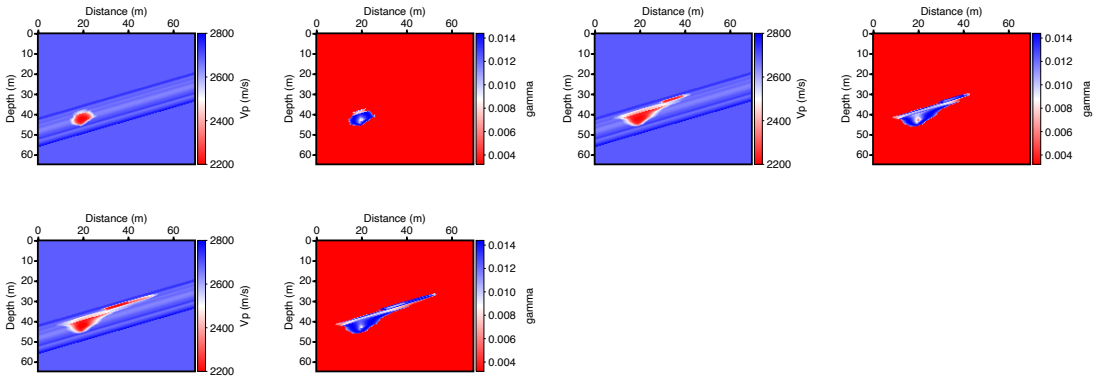

Figure 9: True time lapse velocity (left) and attenuation (right) models at the injection time of 3 hours (top), 48 hours (middle) and 93 hours (bottom), respectively.

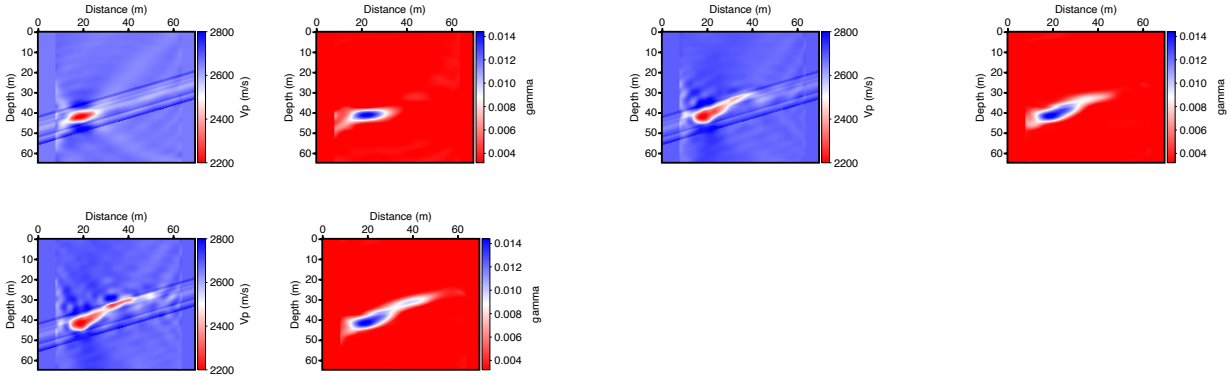

Figure 10: Inverted time lapse velocity (left) and attenuation (right) models at the injection time of 3 hours (top), 48 hours (middle) and 93 hours (bottom), respectively.

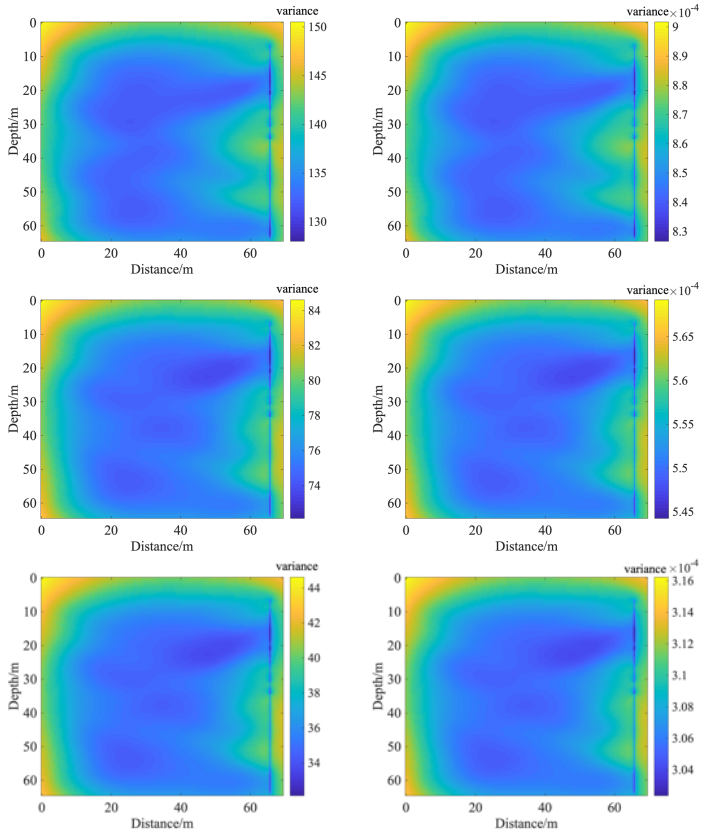

Figure 11: The corresponding variance distribution of velocity (left) and attenuation (right) at the injection time of 3 hours (top), 48 hours (middle) and 93 hours (bottom), respectively.

3D Cranfield model

In this section, we demonstrate the applicability of the proposed TLFWI-HiEKF method in the 3D Cranfield CO_2 injection time-lapse models.

The Cranfield site is located at Denbury Resources Cranfield Field in southwest Mississippi. It was discovered in 1946 and abandoned in 1965 at the end of primary oil and gas production. The reservoir was redeveloped by Denbury Onshore LLC and brought on as a CO_2-EOR field in 2008 using CO_2 transported via pipeline from a natural accumulation near Jackson, MS, USA. The main CO_2 injection test was conducted in the water leg of the structure beyond producible hydrocarbon accumulations (Ajo-Franklin et al. 2013). The baseline seismic P-wave velocity model is built from the 3D baseline seismic migration section and two well-logs (Figure 12a) based on seismic structural and stratigraphic features (Wu 2017). To meet the memory limits in our high-performance computing cluster, we modify the size of the original velocity model ($2.75km \times 3.0km \times 1.5km$) as shown in Figure 12b. Six time-lapse velocity models are manually constructed (Wu 2017) and shown in Figure 14, where the layered structures are in the color scale and black blocks drawn by isosurface indicate the velocity changes induced by CO_2 plumes.

Similar to field surveys, we adopt a surface seismic acquisition survey to collect 3D time-lapse data. We deploy 24 receiver lines along the Y-direction with an interval of 125 m and 22 receivers are evenly distributed in each receiver line from 0 km to 2.75 km along the X-direction (Black dots

in Figure 12b). At each time lapse, we design 12 shot lines along the Y-direction with an interval of 250 m with 11 shots evenly distributed along each shot line from 0 km to 2.75 km in X-direction on the surface. In total, 132 sources are fired in each timeframe (red stars in Figure 12b). A 3D finite-difference scheme with 8th-order accuracy in space and second-order in time is used to generate the observed seismic data using the true velocity models in each time lapse. Again, we contaminate the synthetic observed seismic data with Gaussian noise (SNR=25). The source function is a Ricker wavelet with the dominant frequency of 15 Hz. The grid size is $25\ m \times 25\ m \times 25m$. Baseline shot gather data and time-lapse data at different time lapses are shown in Figure 8 and time-lapse waveform differences are caused by the CO_2 injection (Figures 13b-13f). TLFWI-HiEKF has been applied from 1 to 25 Hz with an interval of 1 Hz. Totally two frequency groups are used for TLFWI in this test: one is from 1 Hz to 12 Hz and the other is from 12 Hz to 25 Hz. The initial settings of δ^2, the noise matrix $\boldsymbol{R}$ and the cross-covariance $\boldsymbol{A}$ are identical to those in the Frio-II test.

The results are shown in Figure 15, where black blocks represent inverted time-lapse velocity changes at different time lapses. Compared to the ground truth models in Figure 14, time-lapse velocity changes (the CO_2 plume in the subsurface) are well captured by 3D TLFWI-HiEKF. Figure 16 compares the true velocity models (left column) with the inverted results (middle column) from the first time lapse to the fifth time lapse. Similar observations are that the inverted results successfully capture the velocity changes induced by the CO_2 plume. In addition, the corresponding standard deviation map (the square root of diagonal of the posterior covariance matrix) at each timelapse is shown in Figure 15 (right column). It is clear that the standard deviation maps (timelapse one trough five) are all dominated by surface seismic wave illumination, and the uncertainty increases toward the depth where poor illumination is expected. To compare the standard deviation over time, we sum the standard deviation matrix and plot these values in Figure 18. We found that the standard deviation values decrease over time lapse, similar to 2D Frio tests, which indicate that TLFWI-HiEKF is able to continuously update the results with more incoming time-lapse seismic data. From the model error distributions in Figure 17, we can still see the trend of decreasing values over time.

Figure 19 presents the comparison between the true and inverted CO_2-induced velocity perturbations at the fifth time lapse. The 3D velocity changes induced by CO_2 injection are well captured, showing the successful applicability of the TLFWI-HiEKF method in a 3D time-lapse seismic experiment.

6 Conclusions

We have presented the TLFWI-HiEKF method to process dense time-lapse seismic data. We showed that the velocity estimate at current time lapse by TLFWI rather than the random walk model can serve as a better guess of the *a priori* velocity model in the update step. This step reduces the nonlinearity in the subsequent update step but also speed up the convergence of the inversion. Moreover, HiEKF allows to store and update a data-sparse representation of the cross-covariance matrices using $\mathcal{H}^2$-matrices algebra and propagate model errors without expensive operations involving covariance matrices. As a result, the proposed TLFWI-HiEKF algorithm can handle large-scale 3D problems with affordable memory and computational requirements. The proposed HiEKF can be easily modified to 3D FWI by applying multi-scale FWI from low frequency to

high frequency and treating seismic data as a dynamic evolution over the frequency axis (Thurin et al. 2019).

Taking advantage of both TLFWI and HiEKF, the proposed TLFWI-HiEKF method can impose both spatial and temporal constraints for inverting spatiotemporal subsurface time-lapse velocity changes while simultaneously allowing to quantify the uncertainty of the inverted velocity changes over time. The standard deviation maps provide us a straightforward way of evaluating the results. It is worth to note that the proposed method can continuously update the subsurface velocity model and the accuracy of the model is increasing over time by assimilating more input time-lapse data. This is advantageous over other time-lapse strategies.

In the HiEKF algorithm, we have to calculate and store the Fréchet kernel matrix during inversion which is the most memory consuming part in the TLFWI-HiEKF implementation. The Fréchet kernel matrix $\boldsymbol{H}$ in our algorithm is calculated by the scattering-integral approach method (Liu et al., 2015). Based on the fact that the number of observations is often much smaller (at least one or two orders) than that of model parameters, storing the Fréchet kernel matrix is possibly affordable in most 3D seismic cases. Rather than calculating the Fréchet kernel matrix itself, however, the adjoint state method is to calculate the product of Fréchet derivative with a vector (data residuals), which is the gradient in FWI.

We have demonstrated that the TLFWI-HiEKF is feasible and efficient in two different seismic time-lapse surveys: 3D surface seismic sparse surveys in Cranfield and 2D crosswell dense seismic surveys in Frio-II. In terms of the continuous active-source seismic monitoring (CASSM) that has extremely high temporal sampling rates and can reveal the corresponding rate of changes in the monitored physical parameters (Daley et al. 2007), our perspective is to equip the proposed full waveform processing (TLFWI-HiEKF) with the CASSM system for long-term and large-scale CO_2 monitoring. Although the early demonstration of CASSM is restricted to the crosswell acquisition due to limited seismic source power (Daley et al. 2007), newly developed seismic sources and sensors including the Accurately Controlled Routinely Operated Signal System (Ikeda T et al. 2017), distributed acoustic sensing sensors (Daley et al. 2013), and distributed sensor networks (Song et al. 2019) offer a path for surface CASSM surveys. Moreover, with the capability of seismically inverting elasticity and attenuation (Xing & Zhu 2019), multi-parameters TLFWI including elasticity and attenuation will be incorporated in the future development. We anticipate that the proposed method will become a companion processing tool for processing CASSM data in future large-scale subsurface monitoring applications (e.g., CO_2 sequestration, geothermal monitoring, reservoir monitoring).

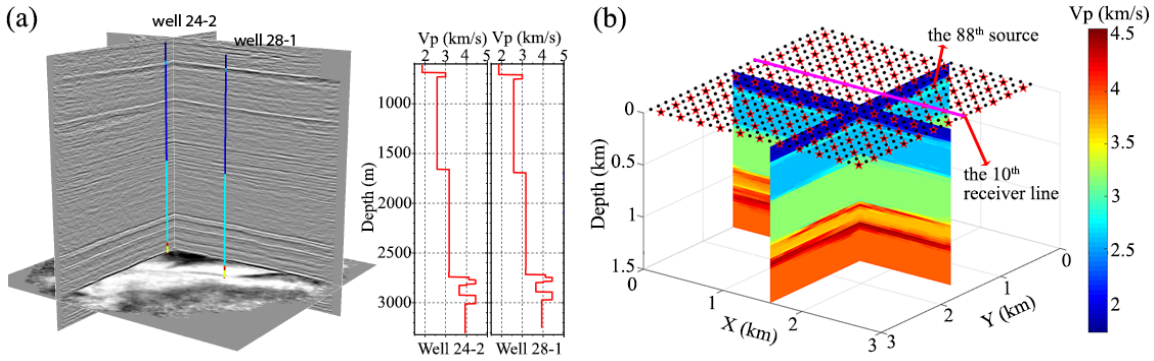

Figure 12. (a) 3D seismic migration data and two P-wave velocity logs for Cranfield; (b) 3D baseline velocity model with arrays of seismic sources and receivers (Black dots represent receivers and red stars stand for sources).

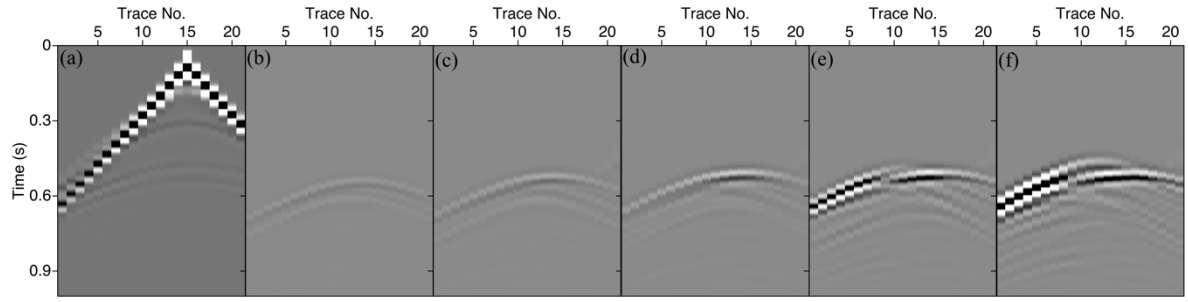

Figure 13. A time-lapse shot gather profile from a selected receiver line (the 10th receiver line in Figure 6b). (a) Baseline data. (b)-(f) data residual by subtracting baseline data (a) from five time-lapse data. (b) 1st time-lapse; (c) 2nd time-lapse; (d) 3rd time-lapse; (e) 4th time-lapse; (f) 5th time-lapse. Seismic reflections are caused by injected CO_2.

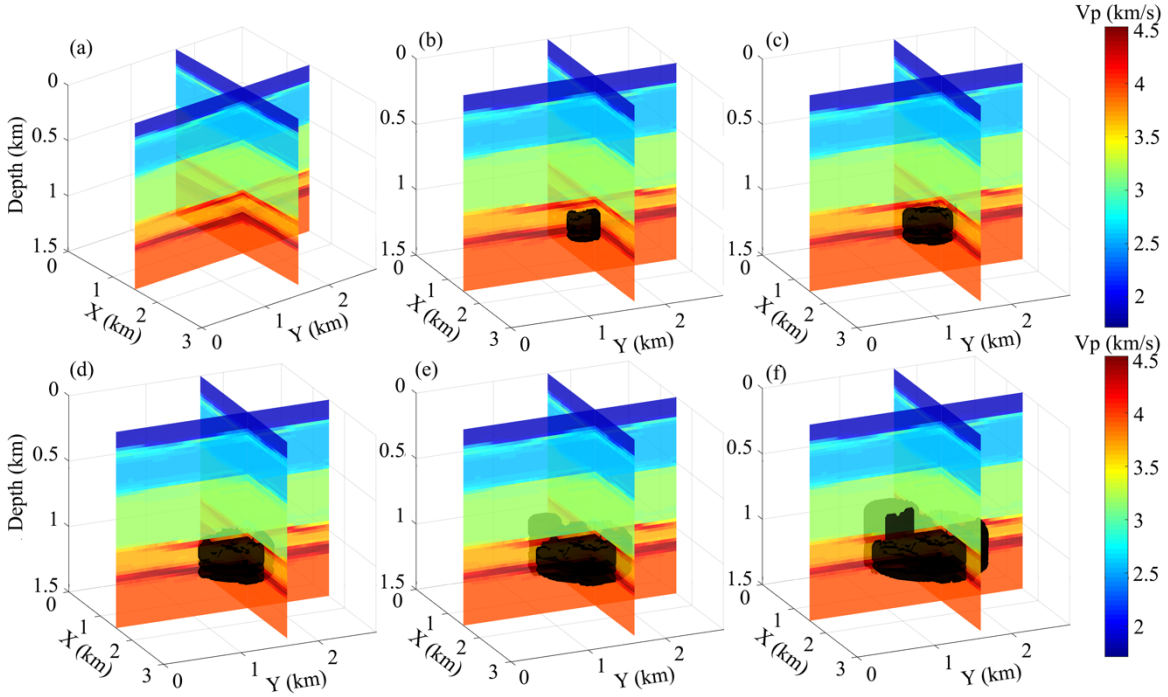

Figure 14. True velocity models at different time lapses with an isosurface plot of time-lapse velocity changes (black blocks) induced by CO_2 plumes. (a) baseline model; (b) 1st time-lapse; (c) 2nd time-lapse; (d) 3rd time-lapse; (e) 4th time-lapse; (f) 5th time-lapse.

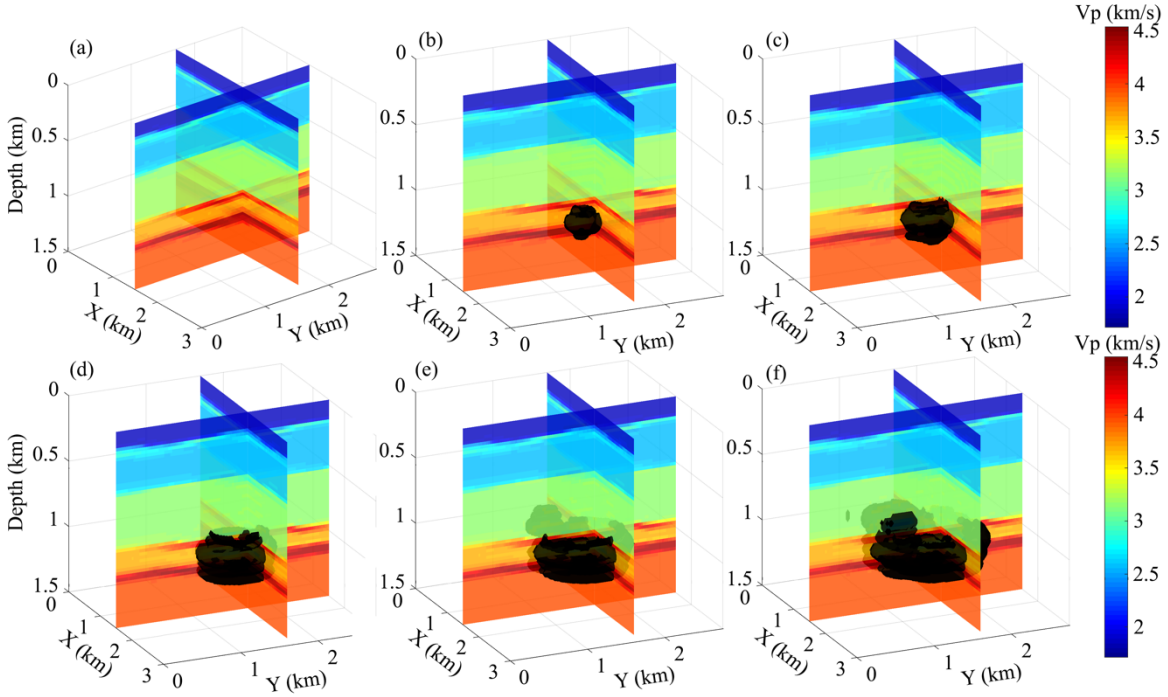

Figure 15. Inverted velocity models at different time lapses with an isosurface plot of time-lapse velocity changes (black blocks) induced by CO_2 plumes. (a) baseline model; (b) 1st time-lapse; (c) 2nd time-lapse; (d) 3rd time-lapse; (e) 4th time-lapse; (f) 5th time-lapse.

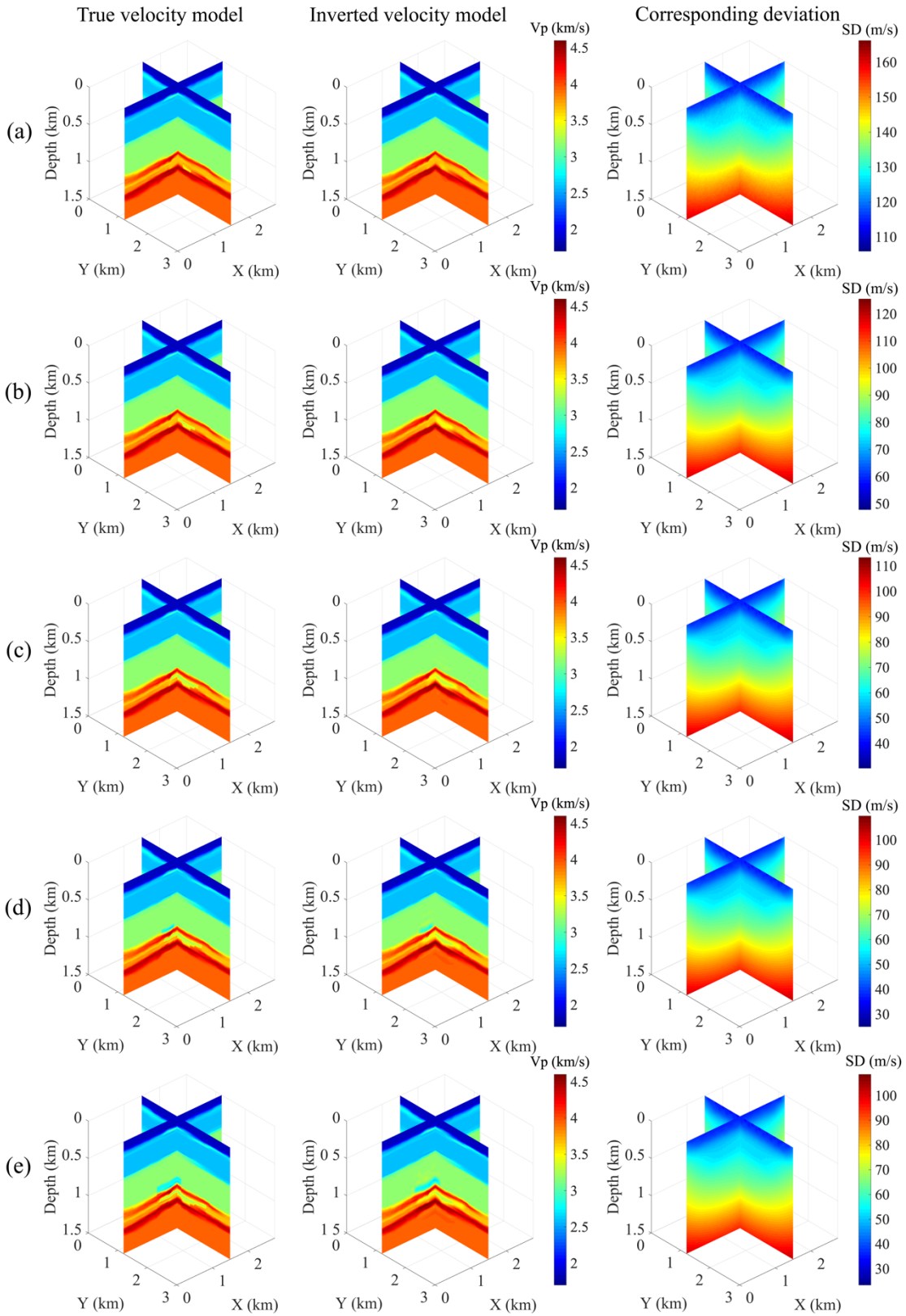

Figure 16. Slices of true velocity models (left column), inverted results (middle column) and corresponding standard deviation (right column) at (a) 1st, (b) 2nd, (c) 3rd, (d) 4th and (e) 5th time lapses.

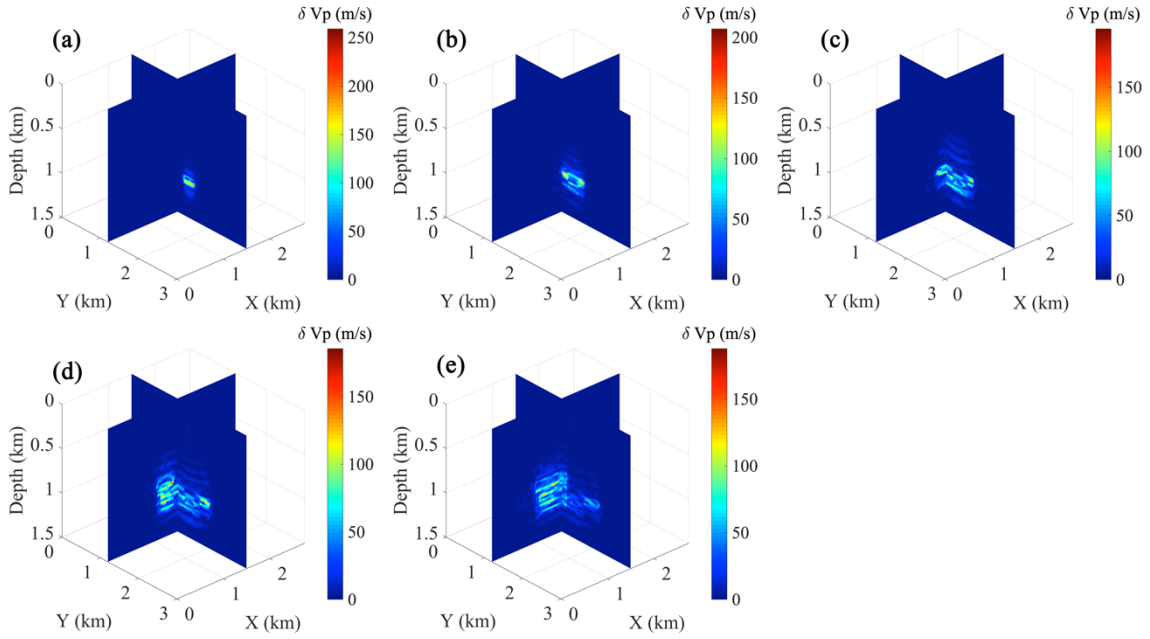

Figure 17. The velocity model error distribution at (a) 1st, (b) 2nd, (c) 3rd, (d) 4th and (e) 5th time lapses.

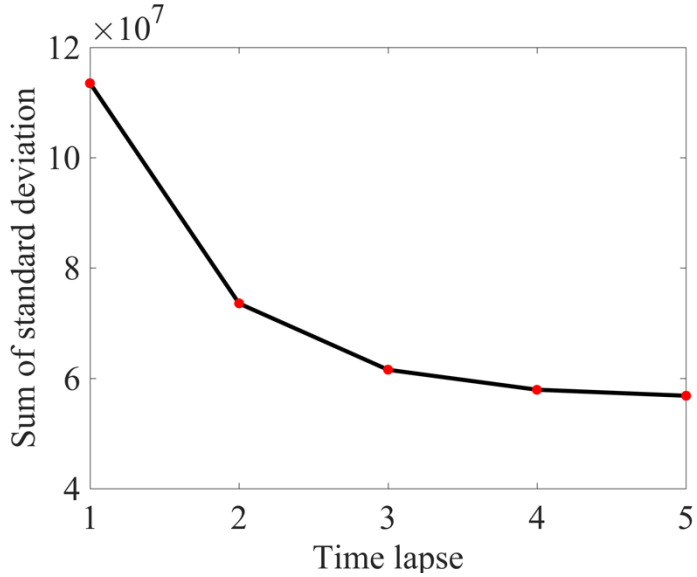

Figure 18. Summed values of the standard deviation matrix over five time lapses (red dots stand for the values of standard deviation at each time lapse).

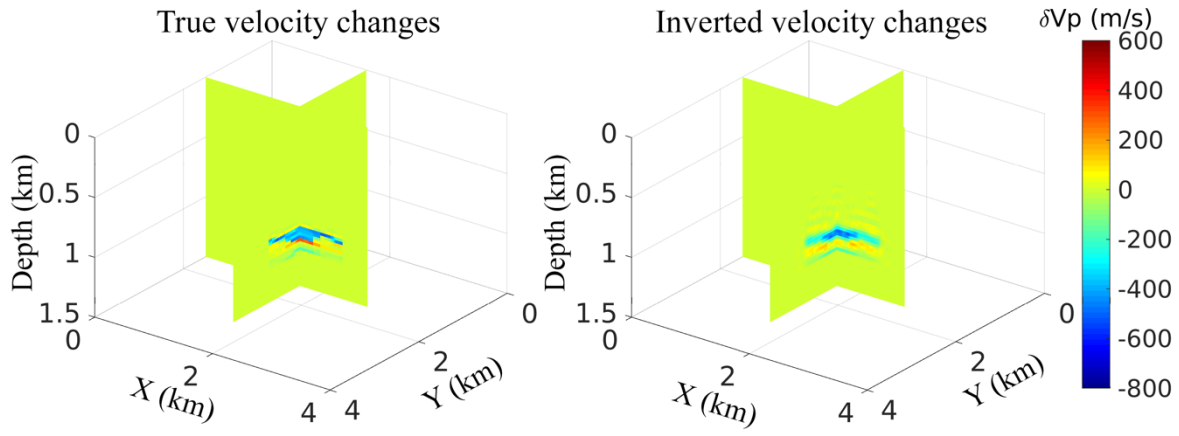

Figure 19. Comparison between true perturbations and the inverted perturbations at the fifth time-lapse.

7 References

Ambikasaran, S., Li, J. Y., Kitanidis, P. K., & Darve, E., 2013, Large-scale stochastic linear inversion using hierarchical matrices. Computational Geosciences, 17(6), 913-927.

Ajo-Franklin, J. B., Peterson, J., Doetsch, J., & Daley, T. M., 2013, High-resolution characterization of a CO_2 plume using crosswell seismic tomography: Cranfield, MS, USA. International Journal of Greenhouse Gas Control, 18, 497-509.

Asnaashari, A., Brossier, R., Garambois, S., Audebert, F., Thore, P. and Virieux, J., 2015, Time-lapse seismic imaging using regularized full-waveform inversion with a prior model: which strategy? Geophysical Prospecting 63, 78–98.

Daley, T. M., J. B. Ajo-Franklin, and C. Doughty, 2011, Constraining the reservoir model of an injected CO_2 plume with crosswell cassm at the frio-ii brine pilot: International Journal of Greenhouse Gas Control, 5, 1022–1030.

Daley, T. M., Freifeld, B. M., Ajo-Franklin, J., Dou, S., Pevzner, R., Shulakova, V., ... & Lueth, S., 2013, Field testing of fiber-optic distributed acoustic sensing (DAS) for subsurface seismic monitoring. The Leading Edge, 32(6), 699-706.

Daley, T. M., Myer, L. R., Peterson, J. E., Majer, E. L., & Hoversten, G. M., 2008. Time-lapse crosswell seismic and VSP monitoring of injected CO_2 in a brine aquifer. Environmental Geology, 54(8), 1657-1665.

Daley, T. M., R. D. Solbau, J. B. Ajo-Franklin, and S. M. Benson, 2007, Continuous active-source seismic monitoring of CO_2 injection in a brine aquifer: Geophysics, 72, A57–A61.

Eikrem, K. S., G. Nævdal, and M. Jakobsen, 2019, Iterated extended kalman filter method for time-lapse seismic full-waveform inversion: Geophysical Prospecting, 67(2): 379-394.

Huang, C., Dong, L. G., & Chi, B. X., 2015. Elastic envelope inversion using multicomponent seismic data with filtered-out low frequencies. Applied Geophysics, 12(3), 362-377.

Huang, C., & Zhu, T., 2019. Time-lapse full waveform inversion plus extended Kalman filter for high-resolution seismic models and uncertainty estimation. In SEG Technical Program Expanded Abstracts 2019 (pp. 5239-5244). Society of Exploration Geophysicists.

Ikeda T, et al. (2017) Temporal variation of the shallow subsurface in the Aquistore CO_2 storage site associated with environmental influences using a continuous and controlled seismic source. J Geophys Res 122:2859–2872.

Kepert, J. D., 2004. On ensemble representation of the observation-error covariance in the Ensemble Kalman Filter. Ocean Dynamics, 54(6), 561-569.

Li, J. Y., S. Ambikasaran, E. F. Darve, and P. K. Kitanidis, 2014, A kalman filter powered by h2-matrices for quasi-continuous data assimilation problems: Water Resources Research, 50, 3734–3749.

Plessix, R. E., 2006, A review of the adjoint-state method for computing the gradient of a functional with geophysical applications. Geophysical Journal International, 167(2), 495-503.

Raknes, E.B. and Arntsen, B. 2015. A numerical study of 3D elastic time-lapse full-waveform inversion using multicomponent seismic data. Geophysics 80, R303–R315.

Raknes, E.B.,Weibull, W. andArntsen, B. 2013. Time-lapse full waveform inversion: Synthetic and real data examples. SEG Technical Program Expanded Abstracts, 944–948.

Sirgue, L., and R. G. Pratt, 2004, Efficient waveform inversion and imaging: A strategy for selecting temporal frequencies: Geophysics, 69, 231–248.

Song, W., F. Li, M. Valero, L. Zhao, 2019, Toward Creating Subsurface Camera: Sensors, 19 (2), 301.

Tarantola, A., 2005, Inverse problem theory and methods for model parameter estimation: siam, 89.

Thurin, J., Brossier, R., & Métivier, L., 2019, Ensemble-based uncertainty estimation in full waveform inversion. Geophysical Journal International, 219(3), 1613-1635.

Wu, X., 2017, Building 3D subsurface models conforming to seismic structural and stratigraphic features. Geophysics, Vol.82(3), IM21-IM30.

Xing, G. and T. Zhu, 2019, Fréchet kernels based on a fractional viscoacoustic wave equation. SEG Technical Program Expanded Abstracts, 1455-1459

Zhu, T., Ajo-Franklin, J. B., and Daley, T. M., 2017, Spatiotemporal changes of seismic attenuation caused by injected CO_2 at the Frio-II pilot site, Dayton, TX, USA. Journal of Geophysical Research: Solid Earth, 122(9), 7156-7171.

Zhu, T., J. Ajo-Franklin, T. M. Daley, and C. Marone, 2019, Dynamics of geologic CO_2 storage and plume motion revealed by seismic coda waves: Proceedings of the National Academy of Sciences, 116 (7) 2464-2469; DOI:10.1073/pnas.1810903116

Multiscale reservoir modeling of plume migration

This task includes the development of a workflow for predicting the CO2 plume, as well as formation pressure. The workflow will integrate both seismic inversion (in the form of the full-waveform inversion fed into the Bayesian inversion of a rock physics model) and pressure monitoring inversion (data assimilation with forward fluid flow modeling). Specifically, our goal was to develop accurate geologic and fluid flow models of the Cranfield site to effectively perform inversion of CO2 flow properties from seismic and pressure data. The prior models consider the complexity of the reservoir and integrate the available information (e.g. well logs). The static geomodels that we have developed cover the spatial domain of the CASSM survey and incorporate all prior data into best estimates of reservoir properties, including pressure. Dynamic reservoir modeling was also performed on the ensemble of geomodels developed using multi-phase flow models. The Cranfield geology is described as a fluvial point bar system and the modeling approach adopted is described in this report.

1 Introduction

The objectives of this study are to a) develop a geologically realistic framework for modeling heterogeneities in point bar geologic systems b) access the impact of the heterogeneities on CO_2 sequestration potential. The results of this study will provide the Department of Energy (DOE) an insight into the long-term CO_2 sequestration potential of the Cranfield injection site. This document is in two main parts, the first part is essentially the modeling of the Cranfield point bar reservoir. For this section, the work flow in modeling point bar heterogeneities with its application to the Cranfield dataset is presented. This is followed by presentation of the results of our gridding scheme, which generates curvilinear grids representative of the point bar geometry. In addition, Geostatistical simulation procedure is illustrated, and as part of this, a grid transformation scheme is implemented to allow for optimal modeling of the point bar reservoir properties. The presence of shale drapes have also been incorporated. In the second part, a CO_2 flow simulation study was conducted where the effect of point bar heterogeneity (i.e. shale drapes) on CO_2 plume was investigated.

2 Geological Model Construction

2.1 Modeling the channel path

A stochastic process-based approach was adopted to model the point bar heterogeneities, and the first step in achieving this was to model the channel path. The algorithm proceeds as follows:

Identifying meander direction: Channel direction was inferred considering the variation in channel thickness reported in literature as the channel migrates from upstream to downstream and from well log interpretation. Well coordinates were then sorted accordingly in the direction of channel progression. Figure 1 illustrates the stepwise procedure in recreating the meander path, the blue points are channel nodes and the red points are point bar nodes. The direction of channel or meander progression is in the East-West direction from channel node 1 through 13.

Conditioning meander path through channel nodes: Here, two constraints were imposed - the primary constraint is that the meander path must go through channel nodes sequentially in the

direction of channel progression. In the case of insufficient channel nodes, additional nodes (i.e. secondary nodes) are stochastically generated to guide the meander path. The secondary constraint is that the meander path must bend around the point bar locations. As could be seen in all the modeling stages in figure 1, the meander path while going through the channel nodes, is conditioned to bend around the point bar nodes. The secondary constraint is necessary to satisfy the geological and morphological phenomenon that point bars are formed at the bends of meandering fluvial bodies. The meander path is defined by a parametric natural cubic spline which passes through the given sequence of channel nodes.

The basic form of cubic spline, with co-efficient a, b, c and d is given as

$$P(t) = at^3 + bt^2 + ct + d$$

The parameter value $t(j)$ for the jth channel node, is the cumulative sum of chord length defined according to the centripetal scheme by Lee, (1989), and it is expressed as

$$t(j) = \sum \sqrt{\left\| channel\ nodes(i+1) - channel\ nodes(i) \right\|_2}$$

Similar technique to the above procedure has also been employed earlier by Olulana, (2015)

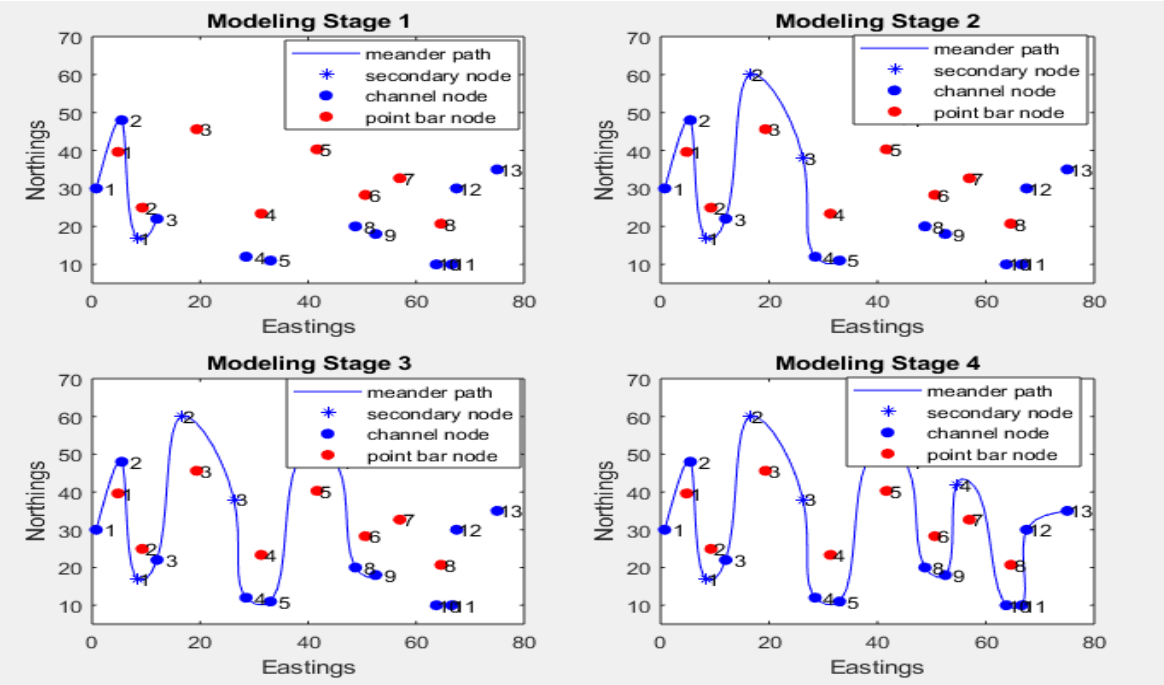

Figure 1. Workflow displaying stages in meander path generation

2.2 Channel and point bar identification

Different techniques have been used in different studies to identify point bars and channels. Some of these include outcrop examination as in the work of Pranter *et al.*, (2007) and well log interpretation by Durkin *et al.*, (2017), Nazeer, Abbasi and Solangi, (2016) and Odundun and Nton, (2011). In these works it has been shown that a bell shape signal in Spontaneous Potential (SP) log

and Gamma Ray (GR) log is an indication of point bar whiles a blocky or cylindrical shape signal indicates a channel. In this study, well logs SP logs and GR logs were used for facies interpretation (see the figure 2).

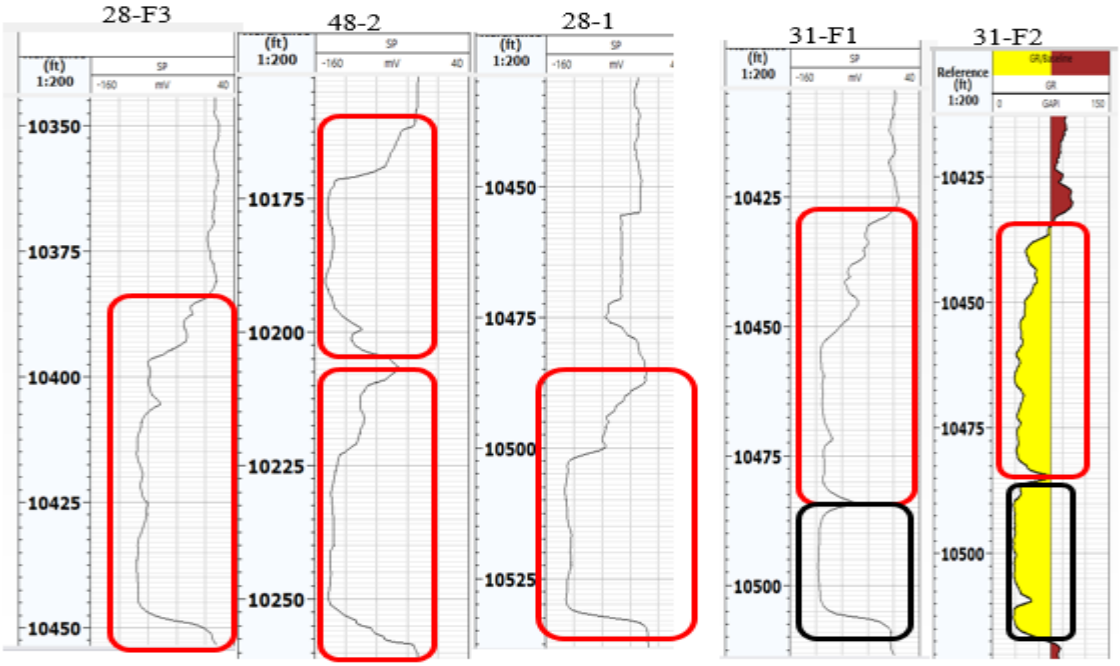

Figure 2 Well log readings for wells 28F-3, 48-2, 28-1, 31-F1 and 31F-3 at Cranfield. The first four well logs show SP reading while the last represents GR logs. Identified channel facies are demarcated in black. Point bar facies are in red demarcations.

2.3 Application to the Cranfield Dataset

The Cranfield injection reservoir geology is a point bar geologic system formed as a result of lateral migration of channels. The reservoir is about 13.72 to 24.38 m. thick, and is located at a depth approximately 3000 m below the ground surface. The injection zone is characterized by a fining upward fluvial depositional trend where cross-bedded conglomerates occupy the bottom of the sequence, followed by sandstones, and muddy sandstones. (Hosseini *et al.*, 2013; Lu *et al.*, 2013). In order to establish fluvial continuity, an attempt was made to correlate well logs using the channel signature. By analyzing well logs, facies were identified either as channels or point bars. Well log signatures that showed bell shapes were interpreted to be point bars whiles those that showed blocky signatures were inferred to be channels. Figure 3 shows the application of the above workflow to the modeling of meander path for the Cranfield dataset. The encircled region in the last modeling stage is the Detailed Area of Study (DAS) which is the Cranfield injection site. This area would be selected for channel migration to model the point bar

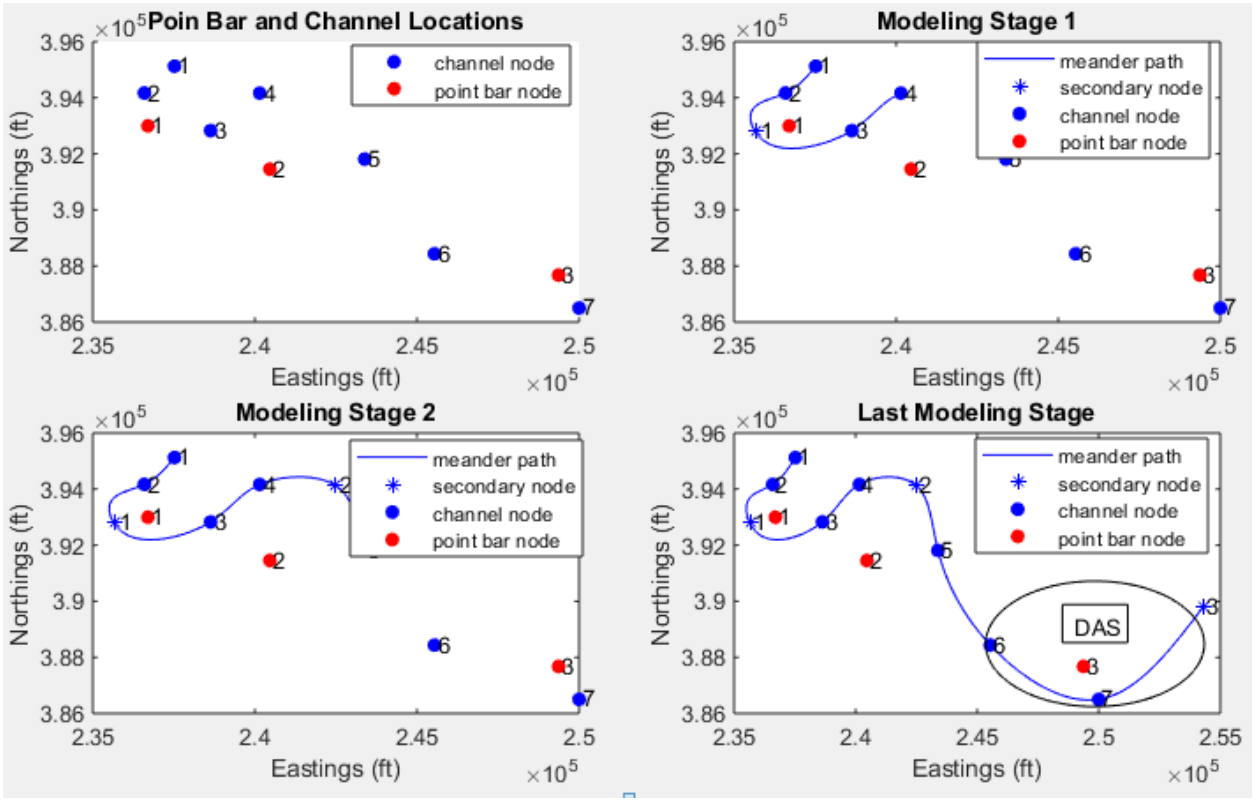

Figure 3 Channel Meander Simulation for the Cranfield dataset. Blue points are channel facies interpreted using well logs. Red points are point bar facies.

2.4 Modeling Meander Migration

Channel meander migration is necessary to capture the main heterogeneities in point bar: lateral accretions and inclined heterolithic stratifications (IHS). To model the accretions, Sine Generation Function (SGF) was used as it provides a convenient closed-form approximation of channel path as the river meanders from one point to another (Hathout, 2015). A confirmation of this close match is illustrated in Fig 4a. Using the SGF, the channel was laterally migrated back in time to recreate the initial meander path (refer to Fig 4b)—and at every migration step, lateral accretions are formed. A cross-section across the initial and current position of meander (see figure 4c) reveals the vertical heterogeneity of the point bar, which is the IHS as shown in Fig 4d. The IHS were modeled using sigmoidal function as described by Thomas et al, (1987).

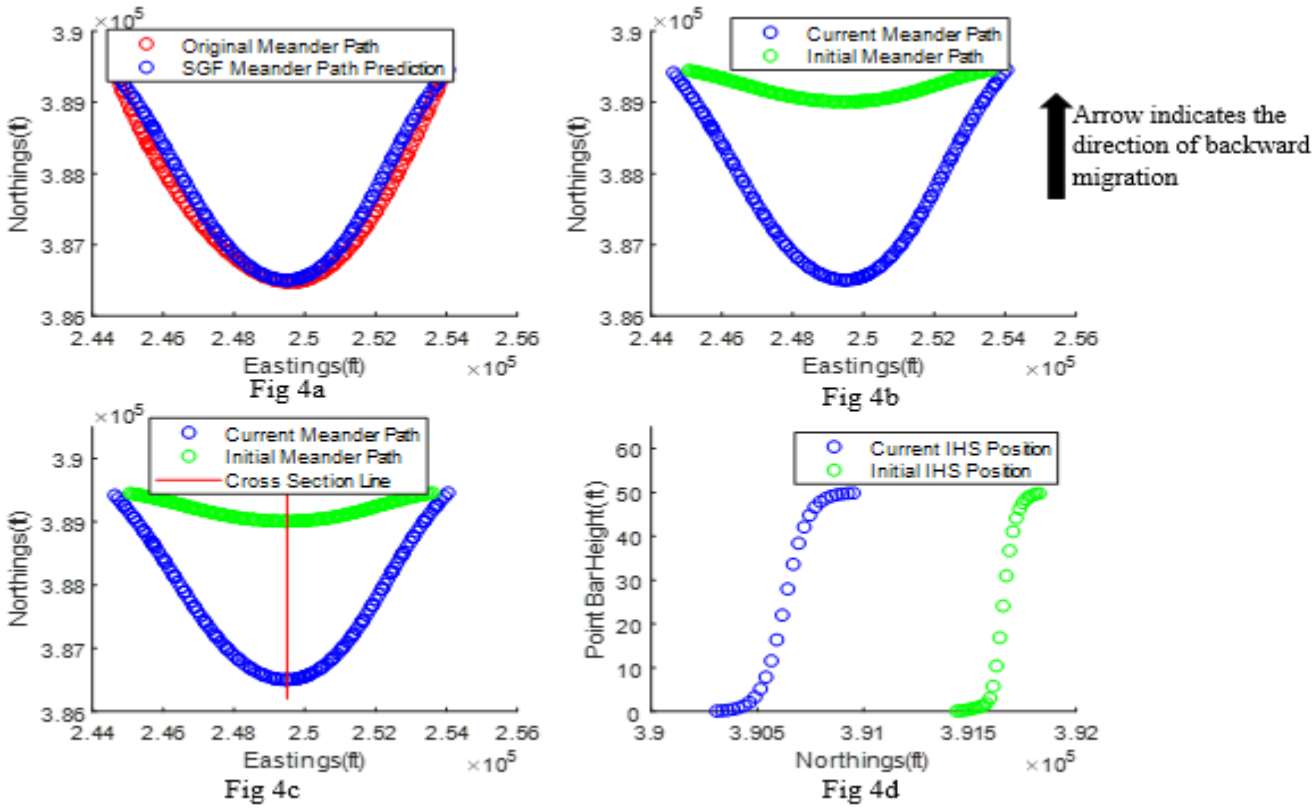

Figure 4: Meander Migration Process

Combining the aerial and vertical gridded surfaces produces 3D surfaces for the initial and final meander. In total there are 6 migration episodes that were modeled.

2.5 Grid Generation for the Meander Geometry

To ensure proper modeling of petrophysical properties, we developed a more representative gridding scheme which generates curvilinear grids representative of the point bar geometry (i.e. curvy shape of the accretion surfaces and the sigmoidal shape of the IHS). Curvilinear grid was generated within the domain bounded by initial and final location of the meander as follows. The gridding is done such that the grid blocks are of varying dimensions and orthogonal to the bounding surfaces. This is shown in Figure 4. The algorithm is able to perturb the meander geometry—spanning from low to high angular sinuosity channels—and recreate the grids accordingly. In all these, the location of wells within the reservoir in terr
points in figure 5) are reported during the meander geo

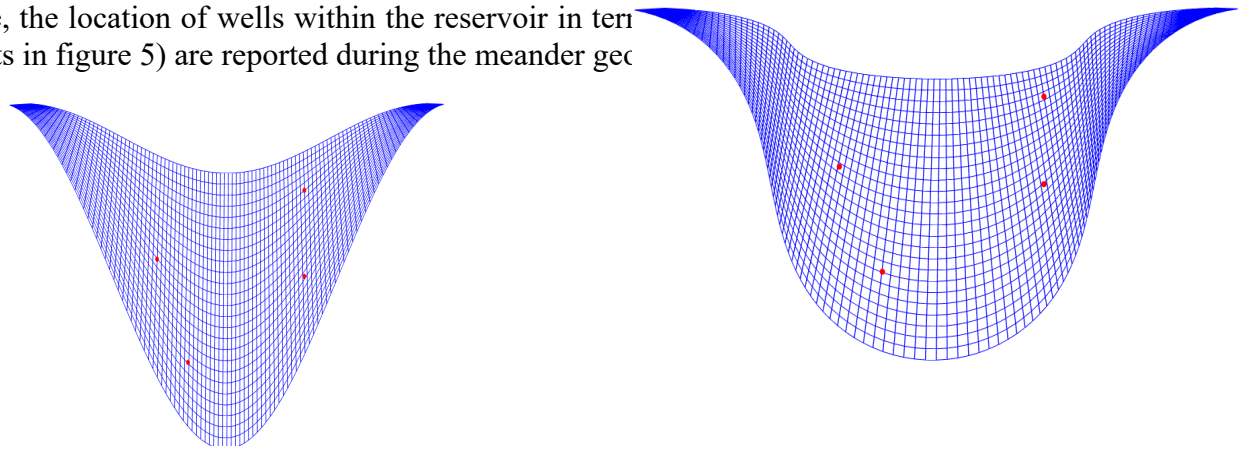

Fig 5a Geometry perturbation at lower angle channel sinuosity, and subsequent regeneration of grid

Fig 5b Geometry perturbation at higher angle channel sinuosity, and subsequent

A cross section across the accretion surfaces reveals the vertical heterogeneities which, as indicated earlier, were modeled with sigmoidal function, and gridded as shown below. One uniqueness of our gridding approach—as shown in figure 6b— is that it conforms to the bedding orientation.

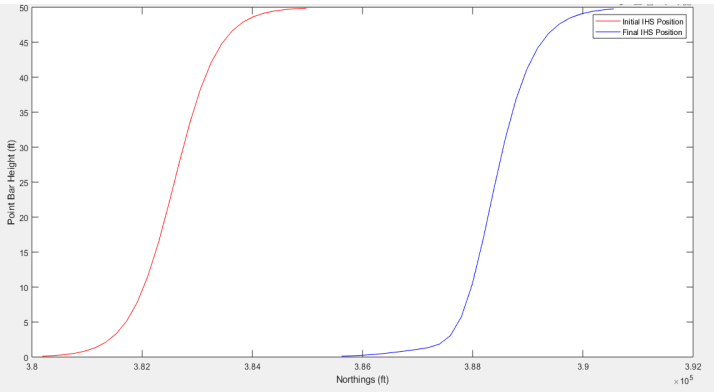

Fig 6a: IHS surfaces: The vertical component of the heterogeneity corresponding to the initial (green plot) and current (red plot) location of the meander

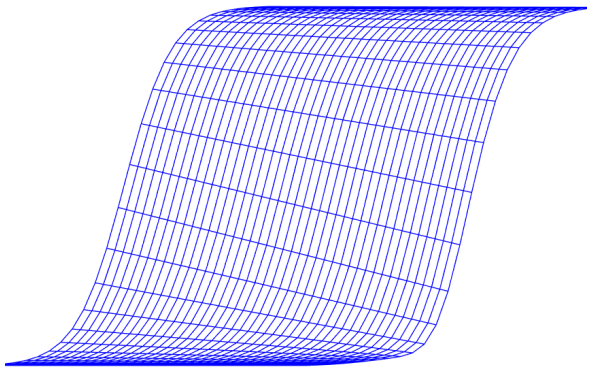

Fig 6b. IHS surfaces gridded

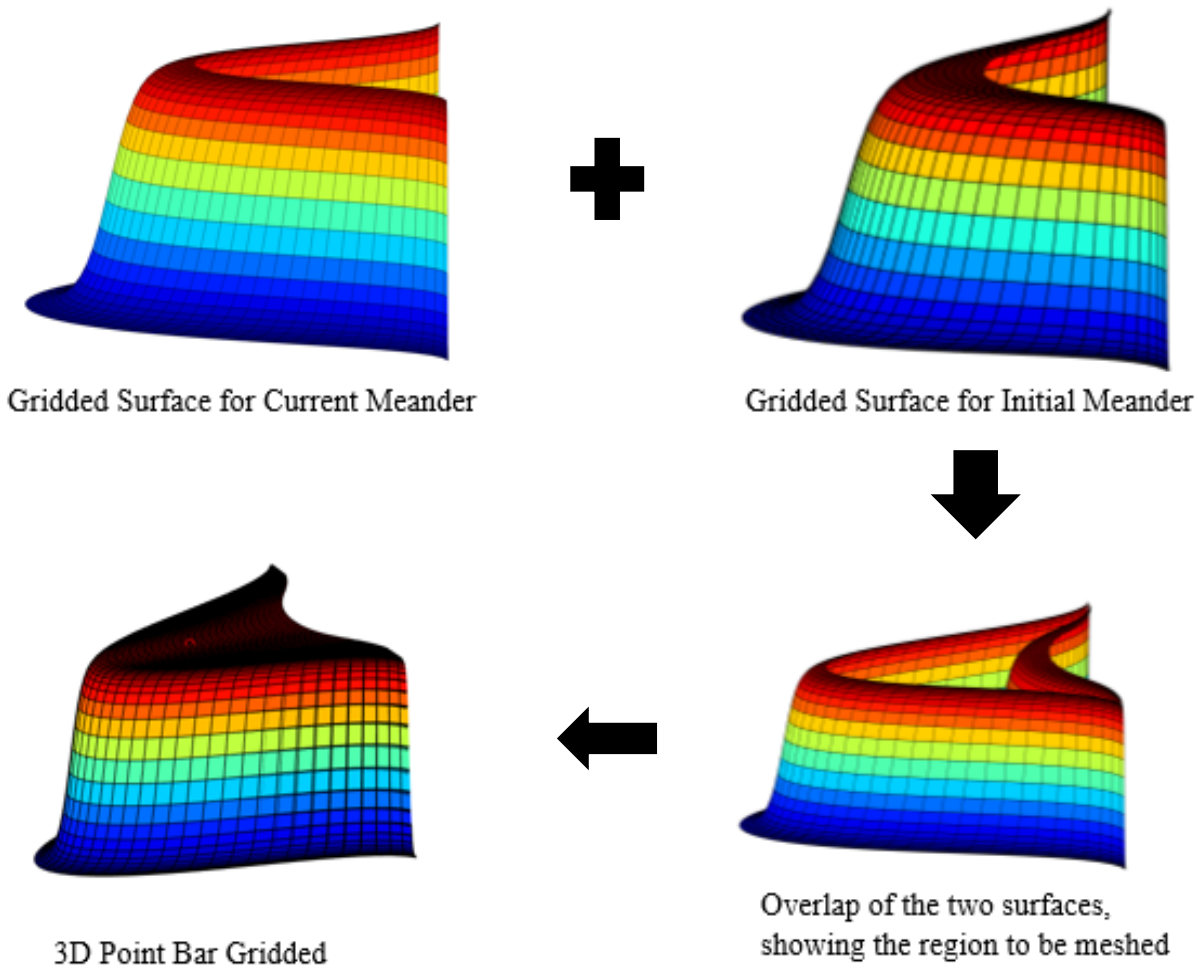

Figure 7 Gridded 3D Surfaces, forming 3D Point Bar

The region bounded by these surfaces were also gridded to form a complete 3D point bar model as illustrated in figure 7. For better visualization, the 3D point bar model, as displayed in Computer Modeling Group (CMG) software would be used henceforth.

2.6 Grid Transformation Scheme Implementation and Geostatistical Simulation

Geostatistical simulation algorithms run on rectilinear type of Cartesian grid, therefore the curvilinear grid generated was transformed into rectilinear grid first, before simulation was run. After simulation, all properties were mapped back into the original curvilinear grid. Figure 8 illustrates how grid transformation was coupled with geostatistical simulation for modeling the properties of the point bar

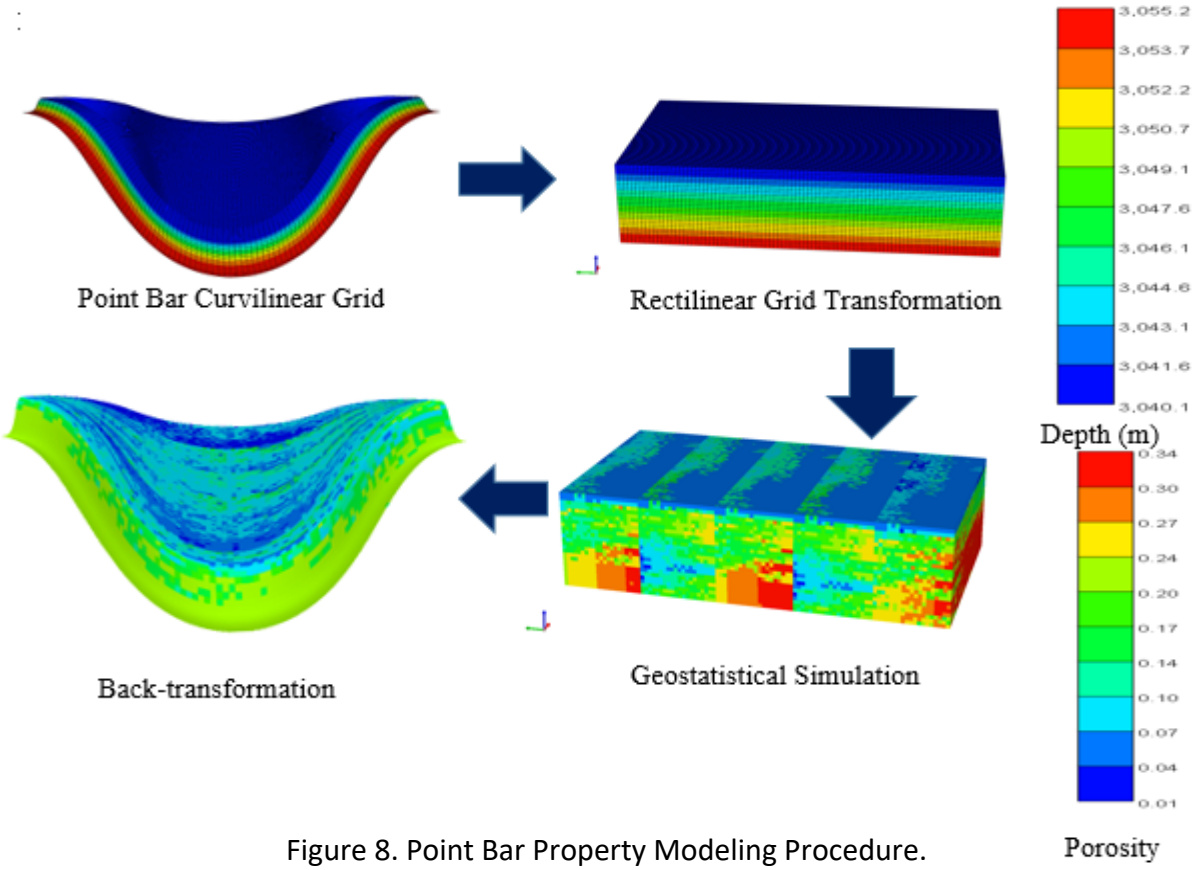

Figure 8. Point Bar Property Modeling Procedure.

Two key depositional trends in point bars are the overall fining upward trend in grain sizes of sediments and also, fining of sediments in the direction perpendicular to the inclined bounding surfaces. Coarser and heavier sediments (e.g. conglomerates) tend to settle at the bottom of the sequence followed by relatively finer and lighter ones like sandstones, muddy sandstones and mudstone. These trends directly manifest in the petrophysical property distribution of the sediments in the point bar. Conscious effort was made to honor the trends in our geostatistical simulation of petrophysical properties. Vertical and horizontal slices taken across the point bar illustrate these trends as shown in figure 9.

2.6.1 Stochastic Representation of Shale drapes across interfaces

The interfaces between successive accretion surfaces are erosional surfaces which mark a flooding event in the depositional history of the point bar reservoir. These surfaces form internal heterogeneities and are characterized by existence of shale drapes on the IHS and accretion surfaces. These shale drapes could act as flow baffles which could impact the CO_2 storage potential of the point bar reservoir, hence the need to model them. In modeling the shale drapes, the GSLIB program called ELLIPSIM was used to simulate Boolean variables of 1s (ones) and 0s (zeros) with 1 indicating existence of ellipsoid (in this case shale drape) and 0 indicating no ellipsoid (i.e. no shale drape). These ellipsoids were dropped at random across the accretion surfaces and IHS until a target proportion of these surfaces was reached. The output file was then imported into our algorithm for incorporation. Petrophysical properties that are typical of shale drapes were

stochastically generated, and randomly assigned to sections where ellipsoids were found. The following Figure 10 are some sections showing shale drapes captured at interfaces.

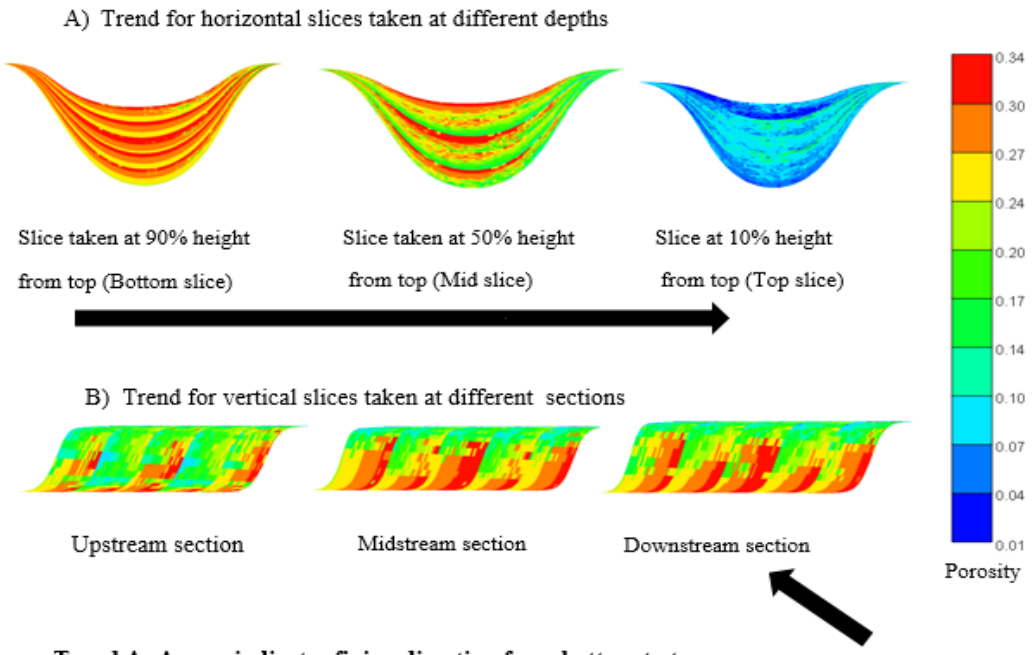

Trend A: Arrow indicates fining direction from bottom to top

Trend B: Arrow indicates fining direction within each inclined bed

Figure 9 Fining trends observed within the point bar

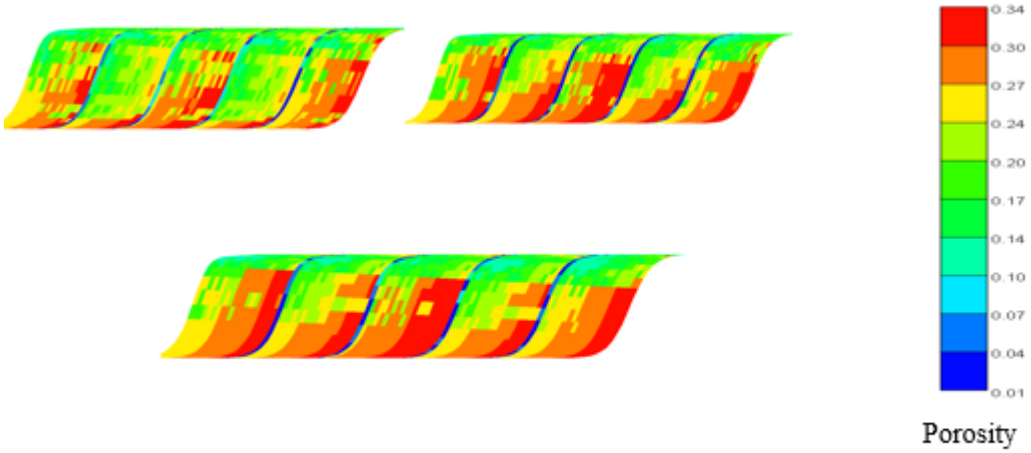

Figure 10 Sections showing incorporation of shale drapes across the interfaces

3 Flow Simulation Study

3.1 Simulation Grid

The CO_2 flow simulation study was conducted for two different cases: one with shale drapes and the other without shale drapes—all with the same grid geometry as that for the point bar model developed for the Cranfield. The reservoir simulation software used was CMG GEM—an advanced Equation of State (EOS) reservoir simulator for compositional modeling.

It was realised that the size of the entire point bar model was too large to be considered for a flow model. Flow simulation using the entire model was found to be very computational expensive and time consuming. In addition, the injection period (based on the data we have) was relatively short, and thus the CO_2 plume will most likely affect the region closer to the vicinity of the injection well and not affect the region far away from the injection zone. In line with these, the simulation grid was defined to be a sub-section of the geologic model that will still honor the shale drape effects and the depositional trends. The sub-section of the grid to be used for this simulation is the region bounded by the dark-blue rectangular box shown in Figure 10 The simulation grid dimensions are 20 X 20 X 25 making up 10000 grid bocks. The specified grid accounts for the entire length of the injection zone (which is about 15 m). The injection well (31 F1) is located in the middle of the demarcated section in Figure 11.

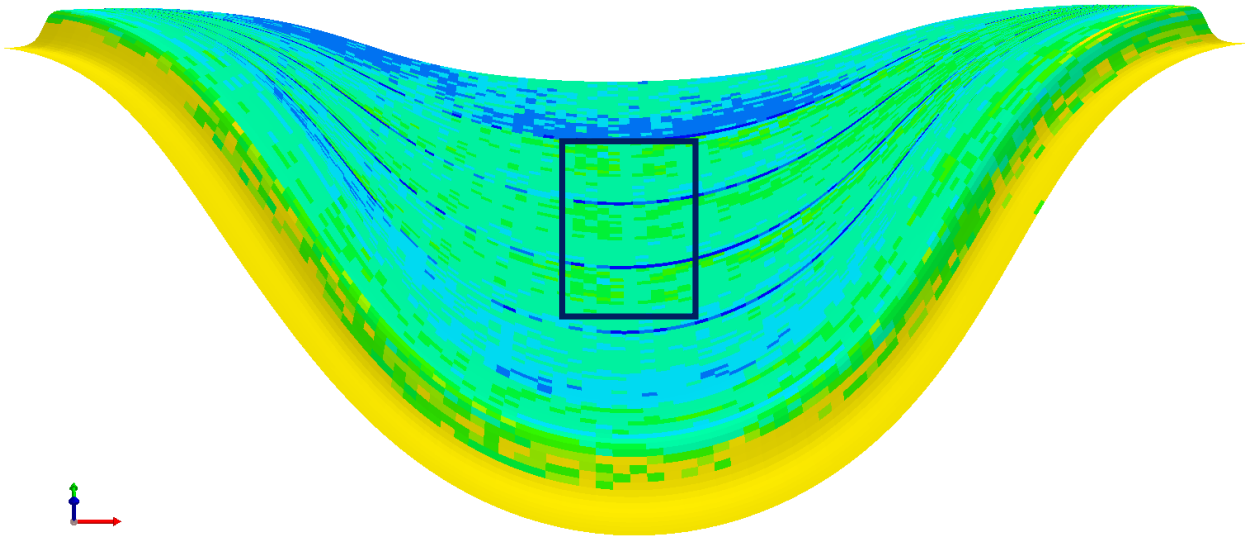

Figure 11 Sub-section of the Cranfield point bar model used for flow simulation.

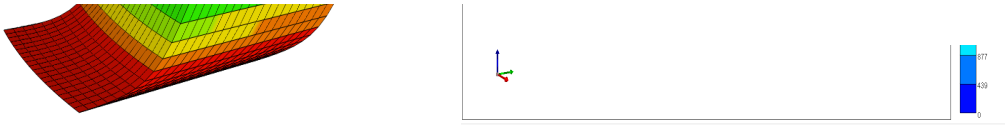

Depth of cell blocks

Permeability of cell blocks in i-direction

Figure 12 Flow simulation grid cut from the point bar geologic model. Note the vertical resolution has been exaggerated to show the sigmoidal shape in cross section.

3.2 Simulation Parameters

Table 1 Reservoir Properties at Initial Conditions

Reservoir Property	Value
Reservoir Depth	3000 m
Average Thickness	15 m
Rock Compressibility	7.3 X 10^{-7} kPa^{-1}
Initial Reservoir Temperature	125ºC
Initial Reservoir Pressure	32000 kPa
Salinity	155752 ppm
Boundary Condition	Open
Initial Water Saturation	100 %

The Salinity, initial reservoir pressure and temperature were obtained from the following literature on the Cranfield, Mississippi injection site. Initial reservoir pressure and temperature (Delshad *et al.*, 2013)

3.3 Rock-Fluid Interaction Property

The relative permeability curves used in this study was obtained from experimental data presented by Bennion and Bachu, (2005) for supercritical CO_2 displacing brine system. The end point of water relative permeability curve is 1.0 at a residual CO_2 saturation of zero; that for CO_2 relative permeability curve is 0.5446 at an irreducible gas saturation of 0.45.

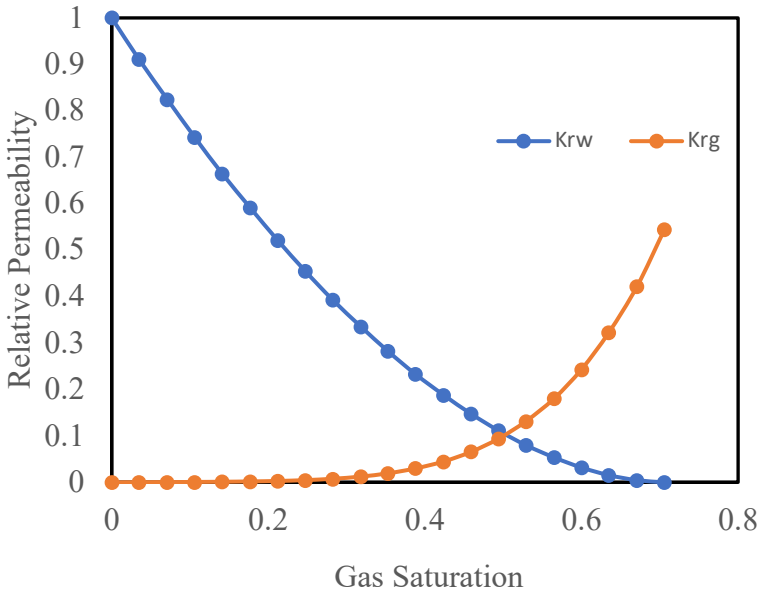

Figure 13 Relative Permeability curve used for simulation (Bennion and Bachu, 2005)

3.4 Fluid Property Modeling

CMG-WinProp was used to model the phase behavior and the reservoir fluids properties. The Peng and Robinson, (1976) EOS was used to model phase-equilibrium compositions and to derive EOS parameters characteristic of supercritical CO_2. CO_2 solubility was modelled with Henry's law Li and Nghiem, (1986) for brine at a salinity of 155752 ppm. The brine phase viscosity and density were respectively estimated using the correlations from Rowe and Chou, (1970) and Kestin et al (1981).

3.5 Well and Recurrent

The Cranfield injection well is located approximately in the middle of the point bar section and was perforated in two layers located at the lower half of the injection zone. The injection well was

set under two operating constraints: a primary constraint operating at a maximum injection rate of 136798.7 m^3 per day at standard conditions and a secondary constraint operating at a maximum bottom-hole pressure 38000 kPa. (See the table 2 for details)

Table 2 Injection Well Parameters

Well Perforation Address (1, J, K)	10, 12, 8-7
Injection Period	Dec 1 2009 — Nov 3 2011
Well Radius	0.0762 m
Skin	0
CO_2 Mole Fraction	1
Maximum Injection Rate	136798.7 m^3/day at standard conditions
Maximum Bottom-hole pressure	38000kPa

These injection conditions mimic the actual field injection strategy adopted at Cranfield.

3.6 Simulation Strategy

The numerical simulation model was developed for two cases: reservoir model taking into account effect of shale drapes and that without considering shale drape effects—all evaluated for structural, residual and dissolution trapping mechanisms. The injection well was run at a constant rate such that the total amount of supercritical CO_2 injected was the same for both cases under consideration.

3.7 Shale drape effects

In order to understand the impact of shale drapes on CO_2 plume migration and storage, two simulation runs were made. In both cases the injection well was made to run for a period of about 2 years and the CO_2 plume migration was studied. The first simulation run ignored the effect of shale drapes on the accretion and inclined heterolithic stratification surfaces. As could be observed in (figure 14a and 15a) the CO_2 Plume preferentially migrated laterally within the lower layers before rising upwards towards shallower depths. This resulted in a CO_2 plume with a broader base (see encircled regions in figure 14a and 15a) and an overall relatively larger contact area with the reservoir rock. In the second simulation run, however, effect of shale drapes was taken into account—and by contrast— CO_2 plume migration saw a lateral restriction, forcing more of the gas to flow between the shale drapes and rising upwards towards shallower layers (see figure 14b and

15b). CO_2 plume had a relatively narrower base within the lower layers in the injection (see encircled region in figure 14b and 15b) and had a relatively smaller contact area with the reservoir rock.

The relatively rapid upward movement of gas observed in the second simulation run could lead to a situation where high volumes of CO_2 rise, accumulating below and exerting pressure on any available seal, increasing the risk of seal failure and potential leakage. This has been reported by (Hovorka *et al.*, 2004)

Dissolved Gas: Molality

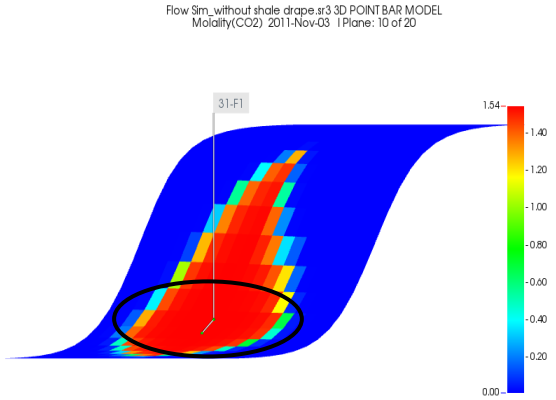

Figure 14a CO_2 molality for Simulation Run 1

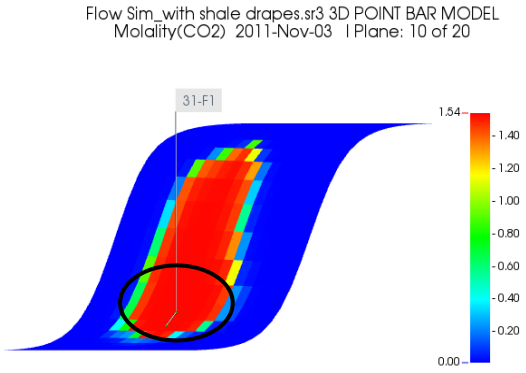

Figure 14b CO_2 molality for Simulation Run 2

Figure 14: The effect of shale drapes on the dissolved CO_2 concentration. When the shale drape is absent, the dissolved plume moves laterally in the injection zone before moving upwards. In the case with the shale drapes, the shale curtails lateral movement of the plume.

Free Gas Saturation

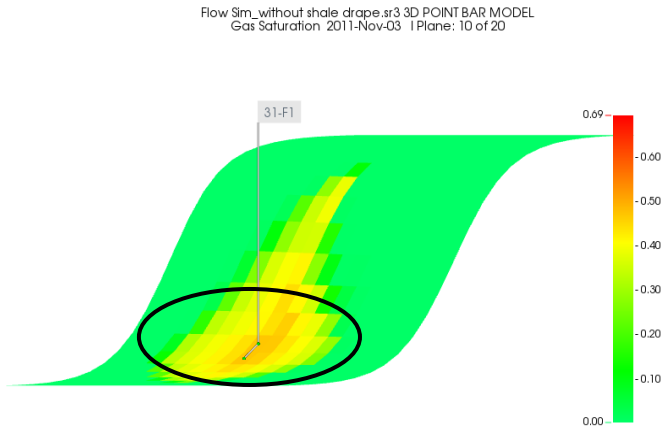

Figure 15a CO_2 saturation for Simulation Run 1

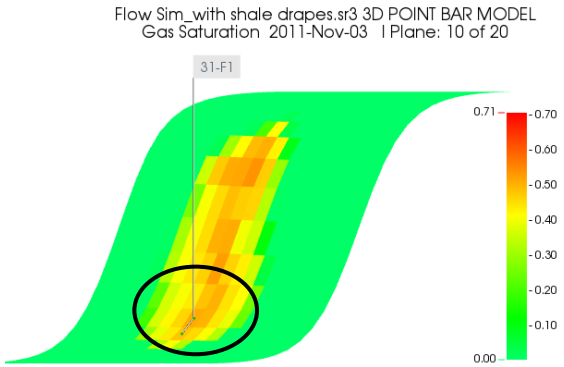

Figure 15b CO_2 saturation for Simulation Run 2

Figure 15: The effect of shale drapes on the free gas CO_2 saturation. The shale drape causes vertical migration of the CO_2 plume.

Trapped Gas

Gas trapping occurs after drainage of resident water (i.e. brine) due to injection has ended, allowing imbibition of water to begin. The water re-occupies the pores and displaces the injected gas in the process. However, not all of the gas is displaced from the pores, consequently some residual amount of gas is left in the pores as trapped gas (Delshad *et al.*, 2013). Figures (16 and 17) show the results of trapped gas realised in the two simulation runs. It could be observed that more gas was trapped for the simulation run where shale drape effects were not considered (see figure 16). This is due to the higher contact area as opposed to the case where shale drape effects were considered.

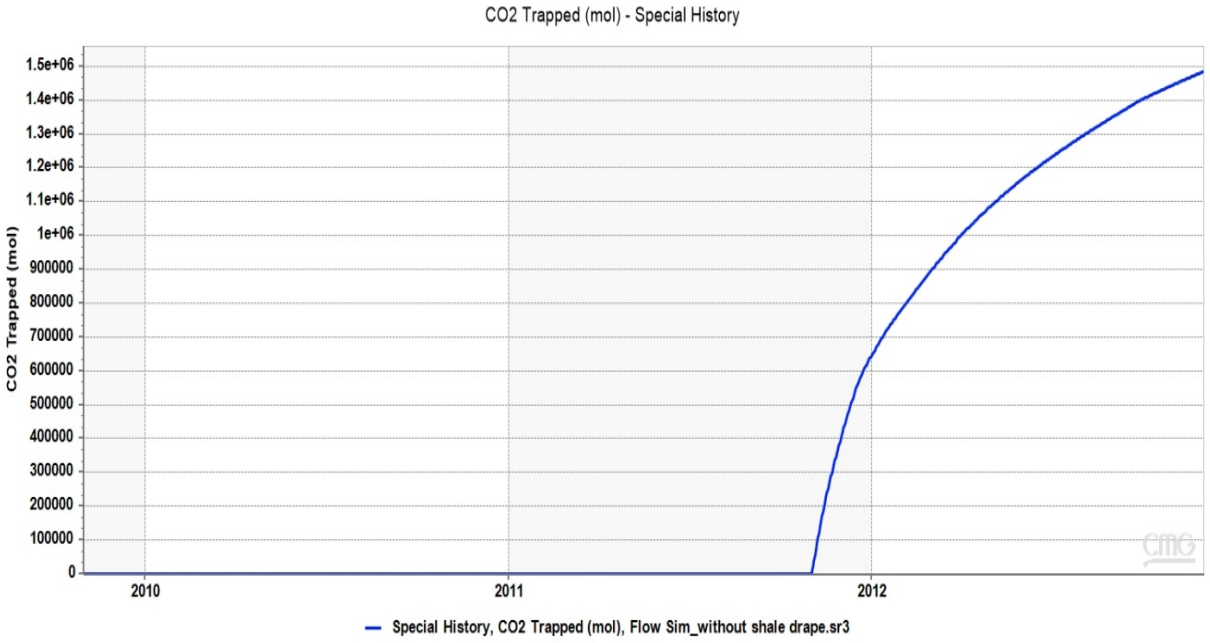

Figure 16: Trapped CO_2 volume as a function of time for Simulation Run 1.

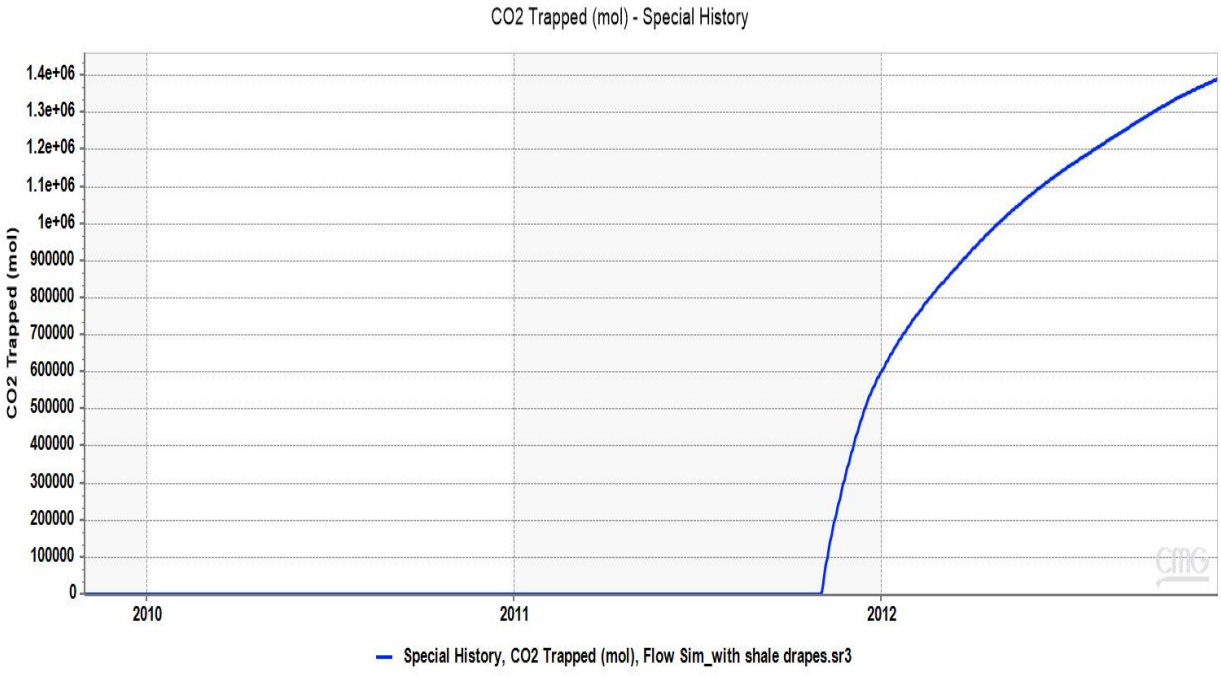

Figure 17: Trapped CO_2 volume as a function of time for Simulation Run 2.

4 Summary and Conclusion

The first part of this study developed a framework for modeling point bar geology and its heterogeneities via a stochastic process-based approach. The application of the workflow to the Cranfield, Mississippi dataset was also demonstrated. Modeling point bar properties is difficult due to its complex geometry but this was overcome by developing a gridding scheme which accounts for the aerial shape of the accretion surfaces as well as sigmoidal shape of the inclined heterolithic stratifications. A grid transformation scheme was also implemented to allow for optimal Geostatistical simulation of the point bar properties.

The second part of this work performed CO_2 flow simulation on the point bar geology to show the effect of heterogeneities on CO_2 plume migration and storage. The flow model used a subsection of the Cranfield geologic model. Two cases were considered for flow simulation: case 1 where shale drape effects were ignored and case 2, which accounted for shale drape effects. In case 1, CO_2.plume was unrestricted and had a higher contact with the reservoir. Amount of CO_2 trapped was relatively higher. For case 2, which considered the effect of shale drapes, CO_2 plume migration was restricted along the IHS surfaces due to the presence of shale drapes inhibiting flow and reducing CO_2 contact area with the reservoir. The amount of CO_2 trapped was relatively lower as a result of this. The CO_2 storage potential is therefore limited due to the presence of shale drapes acting as flow barriers. The study indicates that accurate modeling of reservoir heterogeneity is important to predict the fate of the CO_2 plume.

5 References

Bennion, B. and Bachu, S. (2005) 'Relative permeability characteristics for supercritical CO2 displacing water in a variety of potential sequestration zones in the Western Canada sedimentary basin', *SPE Annual Technical Conference Proceedings*.

Delshad, M. *et al.* (2013) 'Modeling and simulation of carbon sequestration at Cranfield incorporating new physical models', *International Journal of Greenhouse Gas Control*. Elsevier Ltd, 18, pp. 463–473. doi: 10.1016/j.ijggc.2013.03.019.

Durkin, P. R. *et al.* (2017) 'Three-Dimensional Reconstruction of Meander-Belt Evolution, Cretaceous Mcmurray Formation, Alberta Foreland Basin, Canada', *Journal of Sedimentary Research*, 87(10), pp. 1075–1099. doi: 10.2110/jsr.2017.59.

Hathout, D. (2015) 'Sine-Generated Curves: Theoretical and Empirical Notes', *Advances in Pure Mathematics*, 05(11), pp. 689–702. doi: 10.4236/apm.2015.511063.

Hosseini, S. A. *et al.* (2013) 'Static and dynamic reservoir modeling for geological CO2sequestration at Cranfield, Mississippi, U.S.A.', *International Journal of Greenhouse Gas Control*. Elsevier Ltd, 18, pp. 449–462. doi: 10.1016/j.ijggc.2012.11.009.

Hovorka, S. D. *et al.* (2004) 'The impact of geological heterogeneity on CO 2 storage in brine formations: A case study from the Texas Gulf Coast', *Geological Society Special Publication*, 233, pp. 147–163. doi: 10.1144/GSL.SP.2004.233.01.10.

Kestin, J., Khalifa, E. and Correia, J. (1981) 'Tables of the Dynamic and Kinematic Viscosity of Aqueous NaCl Solutions in the Temperature Range 20-150°C and Pressure Range 0.1−35 MPa', *Journal of Physical and Chemical Reference Data*, 10(1), pp. 71–87.

Lee, E. T. Y. (1989) 'Choosing nodes in parametric curve interpolation', *Computer-Aided Design*, 21(6), pp. 363–370. doi: 10.1016/0010-4485(89)90003-1.

Li, Y.-K. and Nghiem, L. X. (1986) 'Phase Equilibria of Oil, Gas and Water/Brine Mixtures', *The Canadian Journal of Chemical Engineering*, 64(3), pp. 486–496. doi: 10.1002/cjce.5450640319.

Lu, J. *et al.* (2013) 'Reservoir characterization and complications for trapping mechanisms at Cranfield CO2injection site', *International Journal of Greenhouse Gas Control*, 18, pp. 361–374. doi: 10.1016/j.ijggc.2012.10.007.

Nazeer, A., Abbasi, S. A. and Solangi, S. H. (2016) 'Sedimentary facies interpretation of Gamma Ray (GR) log as basic well logs in Central and Lower Indus Basin of Pakistan', *Geodesy and Geodynamics*. Elsevier Ltd, 7(6), pp. 432–443. doi: 10.1016/j.geog.2016.06.006.

Odundun, O. and Nton, M. (2011) 'Facies Interpretation from Well Logs: Applied to SMEKS Field, Offshore Western Niger Delta', *American Association of Petroleum Geologists*, p. 25.

Olulana, O. O. (2015) 'Stochastic Modeling of Channel Meanders and Resultant Point Bars'.

Peng, Y., and Robinson, B. (1976) 'A New Two-Constant Equation of State.', *Industrial &Engineering Chemistry Fundamental*, 15(1), pp. 59–64.

Pranter, M. J. *et al.* (2007) 'Analysis and modeling of intermediate-scale reservoir heterogeneity based on a fluvial point-bar outcrop analog, Williams Fork Formation, Piceance Basin, Colorado', *AAPG Bulletin*, 91(7), pp. 1025–1051. doi: 10.1306/02010706102.

Rowe, M. and Chou, S. (1970) 'No Title', *Journal of Physical and Chemical Reference Data*, 15(1), pp. 61-66.

Thomas, R.G., Smith, D.G., Wood, J.M., Visser, J., Calverley-Range, E.A. and Koster, E. H. (1987) 'Inclined heterolithic stratification-terminology, description, interpretation and significance.', *Sedimentary Geology*, 53, pp. 123–179.

Bayesian Inversion of Seismic-Pressure Models

The goal is to develop a flexible data integration framework to assimilate multiple physical measurements to adequately capture the spatiotemporal changes in dynamic reservoir properties at geological carbon storage (GCS) sites. We have developed a rock physics-guided data assimilation workflow for continuously inferring changes in CO_2 saturation and pressure distributions from distributions of seismic velocity and attenuation along with wellbore pressure measurements. In this report we demonstrate the applicability of this workflow at two GCS sites: the Cranfield site in Mississippi and the Frio II brine pilot near Houston, Texas. We summarize the key findings of using a joint seismic-pressure-petrophysical data assimilation framework to continuously infer CO_2 saturation and pressure changes from continuous active-source seismic monitoring (CASSM) data and wellbore pressure measurements. This methodology has been successfully demonstrated in an Observation System Simulation Experiment (OSSE) environment and is currently being validated using the time-lapse full waveform inversion results from Task 3.0 at the Frio II site. The next section describes the methodology of the proposed workflow followed by results from the two synthetic case studies and preliminary results from the FWI-integrated tests.

1 Methodology

Data assimilation methods, namely those of the ensemble-based variety, have proven successful at generating probabilistic forecasts from monitoring data for geophysical applications. Such methods have been previously adopted to study GCS-related projects (Chen et al. 2020, González-Nicolás, Baù, and Alzraiee 2015, Ma, Jafarpour, and Qin 2019) and are frequently applied in reservoir engineering (Emerick and Reynolds 2013a, b, Evensen et al. 2007, Raghu et al. 2018, Aanonsen et al. 2009) for history-matching purposes. The main attraction of using data assimilation lies in its ability to combine the known physics of reservoir systems with observed monitoring data. The ensemble Kalman filter (EnKF) is an extension of the original Kalman filter that uses a Monte Carlo approach to estimate the model state and associated uncertainty from a finite set of model realizations. The EnKF consists of a forecast step and an update step where the model state is forecasted forward in time and then calibrated by the filter based on the observed data. The forecasted model state, indirect measurements, and corresponding error are described as,

$$X_t = f(X_{t-1}, \alpha), \quad (1)$$

$$Y_t = g(X_t) + \epsilon_t, \quad (2)$$

$$\epsilon_t \sim N(0, \sigma_o^2), \quad (3)$$

where, state vector, X, at time t, represents the reservoir model state and is propagated forward in time by a non-linear function f with static input parameters α. Typically, the state vectors are composed of multiple reservoir models, known as ensembles, which are calibrated by the recursive EnKF. The function g maps the model state variables from state space to observation space. Geophysical measurements are denoted by Y_t and are assumed to capture the true model dynamics with normally distributed measurement error ϵ_t.

In the context of reservoir engineering, f is replaced by numerical reservoir simulators and g by rock physics models. If we consider CO_2 saturation and reservoir pressure as the variables that describe the ensemble model state X_t then it can be represented as,

$$X_t = f\begin{pmatrix} S_g^1(x, t-1) & \dots & S_g^N(x, t-1) \\ P^1(x, t-1) & \dots & P^N(x, t-1) \end{pmatrix}, \quad (4)$$

where N represents the number of ensemble members. The ensemble of reservoir model state predictions from the previous time step are propagated forward in time to generate an ensemble of model forecasts as described by Eq. 1 and Eq. 4. During the update step, the ensembles of model forecast are calibrated by the new observed data, such that,

$$X_t^a = X_t^f + K_t\left(Y_t^o - HX_t^f\right). \tag{5}$$

where the superscripts X_t^a and X_t^f represent the assimilated analysis and forecasted model state at time t. The H-operator is a forward operator that relates the observations to the model state. The H-operator matrix consists of only zero and one element entries in the case of direct measurements (difference between observations and state computed without state transformation). In the case of indirect measurements, such as mapping gas saturation changes from seismic observations, the H-operator matrix is augmented with a rock physics model (for example, using White's patchy gas saturation model) to guide the state transformation to observation space. The product of $HX^f(t)$ maps the state vector ensemble forecasts to their corresponding seismic responses in the observation space to compute the innovation factor $(Y_t^o - HX_t^f)$. The Kalman gain, K, is the calibration parameter for updating the model forecasts which scales with the difference between the forward-modelled model state and observed data. It takes the value of 0 when measurement error is high, and I when the measurement error is low. It is computed as:

$$K_t = C_t^f H^T\left(HC_t^f H^T + C_t^o\right)^{-1}. \tag{6}$$

In our experimental design, we use White's model as the H-operator to estimate V_p and Q_p responses to infer changes in CO_2 saturation in the reservoir. We utilize the Stanford RockPhysics Toolbox in MATLAB to forward model seismic observations. To emulate the seismic attributes gathered during a CASSM survey, synthetic seismic attributes in the form of p-wave seismic velocity (V_p) and attenuation ($1/Q_p$) are forward modeled using the same rock physics model while wellbore pressure measurements are recorded during the ground truth generation from numerical reservoir simulations. In the case where V_p, Q_p, and wellbore pressure (p_{wf}) make up our composite observations, the H-operator transforms the state variable forecasts, such that,

$$HX^f = \begin{bmatrix} V_p^f \\ Q_p^f \\ p_{wf}^f \end{bmatrix} \tag{7}$$

$$= \begin{bmatrix} f_{RP}\left(X_m^f(x,t), \alpha^1(x,t)\right) & \cdots & f_{RP}\left(X_m^f(x,t), \alpha^N(x,t)\right) \\ \vdots & \ddots & \vdots \\ X_p^1(x,t) & \cdots & X_p^N(x,t) \end{bmatrix},$$

where the function f_{RP} represents the rock physics model, which takes rock and fluid properties as inputs and outputs seismic attributes, such as V_p and Q_p. The subscript m denotes state variable elements that need to be projected into the observation space and the subscript p denotes the elements of the state vector that are directly being observed. The sets defined by m and p may be mutually exclusive, or there may be overlap. The model parameters, α, contain static reservoir parameters (permeability and porosity) that are the petrophysical inputs for the rock physics model. To accommodate for the nonlinearity of the RPM-based H-operator, a heuristic covariance localization strategy is adopted by performing a Schur product between the above matrix and an empirically defined correlation matrix with a fixed radius of influence. This localization scheme restricts the influence of observations to state variables that are in proximity of the observations. The choice of rock physics model (RPM) depends on the geological context, the rock and fluid

properties, operational parameters of the seismic survey, and available seismic attributes. One could use this proposed framework to include multiple candidate RPMs during data assimilation by pairing each ensemble with a RPM, such that one has $f_{RP}^{1}(\cdot)$ ... $f_{RP}^{N}(\cdot)$ in Eq. 7 and making sure to include the necessary inputs for all RPMs in X_m^f and α.

This rock-physics guided data assimilation framework is used as a template for testing the efficacy of different monitoring tools and different combinations of tools to infer CO_2 saturation and reservoir pressure changes. In the case studies presented in the next section, we perform the data assimilation with different combinations of V_p, Q_p, and p_{wf} measurements in an OSSE environment. In particular, we demonstrate the value-added benefit of combining seismic measurements with wellbore pressure data to reduce the non-uniqueness of CO_2 properties inferred from seismic data.

2 Results

This section discusses the results from conducting joint seismic-pressure-petrophysical data assimilation on reservoir models of two GCS sites: Cranfield, Mississippi, and Frio II brine pilot, near Houston, Texas. The work pertaining to the Cranfield dataset has been published in the SPE Journal (Joon et al. 2022). For each case study we provide a brief background on the geological context of the GCS site, the reservoir model, and simulated seismic observations prior to discussing the data assimilation results. This report summarizes the key takeaways from the publication and the ongoing research pertaining to the Frio II site.

Cranfield Site

The GCS site at Cranfield, Mississippi was identified as a viable storage site for commercial scale CO_2 sequestration testing and as of 2003, more than 4 million metric tons of CO_2 has been injected. We conduct a 100-year OSSE of CO_2 injection into the Cranfield reservoir geomodel using a numerical commercial software. An OSSE is a form of synthetic analysis that allows us to estimate the potential impact of a new monitoring design before it is deployed in the field. It evaluates different types of monitoring designs and data assimilation methods by comparing their relative performances in a simulated environment. In an OSSE, a ground truth is generated by running a numerical reservoir simulation with the assumption that the input parameters, initial conditions, and model dynamics are perfectly known. The initial conditions and input parameters are then perturbed to create an ensemble of reservoir realizations and are independently propagated forward in time to generate an ensemble of model forecasts. To reduce the variability among the ensemble members and improve prediction estimates of model state, the model forecast ensembles are calibrated by assimilating measurements from different types and combinations of monitoring tools. The efficacy of the rock physics-guided EnKF framework at reducing the prediction uncertainty of CO_2 saturation and pressure changes are compared using the ground truth during the 100-year CO_2 injection. Furthermore, we can also quantify the improvement afforded by combining multiple forms of measurements at reducing prediction uncertainties.

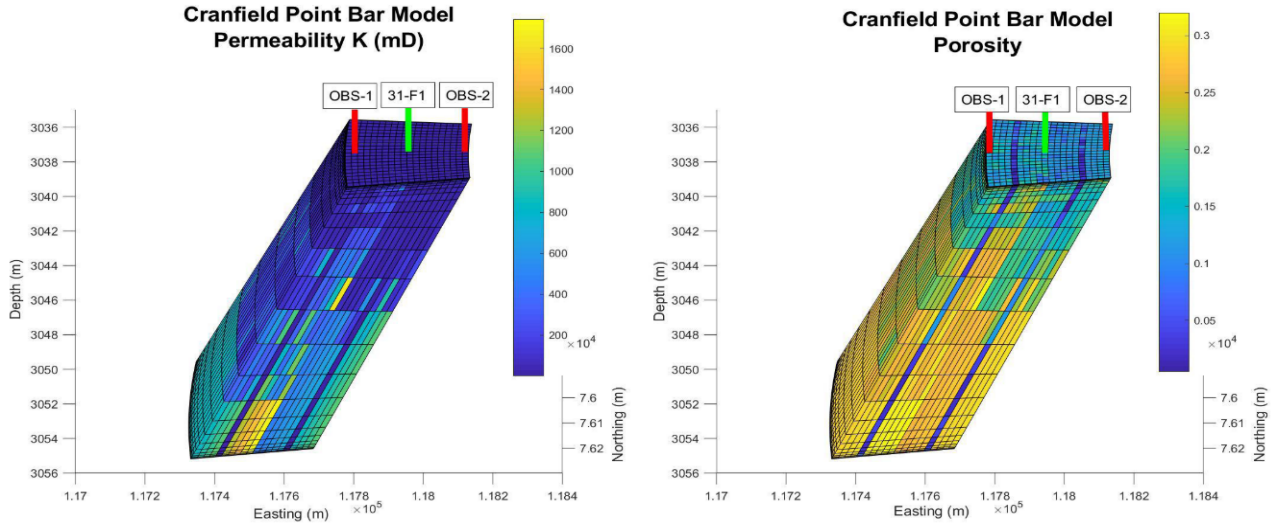

Figure 1. Cranfield point bar reservoir model properties: vertical permeability (left) and porosity (right). (Vertical exaggeration= 45)

A point bar reservoir model that represents the Cranfield site was created to test out the data assimilation framework. Fig. 1 illustrates the 'true' permeability and porosity fields of the target formation where CO_2 is injected for storage. The Cranfield reservoir model is characterized by two main heterogeneities in the form of lateral accretions and inclined heterolithic stratification. Using this geomodel, CO_2 injection over a period of 100 years is simulated using MATLAB Reservoir Simulation Toolbox (MRST). In Fig. 2 the spatiotemporal evolution of the CO_2 plume is illustrated at 1, 10, 25, and 100 years. In addition to the injection well (31-F1), two observation wells (OBS-1 and OBS-2) are made available to emulate the crosswell seismic setup. Seismic attributes like V_p and Q_p are inferred via seismic inversion along the crosswell geometry and are illustrated in Fig. 3. The movement of the CO_2 plume can be indirectly inferred from the observed seismic attributes along the crosswell geometry. As CO_2 displaces the in-situ fluid along this geometry V_p decreases by 100-600 m/s and Q_p scales nonlinearly based on the degree of gas saturation. The changes in the true CO_2 saturation distribution at 4 timesteps during the 100-year injection period are shown in Fig 2.

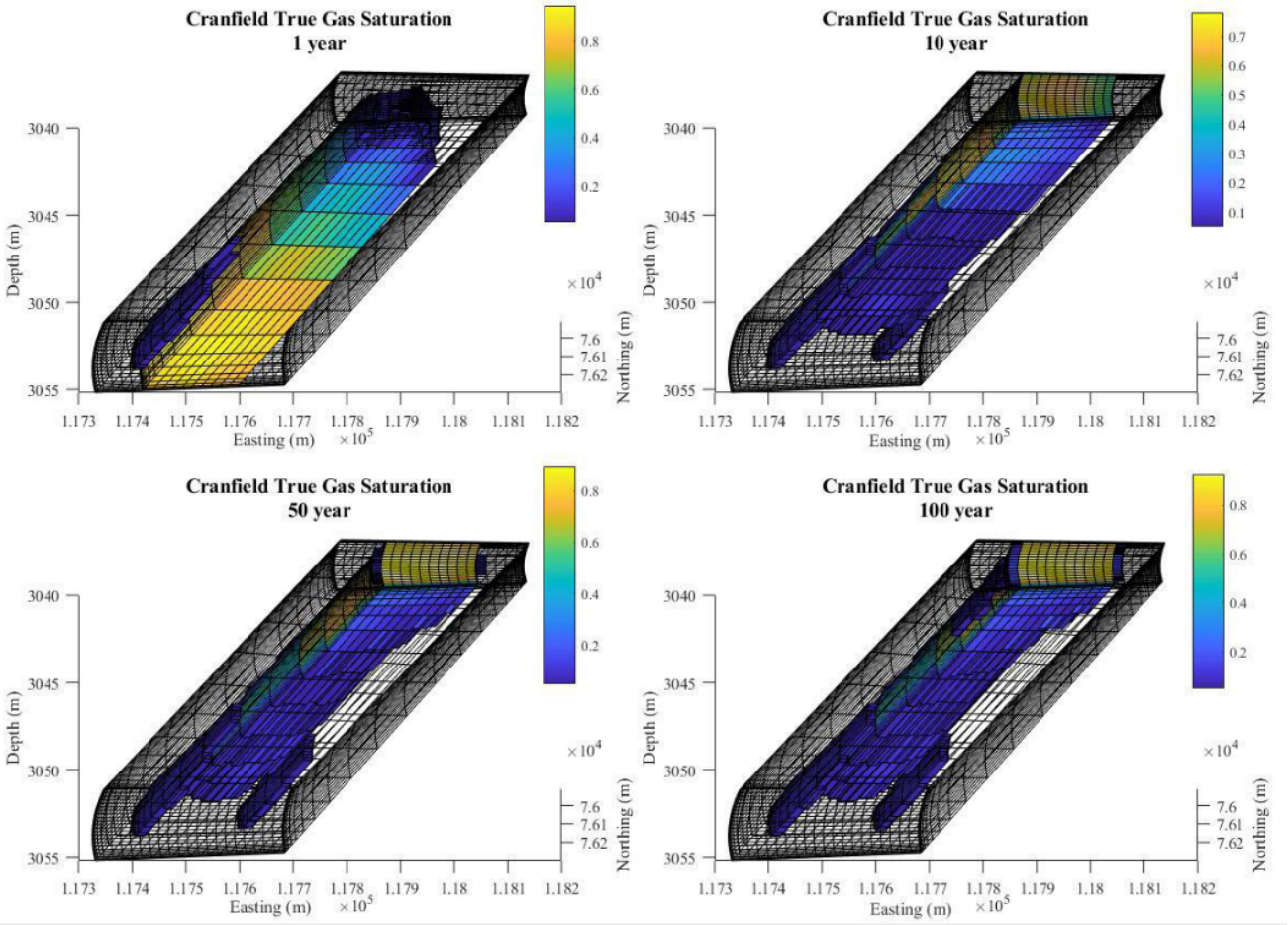

Figure 2. Ground truth CO_2 saturation distribution at 1-, 10-, 25-, and 100-year time periods.

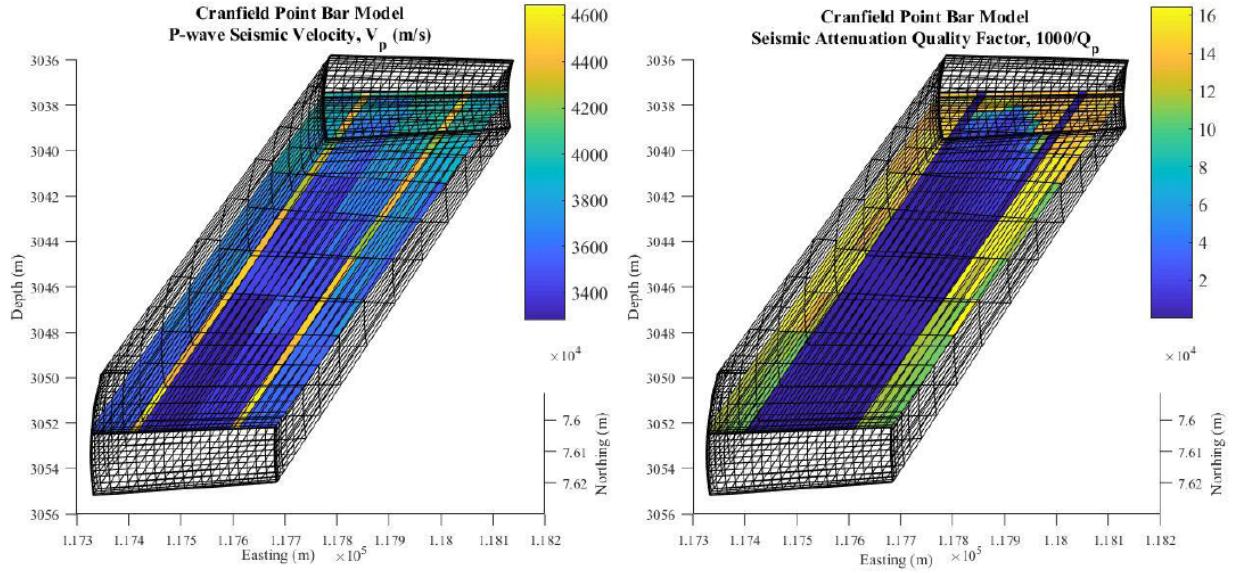

Figure 3. Forward modeled seismic attributes using White's patchy gas saturation model (vertical exaggeration = 45): V_p (left) in m/s and $1000/Q_p$ (right). Seismic attributes are measured along the cross-section between the monitoring and injection wells.

One of the added benefits of using an OSSE is that it allows us to synthetically test the risk-based value added of a new observation instrument. In the context of evaluating crosswell CASSM and wellbore pressure monitoring systems, this implies that we can estimate how each observation attribute (V_p, Q_p, and p_{wf}) improves the model state variable (S_g and P_r) estimates in our data assimilation model. To elaborate, we study five scenarios of permanent sensor setups by comparing the predictive accuracy of (1) p_{wf} only, (2) V_p only, (3) Q_p only, (4) V_p and Q_p, and finally (5) V_p, Q_p, and p_{wf} monitoring designs. By comparing these five scenarios, we measure the risk-based value added of different types of monitoring tools and different combinations of monitoring tools. An error analysis of the different scenarios above will quantify such improvement, which is useful in practice when assessing the value-added contribution of these different sensors. In Fig. 4 the prediction error for CO_2 saturation and pressure, as estimated by computing the difference between the known ground truth and assimilated state estimates, is plotted for each monitoring design over the 100-year time period. The prediction error is computed by averaging the error for all gridblocks at every timestep to produce a scalar metric.

All monitoring designs capture the spatiotemporal evolution of CO_2 saturation and pressure with varying degrees of prediction uncertainty. Among the five EnKF-assimilated monitoring designs, the composite monitoring design consisting of V_p, Q_p, and P_{wf} measurement data produces the best gas saturation prediction estimates over time. The assimilated state estimates using the composite monitoring design are plotted in Fig. 5 at different stages of the simulation period: at the end of 1,10,50, and 100 years. When comparing the assimilated results in Fig. 5 with the simulated ground truth in Fig. 3 we observe that the maximum uncertainty in CO_2 saturation distribution is located at the boundary of the CO_2 plume where CO_2 levels are low. The prediction uncertainty of CO_2 saturation increases after the injection well is shut in. These changes are due to differences in reservoir dynamics pre- and post-shut in which influences the ensembles of model forecasts and the measurement data during data assimilation. Spatially limited observations like P_{wf} and highly nonlinear measurements like Q_p perform poorly by themselves at capturing the subsurface dynamics. Assimilated model state predictions from such measurements diverge away from the ground truth at later stages of the simulation period which has a negative impact on the risk and prediction accuracy associated with the monitoring design of the storage site. The data assimilation methodology is vulnerable to over-, under-shooting and filter divergence for highly nonlinear systems. The nonlinear relationship between Q_p and the model state variable, vis-à-vis White's model, demonstrates this vulnerability. Additional parameterization by truncating unreasonable Q_p measurements, increasing the ensemble size, or a different RPM may improve these prediction estimates. The conclusion from this study indicates that a composite system consisting of both seismic and pressure measurements affords greater prediction accuracy and is a more reliable form of monitoring design.

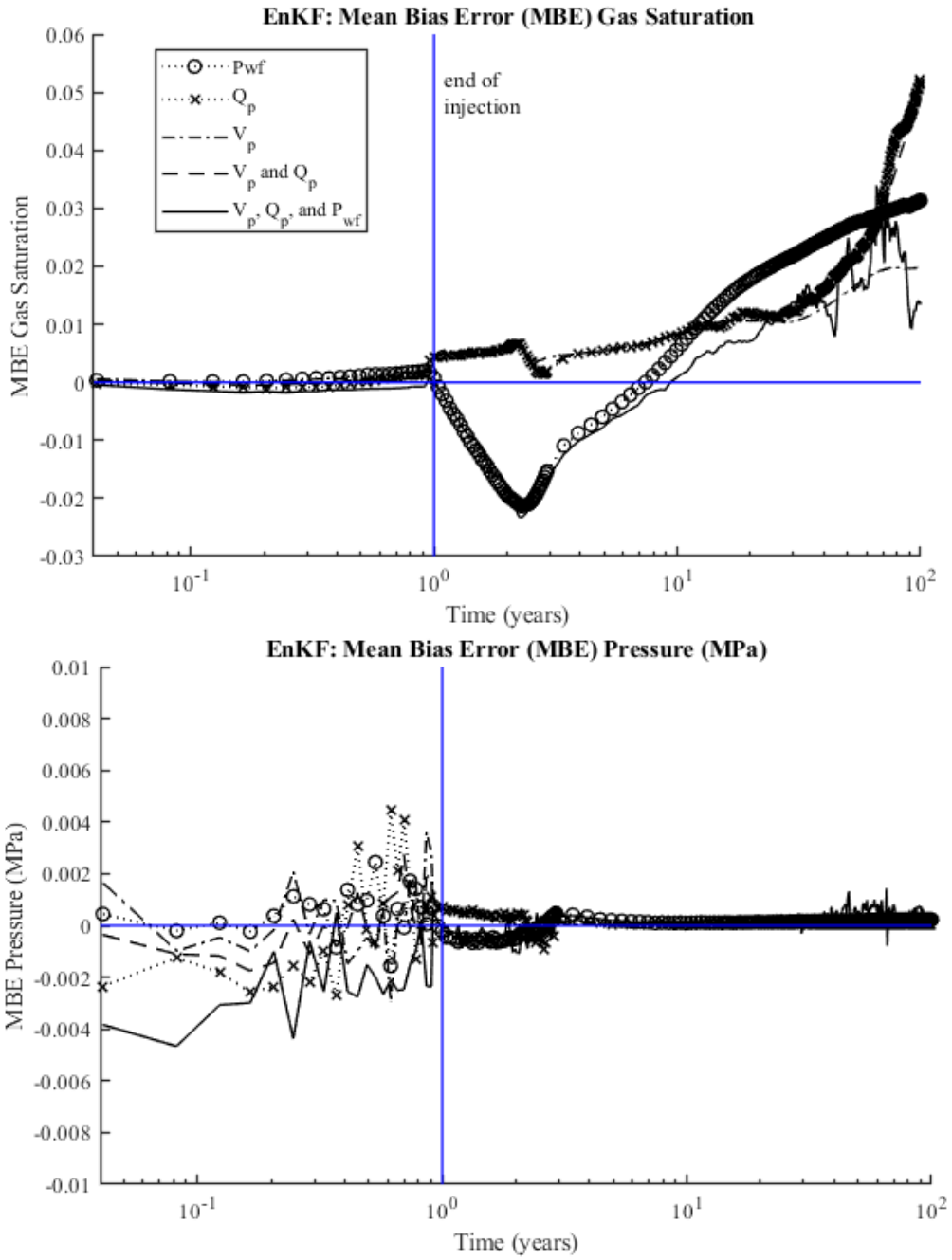

Figure 4. Gas saturation (top) and reservoir pressure (bottom) prediction uncertainty using both EnKF assimilation models. The prediction uncertainty is plotted as the mean bias error (MBE) between the ground truth and the assimilated state variables. The black curves represent the time-varying MBE for the EnKF and EnKS assimilated state variables.

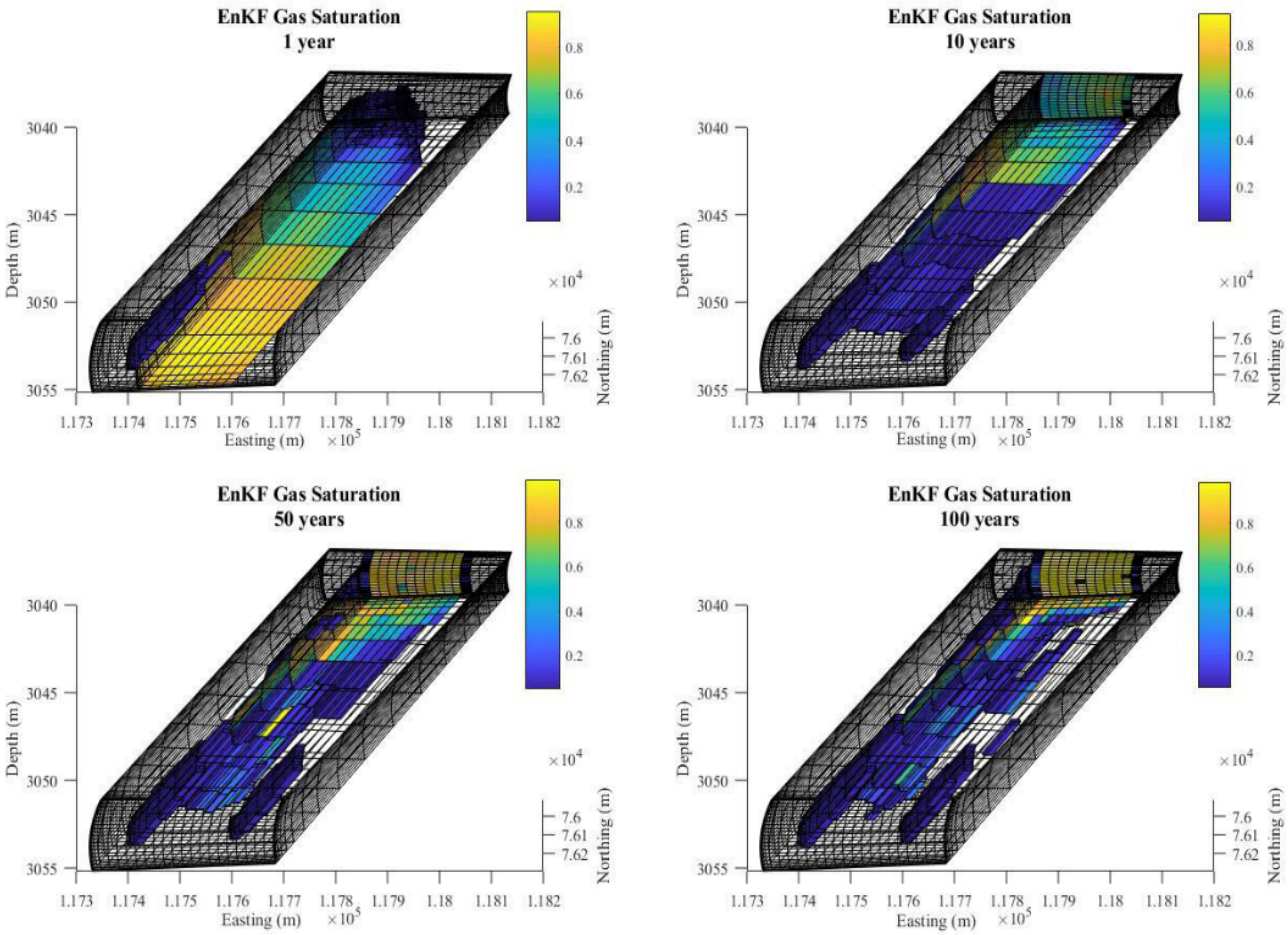

Figure 5. EnKF assimilated prediction estimates of CO_2 saturation distribution at 1-, 10-, 25-, and 100-year time periods using V_p, Q_p, and P_{wf} measurement data.

Frio II Brine Pilot

The Frio test site is located near Houston, Texas, and was identified during a national evaluation of saline formations. In 2004, 1600 tons of CO_2 was injected at a depth of 1530-m and monitored using time-lapse crosswell tomographic imaging as part of the Frio-I test (Hovorka et al. 2006, Daley et al. 2007b). Following this test, in 2006, another 300 tons of supercritical CO_2 were injected into the Blue sand at a depth of 1650-m. The blue sand has similar porosity (25%) and permeability (2000 mD) as the Frio I injection site. The Frio II test was monitored using a crosswell continuous CASSM setup in which data were acquired along a set of fixed raypaths between the injection (source) and monitoring (receiver) wells (Daley et al. 2007a, Daley, Ajo-Franklin, and Doughty 2011).

To emulate the Frio II GCS operation and evaluate the efficacy of the joint seismic-pressure-petrophysical data assimilation framework, a 3D reservoir model of the storage site is created using MRST. An OSSE environment like the Cranfield model is used in this study. The geological model consisting of 21x21x19 gridblocks is used to represent the volume of the storage site. CO_2 is injected into the 17-meter-thick fluvial Blue sand formation that is at a depth of 1657 m with a dip of 18°. The monitoring design consists of one injection well (INJ) and two monitoring wells (OBS-1 and OBS-2) as illustrated in Fig. 6. In Fig. 7 the ground truth permeability and

porosity are plotted along with the perturbed realizations that are used to populate the ensemble members for data assimilation. The variation in model parameters between the ground truth and ensemble members causes the CO_2 plume movement to deviate from the ground truth. Assimilating measurements from synthetic CASSM and wellbore pressure data calibrates the forecasted ensemble members and pushes the model state predictions toward the ground truth. The ground truth represents a perfectly known system and is used to test the accuracy of the assimilated predictions. Forward modelled seismic observations using RPM and the ground truth model are used as measurements for data assimilation. The *H*-operator also uses the same RPM to forward model the forecasted model state variables from state space to observation space but with the perturbed model parameters.

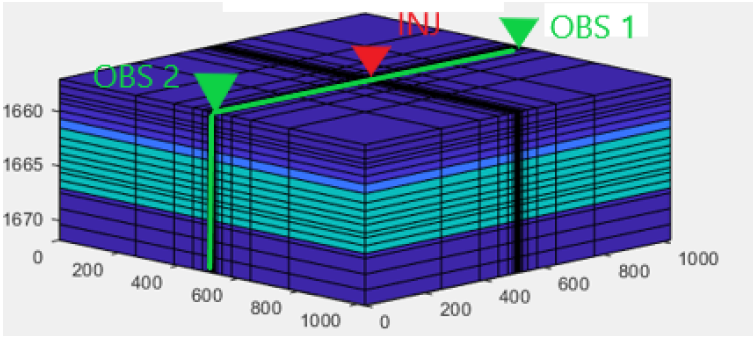

Figure 6. Crosswell seismic monitoring design. Injection well (INJ) is embedded with the seismic source and wellbore pressure sensors. Observation wells (OBS 1 and OBS 2) emulate receivers embedded with an array of geophones.

The EnKF was then used to assimilate measurements from different monitoring designs. In Fig. 8 the model state prediction errors are plotted for each monitoring design. Starting from top, the monitoring design consists of (1) V_p, (2) Q_p or Q_p^{-1}, (3) V_p and Q_p or Q_p^{-1}, (4) P_{wf}, and (5) V_p, Q_p, and P_{wf}. The ensemble model state is represented by reservoir CO_2 saturation (left) and pressure (right), in MPa. The mean ensemble estimate is plotted in black with the corresponding ensemble members plotted in red. In the case of Q_p inclusive monitoring designs, we investigate using Q_p^{-1} (inverse of Q_p) instead of Q_p due to the potential numerical stability it may afford in the data assimilation algorithm. All monitoring designs capture the model state evolution with varying prediction error. Within the seismic-only monitoring designs, combining V_p and Q_p measurements decreases the prediction error and ensemble spread as compared to their individual counterpart. All seismic-only monitoring designs have high pressure prediction error. This behavior, while not surprising, highlights the insensitivity of seismic attributes to changes in reservoir pressure. The pressure prediction error and ensemble spread collapses shortly after the injection well is shut-in and V_p, Q_p, and V_p-Q_p average reservoir pressure prediction error stabilizes to 0.9, 0.7, and 0.6 MPa, respectively. Assimilating V_p, Q_p, and P_{wf} measurements provide the smallest prediction error and ensemble spread for CO_2 saturation and reservoir pressure. This reduction in uncertainty highlights the value-added benefit of combining multiple observations for monitoring GCS sites.

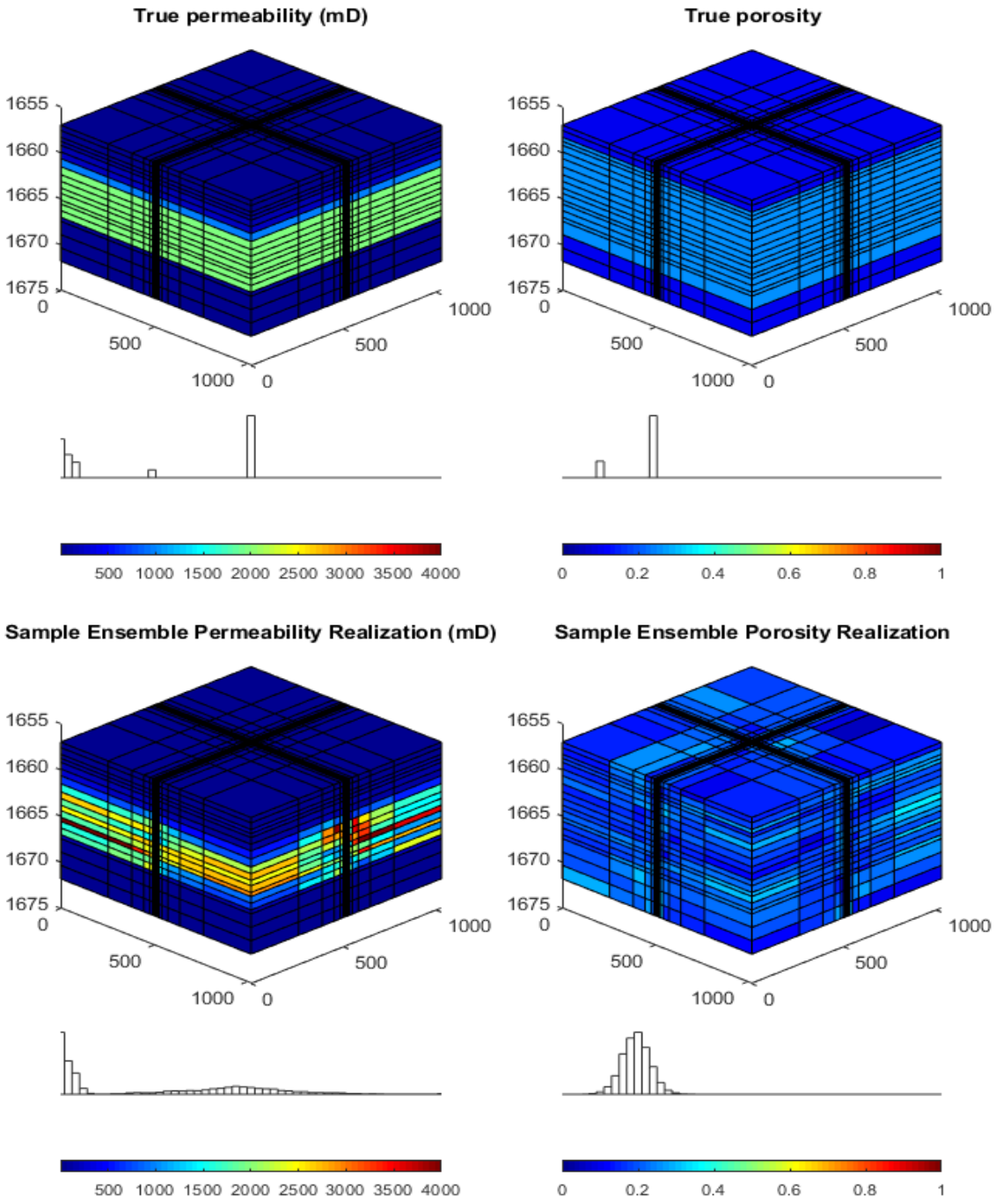

Figure 7. The ground truth permeability (top left), in mD, and porosity (top right) of the Frio II reservoir model. The ensemble permeability (bottom left), in mD, and porosity (bottom right) fields are approximated as Gaussian fields and are computed by taking the logarithm of permeability distribution.

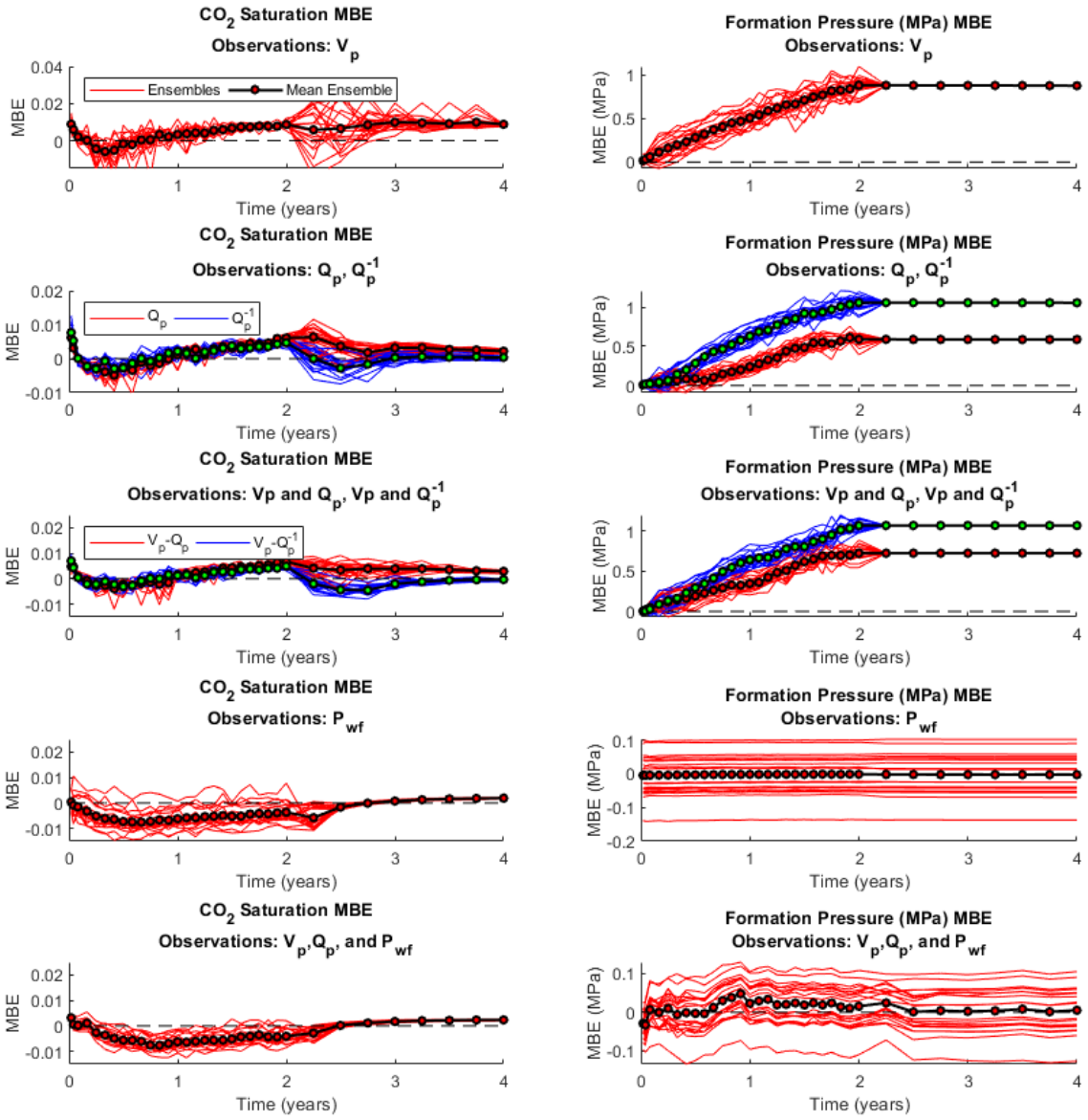

Figure 8. Mean bias error (MBE) between the ground truth and EnKF estimated ensemble predictions (red lines) for varying geophysical observation setups: (1) V_p, (2) Q_p/Q_p^{-1}, (3) V_p and Q_p/Q_p^{-1}, and (4) V_p, Q_p, and P_{wf} from top to bottom, respectively. The CO_2 saturation and reservoir pressure, MPa, bias is shown on the left and right, respectively. The seismic attenuation factor (inverse quality factor, Q_p^{-1}) is approximated as $1/Q_p$ and plotted (blue lines) alongside Q_p runs.

FWI-integrated Frio II Tests

The successful implementation of the rock physics-based data assimilation framework on the two synthetic studies is now being used as a template for integrating time-lapse full waveform seismic inversion results from Task 3.0 into the data assimilation framework. In this work, seismic inversion results in the form of V_p and Q_p measurements along the crosswell geometry at the Frio II site are incorporated into the ensemble Kalman filter. Fig. 9 illustrates this geometry along which changes in seismic responses to injected CO_2 are observed. These seismic attributes along with wellbore pressure measurements at the injection and monitoring well are assimilated during a 5-day injection period at 40 equally spaced time intervals.

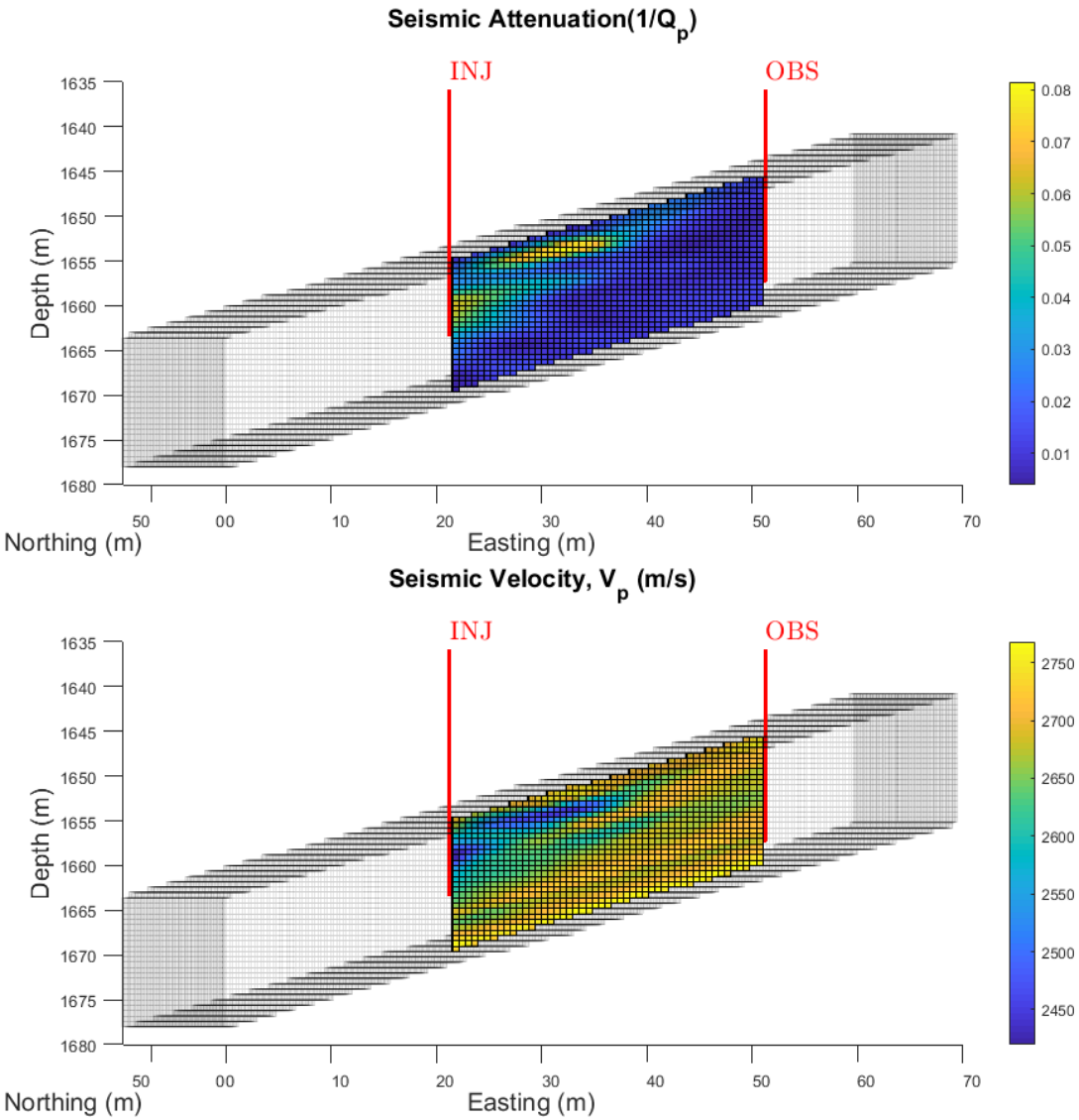

Figure 9. Full-waveform inversion results: seismic attenuation (top) and seismic velocity (bottom).

In Fig. 10 the assimilated CO_2 saturation predictions at the end of the 5-day injection period are plotted along with the ground truth from which the seismic attributes were derived as well as the error computed by taking the difference between the two CO_2 saturation profiles. We observe that the assimilated results are unable to capture the lateral movement of CO_2 that is observed in the ground truth and thus leads to the increased prediction errors over time. To evaluate the value-added benefit of assimilating different types of measurements together, another data assimilation test using only pressure monitoring data was conducted. The improvement afforded from assimilating multi-sensor data is shown in Fig. 11 where the mean prediction error with respect to time is plotted for the two monitoring designs. While neither of the tests were able to capture the true spatiotemporal changes in CO_2 saturation, the multi-sensor data assimilated results have lower CO_2 saturation prediction error compared to the pressure sensor only predictions. More tests need to be conducted to evaluate the reason for such differences between the simulated forecasts and the ground truth CO_2 saturations.

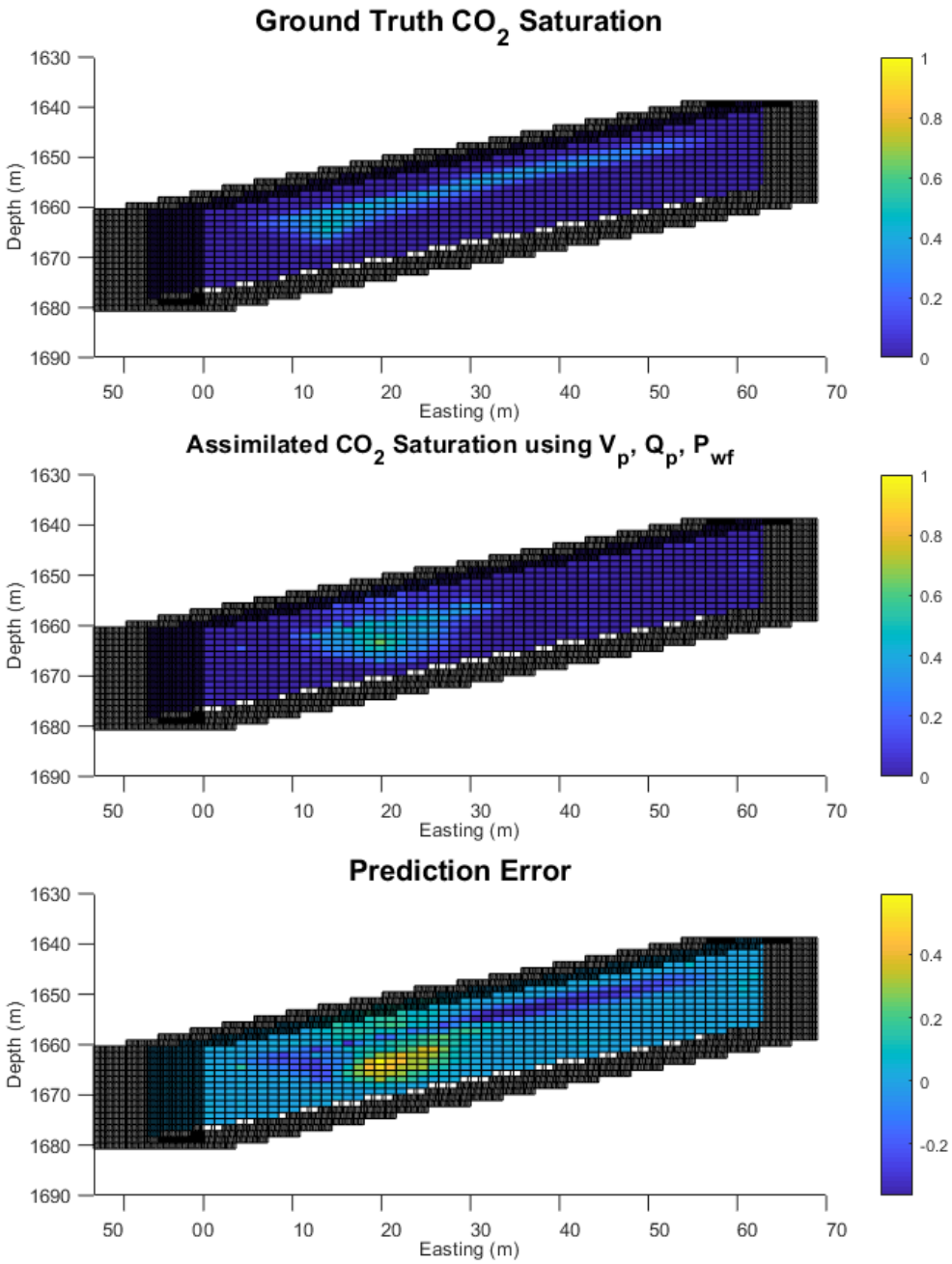

Figure 10. EnKF assimilated CO_2 saturation results. The ground truth CO_2 saturation from which seismic attributes are derived are plotted on the top. The assimilated CO_2 saturation using EnKF and V_p, Q_p, and P_{wf} measurements is plotted in the middle and the difference between the assimilated model state and the ground truth are plotted at the bottom.

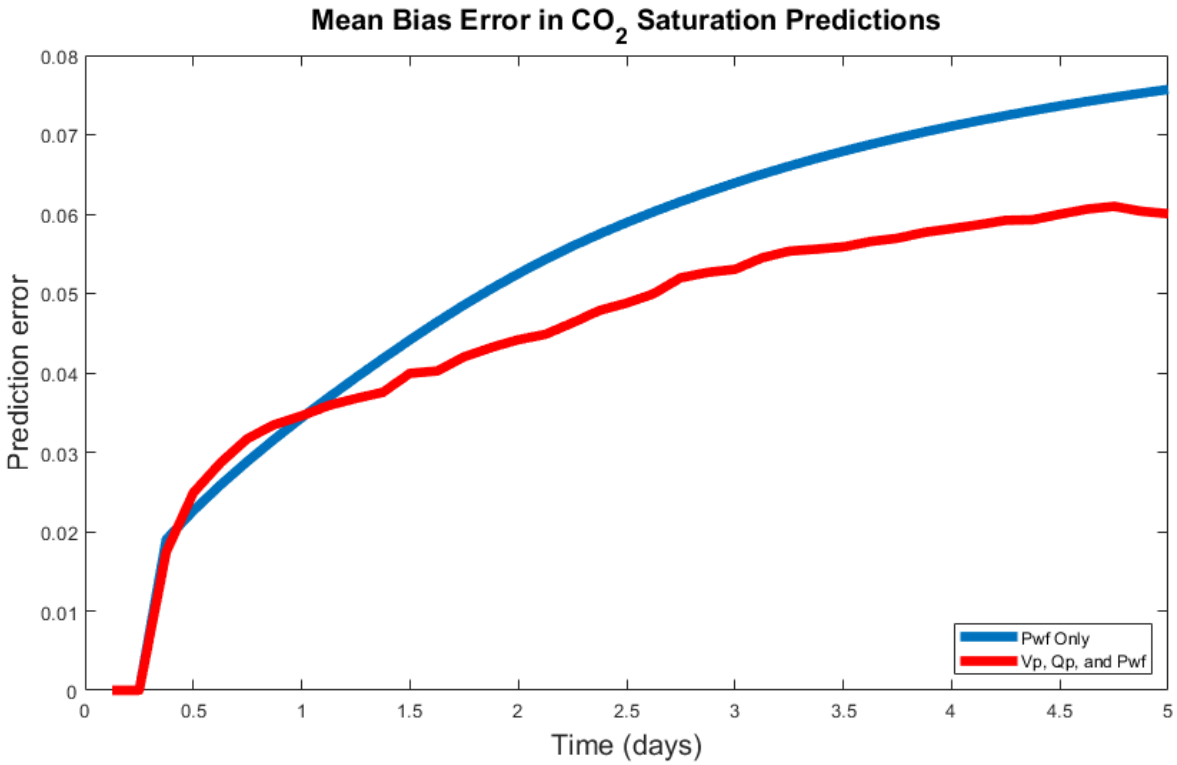

Figure 11. Prediction error, in the form of mean bias error, for two monitoring designs, i.e., a composite monitoring design with V_p, Q_p, and P_{wf} measurement (red) and a monitoring design with only wellbore pressure sensors at the injection site (blue).

3 Conclusions

In every case study presented in this report, we observe that combining multiple observation in an EnKF data assimilation framework yield improved prediction accuracy. In particular, combining pressure measurements with seismic attributes reduces the non-uniqueness of CO_2 properties inferred from seismic data. However, the prediction accuracy of the assimilated model state is also dependent on other various reservoir and data assimilation parameters. Reservoir parameters like permeability, porosity, and elastic properties and their corresponding uncertainty directly impacts the simulated forecast predictions as well as the forward modeled seismic observation used to compute the innovation factor. In the case of the FWI-integrated Frio II tests, the differences between the true subsurface changes and the numerical simulated forecasts lead to poor predictions even when seismic observations provided strong responses to changing fluid saturations. Data assimilation parameters like filter choice, ensemble size, covariance localization length, assimilation frequency, and how measurement uncertainty is modeled, all have an influence on the prediction accuracy and ensemble spread. Tuning these reservoir and data assimilation parameters that impact prediction accuracy is site-specific and are, in general, dependent on the types of monitoring tools and the spatiotemporal coverage afforded by them. The larger point to be made here is that the improvements afforded by different sensors, in this multi-physics fashion, are sensitive to assimilation algorithm choice, and more advanced assimilation algorithms may introduce large accuracy and show different trade-offs in uncertainty reduction from different sensor combinations. This workflow is feasible to implement at an active GCS site and presents a closed-loop approach to continuously update reservoir properties and parameters as more measurements are made available.

Significance for task 6&7

The developed EnKF data assimilation framework in task 4.3 along with time-lapse full waveform inversion developed in task 3 will be the core algorithms of jSPPI. The jSSPI will be applied to new laboratory/mesoscale experimental datasets collected in task 5 (task 6.1). The estimated seismic and saturation models will be calibrated from the inversion algorithms with prior knowledge of the laboratory model. We will use newly developed jSPPI methods to reprocess the 5-day long field CASSM dataset from the Frio II test (task 6.2). In task 7, we will document software development and quality assurance practice, including developing functional specification, examples, and documentation.

4 References

Aanonsen, Sigurd I., Geir Nævdal, Dean S. Oliver, Albert C. Reynolds, and Brice Vallès. 2009. "The Ensemble Kalman Filter in Reservoir Engineering--a Review." *SPE Journal* 14 (03):393-412. doi: https://doi.org/10.2118/117274-PA.

Chen, Bailian, Dylan R. Harp, Zhiming Lu, and Rajesh J. Pawar. 2020. "Reducing uncertainty in geologic CO2 sequestration risk assessment by assimilating monitoring data." *International Journal of Greenhouse Gas Control* 94:102926. doi: https://doi.org/10.1016/j.ijggc.2019.102926.

Daley, T. M., J. B. Ajo-Franklin, and C. Doughty. 2011. "Constraining the reservoir model of an injected CO2 plume with crosswell CASSM at the Frio-II brine pilot." *International Journal of Greenhouse Gas Control* 5 (4):1022-1030. doi: https://doi.org/10.1016/j.ijggc.2011.03.002.

Daley, T. M., R. D. Solbau, J. B. Ajo-Franklin, and S. M. Benson. 2007a. "Continuous active-source seismic monitoring of CO2 injection in a brine aquifer." *Geophysics* 72 (5):A57-A61. doi: https://doi.org/10.1190/1.2754716.

Daley, Thomas M., Ray D. Solbau, Jonathan B. Ajo-Franklin, and Sally M. Benson. 2007b. "Continuous active-source seismic monitoring of C O2 injection in a brine aquifer." *GEOPHYSICS* 72 (5):A57-A61. doi: 10.1190/1.2754716.

Emerick, Alexandre A., and Albert C. Reynolds. 2013a. "Ensemble smoother with multiple data assimilation." *Computers & Geosciences* 55:3-15. doi: https://doi.org/10.1016/j.cageo.2012.03.011.

Emerick, Alexandre A., and Albert C. Reynolds. 2013b. "History-Matching Production and Seismic Data in a Real Field Case Using the Ensemble Smoother With Multiple Data Assimilation." SPE Reservoir Simulation Symposium, The Woodlands, Texas, USA, 2013/2/18/.

Evensen, Geir, Joakim Hove, Hilde Meisingset, Edel Reiso, Knut Sponheim Seim, and Ø Espelid. 2007. "Using the EnKF for Assisted History Matching of a North Sea Reservoir Model." SPE Reservoir Simulation Symposium, Houston, Texas, U.S.A., 2007/1/1/.

González-Nicolás, Ana, Domenico Baù, and Ayman Alzraiee. 2015. "Detection of potential leakage pathways from geological carbon storage by fluid pressure data assimilation." *Advances in Water Resources* 86:366-384. doi: https://doi.org/10.1016/j.advwatres.2015.10.006.

Hovorka, Susan D., Sally M. Benson, Christine Doughty, Barry M. Freifeld, Shinichi Sakurai, Thomas M. Daley, Yousif K. Kharaka, Mark H. Holtz, Robert C. Trautz, H. Seay Nance, Larry R. Myer, and Kevin G. Knauss. 2006. "Measuring permanence of CO2 storage in saline formations: the Frio experiment." *Environmental Geosciences* 13 (2):105-121. doi: https://doi.org/10.1306/eg.11210505011.

Joon, Shams, Ismael Dawuda, Eugene Morgan, and Sanjay Srinivasan. 2022. "Rock Physics-Based Data Assimilation of Integrated Continuous Active-Source Seismic and Pressure Monitoring Data during Geological Carbon Storage." *SPE Journal*:1-15. doi: https://doi.org/10.2118/209585-PA.

Ma, Wei, Behnam Jafarpour, and Joe Qin. 2019. "Dynamic characterization of geologic CO2 storage aquifers from monitoring data with ensemble Kalman filter." *International Journal of Greenhouse Gas Control* 81:199-215. doi: https://doi.org/10.1016/j.ijggc.2018.10.009.

Raghu, Abhinandhan, Xiongtan Yang, Swanand Khare, Jagadeesan Prakash, Biao Huang, and Vinay Prasad. 2018. "Reservoir history matching using constrained ensemble Kalman filtering." *The Canadian Journal of Chemical Engineering* 96 (1):145-159. doi: https://doi.org/10.1002/cjce.22965.

Development of a Meso-Scale CASSM Testbed for Geological Carbon Storage Experiments & Data Analysis

We describe the detailed design phase, procurement, assembly, and testing of a mesoscale CASSM testbed designed to provide a validation dataset for full wavefield inversion (FWI) algorithms targeting the monitoring technology.

1 Introduction

The goal of the experimental components of this project were to develop an mesoscale testbed (i.e. physical model) to record high-density CASSM dataset during simulated GCS operations. While the bulk of the theoretical/computational activities in this project have focused on analysis of either synthetic datasets or previously recorded field datasets, both data sources have their limitations. A challenge with the utilization of synthetic datasets is their inclusion of limited physics in both the forward and inversion stages. While synthetic studies allow a high degree of flexibility in designing experiments and testing hypotheses, the ultimate validation of monitoring strategies is application to real datasets. Field CASSM datasets acquired at pilot GCS sites are obviously the best validation approach; unfortunately, only a very limited set of datasets are available demonstrating CASSM in this context (e.g. Frio 2) and all have sparse source and receiver distributions due to cost limitations. This sparsity makes evaluation of more sophisticated imaging algorithms challenging, particularly FWI approaches which need a high measurement density to resolve spatial variations in seismic properties.

A compromise between realism and flexibility is the use of scaled mesoscale physical models to generate CASSM datasets. In this case, while physical model construction is challenging, experiments utilizing known materials, structure, and CO_2 injections can be easily executed. Most importantly, dense source and receiver arrays can be deployed to replicate geometries appropriate for FWI and other sophisticated imaging approaches. A final important advantage is the capacity to deploy secondary measurement methods to assist in ground-truthing hydrogeologic boundary conditions and plume gas saturation, two parameters which are often poorly constrained in field experiments.

2 Mesoscale Tank Design and Procurement

As with all large experiments, development of mesoscale testbeds requires substantial modeling in the design phase and some degree of effort to procure the materials including large sensor arrays and packing materials. In our case, these initial phases were complicated by an institutional move and associated laboratory remodel as well as operations and supply chain challenges during the COVID pandemic. In this section, we will discuss these initial phases of testbed development.

2.2 Broad Spatial Constraints & Lab Design

A challenge when developing mesoscale experimental facilities is locating an appropriate physical space capable of housing the large tanks planned for the study. Floor load ratings are a particular issue since our testbed weight was estimated to be in excess of 7 tons. As part of an on-going laboratory renovation (not funded by the project) we designed and built a new space to support the experiment. Figure 1 shows a plan view (A) and side view (B) of the mesoscale system facility in the newly constructed laboratory with utilities (water, power, N_2, and CO_2) as well as an overhead hoist for heavy equipment deployment and sand packing. The space was designed to support two

side-by-side mesoscale systems up to 5’ x 6’ (diameter/height) in dimensions of which one will be used for this study. The renovation of the laboratory was completed in February 2020.

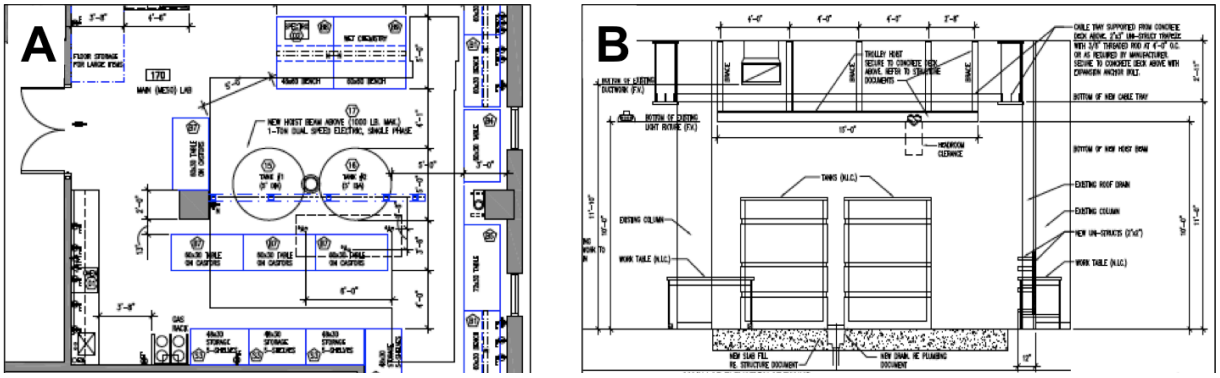

Figure 1. Plan cut-outs for tank facility in Rice Environmental and Applied Geophysics Laboratory (REAGLe). Section A shows the top view of the tank installation assuming a 5’ diameter, 6’ tall mesoscale experimental system. Section B shows the same location in cross-section with the overhead material handling hoist visible.

2.3 Modeling Exercise

Before deciding on a testbed design, we conducted a pre-modeling phase to evaluate expected system response given a range of dimension and acquisition parameters. Questions which we considered included the kinematics of edge reflections from the tank walls and the expected data characteristics for different CASSM acquisition geometries. These models were then refined as more concrete decisions were made during procurement and construction.

As mentioned previously, a challenge in any mesoscale study is the finite domain and the resulting boundary impacts on recorded signals. In a natural environment these boundaries due not exist except for the free boundary at the earth’s surface. For our initial modeling tests, we assumed a 925-gallon tank, approximately 5’ (1.52 m) in diameter and 6’ (1.83 m) high, one of several possible tanks appropriate for our laboratory. We assumed a cross-well geometry with 24 sources and 24 receivers, within the scope of our planned acquisition systems. The source and receiver wells were located ~20 cm from the tank walls and a Ricker source with a center frequency of 30 kHz. These parameters are well within the range of the proposed experiment. The mesoscale tank was modeled as a homogeneous material initially with a V_p of 1800 m/s. The system was modeled using a time-domain finite difference solution to the acoustic wave equation (8^{th} order in space, 2^{nd} order in time) for the full source/receiver geometry.

Figure 2 shows three wavefield snapshots for a source located in the top left of the tank. As can be seen, to provide a large enough interwell distance for a CO_2 injection experiment, the wells are necessarily close to the tank boundary. This generates a boundary reflection following the direct arrival with a relatively short time delay (~0.25 ms) as can be seen in the common shot gathers in Figure 3. As can also be seen in Figure 3, boundary reflections from the top and bottom surfaces will be visible in a similar time window due to the relatively square aspect ratio of the tank. While the dimensions of the mesoscale are ultimately limited by logistical constraints (the size of the entry door etc), this short study suggests that it will be crucial to properly mimic the boundaries to allow effective FWI inversion of the experimental datasets. In contrast, P-wave travel-time inversion should be relatively straight-forward since boundary effects should not interfere with the direct P-wave; additionally, the close to 2-to-1 aspect ratio when considering the well locations should provide for sufficient aperture for tomographic imaging.

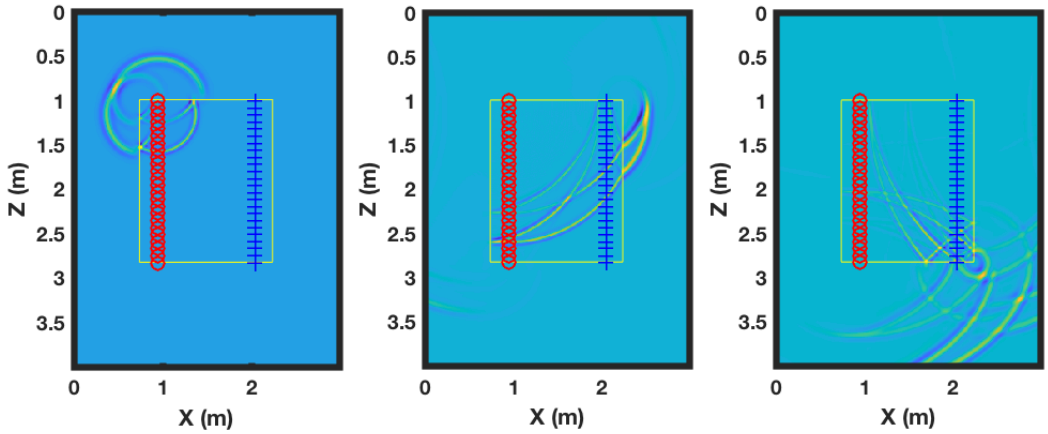

Figure 2. Three snapshots of a 2D viscoacoustic simulation used to explore tank response (prior simplified version). The left, middle, and right panels correspond to three times at the beginning, middle, and end of the simulation run.

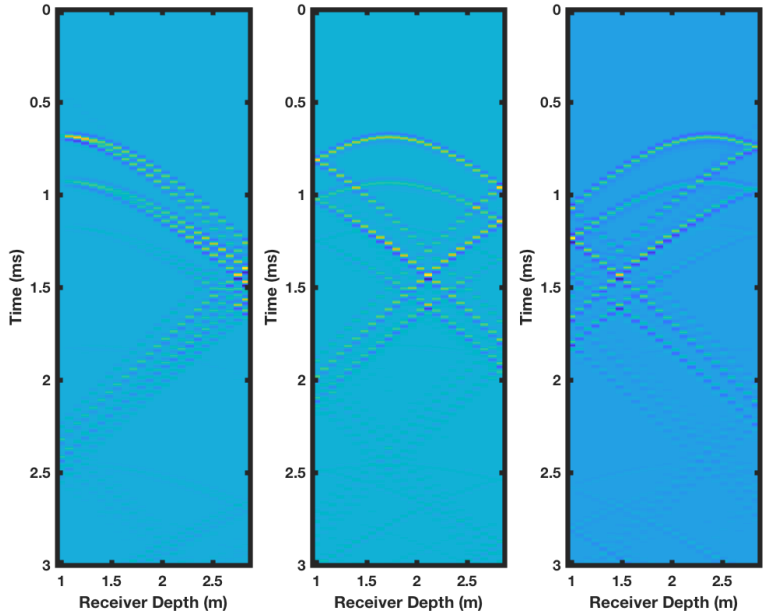

Figure 3. Three simulated common shot gathers for the tank geometry shown in Figure 2. Note the ghost arrival behind the direct arrival as well as the top and bottom reflections.

2.4 Proposed Tank Design

After initial modeling tests, we finalized an tank and packing design to guide procurement. Figure 4, a scale drawing of the mesoscale experiment, shows the overall geometry of the tank, fill material, source and receiver boreholes, injection well, and side-wall ports. The experimental container selected was a large 960-gallon, cylindrical open top tank with 17 side-wall ports (detailed explanation below). We planned to fill the tank with washed silica sand in an upwards coarsening sequence with a dip of ~4°. The upwards coarsening sequence is to mimic a CO_2 storage reservoir formation, which is capped by an impermeable bentonite layer and in turn is overlain by a sand layer to mimic a surficial aquifer. Four 2”-diameter PVC boreholes are positioned 90-degrees apart and ~8” from the tank wall, for housing the CASSM arrays (two source

and two receiver boreholes). One 1”-diameter borehole, located down dip, will be used as the CO_2 injection well.

The 17 side-wall ports house pressure gauges and thermocouples designed to allow monitoring and control of hydrogeologic boundary conditions on the testbed. The side-wall ports can also be utilized to induce cross-flow of brine for dissolution experiments or for controlling aquifer state. In our case, we intend to use them to generate lateral pressure gradients to allow for brine flow within the reservoir formation. Figure 5 shows the setup for these two systems. They both include storage containers for brine or water, a pump, and a pressure gauge on the input side. On the output side the systems include a back pressure regulator for pressure control within the tank and a system that allows us to quantify the liquid outflow (i.e., a scale or flow meter).

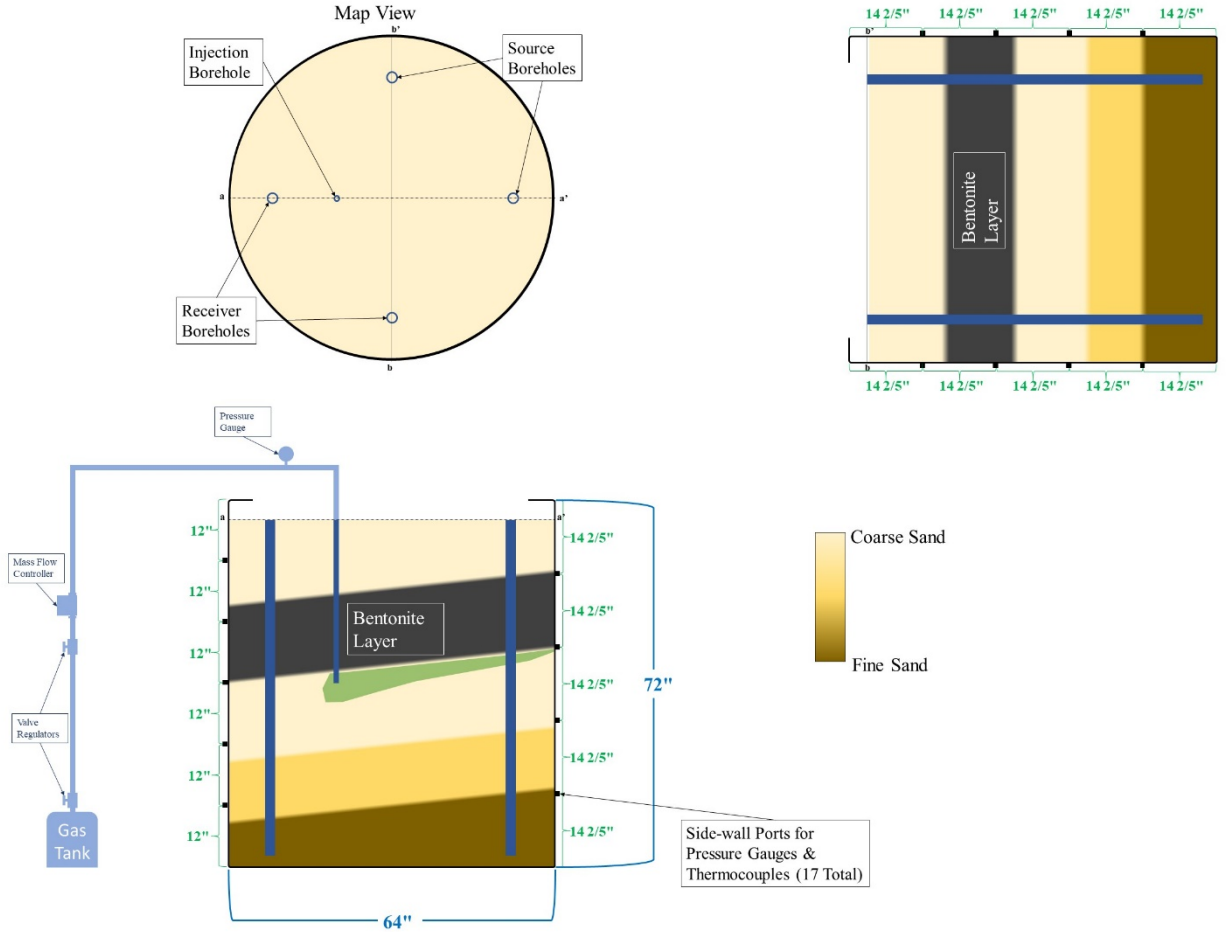

Figure 4. Drawing of the mesoscale CASSM experiment in map and two cross-sectional views. Drawing includes tank size, fill material, fill geometry, source and receiver borehole locations, side-wall port locations, injection well location, and relative CO_2 tank and pressure gauge locations.

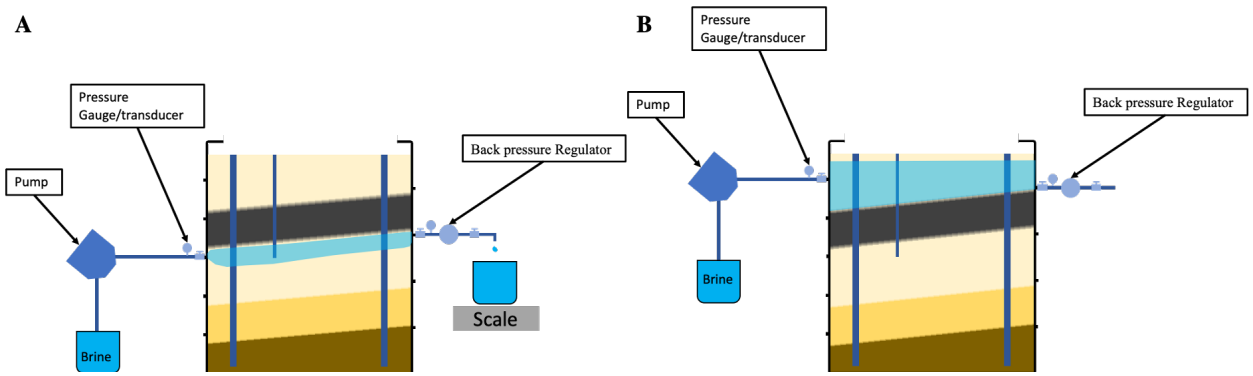

Figure 5. Drawing of the mesoscale tank setup for the (A) dissolution experiments and (B) aquifer state system.

2.5 Procurement of Experimental Tank

One challenge when finalizing and purchasing the experimental tank was finding a tank that had the strength to hold wet compacted sand. Most plastic tanks are rated for 1.5 specific gravity, while wet compacted sand has a specific gravity of ~2.1. We were able to locate a vendor (Poly Processing Co. LLC) that would customize the tank with thicker walls such that the specific gravity rating is 2.2 and provide the side ports we required to allow for hydrogeologic control and pressure monitoring.

The final design of the testbed utilized a 960-gallon open top tank with a lid (figure 6). The tank was made of XLPE (cross-linked polyethylene). The system was specified to be 72” tall and 64” in diameter, a size customized to fit in the finished lab space at Rice. The testbed was designed with 17 – 1” side-wall ports; the ports are 90° apart around the circumference of the tank; three of the sides have 4 ports that are equally spaced vertically, and one side has 5 ports that are equally spaced vertically. The side with 5 ports will correspond with the side of the down dip sequence of the fill material (see figure 4). The ports are fitted with threaded 1” bulkheads that house pressure gauges, thermocouples, and flow ports to allow for cross-flow experiments. We should note that the tank is close to the dimensions discussed in our initial modeling studies. The final tank dimensions were determined by the exterior door sizes leading to our laboratory, a hard constraint without building modifications.

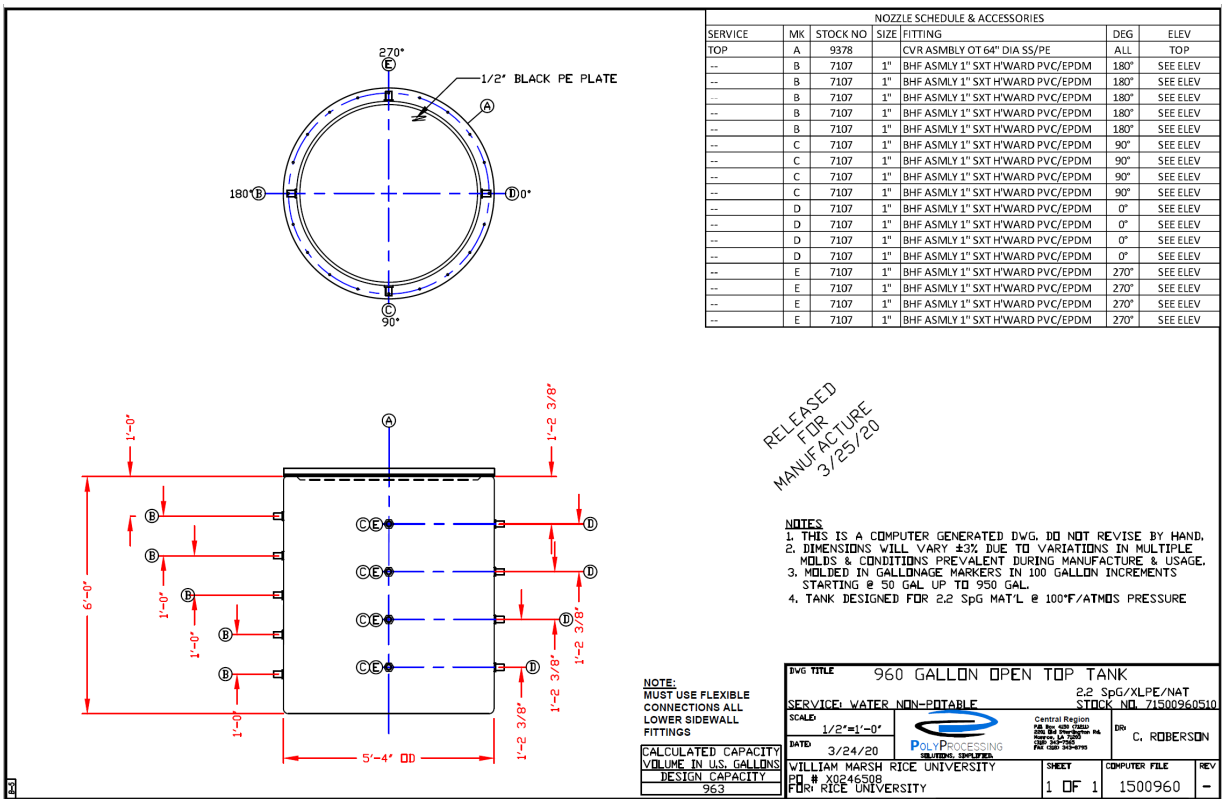

Figure 6. Final technical drawing of the experimental testbed used for the mesoscale CASSM experiments. The drawing includes the size and tank of lid as well as the 17 side-wall port locations.

2.6 Final Experiment Modeling

As part of finalizing the borehole design, particularly the formation dip and injector location, we conducted a final phase of modeling. In this phase of modeling, we included the CO_2 injection and the resulting seismic response. Figure 7 shows an update to the design model that includes the reservoir sand, the cap rock, and CO_2 injection. We utilized realistic flow properties for each layer that map to the sand and clay that was procured. We then utilized the *Matlab Reservoir Simulation Toolbox* (MRST) to simulate the CO_2 injection in a water saturated reservoir. We selected a realistic 3D injection plan which effectively replicated the planned experiment; CO_2 was injected at 0.1 L/min (100 mL/min) for 8.5 hours to generate the plume spanning the tank. The resulting dataset was useful in providing constraints on our fluid handling systems in terms of required rates.

CO_2 saturations were converted to V_p perturbations using realistic models for CO_2 properties and the White-Dutta-Ode model for partial saturation. The V_P model shows low V_P values (i.e. 700 m/s) for the CO_2 plume and high values (i.e. 1600 m/s) for the water saturated zones. This gives a large contrast between the CO_2 plume on the rest of the reservoir once again confirming the viability of our planned CASSM experiment.

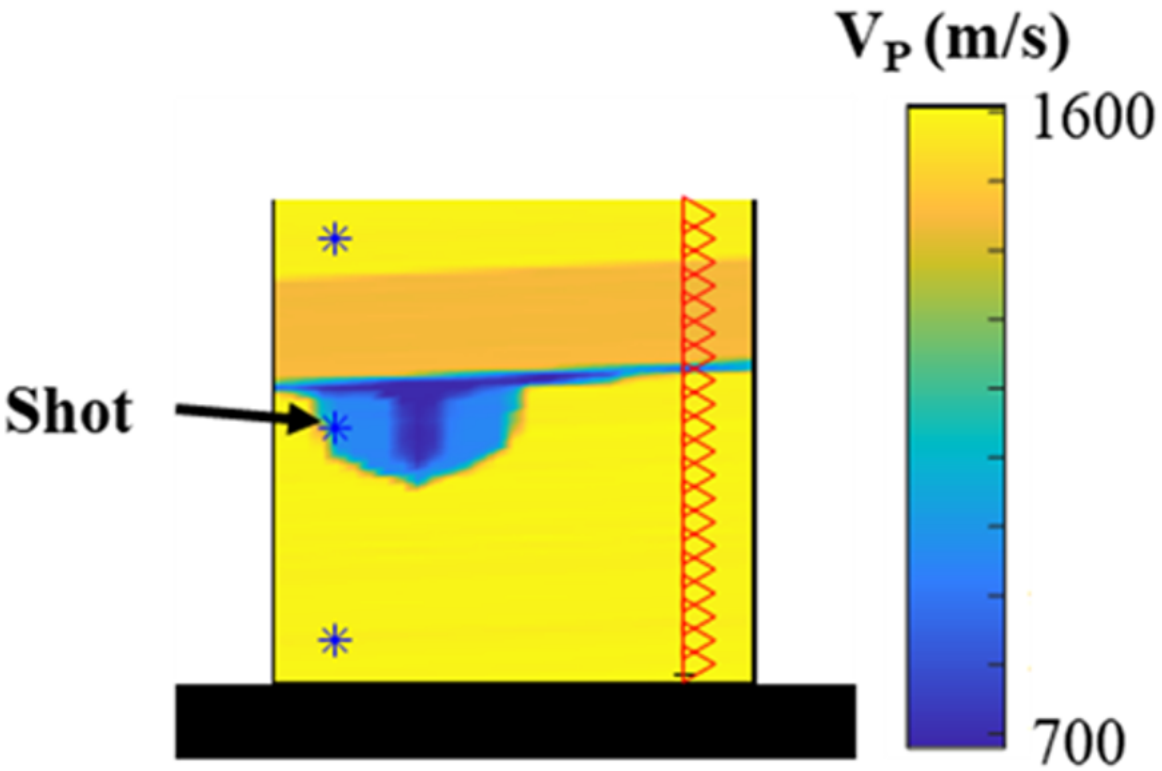

Figure 7: V_p perturbation generated from CO_2 injection model.

After generation of the spatial V_p distribution, the likely CASSM response was again modeled with the finalized well geometry and a high order (8^{th} in space) FD acoustic wavefield code. Shot locations at the top, middle, and bottom of the tank were modeled (see Figure 7 for locations). Figures 8 and 9 show the baseline and repeated modeling result after the simulated CO_2 injection. We should note that this version includes the appropriate air boundary conditions around the tank and that the tank is sitting on a concrete pad. While the CO_2 plume impacts the recorded wavefield for all shot locations, the intermediate depth sources produce the most distorted wavefields, largely due to a dramatic slowdown in the horizontally propagating P-waves and related head waves around the plume exterior. We should also note that the free-surface reflections are also distorted by the CO_2, suggesting that they should either be used to constrain the plume geometry or windowed out of subsequent waveform inversion process.

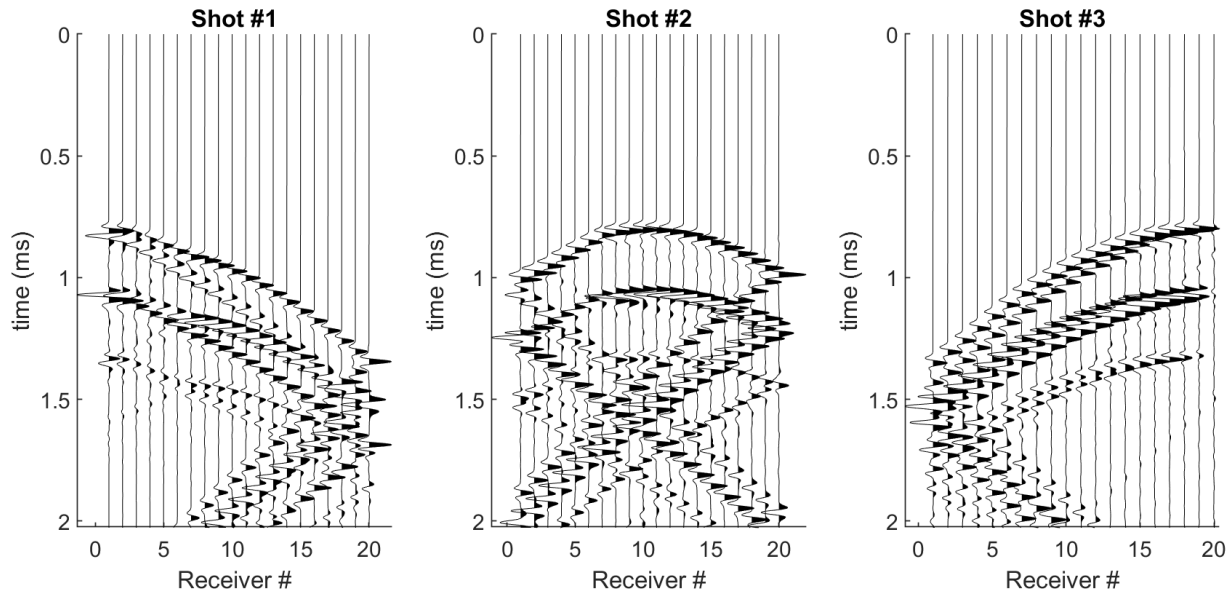

Figure 8: Baseline modeling results for top, middle, and lower shot locations.

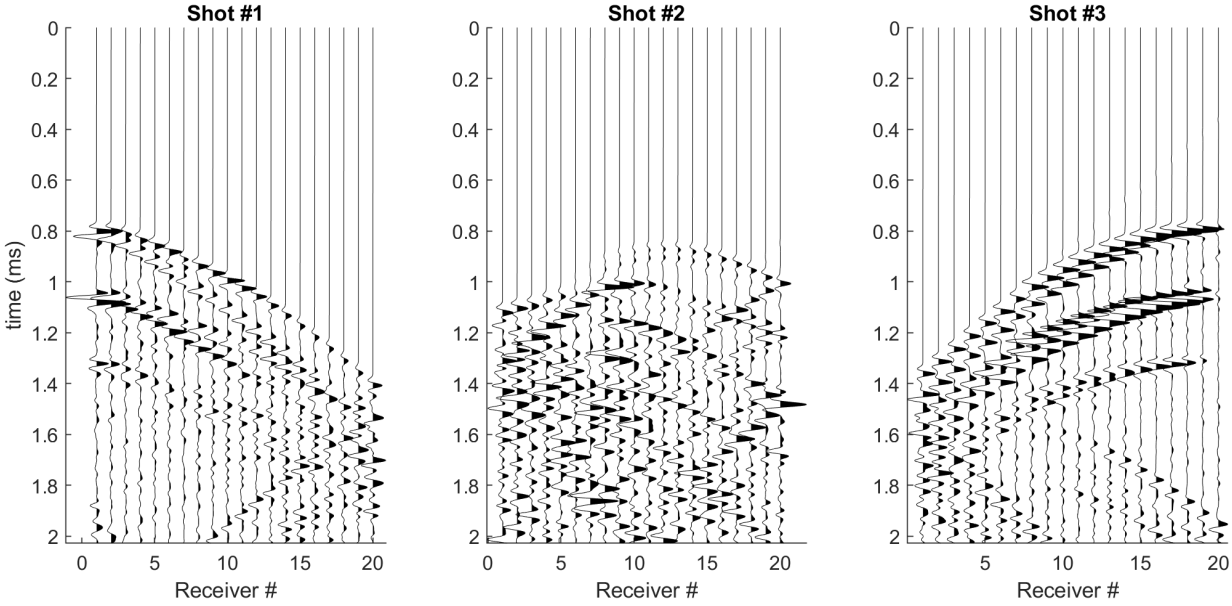

Figure 9: Repeat modeling results for top, middle and lower shot locations after the CO_2 flow simulation.

2.7 CASSM Borehole Design and Instrument Procurement

The mesoscale tank, while the largest component of the testbed, was not the most complicated to design and construct. Other components include the well infrastructure and sensor components needed to monitor the physical systems.

One unexpected issue was the need to keep the monitoring wells installed in the tank properly positioned and spaced during packing. To accomplish this, we designed and purchased parts to build the frame that holds the boreholes in place while sand was packed in the tank (Figure 10). The boreholes are 2" clear PVC pipes, connected to a positioning frame mounted to the bottom of the tank with epoxy. The boreholes are equally spaced from one another; this positioning is maintained using the cross-shaped PVC frame connected to the boreholes by pipe saddles. The

bottom of the CASSM boreholes are capped with expansion plugs so that the reservoir sand and the boreholes are not hydraulically connected and to prevent unwanted tube waves in the reservoir sand.

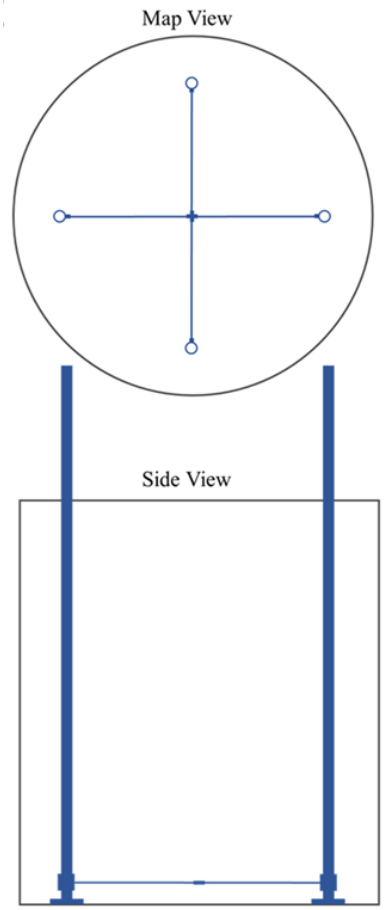

Figure 10. Drawing of the CASSM borehole system.

The CASSM system includes two source boreholes, two receiver boreholes, and an instrument stack (Figure 11C) which includes AD/DA subsystems, a high voltage amplifier and switch, and the associated control PC. For receiving waveforms, we are utilizing 52 hydrophones from High Tech Inc. (Figure 11A). On the source side, we are utilizing 24 piezoelectric sources (Figure 11B) fabricated at LBNL. Each source is a 4" radially-poled piezoelectric crystal, similar to the design used in several recent near-surface projects.

The CASSM control system is similar to that discussed in Ajo-Franklin et al. 2011 except utilizing an off-the-shelf HV amplifier (Trek) and a new high frequency analog-to-digital converter capable of being slaved to an atomic clock to improve long-term stability. Figure 11c shows the electronic stack used for generating and recording the CASSM signals including the amplifier, source switching system (Cytek), atomic clock (SRS), and control computer.

Figure 11. Pictures of a hydrophone (A), Piezoelectric Source (B), and the CASSM control system.

2.8 Sand and Bentonite Clay Procurement

Another challenge when developing mesoscale testbeds of these dimensions is procurement and characterization of the large volumes of sediment needed to pack the tank. In our case, we desired sediment which were pre-sieved to allow for generation of variable permeability units within the tank.

After exploration of several vendors, we purchased 300 50-lb bags of sand (Preferred Sands, Inc.) for packing the reservoir portions of the physical model. A very limited number of vendors offered the combination of sieving and pre-washing for volumes at this scale. The purchase included 150 bags of a 100-mesh sand and 150 bags of a 40/70-mesh sand; the sieve distributions are shown in Figure 12. By mixing sands with two sieve distributions, we were able to create a coarsening upward sequence in the reservoir unit, mimicking natural deposition.

Each pallet weighed ~3100 lbs, making the task of offloading the truck and transport into our laboratory challenging. To cap the reservoir, we procured 15 50-lb bags of a sodium bentonite (Benseal, Bariod, Figure 13A). We tested the bentonite mixture's swelling and sealing capabilities by preforming a mini tank (beaker) experiment. The experiment included dry sand capped by Benseal and water for multiple days (Figure 13B). The sand remained dry confirming that the Benseal sealed properly. To ease the sand packing process, we procured a hanging sediment hopper to use with our existing hoist.

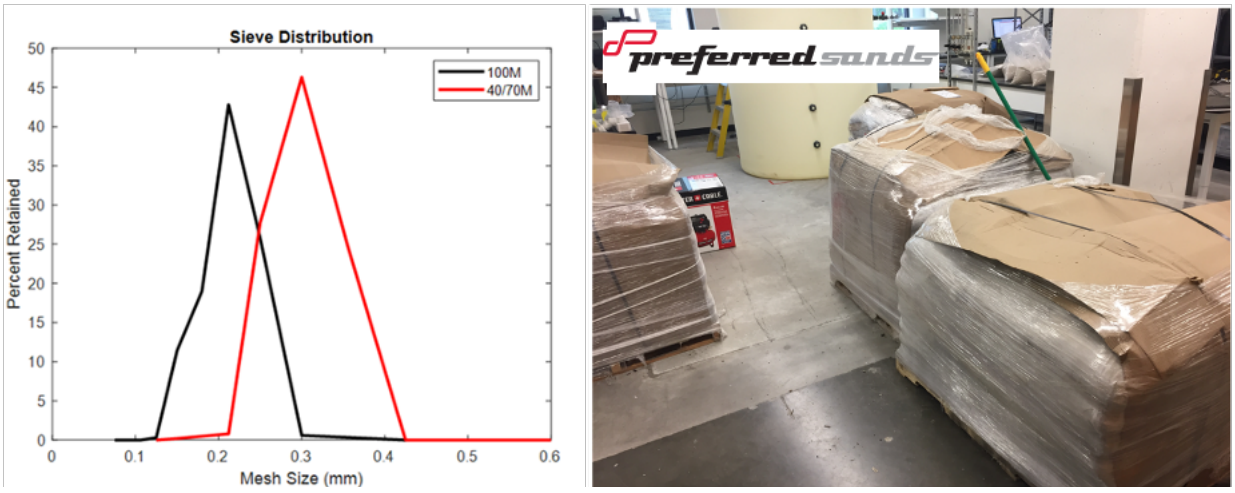

Figure 12. Sieve distribution of the two sands bought from Preferred Sands, Inc. (left) and an image showing the 300 bags of sand on pallets in the lab.

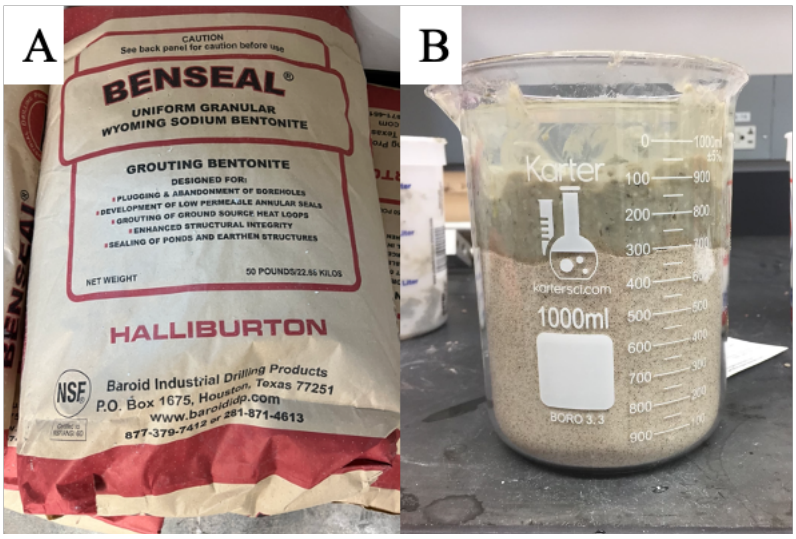

Figure 13. (A) a bag of sodium bentonite and (B) a mini-tank experiment testing the sealing capability.

2.9 Side-Wall Sensor and Flow Component Procurement

As mentioned previously, the tank exterior was designed with 17 sidewall ports which we will utilize for both flow control and sensing. We procured assemblies for the side-wall port construction; each port includes a 60-mesh screen to prevent sand collapse into the ports, a 1" on/off valve, a 1" to ¼" adapter, a tee-connector for pressure/temperature readings, and lastly a ¼" on/off valve.

We have also purchased 20 pressure transducers (Omega Engineering Inc) that can read up to 5 psi accurately. Eight of the pressure transducers are model PX309-005G10V, while the other 12 are PX409-005G10V. These pressure transducers allow us to monitor pressure boundary conditions across the system. We also procured five thermocouple probes (Type T, McMaster-Carr) for temperature monitoring at some of the side-wall ports. For logging data from the side ports, we procured a multi-channel A/D system (Keysight 34970A) which allows for logging both temperature and pressure simultaneously within the same system.

In addition to the pressure and temperature readings, we purchased a computer-controlled peristaltic pump which we will be used to generate lateral groundwater flow velocities. We have also procured an accurate back pressure regulator (Equilibar) and an air compressor required for the back pressure regulator. The back pressure regulator will be used to provide a constant head boundary condition at the far side of the tank from the peristaltic pump.

2.10 Dielectric Probe Procurement

While the focus of our study is the performance of CASSM for CO_2 leakage detection, one challenge in evaluating CASSM inversion results is availability of "ground truth" values for CO_2 saturation. While we do have mass and volume constraints on the injected CO_2, the original tank design did not have a secondary geophysical measurement for CASSM comparison. To remedy this deficiency, we decided to install a vertical array of dielectric sensors, typically used for soil moisture measurements (Onset, RPX-GPx), to provide a secondary measurement of CO_2 saturation. Due to the high dielectric constant of water (~80) and the low dielectric constraint of gas phase CO_2 (~1) such measurements provide a good approach to constrain volumetric gas fraction. We selected an array of two 90 cm dielectric probes, each of which with 6 sensing regions of 15 cm vertical extent; this allows a continuous pseudo-log of CO_2 saturation to be measured

with 12 measurement points along the vertical profile. The dielectric monitoring profile was located along the axis of the injection well, within one of the four-spot profiles to allow tomographic comparisons. Figure 20, panel (a) shows the monitoring array location (blue rods). The dielectric measurements are digitized near the array and transmitted to our web-enabled data logger via Bluetooth (Figure 20, panels b,c).

3 Assembly and Installation

3.1 Mesoscale Testbed

The delivery and installation of the test tank was a challenge due to its size. After unloading the system (Fig 14, panel A) the door to our laboratory building required modification to accommodate entry (Fig. 14, panel B). Fortunately, the zone of the laboratory designed for mesoscale test systems fit the CASSM tank (figure 14C) and the utility locations were more than sufficient for supporting the experiment.

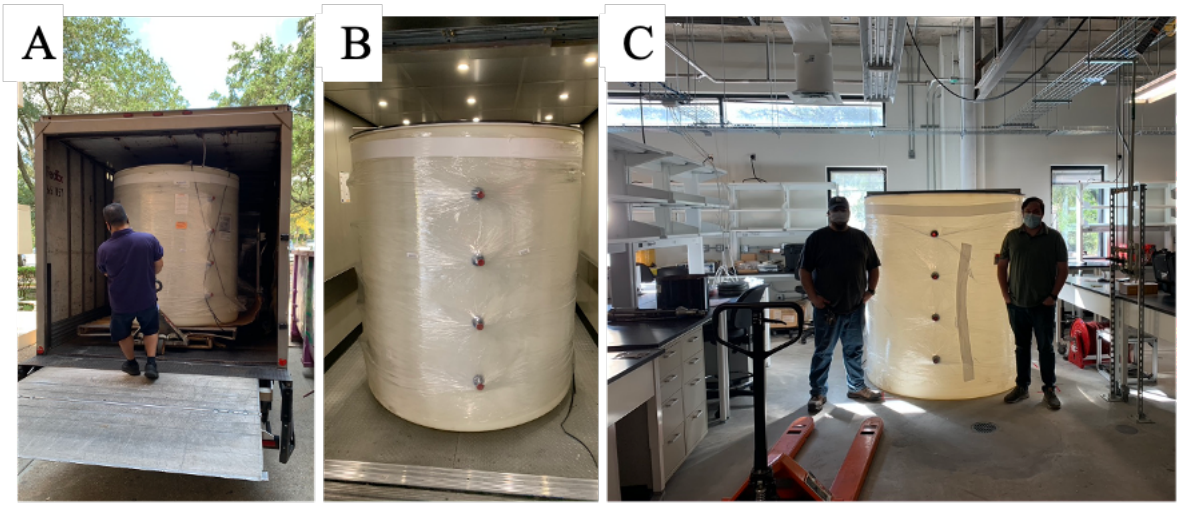

Figure 14. (A) The 960-gallon tank being delivered, (B) the tank inside the building after modifications to the outer doors, and (C) the tank placed in its location inside the REAGLe laboratory at Rice University.

3.2 CASSM Borehole System

Epoxying the borehole frame to the tank floor and guaranteeing positioning without exposing students to the risks of a confined space required some ingenuity. To accomplish this task, the borehole frame was completely fabricated outside the tank and then was lowered in using the 1-ton hoist (figure 15A). As it was being lowered, a viscous epoxy was applied to the bottom of the borehole frame (i.e., the four wall mounts). To center the borehole frame, rope was fed through the bottom sidewall ports and around the four boreholes (Figure 15B). The ropes around each borehole were tightened equally outside of the tank as the borehole frame was lowered in.

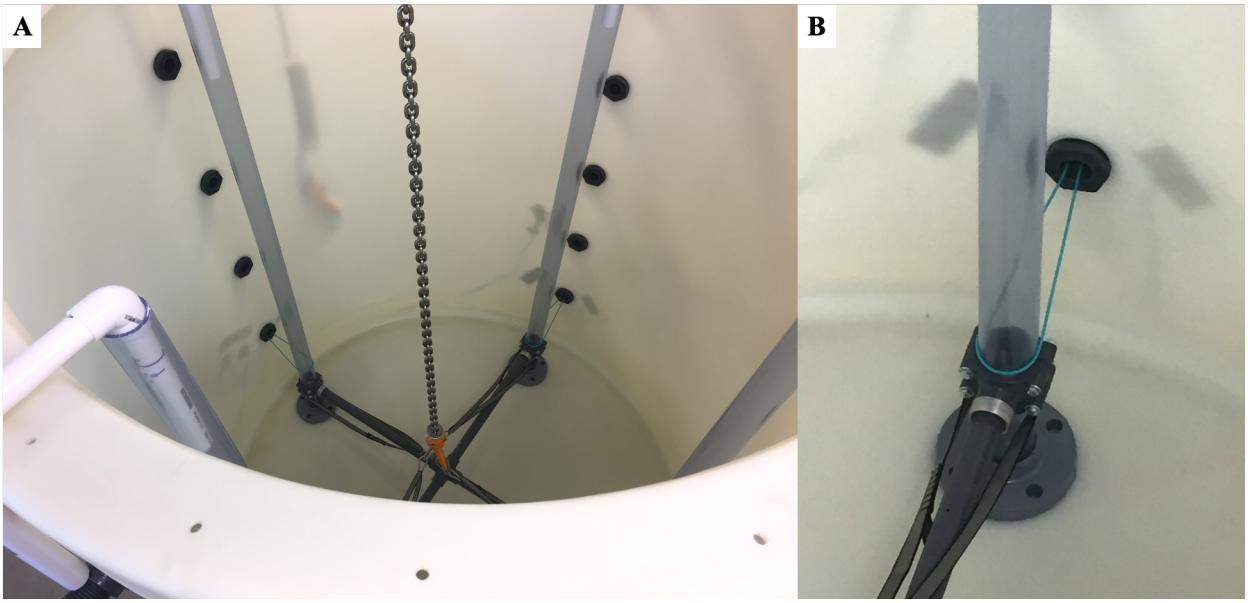

Figure 15. (A) Borehole frame being lowered in during epoxying, (B) an example of the rope being used to help center the borehole frame.

Installation of CASSM hydrophones and sources was more straight forward. The hydrophones strings have 20 hydrophones spaced 3.5 inches (figure 16A), while the source strings have 9 piezoelectric sources spaced 7.5 inches (figure 16B) to fit the length of the boreholes (i.e., ~69 inches). There are two hydrophones (without preamps) attached to the bottom and the middle of the source string to measure the signal coming directly from the sources. Both the hydrophone and source strings were clamped at the top of the boreholes to prevent the instruments from clumping up at the bottom of the borehole (figure 16C). The exact locations of the sources and receivers are shown in figure 23.

Figure 16. (A) a hydrophone string for one of the boreholes, (B) a source string, (C) an example of the source string clamped to the borehole.

In terms of CASSM electronics, as mentioned previously we adopted a control and acquisition stack similar to that show in in Ajo-Franklin et al. 2011. For each source excitation, the computer controlled D/A system generates a pulse which is then fed to a high voltage amplifier. Only one

source is excited at a time with source selection determined by a computer controlled HV switch (Cytec). Figure 17A shows the source array connected to the switching matrix while figure 17C shows the hydrophone array connected to the DtAcq acquisition system. Each hydrophone in must be powered. To apply voltage to each hydrophone, we developed a way to connect a power supply to all the hydrophones using a series of screw terminal strip blocks (Figure 17B-C).

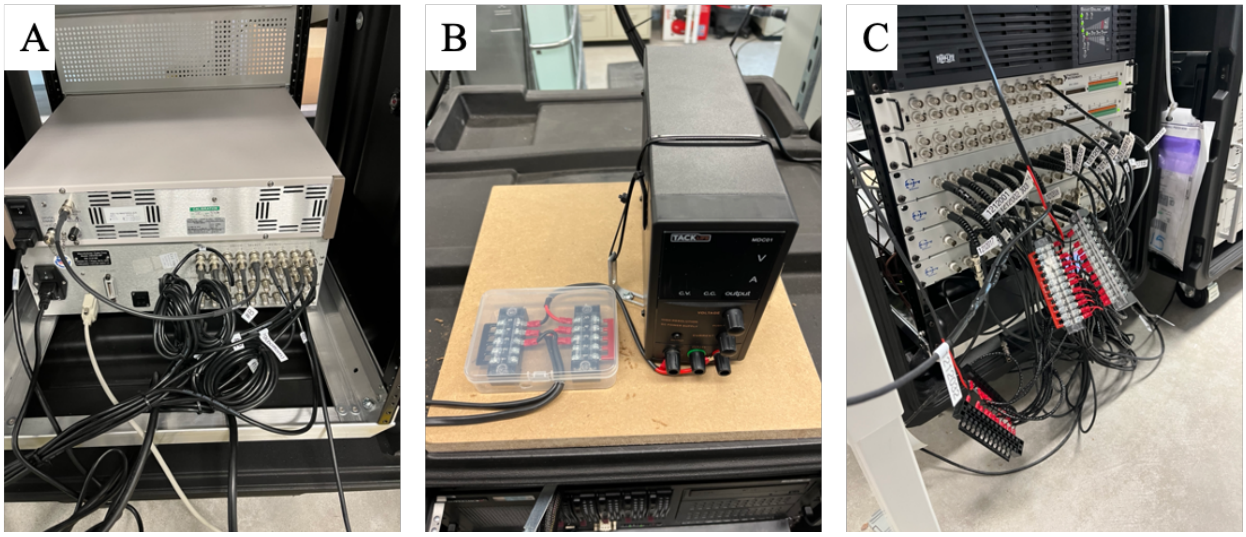

Figure 17. (A) source plugged into the back of the Cytec switch, (B) power supply and screw terminal strip blocks for powering hydrophones, and (C) hydrophones plugged into the DtAcq cards and screw terminal strip blocks for preamp.

3.3 Side-Wall Ports and Flood Test

All 17 side-wall port systems were fabricated using PVC thread paste for proper sealing. Examples of side-wall ports with only a pressure transducer (figure 18A) and with a pressure transducer and thermocouple (figure 18B) are shown below. The lead cables on both the pressure transducers and the thermocouples were only a couple of feet, which was too short to reach around the tank to a power supply and to the data logger. This required us to extend the lead cables to all 17 pressure transducers and 5 thermocouples by ~30ft so that the cables could go over the wire racks (figure 18C) and to the power supply and data logger (figure 18D). To extend the lead cables, it required soldering four wires for each transducer. Screw terminal strip blocks are used to power the pressure transducers (figure 18D).

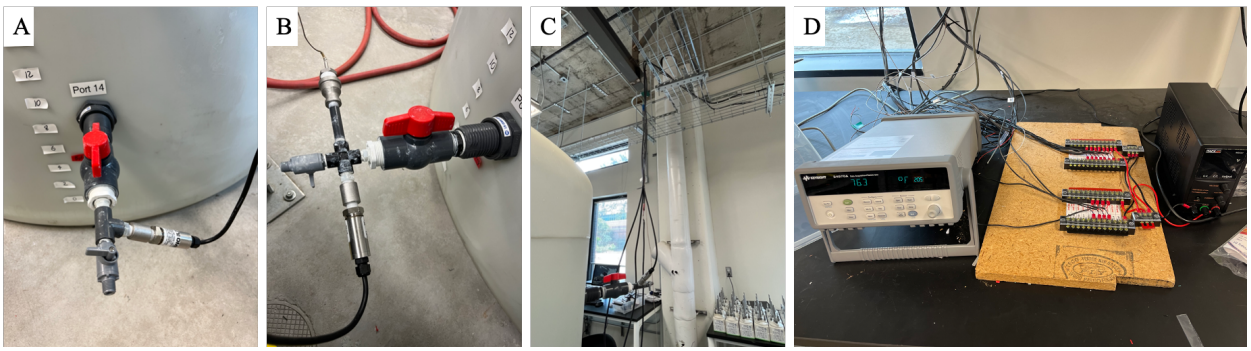

Figure 18. Images of (A) a side-wall port with pressure transducer, (B) side-wall port with pressure transducer and thermocouple, (C) extended lead cables over the cable racks, and (D) power supply and data logging station.

Once the side-wall ports, pressure transducers, and thermocouples were installed, a series of leak tests were performed to ensure the testbed was water tight. This involved flooding the system with 960 gallons of water and checking for leaks within the sidewall ports. With 17 ports and multiple parts at each port, there were over 180 possible leakage locations. To help limit the possible leakage locations at a given time, the tank was filled in multiple steps starting with the bottom four ports (figure 19A). Once it was determined that there were no leakages in these ports, the tank was filled with more water to test the next level of ports until all 17 ports were tested (figure 19B). Only a few leakage locations were detected, including the threading of the thermocouples which only required more thread tape for sealing.

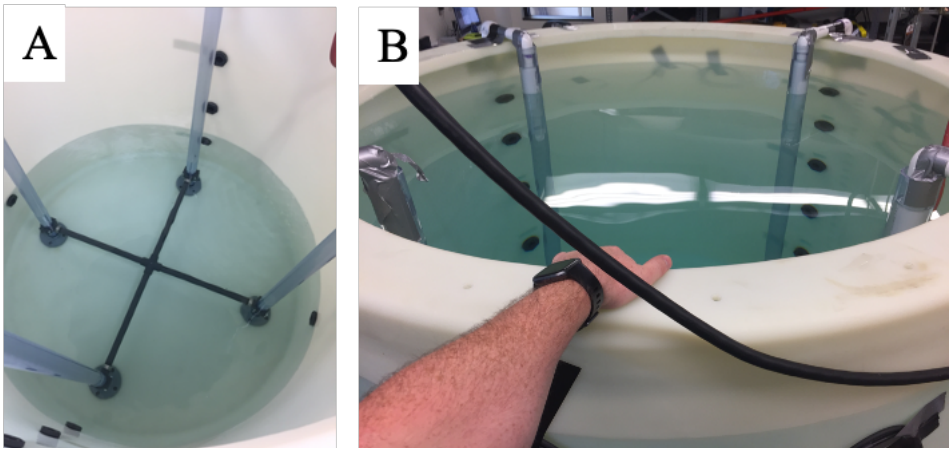

Figure 19. Images of (A) initial flood test of the lower four ports and (B) completion of the flood test.

3.4 Dielectric Probes and Injection Borehole

Installing the dielectric probes and the injection borehole was also a challenge, since we did not want to add more pipes to the system but also wanted the probes and the injection borehole not to move during sand packing. To accomplish this, we fabricated a temporary frame that sat inside the the four CASSM boreholes (figure 20A). This frame allowed us to attach the injection borehole with a saddle-tap tee and to hang the soil moisture probes. After the sand packing, the frame was removed only leaving behind the soil moisture probes and the injection borehole (figure 25B).

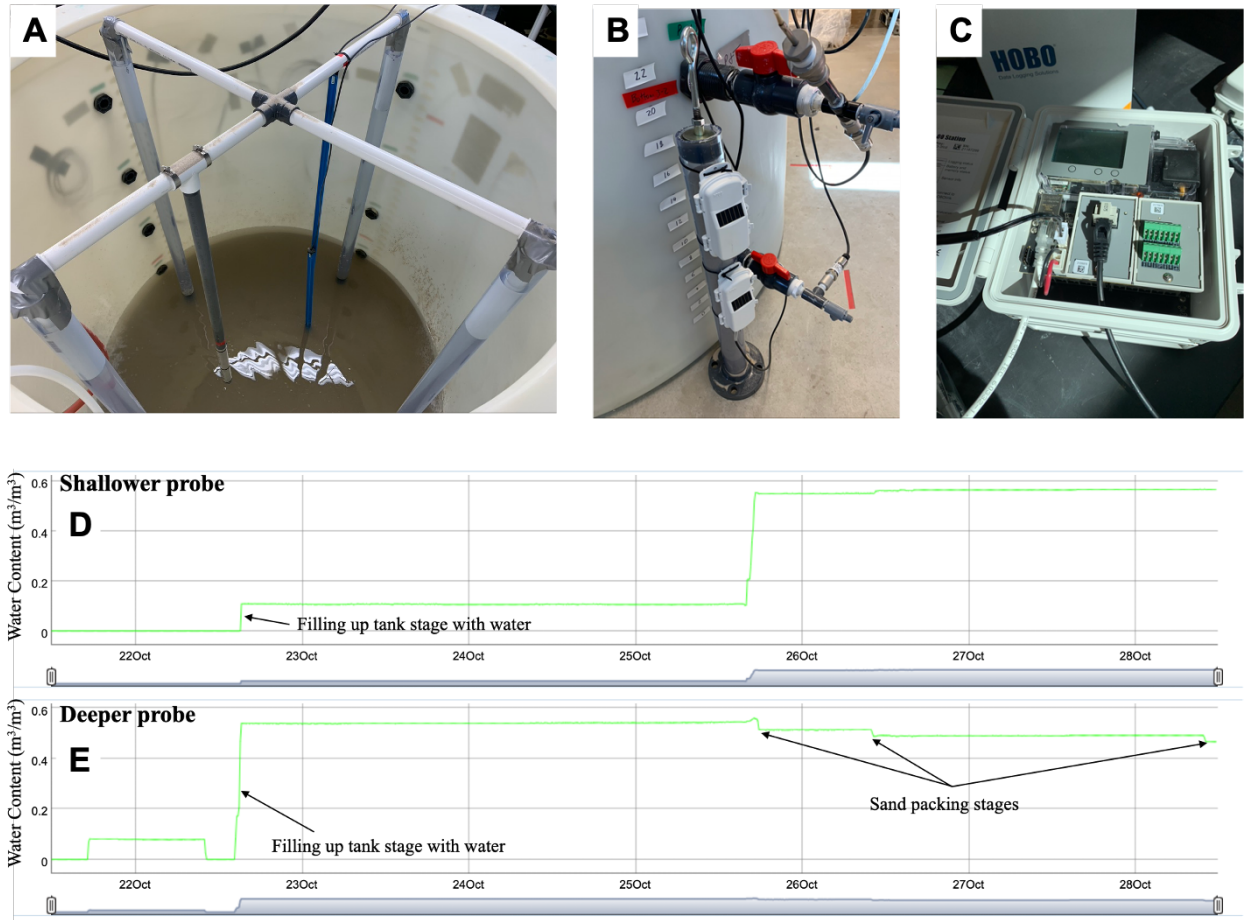

Figure 20: Installation, logging systems, and initial data from the vertical dielectric logging system. Panel (a) shows the mesoscale tank interior with the dielectric probe array (blue) during tank packing. Panels (b) and (c) show the Bluetooth digitizers and web-enabled logger (c) used to record dielectric data. Panels (d) and (e) show the time histories of water content for two different measurement depths. Note that the sensors are limited to arrange of dielectric values equivalent to water content of no greater than 0.55 m^3/m^3, this value represents coverage of the sensor with water while lower values show the effects of sand during packing (panel e).

The injection borehole is a 1-inch PVC pipe that is capped at the bottom with an expansion plug. The bottom 12 inches of the borehole includes a total of 44 holes 1-inch apart on all sides of the pipe (figure 21A). The holes are an 1/8 inch in diameter. A 100-mesh screen was wrapped around the holes to prevent sand from collapsing and clogging the injection borehole (figure 21B).

Before CO_2 is injected in the first experiments, the dielectric monitoring array will be useful in estimating porosity; assuming 100% water saturation, the large dielectric contrast between water (80) and quartz (3.8) will be exploited to obtain a porosity profile with depth after any residual air is purged from the system. Figure 20 panels (d) and (e) show initial time traces for two dielectric sensing locations, converted to volumetric water fraction. In this case, they were not in a steady state an exhibit partial volume effects as water and sand are added to the mesoscale tank system.

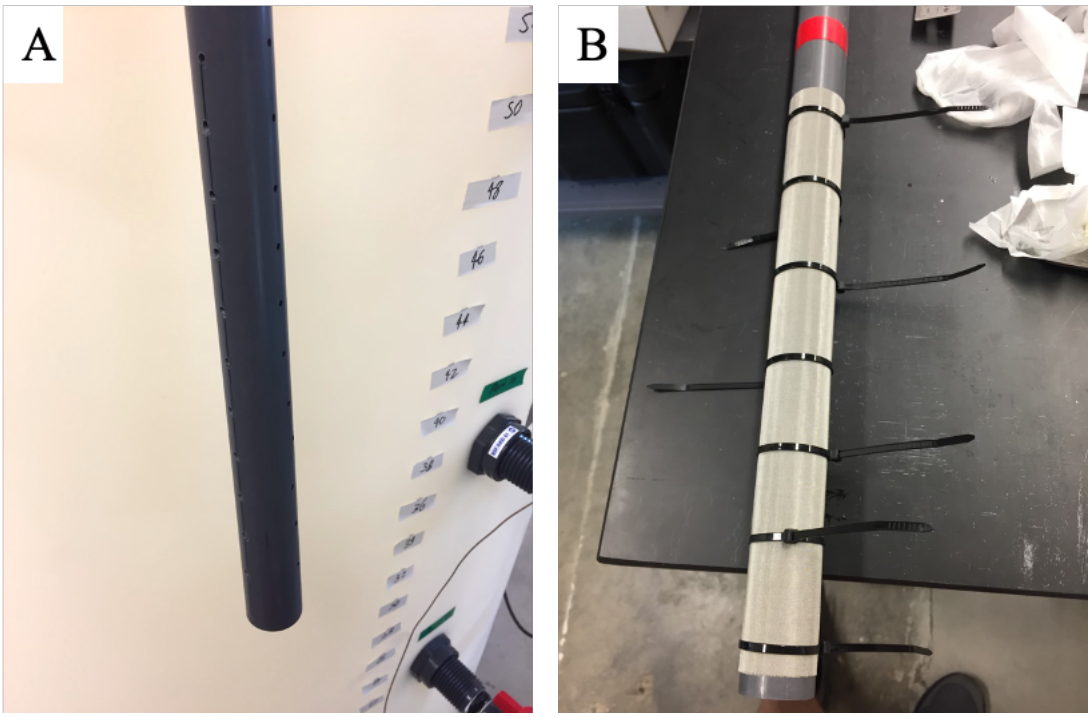

Figure 21. Images of (A) the injection borehole showing the 44 holes for CO_2 injection and (B) the screen attached on the outside borehole to prevent sand from collapsing into the borehole.

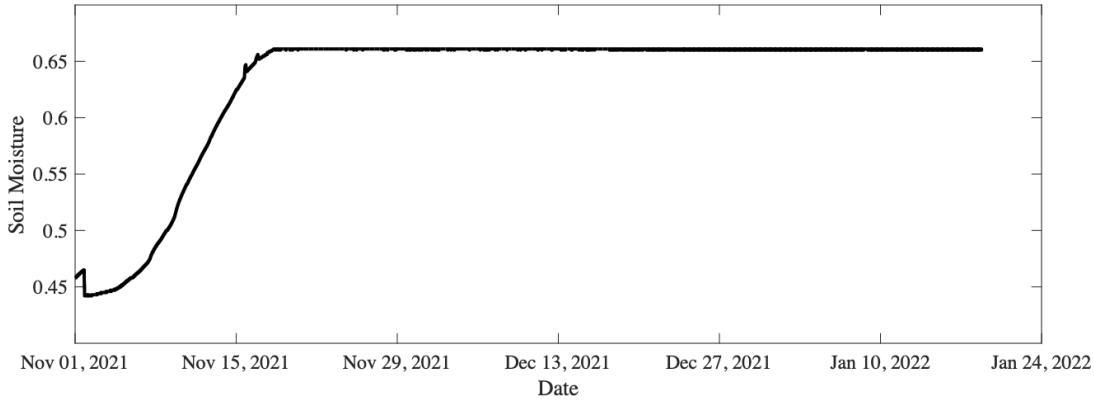

Figure 22. Soil moisture measurements inside the reservoir. Soil moisture reaching plateau is attributed to air bubbles being dissolved by water. Note that the soil moisture estimate is not calibrated yet and should be taken as a qualitative measure.

After the sand and bentonite packing was completed, inside the reservoir (i.e., under the bentonite layer) the soil moisture has plateaued (Figure 22). We attribute this increase in soil moisture to air bubbles being dissolved in the water; the plateau suggests that all air bubbles have been dissolved and that the reservoir has reached an equilibrium. We should also note that the soil moisture estimate is qualitative at this point and still needs to be calibrated using the specific sediment we utilized for the mesoscale testbed.

All instrument locations inside the tank are shown in figure 23; that includes the CASSM sources and receivers, the temperature and soil moisture measurements of the dielectric probes, and the injection borehole.

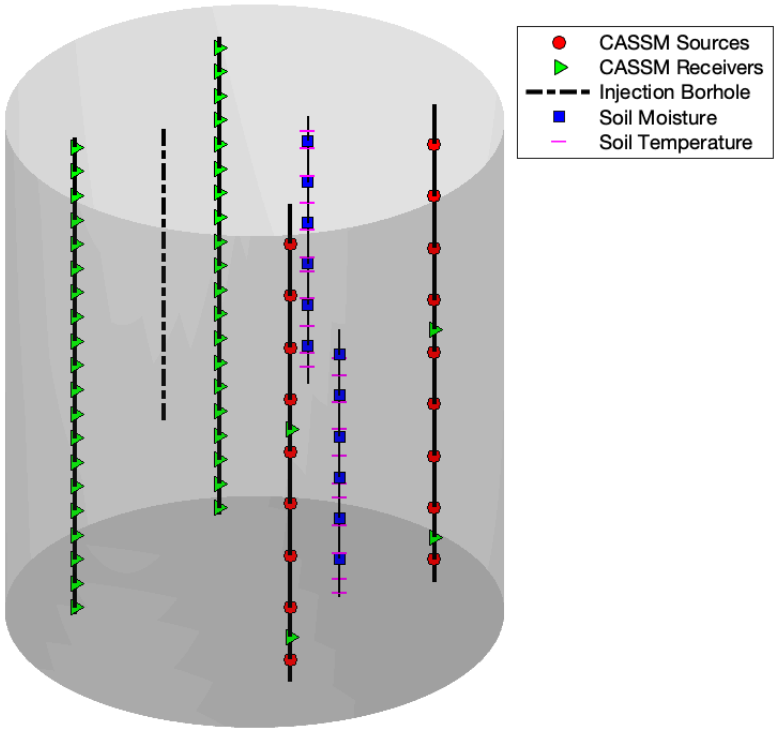

Figure 23. A *MATLAB* plot showing the locations of CASSM sources (red circles) and receivers (green triangles), the injection borehole (dotted black line), and the soil moisture (blue squares) and temperature (magenta dashes) of the dielectric probes**.**

3.5 Sand and Bentonite Clay Packing

The most physically intensive task of fabricating the mesoscale CASSM experiment was the sand packing. After the final leak tests and installation and testing of the dielectric sensing array, we initiated packing the mesoscale tank with sediment. The sieved sand was added in a coarsening upward sequence approaching the sealing unit. The sand was wet-packed by filling the tank with a small height of water and adding 50 lbs batches of sieved sand using a hoist and hopper system (figure 24). Figure 24, panel (A) shows loading of the hopper while panels (B) and (C) show positioning and unloading. After deposition of each batch, the sand surface was smoothed to a uniform angle and depth using measurement marks around the tank. As part of the reservoir layer, we created a coarsening upward sequence between the two sieved sands that were purchased (coarse: 40/70-mesh sand, fine: 100-mesh sand). To do this, we split the reservoir in 5 layers and increased the amount of course sand to each subsequent overlying layer (Table 1). Each layer was graded to ~4° dip and then tampered to increase packing. Starting at the bottom of the tank, we packed approximately 1850-lbs of fine sand. From there, we mixed by hand a 1 to 4 ratio of course to fine sand, then the next layer had a ratio of 2 to 3 course to fine sand, followed by 3 to 2, and finally 4 to 1 to finish the reservoir.

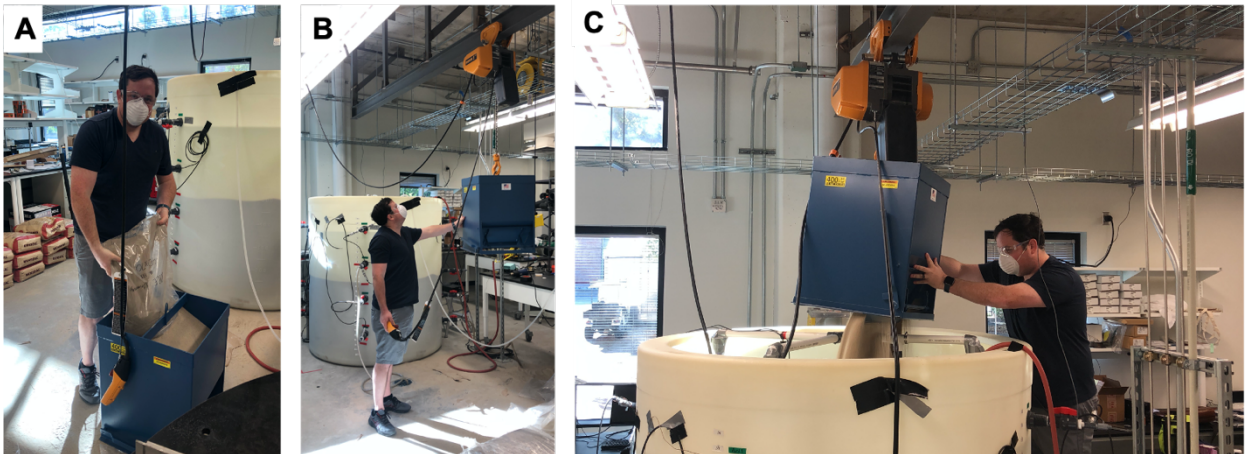

Figure 24. Example photos from mesoscale tank packing. Panel (a) shows loading of our sand hopper with 50 lbs of sieved sand while panels (b) and (c) show positioning and unloading of the sand batch into the tank.

For the sealing unit layer, we packed 500 lbs of bentonite clay on top of the reservoir, which swells to allow for good sealing around the boreholes, the dielectric monitoring array, and the tank walls. We then allowed the clay to swell for ~24h with a head of water on top (figure 25A). Lastly, we finished the mesoscale packing with ~2750 lbs of the coarser sand (figure 25B) to provide an analog surficial aquifer.

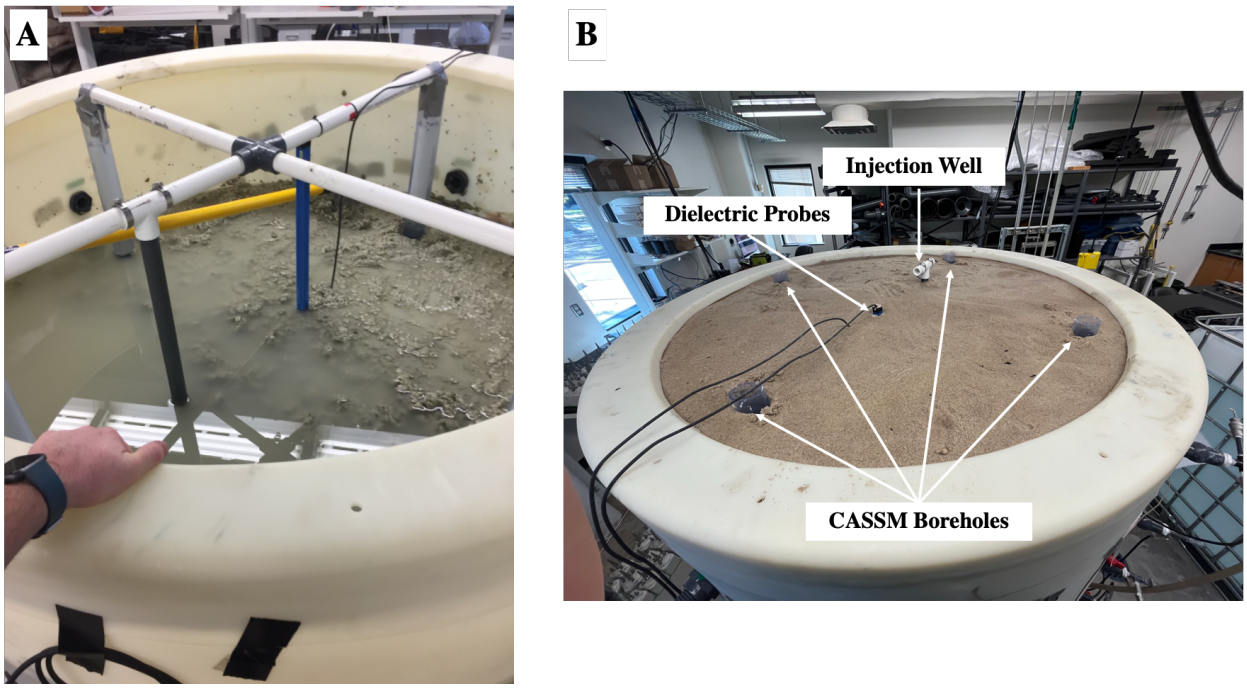

Figure 25. Mesoscale sand and bentonite clay packing. (A) Bentonite clay layer swelling stage and (B) is the final sand packing with upper frame removed showing the locations of the 4 CASSM boreholes, the injection well, and the dielectric probes.

Table 1. Sand Packing Details

Layer	Thickness (inches)	Weight (lbs)	Sand Ratio (R-r)
1, bottom	10.5	1850	0-5
2	8	1500	1-4
3	8	1500	2-3
4	8	1500	3-2
5	8	1500	4-1
6, clay	11	500	N/A
7, top	18	2750	5-0

Note: The sand ratios are by weight and are represented by coarse sand, R, to fine sand, r.

3.6 CASSM Acquisition System

At the beginning of this project, an effort was made to test a new generation of acquisition hardware with potentially improved timing performance. Unfortunately, we have had challenges with the stability of the new CASSM controller system. The new controller was designed to use DtAcq's A-to-D and D-to-A cards to help communicate between the source and receiver systems. Unfortunately, the associated software is sufficiently unstable at present to prevent reliable acquisition, likely due to issues with the software/hardware interface layer.

With these issues, we decided to switch to an older system for CASSM control, which involves a MATLAB interface for source control and an engineering seismograph (Geometrics Geode) for receiver acquisition. J. Ajo-Franklin developed the source controller (figure 26a) in MATLAB; the interface allows design of the source wavelet, control of the Cytec switch, the NI cards for amplifier input, and shot timing and stacking control. For this effort, we modified the controller slightly to add a smooth pulse wavelet component (figure 26b) to assist with future FWI and more control of the data files after each data epoch has been written by the geode system. To enable use of the Geode, we also fabricated a converter (figure 26c) to convert the individual hydrophone channels to a single cable that could be plugged into the geode (figure 26d). We connect two geodes, allowing for a total of 48 channels, which we used to record the 44 hydrophones (40 with pre-amp and 4 without pre-amp), the trigger, encoder, and amplifier monitors.

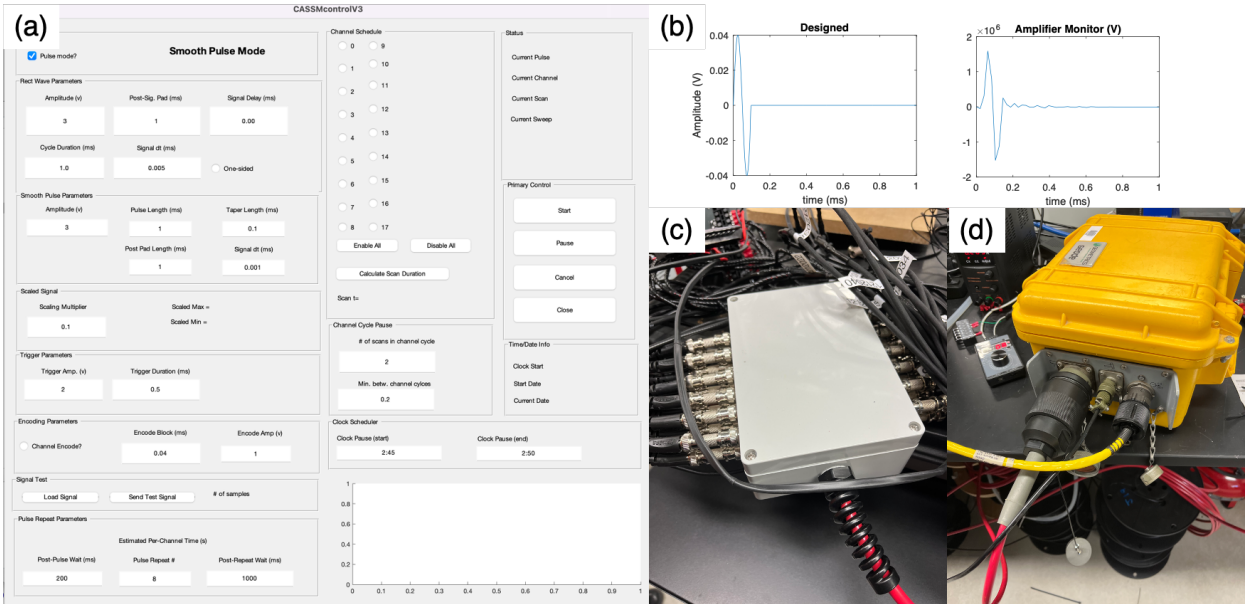

Figure 26. Acuisition Software Subsytem (a) CASSM source controller software, (b) smooth wavelet design and amplifier reading, (c) hydrophone to Geode converter, and (d) Geometrics Geode.

3.7 CASSM Background Data

After solving these hardware difficulties with the CASSM acquisition system, we collected background data (see figure 27) to facilitate initial inversions. The source gathers in figure 27 show first arrival moveouts through both boreholes. The data shows that hydrophones that are within the reservoir layer (traces 1-12 and 21-32 in figure 27) have a significantly better signal-to-noise ratio (SNR) compared to the hydrophones within the bentonite and shallow aquifer layers (traces 13-20 and 33-40 in figure 27). This suggests significant P-wave attenuation within the bentonite layer, potentially either intrinsic or due to trapped air during emplacement.

We turned to vertical stacking to assist in improving SNR. First, we converted the source gathers into temporal gathers (example in figure 28). Observations from the temporal gathers show, at least by eyeball, that the shots are constant from epoch to epoch. We experimented with how many traces should be stacked for quality SNR (figure 29a) that would be used for the CASSM acquisition. We define SNR by computing the root mean square (RMS) of the first arrival and comparing it to the RMS of the data at the end of the trace (green and red windows figure 29b, respectively). SNR values continued to increase up to 10,000 traces in a stack. As can be seen in figure 29a, the relationship between stack count and SNR is roughly linear in log-log space indicating the expected sqrt(N) SNR improvement for vertical stacking in the presence of gaussian noise. However, more traces in a stack significantly increases the time between epochs and lower our temporal resolution. We determined that 100 traces in a stack would be optimal for our purposes. However, it does take more than 10 minutes to complete an entire dataset (i.e., epoch).

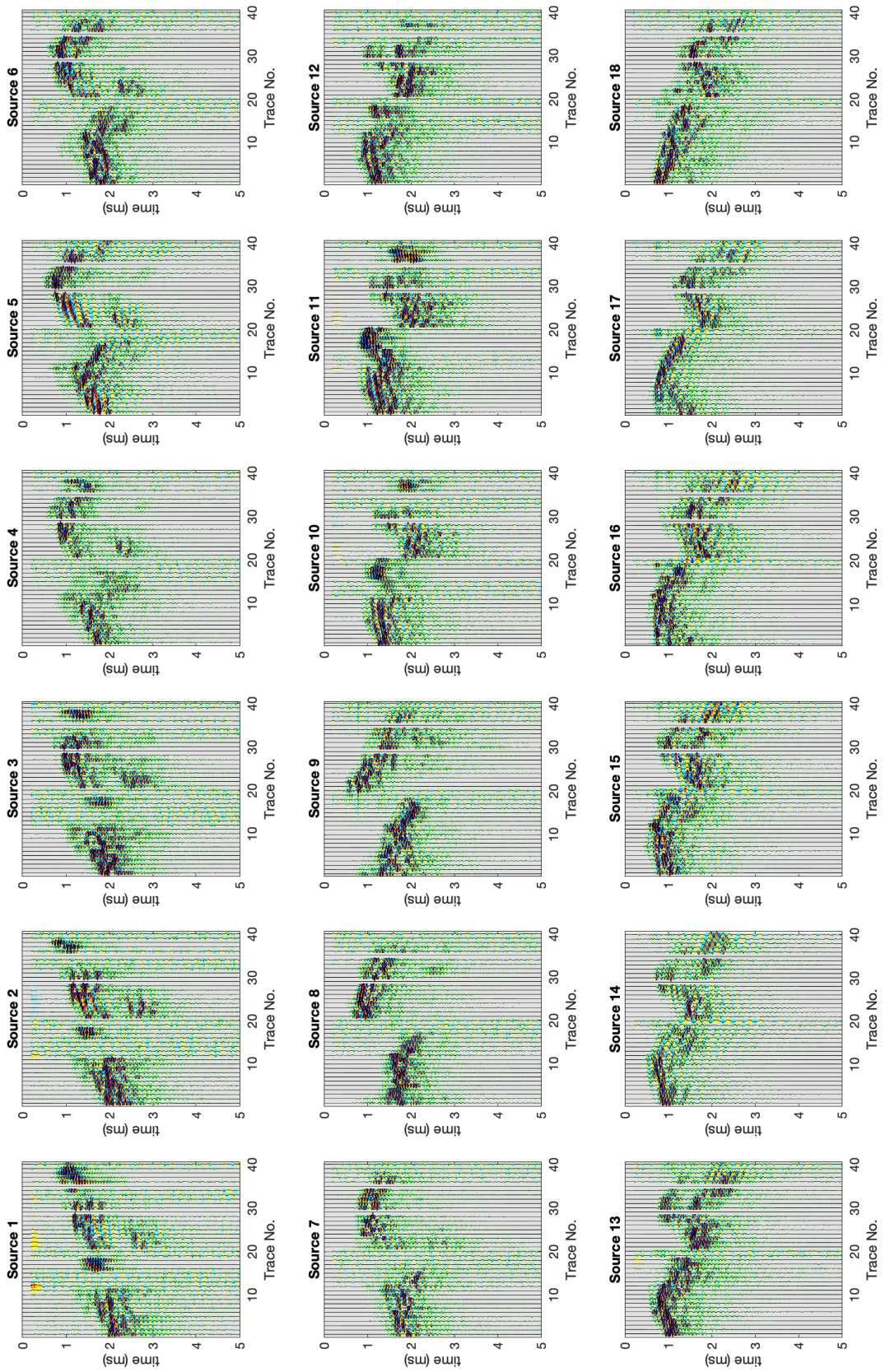

Figure 27. Background source gathers for all 18 sources.

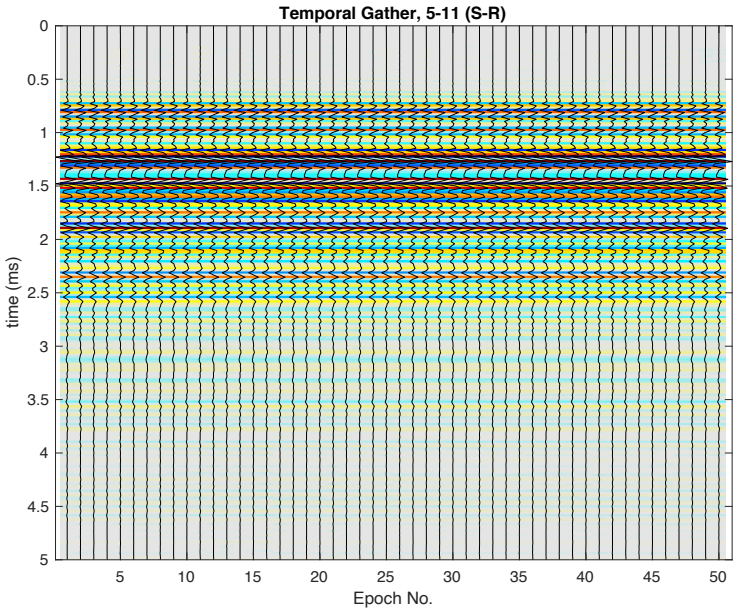

Figure 28. An example of a 100-stack temporal gather (source 5 and receiver 11) spanning 50 epochs. Each epoch requires ~10 minutes to acquire so this gather corresponds to slightly less than 8.5 hours.

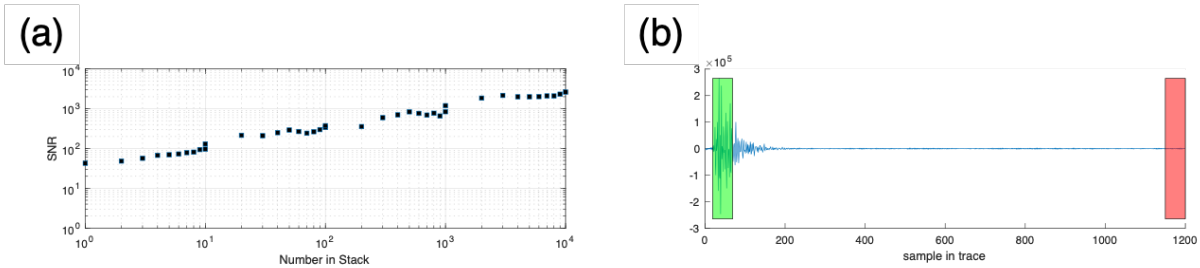

Figure 29. (a) A log-log plot of SNR vs. the number of traces in stack plot. Note that the linear slope indicates the expected sqrt(N) improvement in SNR during vertical stacking. (b) SNR definition where green represents signal and red represents noise.

3.8 Pre-Injection Setup

In preparation for the CO_2 injection experiment, we covered the top of the tank with plastic wrap to help prevent evaporation of water in the upper aquifer layer, tested the CO_2 injection system (explained in the last quarterly report), and set up a monitoring system for observing fluid flow out of the tank. Water loss due to evaporation in the lab has been significant, so much so that we must regularly add water to the upper aquifer system to prevent the bentonite layer from drying out. To slow evaporation during the experiment, we covered the top of the tank with plastic (i.e., unused bubble wrap in the lab, figure 30a).

Before injecting any CO_2 into the tank, we wanted to ensure that the mass flow controller (explained in the last quarterly report) was performing as intended. We executed a small flow test by placing a beaker upside down in a water-filled bucket with the injection hose underneath the beaker (figure 30b). We then set the mass flow controller to inject at 5 ml/min for 20 minutes. We

ended up recovering 100 ml which we deemed sufficient to proceed to our experiment; however, it needs to be noted that more flow tests will be be required for proper calibration of this system.

Lastly, before the injection, we wanted to monitor the fluid exiting the tank (and through the back pressure regulator) during injection. We set up a bucket on top of a scale to measure fluid coming out of the tank and used a timelapse camera to capture the weight of the bucket (figure 30c).

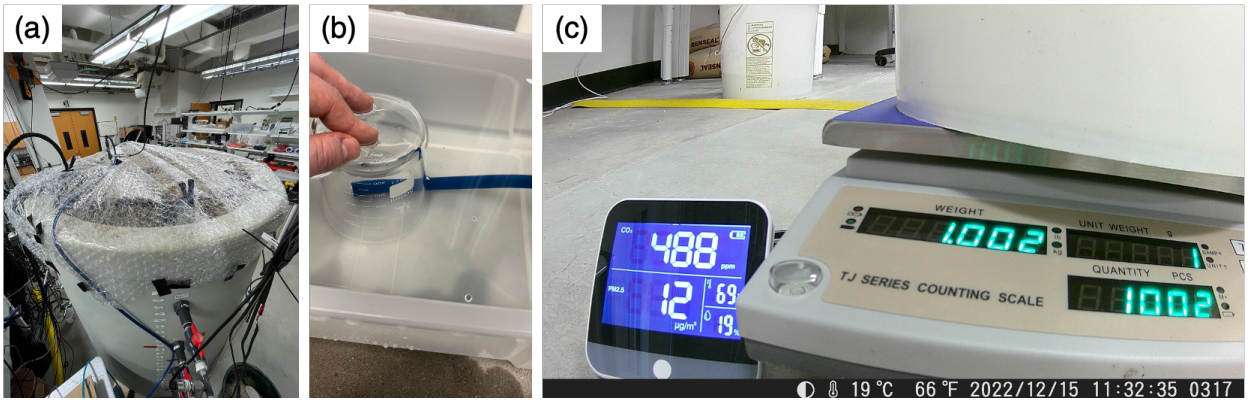

Figure 30. (a) an image of the plastic bubble wrap over the top of the tank to help prevent evaporation, (b) an image of our flow testing experiment, and (c) our outflow monitor system.

4 Experimental Procedures and Analysis

Once all necessary systems were running properly, we began the CO_2 injection experiment. The systems operating were the pressure and temperature sensors at the side-wall ports, back pressure regulator, injection system, and CASSM source/receiver systems. In this section, we go over the detailed experimental procedures for this first experiment.

4.1 Injection Rate Protocol

The injection lasted about 1.5 workdays on December 15th and 16th, 2022 (figure 31). We started injecting on day one at 6:40 am for a total of 10.6 hours, starting at 5 ml/min for ~3 hours, then increased flow rate to 10 ml/min for ~3 hours, and then increased flow rate a second time to 20 ml/min for the last 4.6 hours. Unfortunately, at about 1.6 hours into injection (8:20 am), we noticed a dip in the injection pressure and the mass flow controller monitor. This was related to a valve not being completely open, and the initial injection was from pressures built up in the line. We opened the valve, and the injection proceeded.

We shut in the system overnight by closing all valves to the tank, including the outflow port. With overnight CASSM data analysis (discussed below in section 4) showing unsatisfactory results of a CO_2 plume within the reservoir, we injected at 20ml/min on December 16th for about 2.5 hours before noticing that the injection pressure was decreasing even with a constant injection rate. This suggested a leak; we stopped injecting and shut in the system. In total, we injected about 11.2 liters of CO_2.

Based on the injection pressure data, CO_2 reached the reservoir around 9:15 am, approximately 2.5 hours after injection began. Before this, CO_2 was needed to fill the injection hose and well. At

9:40 am, we increased the injection rate to 10 ml/min. At about 10:30, CO_2 broke through into the outflow port. Therefore, only about 625 ml of CO_2 was injected into the reservoir by the time we had broken through. Unfortunately, our dielectric probes that span the entire mesoscale tank and were designed to give information on water saturation had stopped working before the experiment. The probes were likely crushed from the bentonite swelling and allowed water to enter the electronics.

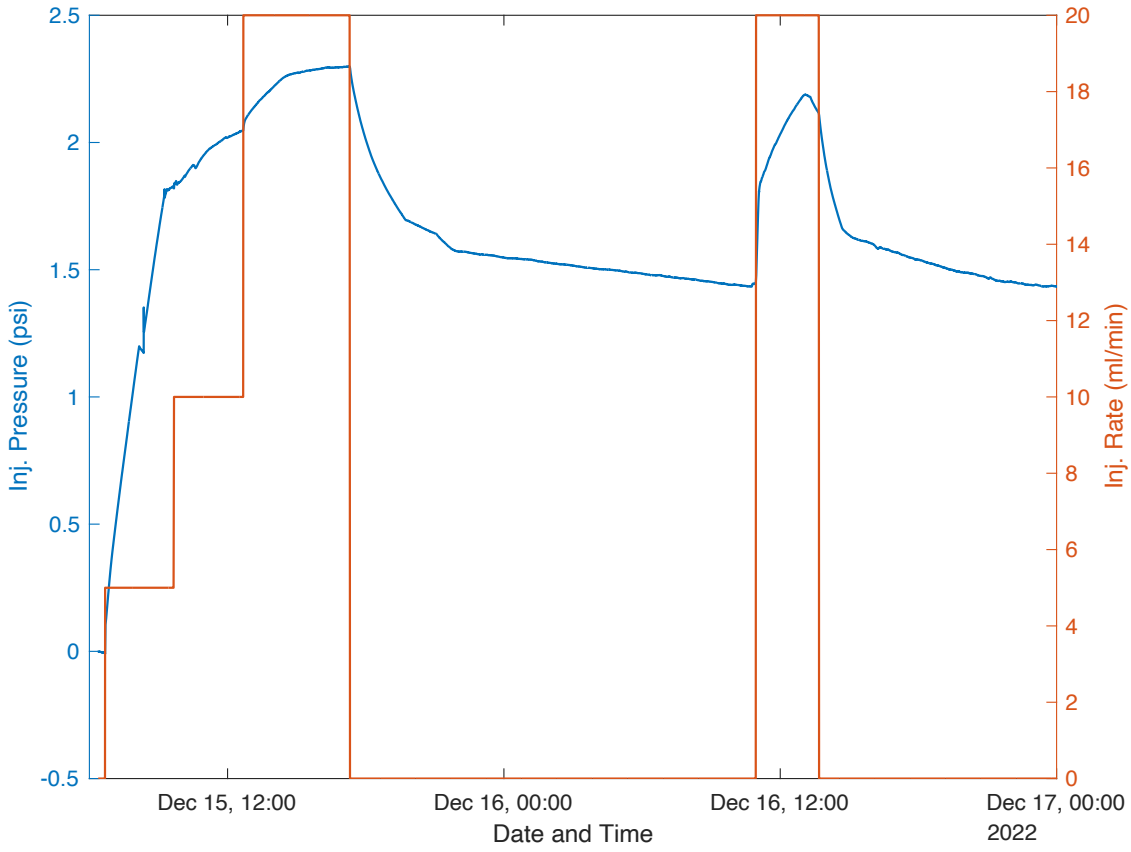

Figure 31. The injection pressure and rate of CO_2 for the injection experiment. Note the low injection pressures since we have a limited hydrostatic column and high permeability matrix.

4.2 Back Pressure Regulator Protocol and Outflow Observations

During the first injection day, the back pressure regulator was connected to the shallowest port within the reservoir and set to 0.55 psi. With this arrangement, we expected a constant water height of ~15 inches above that port. About four hours after the start of the injection, we observed air in that port hose, suggesting CO_2 had traveled up-dip to the port from the injection well. Before injection on the second day, we moved the back pressure regulator to the port just below the previous one to help expand the CO_2 plume.

As mentioned in the previous section, we monitored the weight of the liquid coming out of the outflow-port hose; this way, we could track the rate of fluid coming out of the tank and compare it to the amount we injected in. Unfortunately, only a tiny trickle came out of the hose, which did

not affect the scale enough to provide accurate readings. Two factors likely affected this outflow: (1) High evaporation in the laboratory outpaced the slow outflow trickle. (2) We believe the filter used to prevent sand from collapsing into the ports was clogged, which prevented flow.

4.3 Leakage Detection

After determining that leakage occurred during injection, we tested CO_2 levels with a CO_2 meter at different points around the top of the tank. CO_2 levels rose slightly, 650 ppm (background levels in the lab range between 425 to 500 ppm), near the up-dip section of the layers. It is unknown, however, if the leakage occurred up the closest observation well or the tank's sidewall.

We believe the CO_2 traveled up dip in a thin direct pathway to the outflow port and never generated an extensive plume as we had hoped. This would explain why we observed CO_2 in the outflow port but did not detect a large change in seismic attenuation in the CASSM data (described and shown in section 4). In addition, outflow from the tank was negligible even with constant injection; this caused pressures within the tank to continue to rise. Eventually, leakage occurred through the caprock, likely at an up-dip well or the tank wall.

5 Preliminary Results of CASSM Analysis

5.1 Delay-Time Curves

Since the CASSM method is a time-lapse seismic method, we are primarily interested in the change in travel time between datasets. We computed delay times for all source-receiver pairs during the injection cycle (figure 32). Delay-times were computed by following the steps from Silver et al. (2007). We window around the first arrival of temporal gather (i.e., figure 28), interpolate the data 10,000x the sampling rate, and cross-correlate all traces to the legacy trace to get delay times. The legacy trace is the last full dataset before injection.

Each image represents delay-times for all 18 sources. For each image, the x-axis is calendar time over the course of the two-day injection represented by epoch number, the y-axis is the receiver number, and the colors represent the delay-times in microseconds. Source-receiver pairs with poor SNR have noisy delay-time curves that are highly variable and hard to interpret. Other than those poor SNR source-receiver pairs, all receivers captured the effect of injection pressures which is represented by an increase in delay-time (i.e., a decrease in apparent velocity). We have observed no impact of CO_2 on the delay-times, suggesting that no ray paths intersected the CO_2. This indicates that the CO_2 ‘plume’ was a localized channel that traveled up-dip towards the outflow port.

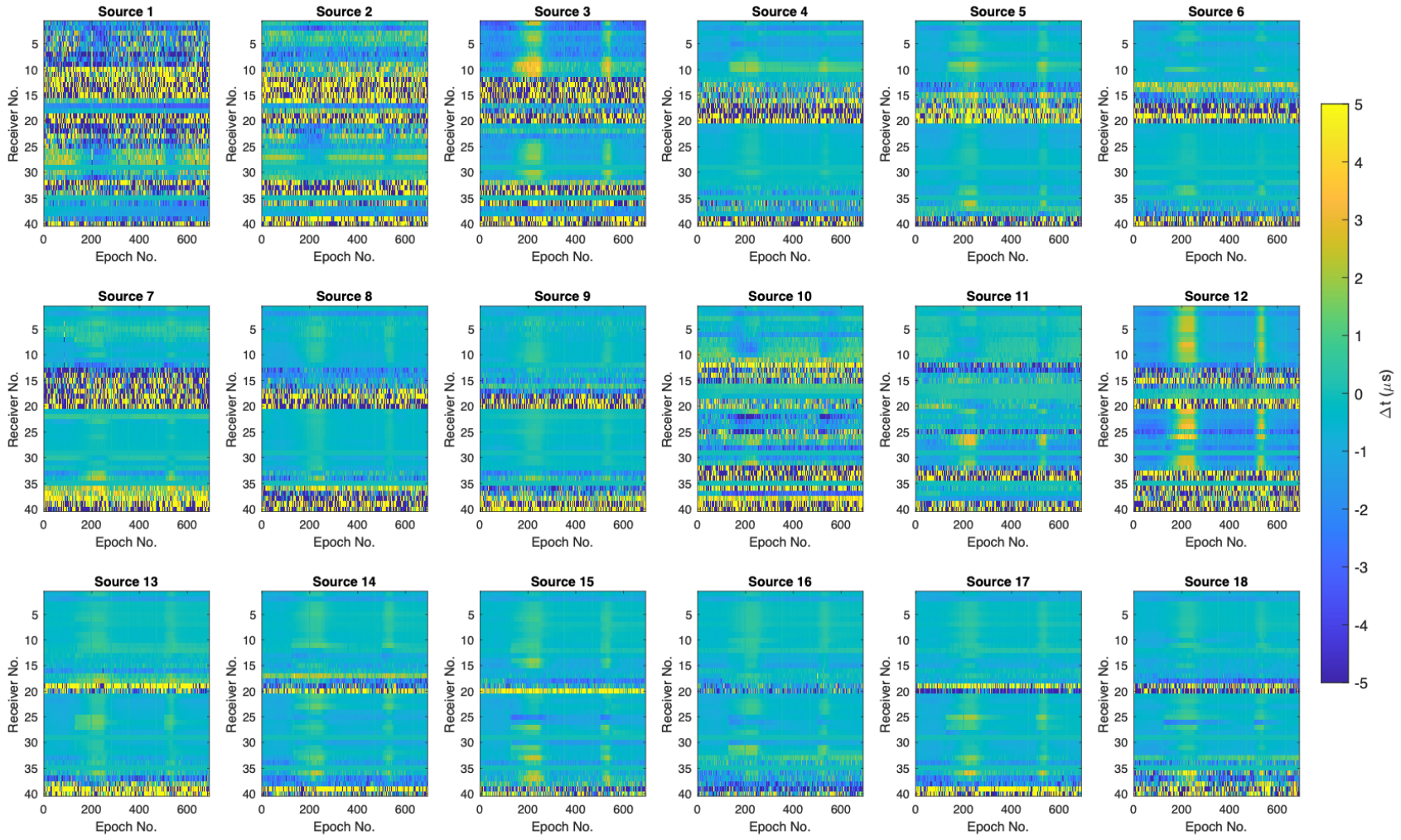
Source 1
Source 2
Source 3
Source 4
Source 5
Source 6
Source 7
Source 8
Source 9
Source 10
Source 11
Source 12
Source 13
Source 14
Source 15
Source 16
Source 17
Source 18
Receiver No.
Epoch No.
Δt (μs)

Figure 32. Delay-time source temporal gathers during the injection experiment.

5.2 Apparent ΔV_P Modeling

From these delay-time curves, we can easily compute the apparent change in apparent seismic velocity. During injection, velocity perturbations were about -10 m/s. We wanted to confirm that these velocity perturbations primarily resulted from increased pore pressure (i.e. decreased effective stress). Therefore, we modeled the effects of varying pore pressure on velocity perturbations at the injection well within the reservoir using a granular contact theory. We use Walton's granular contact theory (Walton, 1987) to model velocity as a function of effective pressure (figure 33). We use the explicitly written equations presented in Mavko et al. (2020) that represent a rough granular pack rather than a smooth one. These equations are a function of the elastic properties of the grains (i.e., bulk and shear modulus), porosity, coordination number, and effective pressure. Effective pressure was calculated by subtracting the measured pressure from sidewall ports from the estimated lithostatic load. We made assumptions on the elastic properties of the grains, porosity, and coordination number of the pack based on the quartz sand and how we packed the sand during the fabrication of the mesoscale reservoir.

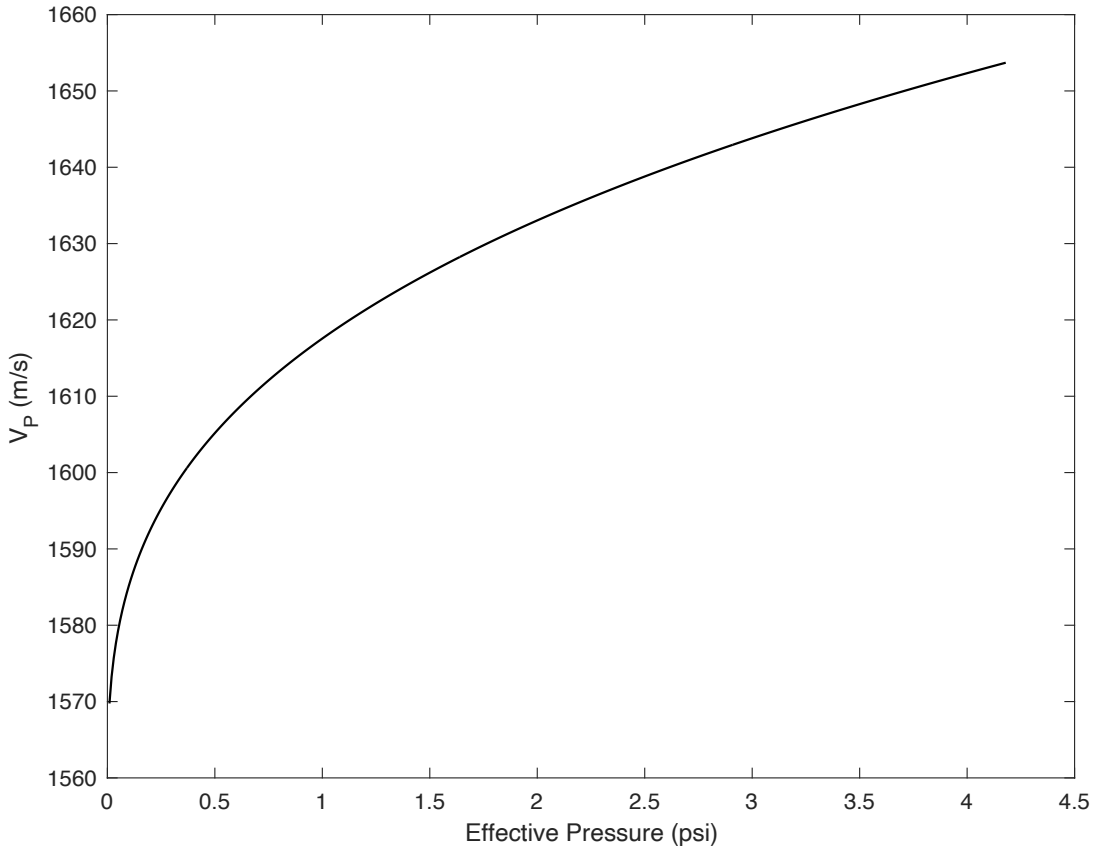

Figure 33. P-wave velocity vs. effective pressure model predicted by the Walton model.

To quickly test the accuracy of this model, we compare it to a subsection of CASSM data. We took the measured pressure at one of the ports within the reservoir (figure 34a), which is ~8 inches

below the caprock, and applied our model (figure 34b). Velocity perturbations were estimated by subtracting the hydrostatic case right before injection. Results show that velocity perturbations during injection were at most -7m/s.

We compare this result to a source-receiver pair around the same depth as the measured pressure, ~8 inches below the caprock. We took the delay-time curve of that source-receiver pair and converted it to an apparent change in velocity (figure 34c). Results are strikingly similar to the model, suggesting CASSM primarily recorded the effects of pressure perturbations rather than a CO_2 plume.

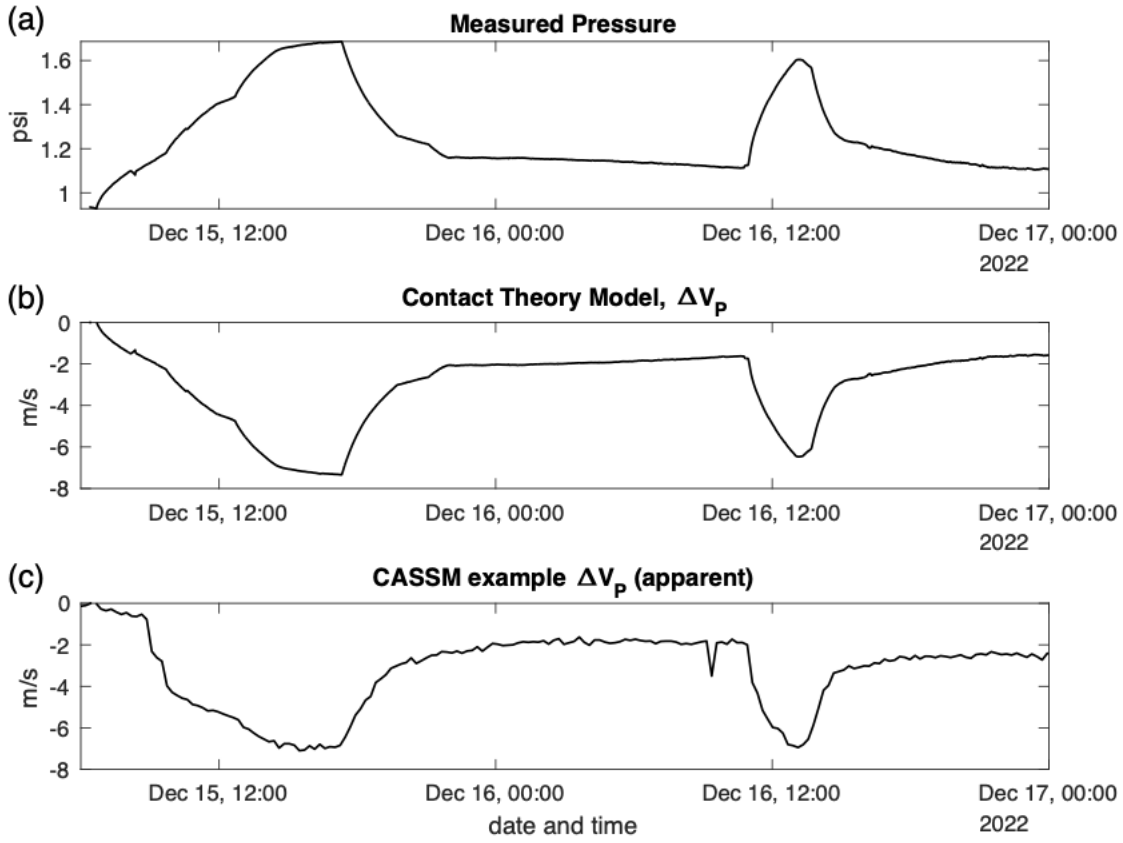

Figure 34. (a) Measured pressure at a sidewall port ~8 inches below caprock, (b) contact theory model of velocity perturbations, and (c) CASSM example of apparent velocity perturbations.

6 Conclusions

In conclusion, we have given details of our first CO_2 injection experiment in the mesoscale CASSM testbed. Many of the components of the experimental system performed well, including pressure and temperature measurements, CASSM acquisition, and the CO_2 injection system. Unfortunately, the outflow system did not work 100% as intended, allowing pressures to build within the tank and generating leakage out of the reservoir through a yet-to-be-determined

pathway. In addition, the CO_2 injected did not form a laterally extensive plume but likely traveled in a thin pathway up-dip that was missed by the CASSM system. We also showed that CASSM could track the effect of pressures on P-wave velocity in a granular medium, a significant result for monitoring stress state perturbations in GCS.

7 References

Mavko, G., Mukerji, T., & Dvorkin, J. (2020). *The rock physics handbook*. Cambridge university press.

Silver, P. G., Daley, T. M., Niu, F., & Majer, E. L. (2007). Active source monitoring of cross-well seismic travel time for stress-induced changes. *Bulletin of the Seismological Society of America*, 97 (1B), 281–293

Walton, K. (1987). The effective elastic moduli of a random packing of spheres. *Journal of the Mechanics and Physics of Solids*, 35 (2), 213–226.

Imaging Fracture Evolution Using Time-Lapse FWI with Continuous Active Source Seismic Monitoring

This chapter describes the application of the correlative double-difference time-lapse full waveform inversion (CDD-TLFWI) workflow to a time-lapse field dataset collected using the multi-level continuous active source seismic monitoring system (ML-CASSM). The development of time-lapse FWI for use with the ML-CASSM system was done in task 3. The CDD-TLFWI workflow was designed to take advantage of the high temporal resolution of CASSM datasets and mitigate the inversion's amplitude dependence. Using this workflow in combination with the CASSM datasets collected at the FE Warren AF Base, we show the spatio-temporal evolution of a fracture network and fluid injection during a shallow hydro-fracturing experiment by modeling reductions in P-wave velocity.

1 Introduction

The main goal of this task was to test the developed TLFWI methodology from task 3 and task 4 on the CASSM field data. Historically, seismic imaging has had limited utility in describing the evolution of fracture networks due to the spatio-temporal limitations of seismic datasets. Often, the spatial resolution of seismic models is hindered by poor receiver density, and temporal details are rarely captured due to the difficulty of repeated acquisitions. The development of the ML-CASSM system addresses these issues and has made it possible to produce seismic datasets with high spatio-temporal resolutions. The semi-permanent installment of ML-CASSM's source and receiver arrays allows for highly repeatable seismic acquisitions. Additionally, these acquisitions are entirely automated by MATLAB scripts, allowing for the collection of full seismic surveys in only 5 minutes, greatly improving upon the temporal resolutions of traditional seismic datasets.

To take advantage of these newly available datasets, an TLFWI workflow designed for time-lapse data is needed. The goal of FWI is to utilize all the information in a seismic recording by iteratively updating model parameters to minimize the difference between observed and synthetic waveforms. The CDD-TLFWI approach relies upon the same principle but is better suited for modeling changes between baseline and monitoring data. Using a baseline model (representing the subsurface before fracture emplacement) as the initial model, and pseudo time-lapse data as the reference (observed) dataset, CDD-TLFWI computes model updates that account for changes between the baseline and time-lapse data. Subtracting the time. lapse models from the baseline then shows changes through time.

In this chapter, we demonstrate the application of CDD-TLFWI to a seismic dataset collected during a shallow hydrofracturing experiment conducted at the FE Warren AF Base and show that the resulting models capture changes in Vp associated with the various stages of the experiment. The sections cover:

- A description of the experiment and data collected at FE Warren AF Base
- The preprocessing of CASSM data
- The methodology of CDD-TLFWI
- Results from FE Warren dataset
- Interpretations of differential Vp models (spatial and temporal)

2 Experiment and Data Description

The CASSM data used in this project was collected during a shallow hydro-fracturing experiment conducted at the FE Warren AF Base, Wyoming. This site hosts a groundwater contamination plume, where a contaminant called trichloroethene (TCE) has leached into the shallow subsurface. To reduce the concentrations of TCE at the site, a remediation amendment called hydrogen release compound (HRC) is introduced to the subsurface to break down TCE into innocuous compounds like water and CO2.

The tight geology at this site makes it challenging to effectively distribute HRC to the subsurface. Composed largely of tightly packed sand and silts, the permeability of the subsurface at the injection site is low. To improve the permeability of the subsurface, hydraulic fracturing is used to create conduits through which the HRC can be distributed. While fracking will certainly improve the distribution of the amendment, determining the true extent of the fracture network is a challenge.

To better characterize the emplaced fracture network, an ML-CASSM system was installed at the injection site. Figure 1 (a) shows a map of the contamination site, complete with markers indicating the location of boreholes where the source and receiver arrays are installed. The ML-CASSM system is composed of 10 piezoelectric sources installed in well 1-M (with vertical spacings of 1.5m), and a total of 72 hydrophones, split between wells 3-M and 5-M (24 hydrophones in 3-M, and 48 hydrophones in 5-M, all with vertical spacings of 0.5m). With this setup, seismic data can be collected along two profiles (profile 1 and profile 2 in Figure 1). The entire acquisition is controlled by a MATLAB script, allowing for rapid data collection (approximately 5 minutes between subsequent surveys). The acquisition began 15 minutes before fracture initiation and continued for 2 hours after the fracture emplacement, yielding a total of 30 surveys. The timing of survey collection, relative to the fracture emplacement and HRC injection can be seen in Figure 1 (b).

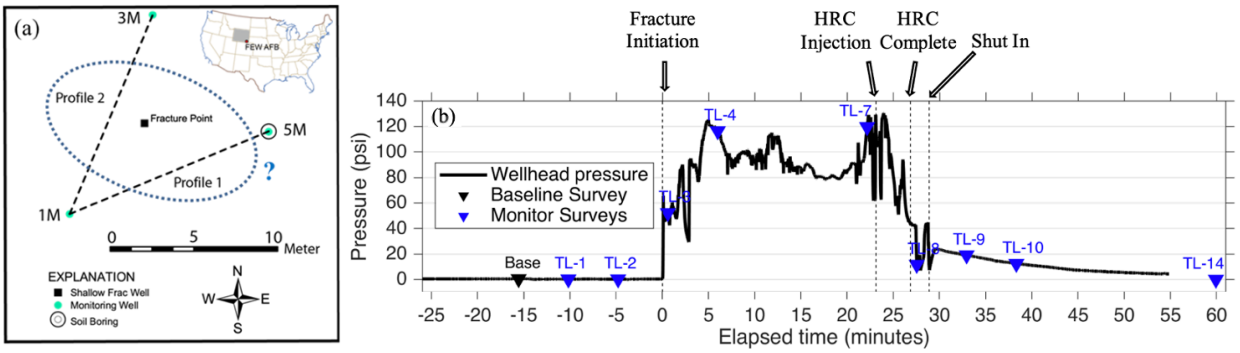

Figure 10) *(a)* Bird's eye view of ML-CASSM system, deployed at the FE Warren AF BASE. Well 1M hosts an array of 10 piezoelectric sparkers, and wells 3M and 5M host two hydrophone arrays (24 and 48 receivers respectively). Additionally, the fracture initiation point is shown as a black square, and a dotted blue line shows a potential radius of impact for the injection. (b) Plot of pressure vs time, annotated to show the stages of the experiment. Triangles show the timing of survey collection. Fracture emplacement begins before time-lapse survey 3, and HRC injection begins shortly after time-lapse survey 7.

Examining the waveforms collected along a single ray path at different time-lapse points shows the impact of fracturing and injection on recorded waveforms. Figure 2 shows a temporal gather collected along profile 2 (source 6, receiver 18). Within this gather we can see three distinct

phases of the experiment. The first three traces (time-lapse-0 through time-lapse-2) have negligible differences, which is expected prior to fracture initiation, but, once the fracture emplacement phase of the experiment begins (at time-lapse-3) we begin to see slightly delayed first arrivals and changes in the shape of the waveforms. The next major change that is observable within the waveforms happens at the beginning of the HRC injection phase (time-lapse-8). We also note that waveform differences are larger in the coda, but for this study we will focus on inverting the first arrivals and primary reflections.

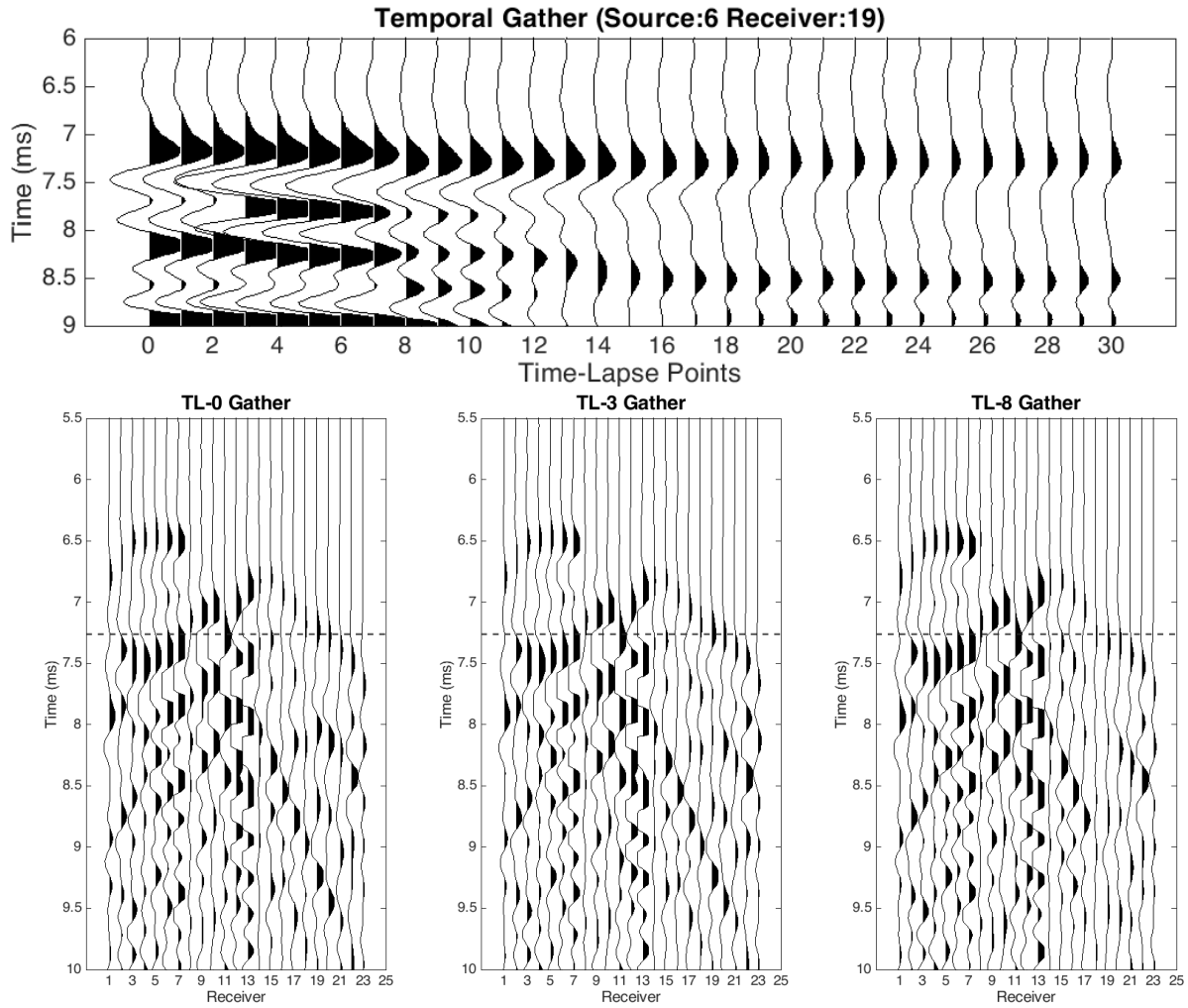

Figure 11) (top) A temporal gather of seismic traces recorded in profile 2 (shot 6, receiver 19), and three shot records (bottom) collected during different phases of the experiment. Time-Lapse 0 represents the baseline survey. Fracture emplacement had begun by time-lapse 3, and HRC injection began just before time-lapse 8. Travel time delays are most apparent in receivers 18-20 during HRC injection. A horizontal line at 7.25 ms can be used as a reference time for comparison between datasets.

3 Preprocessing of Time-lapse Data

The data is first preprocessed to remove noise and large dips (Figure 3). A tapered bandpass filter with a pass band from 400 Hz to 4000 Hz, and cutoff frequencies of 250 Hz and 4500 Hz, is applied to remove low frequency wind noise and any potential high frequency noise. Next an fk-filter is applied to remove large dips from the data (with apparent velocities below 1000 m/s). Even

after filtering, the top 18 traces in the 5M array exhibit low signal to noise ratios and are excluded from the dataset.

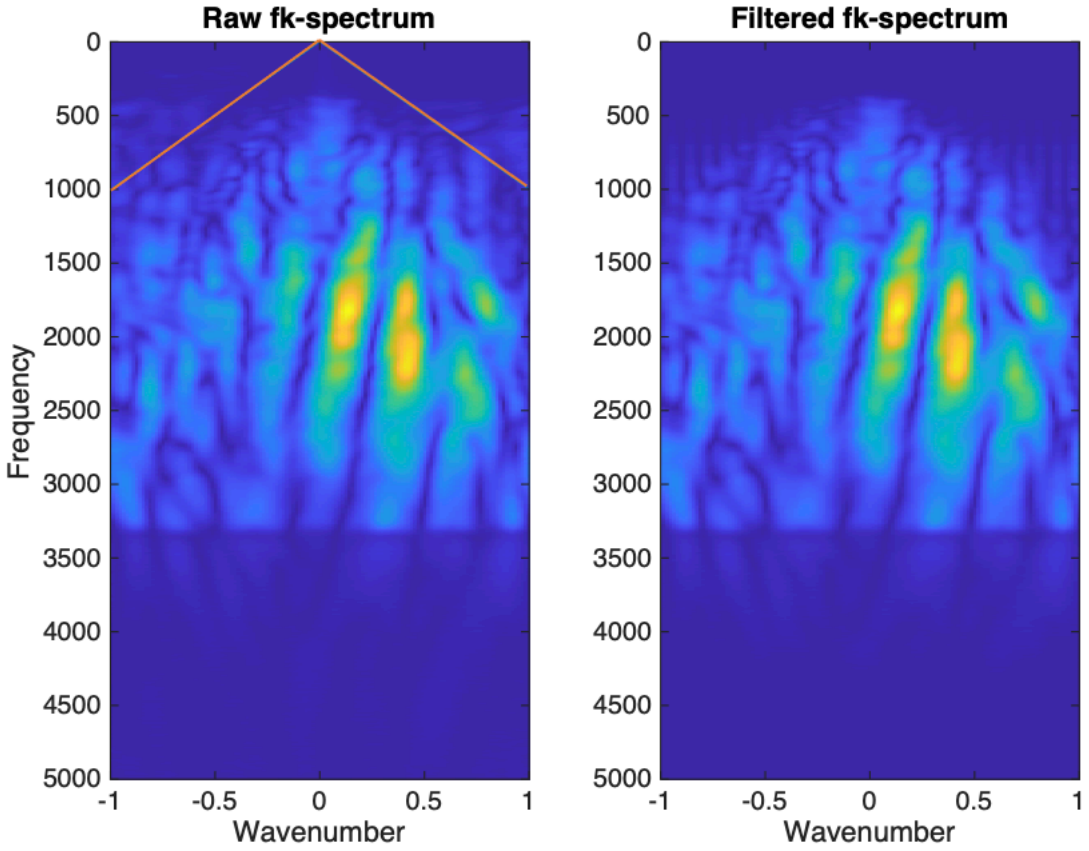

Figure 12) Fk-spectra before and after preprocessing with a bandpass and dip filter. Our bandpass filter uses a passband from 400 Hz to 4000 Hz, and cutoff frequencies of 250 Hz and 4500 Hz. A large contrast can be seen around 3300 Hz, but this is a feature of the raw data and not the result of any processing. A dip filter removes energy with apparent velocities below 1000 m/s (above red lines in panel 1).

Next, the cross-equalization workflow of Rickett and Lumley (2001) is applied to reduce non-physical noise in the time-lapse data. Using the bottom ten traces, where physical changes are not expected, a matched filter is designed to down-weight non-physical noise. We then assume that this noise is present in all of the traces and apply the matched filter to the entire dataset to produce cross-equalized data differences. Figure 4 shows a comparison between direct difference and the results of cross-equalization. In the direct differences, an anomaly can be observed on the bottom 10 traces, around 7 ms, but after cross-equalization, this anomaly is significantly down weighted. Finally, pseudo time-lapse data is created by summing the cross-equalized data differences with a synthetic baseline dataset produced with a baseline model. Figure 5 demonstrates the construction of the pseudo time-lapse data.

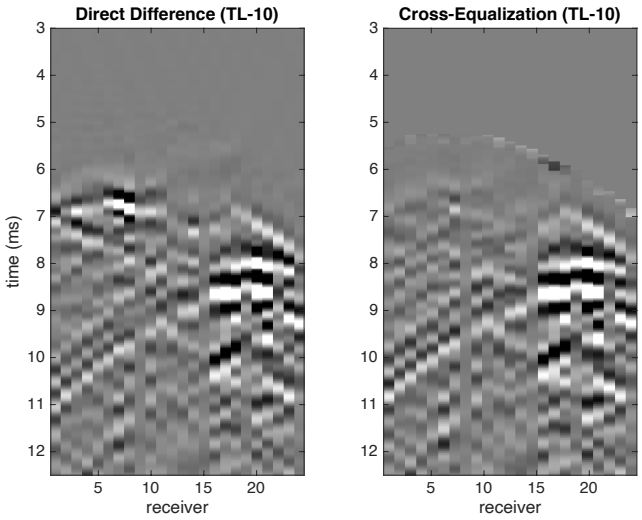

Figure 13) Comparison of direct difference and cross-equalization between baseline and time-lapse-10 dataset (shot 5). Physical changes are not expected in the bottom 10 traces (1-10). Panel 2 shows a reduction in non-physical noise after cross-equalization (around 7 ms on traces 1-10).

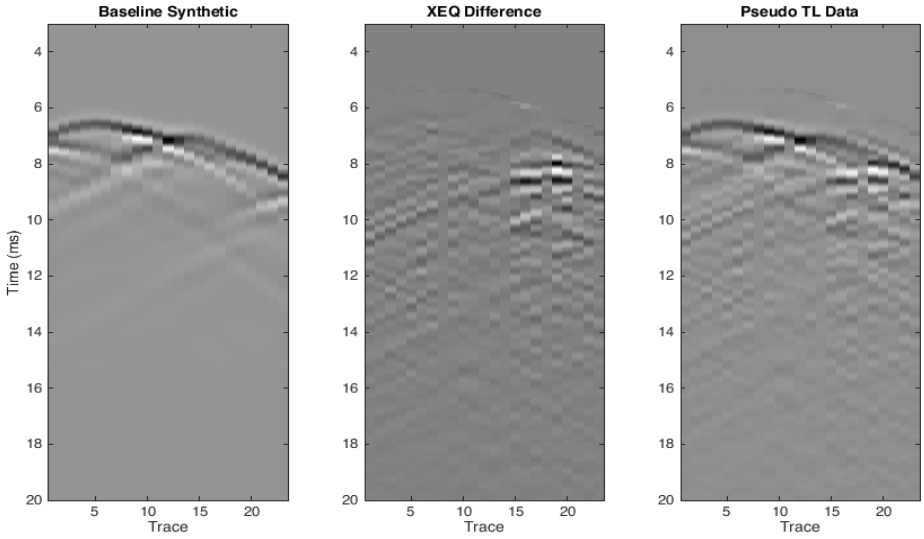

Figure 14) Construction of pseudo time-lapse data. Cross-equalized data differences (center panel) are added to synthetic data (left panel) produced with a baseline FWI model (shown in Figure 7) to create pseudo time-lapse data (right panel).

4 CDD-TLFWI Methodology

Here we describe the methodology of CDD-TLFWI for improving the baseline models (used in the construction of pseudo time-lapse data) and producing time-lapse velocity models. We start with a smooth vertical Vp gradient. Next, we use first arrival time tomography (FATT) to create a first order approximation of the velocity structure in the subsurface. FATT iteratively updates the initial model to fit synthetic first arrival times to arrival times picked within the baseline data.

To improve upon the FATT model, we apply FWI, which attempts to match synthetic waveforms (in our case, computed with the acoustic wave equation) to observed waveforms within a selected time window. The difference between the synthetic and observed data (misfit) is quantified using an objective function. Traditionally, the L2 norm is used as the objective function, but this function relies on direct amplitude differences, which can be problematic in field data where unexpected amplitude losses are observed due to complicating factors (e.g., unknown attenuation parameters or source-receiver coupling). To avoid the issue of amplitude dependence, we use the correlative objective function, which measures the global phase similarity between the synthetic (d_m) and observed datasets (d_{obs}):

$$f(v_p) = \int \int (1 - \frac{\int d_m(x_r, t; x_s) d_{obs}(x_r, t; x_s) dt}{\sqrt{\int d_m^2(x_r, t; x_s) dt} \sqrt{\int d_{obs}^2(x_r, t; x_s) dt}}) dx_r dx_s$$

Where t, x_r, and x_s represent time, receiver coordinates, and source coordinates respectively.

FWI then iteratively updates the starting model using the gradient of the misfit function. We hope to find the global minimum of this function, which should be the best representation of the true subsurface, but, due to the non-uniqueness of the problem, it is also possible for the model to converge towards a local minimum of the misfit function. To improve the likelihood of converging towards the global minimum of the misfit function, the baseline FWI model is calculated with multiple frequency scales. Using the final FATT model as our initial model, we run FWI with a low frequency band (250-400-500-1000 Hz), which is more likely to converge near the global minimum of the misfit function. The final model predicted at this frequency scale is then used as the initial model for the next round of inversion, which includes higher frequencies (250-400-1500-2000 Hz). Including these higher frequencies allows for more details to be resolved in the models and improves the accuracy of the waveform matches. Further improvements to the model's resolution and waveform matches are achieved by inverting with a final frequency band of (250-400-2500-3000 Hz). The final baseline FWI model is now used to produce the synthetic data used in the construction of the pseudo time-lapse data (as described in the preprocessing section).

Now, time-lapse models can be produced by applying CDD-TLFWI to the pseudo time. lapse data, using the baseline FWI model as the initial model for inversion. The misfit in the pre-injection data is very low, as the difference between the baseline data and pre-injection monitoring data is small, but for later surveys the initial misfit is larger due to data-differences resulting from physical changes in the subsurface. As FWI updates the baseline model and reduces the misfit, the models are effectively changing to account for only the differences between the baseline and monitoring data. Once the misfit has been minimized by the inversion process, the time-lapse models can be subtracted from the baseline models to show the location and magnitude of Vp changes.

5 Results

Starting with an initial vertical gradient Vp model, we apply FATT to match the arrival times picked in the baseline datasets of both profiles. After 10 iterations of model updates, the FATT predicted arrivals match closely with the true first arrivals of both profiles (Figure 6).

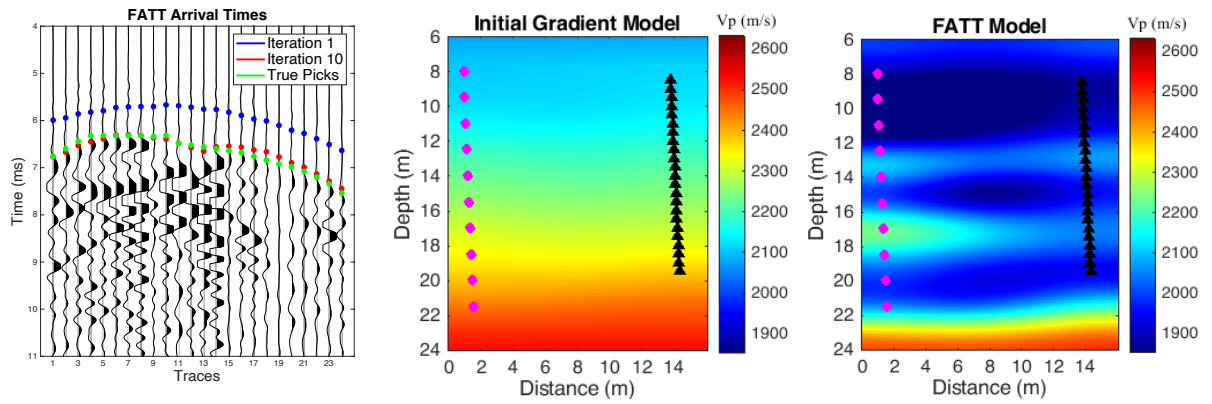

Figure 15) Waveforms from baseline survey (shot 5) with true (green) and predicted first arrivals (left). Blue dots represent arrival times predicted by the initial gradient (center), and red dots represent arrival times predicted by the 10th iteration of FATT (model shown on right).

The baseline FWI models for each profile are then created using the multi-frequency strategy discussed above. The final models as well as the waveform matches for the three rounds of baseline FWI (profile 2) are presented in Figure 7, where we observe improved waveform matches and increased model resolution as we include higher frequencies. The final baseline FWI model is then used for the construction of pseudo time-lapse data.

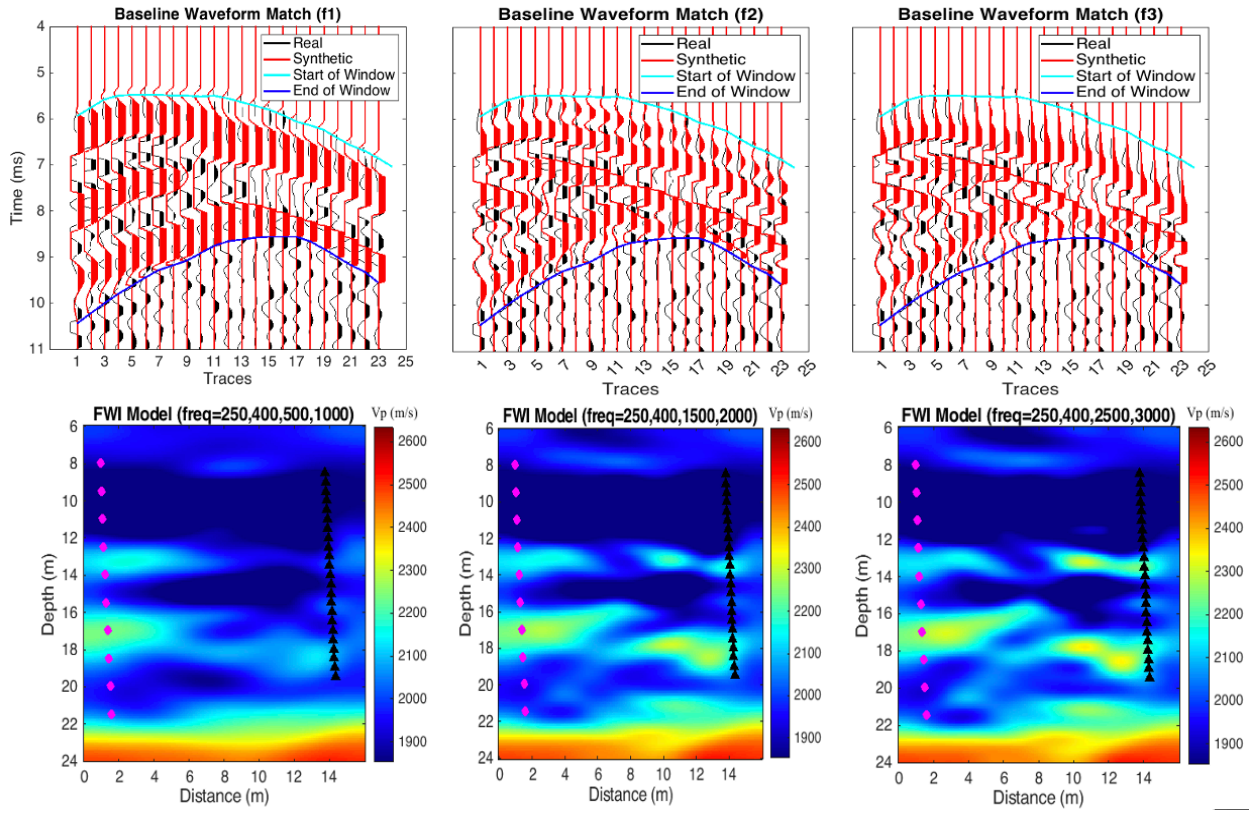

Figure 16) Waveform comparisons (top) and models (bottom) for baseline FWI conducted with increasing maximum frequencies (1000 Hz, 2000 Hz, and 3000 Hz from left to right). Each round of FWI includes 15 iterations. The lowest frequency band uses the FATT model as the starting model. Each subsequent frequency band uses the final iteration of the previous frequency band as the starting model.

We then produce time-lapse FWI models by applying CDD-TLFWI to the pseudo time-lapse data. Figure 8 demonstrates the improved waveform agreement of CDD-TLFWI in when compared to non-time-lapse FWI (Figure 7). In total, 30 differential Vp models are produced by subtracting the time-lapse models from the baseline FWI model (3 models from different stages of the experiment are shown in Figure 8).

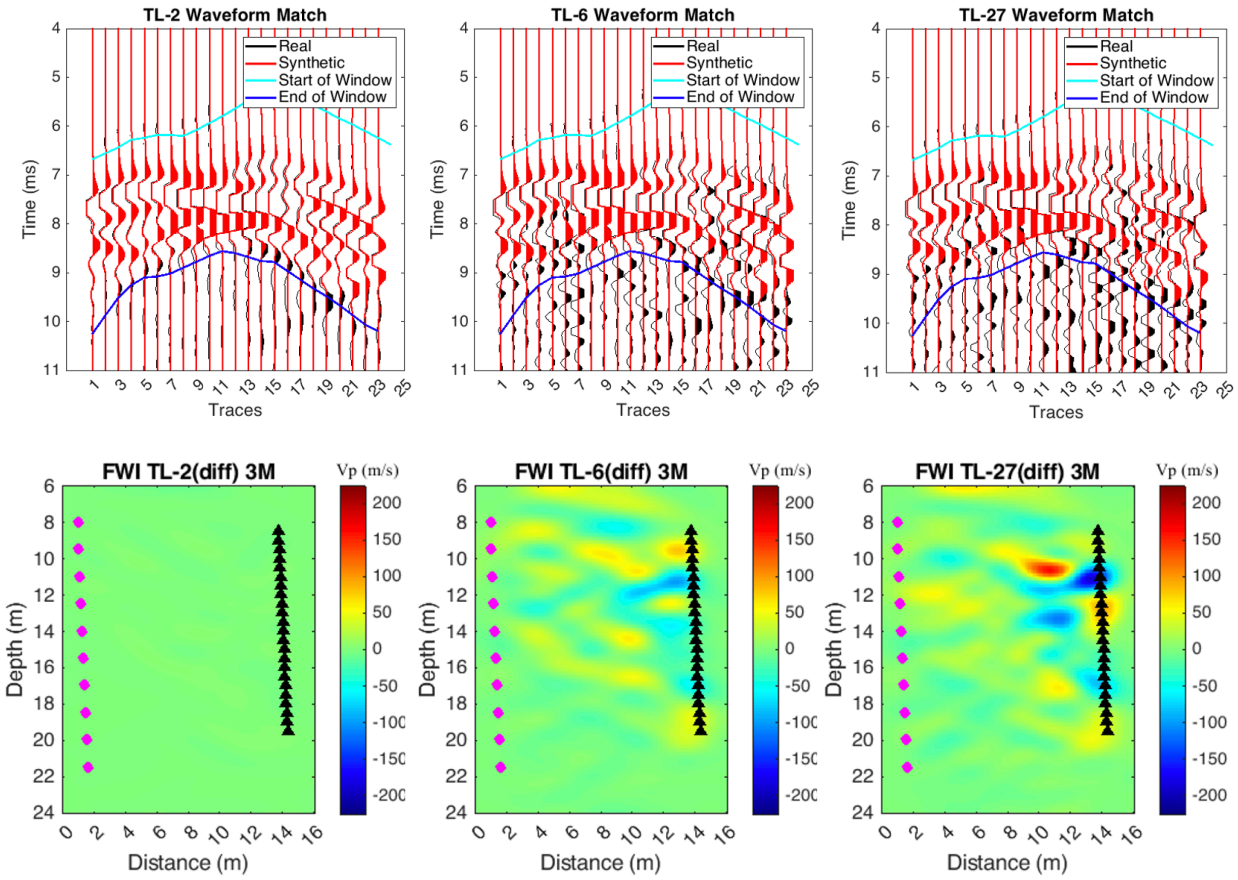

Figure 17) Waveform matches (top) and differential Vp models (bottom) for pre-fracturing (left), post-fracturing (middle), and post-injection (right).

6 Interpretations

Plotting our resulting differential Vp models from profiles 1 and 2 in a shared space, we are able to observe both the spatial and temporal evolution of the subsurface throughout the experiment.

6.1 Temporal interpretation

Three basic regimes can be seen within the differential models which reflect different stages of the experiment (pre-fracturing, fracture emplacement, and HRC injection). Figure 8 presents three time-lapse models from profile 2. Prior to fracture emplacement only negligible velocity changes are observed, but, after fracture emplacement velocity reductions on the order of 40 – 70 m/s can be observed. These reductions are consistent with velocity reductions predicted

by changing pore pressure. Larger velocity reductions (around 120 m/s) can be seen in the differential Vp models after HRC injection. These reductions are the result of changing pore fluid content, where CO2, released by the interaction of HRC with TCE, displaces water. Velocity reductions in the HRC injection phase appear to change over time but reach their final state by TL-14.

6.2 Spatial Interpretation

Several spatial features can be interpreted from our differential Vp profiles, including the spatial evolution of the fracture network, the dip of the main fracture, the radius of impact during HRC injection, and linkages with both previously emplaced fractures and natural fractures.

Figure 9 shows the evolution of the fracture network during fracture emplacement, where Vp reductions on the order of 40-70 m/s near the fracture initiation depth of 11.6 m can be observed in profile 2 (Time-lapse-4) before profile 1 (Time-lapse-5). Additionally, within profile 1, the region of velocity reduction can be observed extending laterally from time-lapse-5 to time-lapse-6.

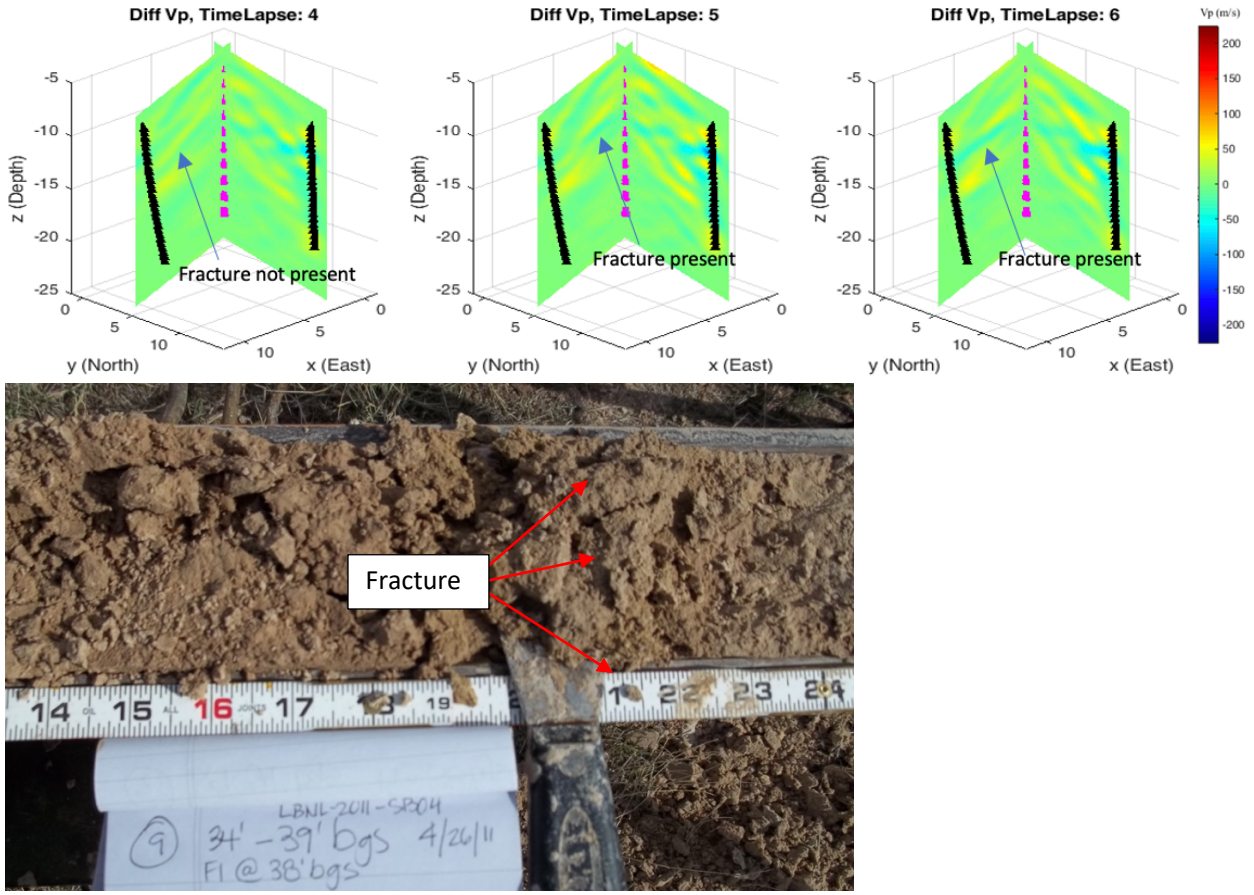

Figure 18) *(Top)* Profiles 1 (left) and 2 (right) plotted in a shared 3D space for 3 subsequent surveys during fracture emplacement. Vp reductions on the order of 40-70 m/s (blue) show regions of high pore pressure in the vicinity of the emplaced fracture. The presence of the fracture can be detected in profile 2 by time-lapse 4, in profile 2 the fracture is not detected until time-lapse 5. *(Bottom) Confirmation drilling core section, collected near 3M well, showing the presence of a fracture at a depth of 38 feet (11.58 m).*

During the HRC injection phase, the main regions of Vp reduction fall within a depth range of 10 m to 11.6 m. Examining both profiles shows that the main regions of velocity reduction in profile 2 are slightly deeper than those in profile 1, indicating that the emplaced fracture propagated at a slightly sub-horizontal northward dip. Additionally, the velocity reductions observed during the HRC injection phase are larger in profile 1. One potential explanation for this observation is that the CO2, once released by the HRC, migrates up-dip along the fracture due to buoyancy, concentrating in profile 1. Another potential explanation could be that profile 1 samples a more developed region of the fracture network. This claim is bolstered when we consider the greater lateral extent of the Vp reduction zone along profile 1.

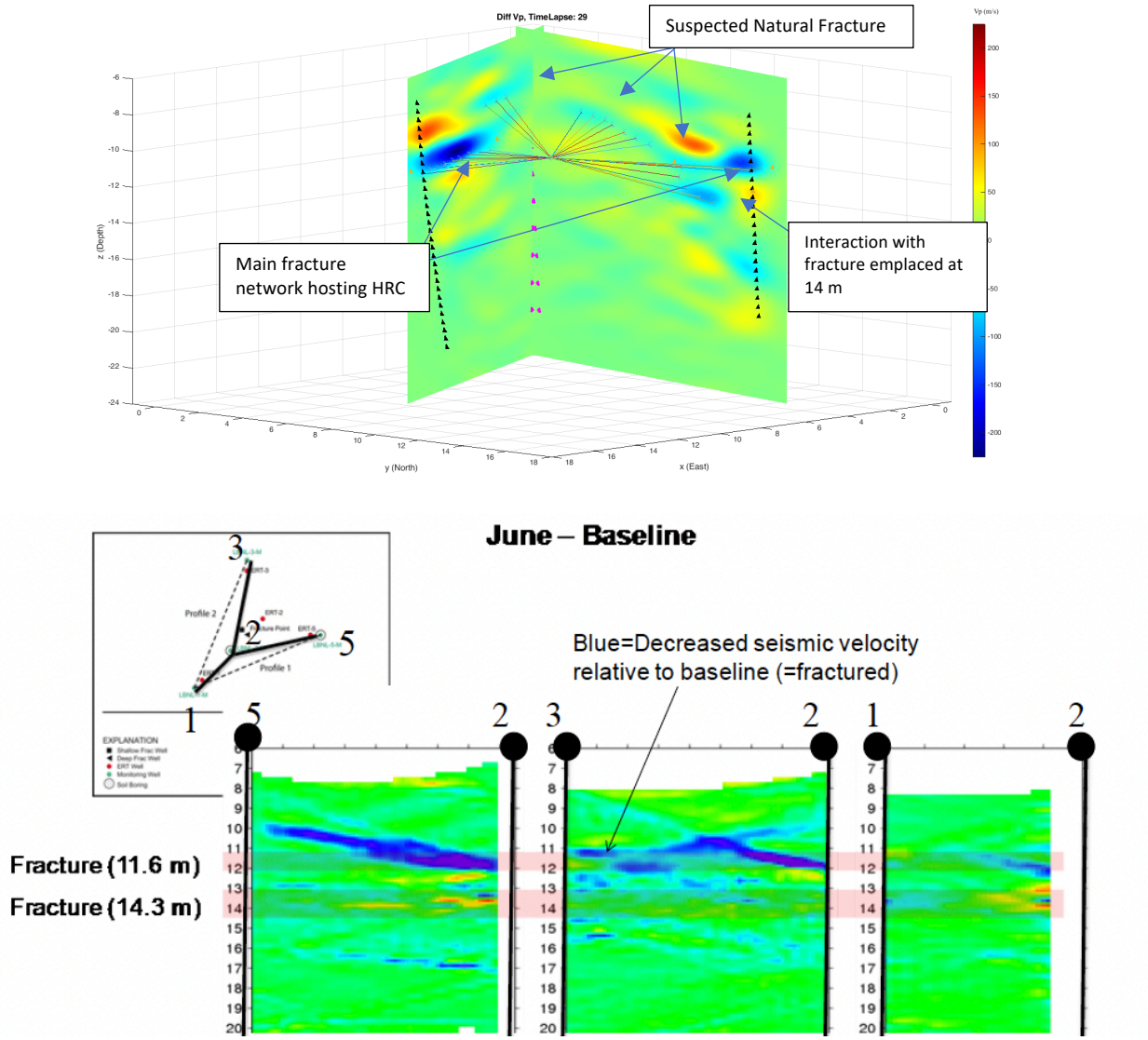

Figure 19) *(Top)* Differential Vp models for profiles 1 (left) and 2 (right) at time-lapse-29 plotted together in 3D. Black triangles represent the locations of receivers while pink dots represent the source locations. Lines connecting areas of Vp reduction converge at the fracture initiation point. *(Bottom) Differential Vp models made with standard tomographic approach (for comparison). Data used in these models were collected 1 week after fracture emplacement along three transects (map).*

Plotting both profiles together in a shared 3D space helps reveal the total extent of the HRC injection. In Figure 11, four points (triangles) were picked at the boundaries of the regions of Vp reduction (two in each profile) and used to fit an ellipse that represents the injection's region of impact. A fifth point (the location of a confirmation well where the fracture was observed) is included in the ellipse fitting process. This ellipse reveals a general north-south preference for fracture propagation. Additionally, the ellipse appears to be somewhat offset to the east from the injection point. Further study on the stresses and the initial porosities present in the site's geology could help to explain this phenomenon.

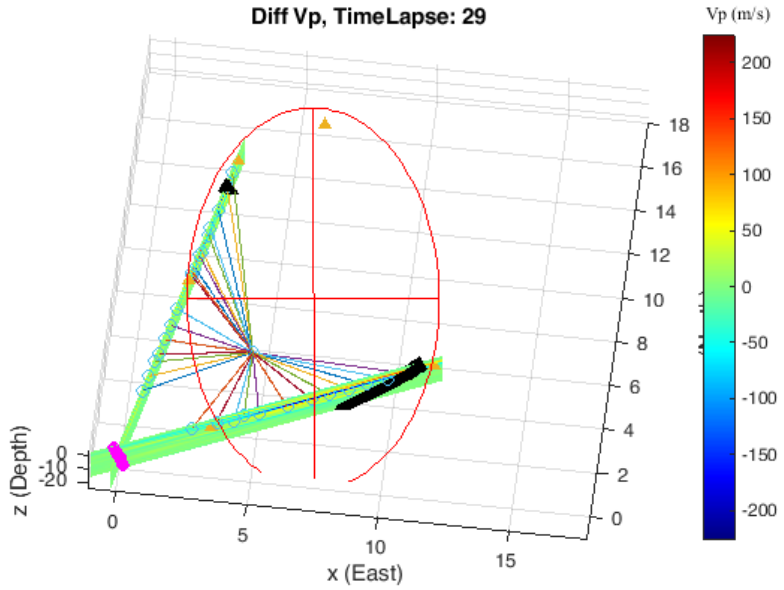

Figure 20) Birds-eye view of profiles 1 (bottom) and 2 (top/left). A red ellipse is fitted to triangles that represent the edge of the region of HRC distribution. A fifth triangle (not on either profile) shows the location of a confirmation well where the fracture is observed (Shown in Figure 9, bottom).

Other spatial features, aside from the main region of Vp reduction, can be observed within the models. In profile 2, a region of Vp reduction on the order of 100-120 m/s can be observed at a depth of about 13.5 m (Figure 10). This finding can be explained by the interaction of the primary emplaced fracture network with a previously emplaced fracture network (initiated at a depth of 14 m). Due to technical issues during the emplacement of this fracture, the footprint of the fracture network is much smaller than the fracture network emplaced during data collection. Judging by the magnitude of the velocity reductions here, it seems likely that the HRC was distributed to greater depths through interaction with this deeper fracture.

There are also coherent regions with smaller Vp reductions observable in both profiles. These features are likely caused by interaction with natural background fractures. Due to the magnitude of the velocity reductions, it seems likely that the HRC itself was not directly present in these fractures, but it is possible that CO2 could have moved through these fractures. Additionally, excitation of these natural fractures during the emplacement stage would have weakened the rock, leading to small velocity reductions. Fluid transport models could shed light on the nature of these velocity reductions (as well as the difference in Vp reductions seen between profiles 1 and 2 in the main region of HRC distribution).

7 Conclusion

In summary, we have developed and employed a time-lapse FWI workflow designed to make use of data collected by the ML-CASSM system. Applying this workflow to the dataset collected along two profiles at the FE Warren AF Base, we resolve changes in Vp that are associated with fracturing and fluid injection. Interpreting these models has improved our spatio-temporal understanding of the emplaced fracture network and remediation amendment distribution. The tests here demonstrated the effectiveness of the developed time-lapse FWI method using field CASSM datasets.

Future directions: Time-Lapse Seismic Inversion for CO2 Saturation with SeisCO2Net: An Application to Frio-II Site

Deep learning (DL) has seen burgeoning applications in solving highly nonlinear inverse problems pertaining to seismic inversion. In recent years, there have been several studies utilizing deep learning for petrophysical and seismic inversion to estimate CO_2 related properties. CNNs and other DL algorithms such as long short-term memory (LSTM) have been adapted to predict CO_2 leakages from seismic and petrophysics data. For example, Sinha et al. (2020) compares performances of multilayer perceptron, CNNs, and LSTMs to estimate future pressure values from past pressure and injection properties to detect leakage during CO_2 injection. Zhou et al. (2019) used densely connected CNNs to invert leakage mass values from time-lapse seismic gathers. On mapping CO_2 saturation to petrophysical properties, Wen et al. (2021) adapted CNNs to predict CO_2 saturation maps from permeability maps and injection depth and duration fields. As for predicting CO_2 saturation from seismic properties, Zhong et al. (2020) used a cycle-consistent generative adversarial network (CycleGAN) to predict CO_2 saturation from changes in acoustic impedance. Li et al. (2021) used CNNs to predict P-wave velocity changes (ΔV_p) maps from time-lapse seismic shot gathers. For predicting CO_2 saturation from seismic data in a broader context, Liu and Grana (2020) combined ensemble smoother methods with deep autoencoders to map time-lapse post stack seismic gathers to permeability and porosity maps. Wang et al. (2020) used support vector machines and basic LSTM network to estimate CO_2 saturation level classes from seismic attributes (e.g., time delay, phase rotation) derived from gathers, downhole pressure, and total dissolved solids measurements. Li and Li (2021) used 3D CNNs to estimate probabilities of CO_2 distribution from seismic migrated images from Sleipner site. Liu et al. (2023) used physics-informed neural networks to estimate CO_2 saturation and porosity from seismic stacked sections.

To our knowledge, direct prediction of CO_2 saturation from seismic shot gathers using CNNs has been largely understudied, particularly with field seismic data. In CCS field collected seismic data, the primary challenge is the lack of field data for training. Other issues include bad data quality (e.g., non-repeatability noise), large data preprocessing challenges (e.g., time-consuming for large datasets), and increased nonlinearity caused by bad data quality, as well as limited availability of benchmark models for result comparison. In DL studies pertaining to CO_2 inversion, the synthetic input and output datasets are scalable, meaning that the dimensions can be scaled up/down or set to be the same for ease of training. Previous work by Leong et al. (2022) and Um et al. (2022) showed that straight-forward CNNs (e.g., UNet by Ronnenberger et al., 2015) can be used for CO_2 saturation inversion from synthetic seismic gathers as long as both the input and output datasets are in the same dimension (data(x,t), saturation(x,z); they are in different domain but the same dimension). However, in practice, field seismic data and benchmark/target CO_2 saturation models may be in different dimension sizes. While adjusting dimensions to achieve same shapes (e.g., downsampling, resampling, cropping) may be feasible, it can result in information loss. For example, downsampling CO_2 saturation models to larger spatial sampling might hinder precise identification of CO_2 plume growth. Moreover, accurate evaluation of DL predictions necessitates comparison with existing benchmark models, requiring similar dimensions for both DL predictions and benchmark models to attain accurate assessments.

Partially supported by this project, we develop SeisCO2Net, an innovative approach for predicting CO_2 saturation maps directly from time-lapse full waveform shot gathers. We showcase its effectiveness by applying it to the intricate Frio-II field data, overcoming the considerable

challenges associated with implementing CNNs in field applications. This first-ever CNN field application highlights the significance of our contribution while addressing the limitations faced in previous research. The overarching idea is to simulate synthetic seismic gathers and CO_2 saturation dataset that closely mimic the field settings. Following that, we train the field-informed synthetic datasets using CNNs and ultimately apply onto field data. By coupling the nonlinear inverse solving capabilities of CNNs with field-informed synthetics, we are essentially bridging the gap between field and synthetic data. This mitigates convergence issues and improves accuracy during inference. This method effectively addresses the scarcity of field training data, indicating the feasibility of long-term CCS seismic monitoring.

1 SeisCO2Net: Seismic gathers to CO_2 saturation neural network

The architecture of SeisCO2Net (Figure 1) is a combination of an autoencoder (SeisCO2Net-AE) and a deep CNN (SeisCO2Net-Main) which takes in time-lapse shot gathers and outputs CO_2 saturation maps directly. The idea behind SeisCO2Net is as follows: first, we train SeisCO2Net-AE which compresses the CO_2 saturation maps into latent representational features (encoded S_{CO2}); second, we train SeisCO2Net-Main that accepts channel-stacked shot gathers and outputs equally stacked encoded S_{CO2} maps; third, only at prediction, we use the trained Decoder part of SeisCO2Net-AE to decode the encoded S_{CO2} maps to reconstruct them to its previous dimension for evaluation purposes.

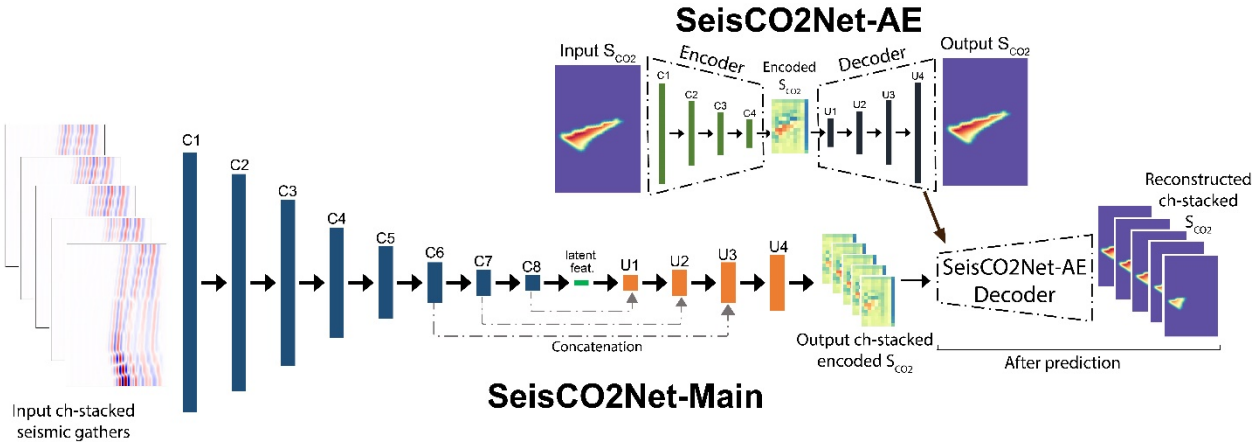

Figure 1: Full architecture of SeisCO2Net. SeisCO2Net-AE is an autoencoder that compresses CO_2 saturation (S_{CO2}) maps into encoded S_{CO2} maps. SeisCO2Net-Main is a deep CNN with skip layers (concatenation) that inputs channel-stacked shot gathers and outputs encoded S_{CO2} maps. After prediction, we use SeisCO2Net-AE Decoder to reconstruct encoded S_{CO2} maps (dimension of 15×10) to the original dimension (dimension of 300×200).

2 SeisCO2Net: training workflow

CNNs randomly initialize their weights and biases according to a predefined statistical distribution, with kernels at every Conv2d layer sampling input data accordingly. In our case, we use the default setting which is Xavier distribution (Glorot and Bengio, 2010). This means we can estimate the neural network's statistical uncertainties by running numerous iterations of training.

From the variation of weights, we can compute the mean prediction as the desired final prediction, and standard deviations as prediction uncertainties.

SeisCO2Net training procedure can be summarized as follows:

1) Train SeisCO2Net-AE to produce encoded S_{CO2} maps,
2) Train SeisCO2Net-Main where input is time-lapse shot gathers and output is encoded S_{CO2} maps,
3) Repeat 20 times to obtain 20 variations of trained weights.
4) Compute average of 20 predictions as final prediction and standard deviations from 20 predictions as uncertainties.

3 SeisCO2Net implementation workflow overview

We introduce a mind map (Figure 2) that aptly summarizes the overall SeisCO2Net implementation workflow. As with every CO_2 storage site, it starts with a geological model which we denote as background geology model. Using the background geology model, we can obtain prior knowledge about the CO_2 storage site such as reservoir petrophysical properties (e.g., permeability and porosity ranges) and seismic survey information (e.g., source-receiver geometry). This prior knowledge can be utilized to generate realistic synthetic datasets, such as CO_2 saturation maps from fluid flow modeling, P-wave velocity from rock physics modeling, and shot gathers from seismic forward modeling. In addition, generating numerous datasets for training essentially benefits the training of a neural network. All that is left is to use SeisCO2Net to map the relationship between seismic data and CO_2 saturation maps. Incorporating field (geo)physics information in SeisCO2Net (details discussed in next section) can promote better neural network generalization, and hence yielding accurate predictions on Frio-II field data. Additionally, the ability of neural networks to solve inverse problems at great efficiency during inference makes DL-guided methods desirable for long-term seismic monitoring projects.

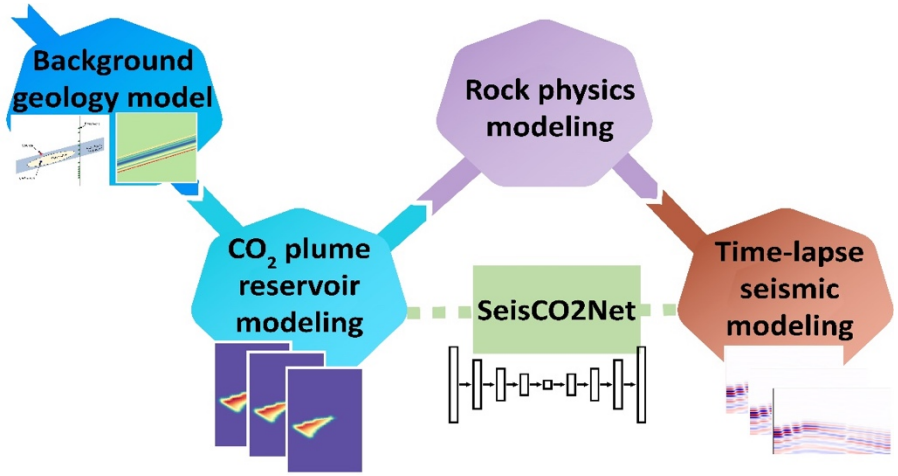

Figure 2: A mind map summarizing the generation of CO_2 saturation maps and seismic shot gathers that pertains to a certain geological site. To create realistic synthetics, we use prior knowledge about the reservoir (e.g., petrophysical property ranges, source-receive geometry) to simulate CO_2 saturation maps, velocity models, and seismic shot gathers. SeisCO2Net maps the relationship between CO_2 saturation maps and shot gathers.

4 Synthetic seismic gather and CO_2 saturation maps generation

We generate 40 reservoir realizations (permeability-porosity maps) based on 40 different variogram azimuths. Figure 3 shows four examples of these realizations. Each of these four reservoir realizations are based on different variogram azimuths. For example, note how the orientation of permeability "clumps" with similar values are different across the four realizations. This encourages injected CO_2 to permeate through the reservoir differently for different realizations. As such, by generating numerous realizations with different variogram azimuths, we are increasing the diversity of dataset.

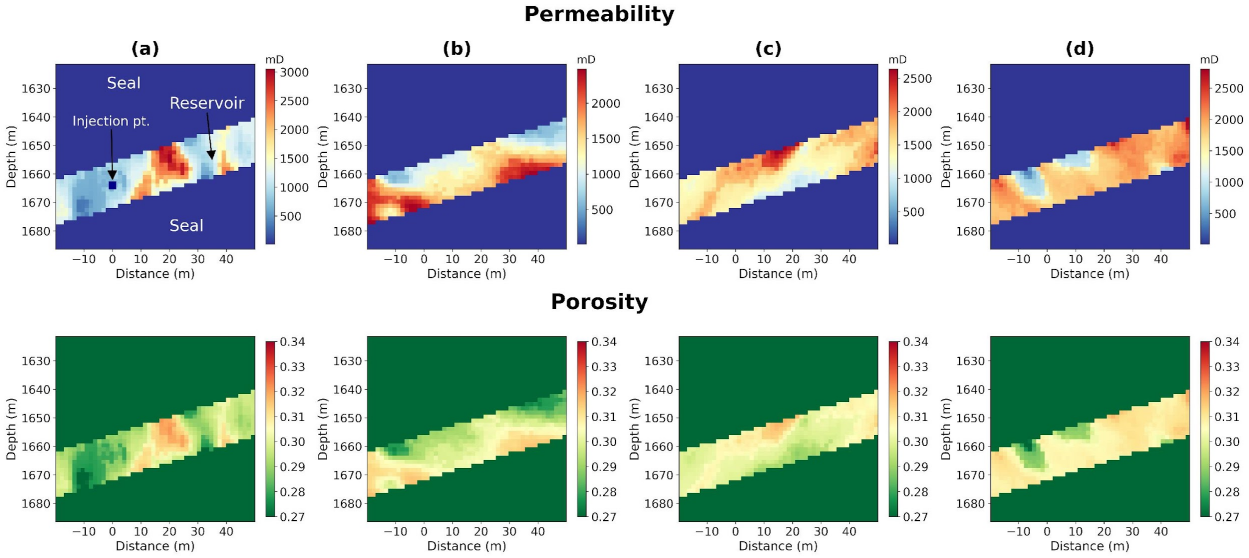

Figure 3: Top row has four examples of permeability realizations; bottom row shows corresponding porosity realizations. Permeability maps are generated using SGSIM. Each of the reservoir realization has different variogram azimuths. We generate a total of 40 reservoir realizations.

5 SeisCO2Net: Applications to Frio-II field shot gathers

The availability of field shot gather data is limited to 47.5 hours post injection. We exclude time-lapse data after 39-hours post-injection, as these time-lapse gathers do not exhibit significant plume growth.

After applying the 20 trained weights to the preprocessed field gathers, we pad the predictions with zeros to reconstruct them back to the original dimension of 467× 434, which allows us to compare our results with the CO_2 saturation maps predicted by the TOUGH2 model from Daley et al. (2011). The TOUGH2 models are computed by careful manipulation of fluid flow, rock physics, and geophysical simulation modeling parameters to generate synthetic traveltimes to match that of the field data. We show the comparison of SeisCO2Net predictions (Figures 4a – 4c) and TOUGH2 models (Figures 4d – 4f) as well as the prediction uncertainties (Figures 4g – 4i) from the 20 trained weights. Visual examination of SeisCO2Net inverted CO_2 saturation maps indicates that the CNN performs favorably in comparison to the physics-based TOUGH2 models, particularly in terms of CO_2 plume shape predictions. While SeisCO2Net's predicted CO_2 saturations show slightly lower values, they generally fall within the range predicted by TOUGH2. It is important to recognize that TOUGH2 predictions are also approximations and cannot be considered the absolute ground truth, as there is no single, completely accurate

observation. In general, when only comparing CO_2 saturation maps predictions, SeisCO2Net's inversion show similarities in terms of plume shape, CO_2 saturation values, and plume extent when compared to the physics-based TOUGH2 model.

The map of predicted uncertainties show that errors tend to be higher at the middle of the plume. This is reasonable because CO_2 saturations are typically highest at plume's center due to its proximity with the injection point. Moreover, we note that the uncertainty maps indicate slightly larger plume shapes (e.g., Figure 4h) than the predictions (e.g., Figure 4b) and generally show greater lateral extent of plume growth. This allows us to assess the risks associated with the spatial extent (boundaries) of plume growth, as well as determine the reliability of predictions. For example, when uncertainties indicate a wider lateral plume extent than predicted, it signals the implementation of more cautious MVA protocols to constrain the plume.

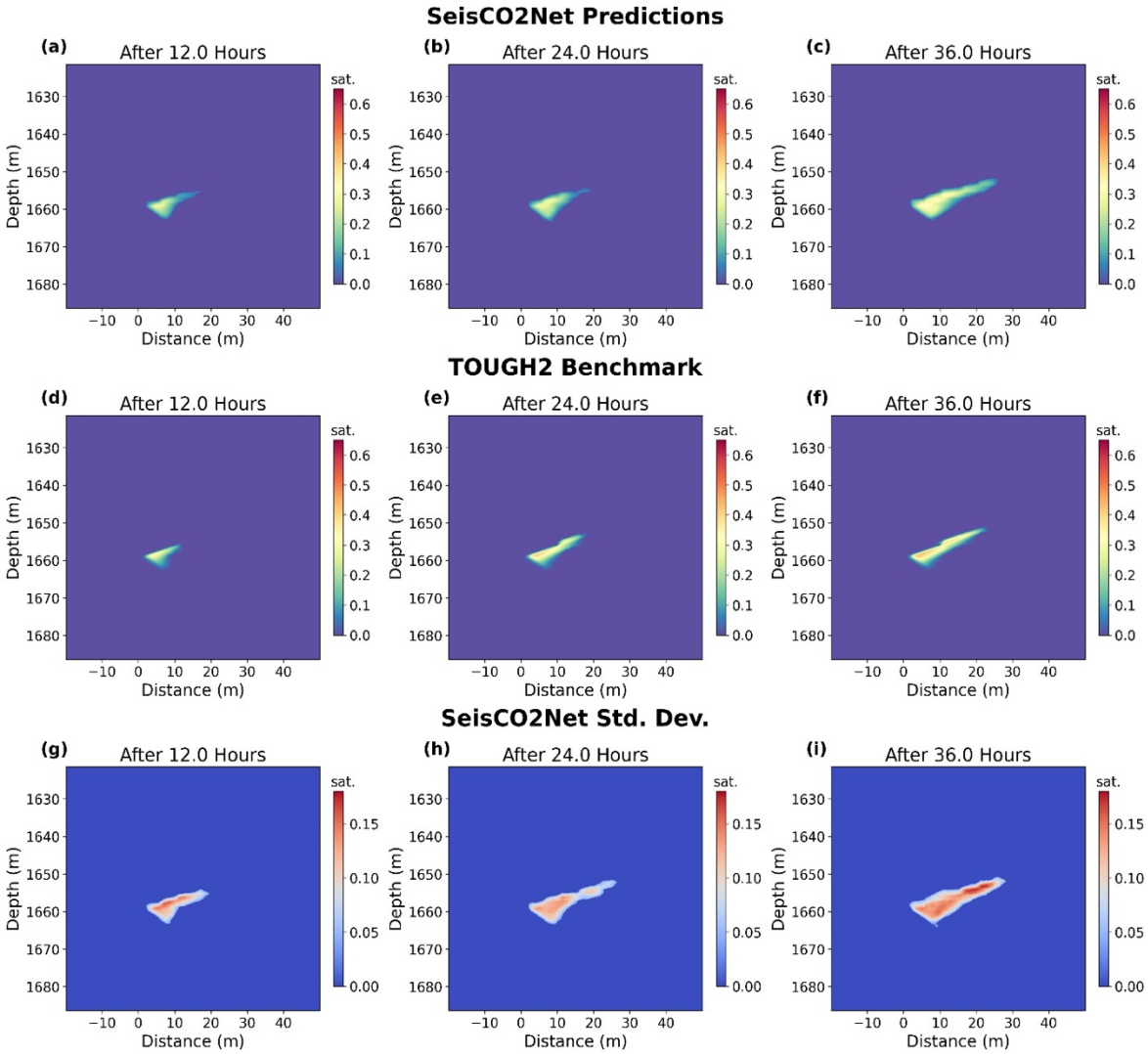

Figure 4: (a)-(c): Predicted CO_2 saturation maps on Frio-II field shot gathers at different elapsed times. We compare the predictions with TOUGH2 benchmark models (Daley et al., 2011) in (d)-(f). From the 20 trained weights, we compute SeisCO2Net's uncertainties (g-i).

From the results, we enlarge the shot gather at 36 hours post-injection (Figure 5) for better visual comparison. We also compare the data matching, and attach the corresponding CO_2 saturation prediction overlay with Frio-II site schematics for illustration purposes. We highlight the good data match in dark blue dashed circles. We see that at receiver of depth 1645m, the synthetic coda waves match with the field data significantly well. The first arriving wavelet and the trailing coda wavelets closely overlap the field data. Besides, at receiver of depth 1653m, the data match also show good matching. At trace of 1669 depth, the first arriving wavelet completely match the field data. Based on these factors, we postulate that the predicted CO_2 plume at 36 hours post-injection is likely to be accurate.

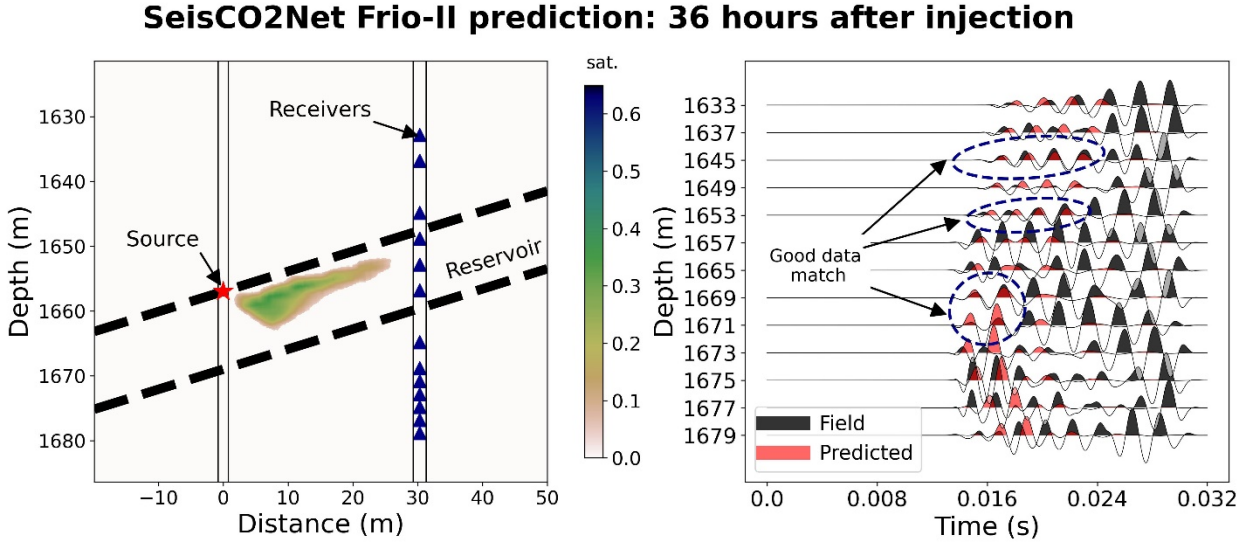

Figure 5: Left panel shows the corresponding CO_2 saturation map predicted by SeisCO2Net on Frio-II field data 36 hours post-injection. Right panel illustrates the comparison of synthetic vs. field data. The dark blue circles highlight several instances where the data matches well, which increases our confidence in the CO_2 plume prediction.

6 Conclusion

Conventional methods for inverting CO_2 saturation from time-lapse seismic data are typically consist of tedious and time-consuming workflows, as well as preprocessing steps that are subjected to human-error. In this paper, we propose a deep learning (DL) solution - SeisCO2Net that estimates CO_2 saturation maps directly from time-lapse seismic shot gathers (only one seismic shot). Compared to the existing DL methods, this study is the first to demonstrate the implementation of neural networks (via SeisCO2Net) on field seismic data by training on realistic physics-informed synthetic datasets (CO_2 saturation and shot gathers) that closely mimic field settings. We show a field application example at Frio-II CO_2 sequestration pilot site. Our implementation workflow enables the generation of numerous training dataset which essentially overcomes the paucity related to field training data. The prediction results of SeisCO2Net exhibit a close resemblance to TOUGH2 in terms of CO_2 plume shape and saturation values. This assessment is further supported by the good match between SeisCO2Net's predicted forward data

and Frio-II field data, particularly at the first few arriving wavelets. In sum, this study investigates the real-world application of DL algorithms on field seismic data to directly estimate CO_2 saturation. Our proposed SeisCO2Net along with its implementation workflow could potentially pave the way in the future of seismic monitoring for long-term geological CO_2 storage.

At the Frio-II storage site, the seismic monitoring setup consists of only one source, which poses a challenge for conventional seismic inversion and imaging. Such conventional methods typically require multiple sources to yield accurate estimates of CO_2 saturation. In situations where field seismic data collection is not ideal (e.g., one-source), conventional methods may be unable to estimate CO_2 saturation. This highlights a significant advantage of SeisCO2Net: its ability to perform inversion even when faced with limited data, such as single-source scenarios. Consequently, SeisCO2Net offers a valuable alternative for estimating CO_2 saturation in situations where conventional methods may struggle due to data limitations.

SeisCO2Net can be modified and adapted to other field sites. In the demonstrated Frio-II site application, SeisCO2Net estimates CO_2 saturation maps using only single source and noisy field data. When applied to CO2 sites with more comprehensive seismic monitoring setups (e.g., multiple sources and additional receivers), SeisCO2Net's performance could potentially improve, as the inverse problem becomes better constrained with increased input information. SeisCO2Net's input and output convolution kernel and padding sizes can be adjusted to accommodate different field seismic gathers and CO_2 saturation models. Although adding more convolution layers can enhance its nonlinear solving capabilities, it may result in reduced efficiency. SeisCO2Net combines autoencoder and deep CNNs, utilizing dimensionality reduction to boost the training and prediction efficiency while minimizing information loss when using encoded CO_2 saturation maps. This underscores its applicability in large field sites (e.g., Sleipner) requiring higher resolution maps. Given site-specific geological information (e.g., reservoir characterization and velocity models), a comprehensive training dataset covering diverse reservoir parameters and seismic responses can be created. By employing advanced deep learning algorithms like SeisCO2Net, CO_2 saturation maps can be efficiently predicted, significantly reducing the need for labor-intensive conventional CO_2 inversion workflows.

References:

Leong, Z. X., T. Zhu, and A. Y. Sun, 2022, Estimating CO2 saturation maps from seismic data using deep convolutional neural networks: Second International Meeting for Applied Geoscience & Energy, SEG/AAPG, Expanded Abstracts, 510-514.

Li, B., and Y. E. Li, 2021, Neural Network-Based CO2 Interpretation From 4D Sleipner Seismic Images: Journal of Geophysical Research: Solid Earth, **126**, e2021JB022524.

Li, D., S. Peng, Y. Guo, Y. Lu, and X. Cui, 2021, CO2 storage monitoring based on time-lapse seismic data via deep learning: International Journal of Greenhouse Gas Control, **108**, 103336.

Liu, M., D. Vashisth, D. Grana, and T. Mukerji, 2022, Joint Inversion of Geophysical Data for Geologic Carbon Sequestration Monitoring: A Differentiable Physics-Informed Neural Network Model: Journal of Geophysical Research: Solid Earth, **128**, e2022JB025372.

Ronneberger, O., P. Fischer, and T. Brox, 2015, U-Net: convolutional networks for biomedical image segmentation: In Medical Image Computing and Computer-Assisted Intervention – MICCAI 2015, **9351**, 234–41.

Sinha, S., R. P. de Lima, Y. Lin, A. Y. Sun, N. Symons, R. Pawar, and G. Guthrie, 2020, Normal or abnormal? Machine learning for the leakage detection in carbon sequestration projects using pressure field data: International Journal of Greenhouse Gas Control, **103**, 103189.

Um, E. S., D. Alumbaugh, Y. Lin, and S. Feng, 2022, Real-time deep-learning inversion of seismic full waveform data for CO2 saturation and uncertainty in geological carbon storage monitoring: Geophysical Prospecting.

Wang, Z., R. M. Dilmore, and W. Harbert, 2020, Inferring CO2 saturation from synthetic surface seismic and downhole monitoring data using machine learning for leakage detection at CO2 sequestration sites: International Journal of Greenhouse Gas Control, **100**, 103115.

Wen, G., M. Tang, and S. M. Benson, 2021, Towards a predictor for CO2 plume migration using deep neural networks: International Journal of Greenhouse Gas Control, **105**, 103223.

Published journal papers:

- Huang C., Zhu T., and Xing G., (2023), Monitoring dynamic evolution of CO2 plumes during geological sequestration using data assimilated visco-acoustic full-waveform inversion, Geophysics.
- Liu X., Zhu T., and Ajo-Franklin J. (2023). Understanding subsurface fracture evolution dynamics using time-lapse full waveform inversion of continuous active-source seismic monitoring data. Geophysical Research Letters, 50, e2022GL101739.
- Xing G., and Zhu T., (2022), Decoupled Fréchet kernels based on a fractional viscoacoustic wave equation, Geophysics 87: T61-T70.
- Joon, Shams, Ismael Dawuda, Eugene Morgan, and Sanjay Srinivasan. 2022. "Rock Physics-Based Data Assimilation of Integrated Continuous Active-Source Seismic and Pressure Monitoring Data during Geological Carbon Storage." SPE Journal:1-15.
- Xing G., and Zhu T., (2021), *A viscoelastic model for seismic attenuation using fractal mechanical network*, Geophys. J. Int, 224(3),1658–1669.
- Huang C., and Zhu T., (2020), Towards real-time monitoring of geological CO2 storage: data assimilated time-lapse full waveform inversion for seismic velocity and uncertainty estimation, Geophys. J. Int, 223 (2), 811-824.
- Zhu T., Ajo-Franklin J., Daley T.M., and Marone C., (2019) Dynamics of geologic CO2 storage and plume motion revealed by seismic coda waves, *Proceedings of the National Academy of Sciences of the United States of America*, 116 (7) 2464-2469
- Xing G. and Zhu T., (2019) Modeling frequency-independent Q viscoacoustic wave propagation in heterogeneous media, *Journal of Geophysical Research: Solid Earth*, 124(11), 11568-11584